Fermilab FERMILAB-THESIS-2002-04

The Forward Preshower System and a Study of the J/ψ Trigger with the DØ Detector

A Dissertation Presented

by

Abid M. Patwa

to

The Graduate School

in Partial Fulfillment of the Requirements

for the Degree of

Doctor of Philosophy

in

Physics

State University of New York
at
Stony Brook

May 2002

State University of New York
at Stony Brook

The Graduate School

Abid M. Patwa

We, the dissertation committee for the above candidate for the Doctor of Philosophy degree, hereby recommend acceptance of the dissertation.

dissertation director
Dr. Michael Rijssenbeek
Department of Physics and Astronomy

chairman of defense
Dr. Jack Smith
Department of Physics and Astronomy

committee member
Dr. Barbara Jacak
Department of Physics and Astronomy

outside member
Dr. Jonathan Kotcher
Physics Department
Brookhaven National Laboratory, USA

This dissertation is accepted by the Graduate School.

Graduate School

Abstract of the Dissertation

The Forward Preshower System and a Study of the J/ψ Trigger with the DØ Detector

by

Abid M. Patwa

Doctor of Philosophy

in

Physics

State University of New York at Stony Brook

2002

This dissertation describes the Forward Preshower system, one of four inner-tracking subdetectors in the DØ Detector, designed and built for operation in Run II at the Fermilab Tevatron collider. The scintillator-based detector has been constructed to enhance the electron and photon triggering capability and offline particle identification at DØ over a broad range in pseudorapidity. A discussion of the design, technology, systematic assembly, and performance of the system is presented along with a description of the relevant physics topics the detector will address.

A study of a $J/\psi \rightarrow e^+e^-$ trigger incorporating the Central Preshower with the Central Calorimeter, Silicon Microstrip and

Fiber Trackers is also presented. A description is given of the trigger algorithm along with selection efficiencies and QCD rejection as measured with Monte Carlo samples. A trigger efficiency of at least 60%, with background rates well within the allocated trigger bandwidth, can be achieved through the use of tracking and electron cluster information from the preshower system.

"Armed with giant machines and grand ambitions, physicists spend billions in the race to discover the building blocks of matter."

- *Time Magazine:* "The Ultimate Quest"
April 16, 1990, Pp. 50-56.

"...Listen, buddy, if I could tell you in a minute what I did, it wouldn't be worth the Nobel Prize!..."

- Richard P. Feynman,
to a journalist

In honor of my parents:

To my mother

And in memory of my father

Contents

Acknowledgements . . . . . **xxxiii**

1 Introduction **1**

2 Theoretical Overview **3**

2.1 The Standard Model 3

2.2 Physics Signatures 8

3 Experimental Apparatus **15**

3.1 Definitions and Conventions 15

3.1.1 Coordinate Systems 15

3.1.2 On Luminosities and Cross Sections 17

3.2 The Tevatron Collider 20

3.3 DØ Detector 24

3.3.1 Silicon Microstrip Tracker 26

3.3.2 Central Fiber Tracker 29

3.3.3 Central Preshower 33

3.3.4 DØ Calorimetry 35

3.3.5 Calorimeter Readout 41

3.3.6 Calorimeter Performance 43

3.3.7 ICD 43

3.3.8 Muon System 44

3.4 DØ Trigger System 49
3.4.1 Level 1 Trigger 50
3.4.2 Level 2 Trigger 51
3.4.3 Level 3 Filter and DAQ System 54

4 Physics Motivation for DØ Preshowers 57
4.1 Physics Topics 58
4.1.1 γ/π° Separation 58
4.1.2 Low-p_T Phenomena 60
4.1.3 Precision Measurements 61
4.1.4 QCD and Electroweak Processes 62
4.2 Case Study for Inclusion of FPS at DØ 65
4.3 Summary 69

5 Properties of Scintillation-based Detectors 71
5.1 Scintillation Principles 71
5.1.1 WLS Fibers 74
5.2 Application: DØ Forward Preshower detector 79
5.2.1 Preshower Scintillator and Fiber 80
5.2.2 FPS Readout Scheme 87

6 Forward Preshower Design 95
6.1 Conceptual Design 96
6.2 FPS Geometry and Technical Design 100

7 Forward Preshower Construction 111
7.1 Module Construction 111
7.1.1 Spherical Template 112
7.1.2 Scintillator Strip Preparation 112

7.1.3 Module Fabrication 115
7.1.4 Module Cutting 123
7.1.5 Strip-to-Strip Alignment Study 125
7.2 Detector Support Structure and Assembly 126
7.2.1 Detector Structure — General Principles 127
7.2.2 Assembly Hardware 131
7.2.3 FPS Inner Ring and Support Rib Structure 134
7.2.4 Modular Frame Box Assembly 139
7.2.5 Lead Absorber and Support 142
7.3 Module Cabling and Certification 157
7.3.1 FPS Optical Connectors – Design and Support 157
7.3.2 Preparation of Fiber & Connector Assemblies 160
7.3.3 Module Cabling 165
7.3.4 LED Monitoring and Calibration Systems 168
7.3.5 Module Certification and Integration 169

8 Installation and Alignment 171
8.1 Installation and Alignment I: FPS Support Hardware 172
8.1.1 Inner Pin Surveying 180
8.2 Installation and Alignment II: FPS Detector 183
8.2.1 Module Survey 187
8.3 Luminosity Monitor and ICD Mounting 192
8.4 FPS Commissioning 195

9 Physics Studies with the Preshower and DØ 197
9.1 Motivation and Constraints 198
9.2 Software and Trigger Framework 199
9.2.1 Event Generation and Processing: J/ψ Signal 199

9.2.2 Event Generation and Processing: QCD background . 201
9.3 Level 3 Analysis 203
9.3.1 Preliminary Studies: Matching and Mass Resolutions . 203
9.3.2 Event Preselection: L1 and L2 Simulation 213
9.3.3 Classification of Electrons at Level 3 215
9.3.4 CPS Detector Efficiency 232
9.3.5 J/ψ Invariant Mass 233
9.3.6 L3 J/ψ Trigger: Signal Efficiency and Rates 236
9.3.7 Signal Improvements 241
9.3.8 Study of L3 b-tagging 245

10 Summary and Conclusions 249

List of Figures

2.1 Measured Run I Tevatron W boson mass vs. top quark mass, shown by (a) cross-hatched oval, in addition with W mass band from LEP2, CERN (d). The four shaded bands (c) represent expected values for a specific Higgs boson mass in the SM, where the 1σ-width in each band is due to $\alpha_s(M_Z^2)$. The solid oval (b) shows a predicted Run II Tevatron measurement (using Run I central values) and is given for comparisons. Adapted from [17]. 8

3.1 Schematic of the Run II Fermilab accelerator complex. Adapted from [20]. 19

3.2 Two-dimensional view of the Run II DØ detector, showing the three integral systems outlined in the text. 26

3.3 Three-dimensional view of the DØ silicon microstrip tracker. 27

3.4 Schematic of an observed displaced vertex originating from b or c quarks in a silicon microstrip detector. 27

3.5 Simulation results for the momentum resolution with the Fiber Tracker as a function of psuedorapity (η) for three different p_T values. 30

3.6 Quarter r–z view of CFT detector as installed at DØ. Shown is a) the nested eight barrel configuration of the device, A magnified r–ϕ end-view of the two ribbon doublet layers per barrel is also given in (b). 31
3.7 a) Distribution for the position resolution measured in the Fiber Tracker for single muons traversing b) an interlocking ribbon doublet configuration. 32
3.8 Central Preshower detector shown in: a) r–z semi-quarter-view and b) cross-sectional (r–ϕ) end-view of the DØ tracking system. The inset in (b) gives a magnified view of the triangular strip nesting and layer configuration. 33
3.9 Cutaway view of the DØ calorimeter. 36
3.10 Schematic view of a representative calorimeter unit cell. The gap structure, grounded absorber plates, and signal boards are shown. 37
3.11 Side-view of one quarter of the DØ calorimeter system, showing segmentation and tower definitions (see text). The lines extending from the center of the detector denote the pseudorapidity coverage of cells and projected "towers". 39
3.12 Calorimeter channel configuration in terms of depth and η. . 40
3.13 Schematic of the primary elements for the DØ calorimeter electronics. 42
3.14 r–z half-view of the Muon System. Components of both the Forward and Central systems are shown. 46
3.15 Illustrative view of one r–ϕ plane in the muon mini-drift tube. The insert shows the cross section of a single Iarocci tube, which consists of eight 1×1 cm^2 cells. 47
3.16 r–ϕ segmentation of the muon scintillator pixel counters. . . . 48

3.17 Summary of the three-level DØ Trigger System for Run II with the decision time and bandwidth allocated to each level. . . . 50

3.18 L1 and L2 trigger data pathway. The arrow indicates the direction of data flow. Multiple arrows from a particular subsystem are present for parallel processing of detector information and thus, to permit fast trigger decisions and sophisticated physics filters. 52

3.19 Configuration of L2 trigger components. 53

3.20 L3 trigger framework. Data flow is indicated by the direction of the arrow. 55

4.1 Simulation of the Run II DØ calorimeter measuring a) the response to $E_T = 2$ GeV electrons at $\eta = 1$ for the cases with (solid-line) and without (dashed-line) a preshower detector. The resolution with calorimetry alone is shown to be about 18% and improves to 13% when preshower information is included. Also shown is b) the response to $E_T = 30$ GeV electrons with a preshower detector. 59

4.2 Simulations of the photon-lepton rapidity difference distribution for $W\gamma$ production for 1 fb^{-1}, using a) central and endcap photons and electrons, and b) central photons and electrons only. Adapted from [58]. 64

5.1 Representation of energy levels indicating the fluorescence mechanism in a scintillator. Shown are: a) the π electron energy levels participating in scintillation light and b) the energy transfer process in a scintillator from a solvent (X) with two fluors (Y & Z). Adapted from [62]. 73

5.2 Schematic configuration of a typical WLS fiber: a) single clad and b) double clad fibers are shown. Adapted from [62, 32]. . 75
5.3 Fluorescence spectrum of BC-404 (top) and K27 (bottom). For BC-404, the two peaks near 350 (400) nm are from pT (DPS). The light transmission curve is also given. The light output from BC-404 is a convolution of the emission and transmission curves. For K27, the emission peak includes the effects of self-absorption and is at ∼500 nm. Adapted from [54]. 81
5.4 Chosen concentrations of scintillating fluors, pT (top) and DPS (bottom) for extruded scintillating strips. The concentration mixtures are determined on the basis of approximating BC-404 scintillator as well as aiming to minimize light re-absorption. Adapted from [67]. 83
5.5 a) Detail of the scintillator dimensions used for the preshower detectors. Dimensions are in inches. Also shown are the scintillator spacing for the (b) preproduction prototype modules and (c) representative modules in the FPS detector. The nesting of each strip, and hence, a layer's thickness is different in the two methods. 84
5.6 Residuals for preshower cluster position relative to a PDT track used to measure the spatial resolution for MIPs in a module readout by 11.0 m lightguide and VLPCs. Shown are distributions for both singlet (dashed) and doublet (dotted) tracks (see text for definitions) as well as the data (circles) fitted to double-Gaussian (solid). MC simulations are shown in histograms. . 86
5.7 Schematic of the FPS readout system. 87
5.8 Cross-sectional illustration of VLPC operation (top) and corresponding electric field profile (bottom). 89

5.9 Picture of a VLPC chip. The chip has 8 pixels of 1 mm diameter mounted on an aluminum-nitride substrate. The gold-plate conduction pads on the substrate are contacts for the 8 signal outputs and the bias. 90

5.10 Measurement of preshower light-yield for MIPs (a) in a cosmic ray system setup. Shown are data corrected for $\cos\theta$ (solid line) as well as singlet (dashed) and doublet (dotted) extrapolations. Charge uniformity, mean charge vs. channel number, is given in (b). Distributions represent results using final scintillator strips, WLS fibers, 11.0 m clear lightguides, and VLPCs. . . . 93

6.1 FPS module's azimuthal geometry with joint u-v MIP and Shower sublayers, each separated by a lead absorber. 97

6.2 Typical GEANT simulated signature of 50 GeV a) electrons and b) neutral pions traversing the FPS detector. 99

6.3 Cross-sectional r–z view of the FPS detector at DØ. Given within the inset is a module's triangular strip nesting configuration. 100

6.4 Three-dimensional view of a trapezoidal shaped FPS ϕ-module in its supporting frame. Shown are the main elements including WLS fibers, optical connectors and brackets, surveying targets, and protective clear frame-covers. See text for complete description. 102

6.5 Module orientation within two successive FPS layers. Given is the $1/2''$ overlap region between two adjacent ϕ-modules as well as dimensions of the active area of each module type (see text for description). 104

6.6 r–ϕ view of the North-FPS detector. For brevity, only (nested) Layers 2 and 4 are shown; Layers 1 and 3 are rotated by 22.5° in ϕ with respect to these layers. Also, the South-FPS is not given here, as it is a symmetric, mirror-image of the north detector. 105

6.7 The three different types of representative FPS modules: a) Large Module (LM), b) Small Module (SM), and c) "Special" Module (SpM). 107

7.1 Schematic of module fabrication: strip-by-strip layout, registration and alignment on the spherical template dome is shown. Given are a) top r–ϕ modular view including the "nested" triangular strip cross-section and b) side r–z profile of assembly. 118

7.2 Strip-by-Strip layout using lateral alignment bars (1) and alignment stops (2) for module fabrication. Shown are a) v-layer, b) u-layer, and c) mated u–v layer, all assembled on d) the spherical (r–z view) "template" dome. The fiducial holes in (2) serve to reference the module's position during water-jet and/or end-mill cutting. 121

7.3 Result for channel-to-channel alignment accuracy measured using a CMM for a FPS module. A narrow distribution with an accuracy of about 60 μm is achieved and well within design specifications. 125

7.4 Three-dimensional view of the layered FPS support structure assembly. For brevity, all modules and lead pieces are not shown. 128

7.5 Production print of the outer support arc in a large module/frame unit. The arc is precisely machined with angles on both the $\pm z$-surfaces to conform to the spherical EC head. For completeness, r–z cross-sectional views along the arc are shown in circles #1–4. The geometry for the SM and SpM arcs is designed and constructed similarly. 129

7.6 Section of FPS outer arc supporting optical connectors and required brackets, all protected by a 1/16″-thick aluminum covering plate. 130

7.7 One-to-one assembly of DØ EC head for detector assembly during FPS construction. The eight stainless steel support pins mounted on the dome are supported by the adjustable rear base-plate aligned on the dome. 131

7.8 Detector inner support pins mounted within the wooden dome/base plate assembly. The pins support the FPS inner ring structure outlined in Sec. 7.2.3. 133

7.9 Vertical mounting of the mocked-EC head for final testing of the assembly procedures prior to installation at DØ. Shown are: a) r–z view and b) r–ϕ view. To facilitate module insertion and removal, the dome is made to rotate about a central axis. . . 134

7.10 Inner support rings for Layers 1–4 (FPS-North). (a) gives each layer's ring and its respective r–z profile. The rings for L1 and L3 are geometrically similar and only differ in the nesting configuration in the r–z plane. (b) gives a limited, expanded r–ϕ view of the different sets of holes used for assembly and mounting, outlined in the text. Rings for FPS-South are a symmetric, mirror-image of the north half. 136

7.11 View of FPS supporting unit for independently constructed modular frames. Shown is an inner ring with machined slots to attach the support rib array. Modules for all subsequent active layers are supported in a similar manner. 137

7.12 Module insertion process into FPS support structure. The lower radius of the module is inserted first until its v-notch rests on dowel pins attached to each rib (1), and the full unit is pitched about z for holes at (2) to be aligned and bolted. 140

7.13 Three-dimensional view of alignment jig used to assemble and align module frames and each element. Details are given in the text. 141

7.14 (a) An r–ϕ view of the outer edge of a layer, showing the means of module fixation within individual supporting frames using aluminum fixation tabs. Each module is held in place in an identical manner at each of its four corners. Also shown are b) and c) details of the fixation tab attached to the surface of a corner fixation plate with pan-head screws in (d). The threaded tube stand-off is held to the tab's platform using a flat-head screw on the $+z$ surface. 143

7.15 Lead absorber layer design with eight 45° wedge-like elements: (a), (b), and (c) showing the side, front, and three-dimensional views, respectively, including the beveled "rabbit-cut" on the ϕ-edges of each absorber. This ensures (d) nesting with adjacent pieces, and thus, full coverage. 145

7.16 Lead absorber design using 7.5° wedge-like elements: (a) and (b) shows the front r–ϕ view of the stainless-steel support unit and lead sublayer, respectively, as individual elements, while the assembled view is given in (c). A cross-sectional profile of each component is given in (d), (e), and (f), respectively. . . 146

7.17 Lead base-plate and tooling hardware used for Pb-SS-Pb bonding and production. See text and Fig. 7.18 for description of tooling items (a), (b), and (c). 148

7.18 Registration hardware for lead-stainless-steel-lead pieces used during bonding. Items (a) and (b) control the r–z alignment of individual Pb-SS-Pb sublayers, whereas (c) defines the ϕ-positioning of each piece. 149

7.19 Precision-machined lead layer's inner support ring with closure segment. Shown are the eight through-holes that mate to supporting inner pins welded on EC wall as well as a cross-section (insert) illustrating the ring's r–z surface. In order to properly nest and anchor a cylindrically-shaped Pb-SS-Pb element, an angular profile is needed on the surface. Note: all fixation holes on the closure segment are made *in situ* during actual lead layer assembly. 153

7.20 Lead layer support assembly showing bonded pieces mounted between inner- and outer-support rings. A 2-D projection of the completed layer (b) and a close-up of the outer-ring's cross-sectional profile (c), which follows the L2 rib's spherical profile are given. 155

7.21 3-D view of detector-side (mating) FPS optical connector assembly and alignment. 158

7.22 Observed light transmission for each channel in a 16-channel one-to-one mated connector assembly (a), and the measured distribution of fiber channel transmissions (b). Both distributions yield, on average, 95% light transmission through the fiber/connector interface. 158

7.23 Front face of the 4×4 array, sixteen-channel FPS a) WLS-fiber (detector-side) optical connector and its mating b) clear-fiber (light-guide side) connector. All dimensions are given for completeness. 160

7.24 ϕ–z view of the single row connector mounting configuration in each FPS module. 160

7.25 r–z view of FPS connectors at the outer periphery of Layers 1 and 2. An angular pitch to these connectors is made for waveguides to clear the existing ICD tiles at this radius. . . . 161

7.26 Sectioning of a) large, b) small, and c) "special" modules into regions with a given quantum of scintillator strip channels for WLS fiber and connector cabling. 164

7.27 An r–ϕ view of a large module in L1 or L2 of the FPS, showing the WLS fiber/scintillation strip layout and connector-by-connector mapped routing. Individually labeled connectors are shown at the top and map to sections of 16 contiguous strips on a module's u- or v-sublayer. Cabling for the u-layer is only shown — the v-layer follows in a mirror-symmetric manner. . 166

7.28 LED calibration and monitoring system. Shown are: a) a hollow-cylindrical cavity grouping sixteen WLS fibers and b) the surface-mounted LED pulser boards supplying the signal. Cavity 1 and 2 in (a) are mated and aligned together, being fixed with five-minute epoxy between their outer and inner cylindrical walls, respectively. 169

8.1 a) r–ϕ view of template used to align and weld eight stainless-steel inner pins for FPS support on EC heads and b) r–z view of assembly. Also shown is an inner ring (B) mounted in z with the template (A) to guarantee each pin is parallel to one another. 173

8.2 a) Stainless-steel FPS inner-support pin with dimensions and b) cross-sectional view of nested FPS layers and inner pin assembly. Eight such pins are aligned and welded on each cryostat head to support the detector. 175

8.3 Welded stainless-steel brackets supporting the FPS support rib and detector structure at its outer radial periphery on the EC head. Shown are a) FPS L2's (two-piece) bracket and spacer as well as b) L1's (one-piece) bracket. At both L1 and L2, an equivalent T-shaped aluminum bracket (a) and (b) allows for a coupled ICD and FPS support. 178

8.4 Lead layer's precision outer support-ring provides a convenient technique to establish the detector's r–ϕ coordinates on the cryostat head, prior to welding and module insertion. 179

8.5 Configuration of the DØ Detector during the FPS installation period at Fermilab. See notes in figure and text for a description of the scenario available for preshower assembly and installation. 181

8.6 Generic FPS module illustrating the six (1-6) CMM installed K&E targets and four (1*–4*) manually placed V-star targets. K&E target #1 defines the origin and reference to which all other V-star mapping positions are made. 189

8.7 Graphical representation of survey target location for the eight modules installed in Layer 1 of FPS-North on the cryostat head. Shown are the actual V-star measurements (asterisk) extrapolated with the mapped K&E (open circle). As described in the text, the location of any V-star target is measured with respect to an arbitrarily chosen K&E (closed triangle), which is taken as the origin (0,0) for the module. 191

8.8 One of sixteen flat ICD panels mounted on each end-cryostat head. Shown are: a) r–ϕ view and b) r–z view of a tile. . . . 192

8.9 3-D frame view in (r, z, ϕ) illustrating two ICD tiles nested on the EC wall. Shown are: a) a view from the innermost z-surface of two panels and b) a similar forward angular view. The brackets supporting the ICD are designed to securely fit within the gap existing between tiles. 194

9.1 Matching resolutions in η and ϕ for MC electrons with (a-b) global tracking (*i.e.,* CFT and SMT) and (c-d) calorimeter, respectively. 204

9.2 Distributions for (a) $\Delta\phi$, (b) $\Delta\eta$, and (c)ΔR for tagged electrons in global tracks and calorimeter clusters in the J/ψ sample. A value of $R_{cone} = 0.2$ has been used to define L3 calorimeter clusters. The correlation in $\Delta\eta$ with $\Delta\phi$ is also shown in (d). 207

9.3 Distributions for (a) $\Delta\phi$, (b) $\Delta\eta$, and (c)ΔR for tagged electrons in global tracks and calorimeter clusters in the J/ψ sample for $R_{cone} = 0.4$. The correlation in $\Delta\eta$ with $\Delta\phi$ is also shown in (d). 208
9.4 $\Delta\phi$ distribution for electrons matched in the global tracker and calorimeter for (a) $\Upsilon \to ee$ and (b) $Z \to ee$ final states. 209
9.5 Distributions for (a) $\Delta\phi$, (b) $\Delta\eta$, and (c)ΔR for calorimeter and CPS clusters using tagged electrons in the J/ψ sample. Results are for calorimeter clusters with $R_{cone} = 0.2$. The correlation in $\Delta\eta$ with $\Delta\phi$ is also shown in (d). 210
9.6 Distributions for (a) $\Delta\phi$, (b) $\Delta\eta$, and (c)ΔR for calorimeter and CPS clusters using tagged electrons in the J/ψ sample. Results are for calorimeter clusters with $R_{cone} = 0.4$. The correlation in $\Delta\eta$ with $\Delta\phi$ is also shown in (d). 211
9.7 Distributions for (a) $\Delta\phi$ and (c) Δz for tracks and CPS clusters using tagged electrons in the J/ψ sample. The correlation between these two variables is given in (d). Also shown in (b) is the $\Delta\phi_{Q-flip}$ distribution without offset corrections, described in the text. 212
9.8 Schematic of the bimodal distribution in $\Delta\phi$ observed in the match between the tracker and CPS. See text for further discussion. 213
9.9 $\Delta\phi$ distribution for CPS clusters and tracks after correcting for the offset resulting from the "Q-flip". The distribution has been fitted to a Gaussian to determine an order of magnitude of the resolution in ϕ. 214
9.10 Match in z for CPS clusters and tracks for (a) $\Upsilon \to ee$ and (b) $Z \to ee$ final states. 215

9.11 Separation of electron pairs from the J/ψ in (a) η and (b) ϕ. 215
9.12 Distribution for the separation of lepton pairs (a) in η and (b) in ϕ, as a function of the reconstructed invariant mass in the J/ψ sample, respectively. Shown is the distribution for electron pairs from J/ψ (closed-circle) and from background combinations (open-circle). 216
9.13 Distribution for the separation of lepton pairs in (a) η and (b) ϕ as a function of the reconstructed invariant mass for the QCD $p_T > 20$ GeV sample. 217
9.14 Invariant mass resolutions for $e^{\pm}$ pairs from J/ψ decays. Shown are reconstructed mass (using Eq.—9.2)from (a) MC generator-level, (b) calorimeter-based variables, (c) combined calorimeter E_T with track's $\Delta\phi$ and $\Delta\eta$ measurement, and (d) track-based variables. 218
9.15 EM_{frac} measured within the central calorimeter fiducial. Shown is the distribution for reconstructed clusters (solid-line) and tagged-electron tracks (dashed-line). An initial cut at 0.8 is applied for basic selection of electrons. 220
9.16 Schematic of the Level 3 algorithm for electron identification and selection. The sum of the efficiencies for the electron categories Type 1 through 4 yield the total calorimeter efficiency, Eff_{CAL}. 221
9.17 Distributions of matching between calorimeter clusters and global tracks for electron selection in (a) η and (b) ϕ for the J/ψ sample. 222
9.18 Distributions of matching between calorimeter and preshower clusters for electron selection in (a) η and (b) ϕ for the J/ψ sample. 222

9.19 Type 1 selection variables and cuts implemented for electron identification on J/ψ sample: track-preshower match in (a) z and in (b) ϕ after correcting for magnetic field effects at the CPS radius. Also, shown are the intervals in which selections have been made. 224
9.20 Similar distributions as in Fig. 9.19 for Type 1 selections implemented on (a-b) QCD $p_T > 2$ GeV and (c-d) QCD $p_T > 10$ GeV samples. 225
9.21 Miscellaneous selection variables studied for Type 1 electrons from the J/ψ: (a) calorimeter EM_{frac} and (b) ΔR match between a track and preshower cluster. See text for complete discussion. 226
9.22 Distribution of E/p measured at L3 for a) signal and b) QCD. In (a), the reconstructed clusters (solid-line) are overlapped with tagged-electron tracks (dashed-line). 228
9.23 Type 3 selection variables and cuts implemented for electron identification in the J/ψ sample: (a) ϕ-match between the tracker and calorimeter and (b) EM fraction measured in the calorimeter. Also, shown are the intervals in which selections have been made. 230
9.24 Similar distributions as in Fig. 9.23 for Type 3 selections implemented on (a-b) QCD $p_T > 2$ GeV and (c-d) QCD $p_T > 10$ GeV samples. 231
9.25 Number of candidates per events for J/ψ sample using calorimeter cluster cone sizes of (a) 0.2 and (b) 0.4. In either case, only those events with two or more electrons are used for the invariant mass calculation. Note the improvement in the number of events with two electrons for ΔR=0.2. 233

9.26 Invariant mass distribution for Type 1 pairs using R_{cone}=0.2. Given is the track-based results for (a) opposite- (os) and same- (ss) sign pairs (open-histogram), and same-sign pairs (shaded-histogram). The distribution in (b) shows results for only os pairs with the mass window shown by the vertical lines. See text for further discussion. 234
9.27 Similar invariant mass distribution as Fig. 9.26 for pairs where at least one electron is of Type 1 while the other is either Type 1 or 3. See text for further discussion. 234
9.28 Similar invariant mass distribution as Figs. 9.26 and 9.27 for Type 3 pairs. See text for further discussion. 235
9.29 (a) Invariant mass distribution as for single electron candidates in the J/ψ signal sample paired with L3 reconstructed tracks. Also shown are corresponding (b) $\Delta\eta$, (c) $\Delta\phi$, and (d) $\Delta z_\circ$ distribution for all pairs. Results for $R_{cone} = 0.2$ are shown. . 242
9.30 ΔR matching distribution for L3 tracks and preshower clusters needed for single electron candidate and L3 track pairing. Value for the cut has been chosen to help suppress QCD backgrounds during invariant mass reconstruction. 243
9.31 Invariant mass distribution for single electron candidates in the J/ψ signal sample paired with L3 reconstructed tracks requiring (a) η, ϕ, and common vertex conditions. Also given is the corresponding distribution requiring (b) a track-preshower match. The mass window in (b) is shown by the vertical bars. 244
9.32 Figurative example of three MC-level electrons in the J/ψ sample. Two of these arise from J/ψ decays while the third must be from the semi-leptonic decay of the b-quark. 246

List of Tables

2.1 Quark family in the Standard Model and some individual properties. The quarks have been divided in terms of their generation with the mass values and ranges obtained from [7]. . . . 4

2.2 Lepton family in the Standard Model and some individual properties. Similar to Table 2.1, the leptons are divided in terms of their generation. 5

2.3 Gauge bosons and their basic properties in the Standard Model. The bosons are divided in terms of the force they transmit. Further, the mass of the W and Z are world average results which include indirect measurements. 5

2.4 Major decay modes of certain high-p_T (W, top, Higgs) and low-p_T (J/ψ) signals. Adapted from [7]. 9

3.1 Various detector-specific L2 preprocessor objects, for electrons, muons, and/or jets. 54

4.1 Dijet cross-sections and corresponding rates (in parantheses) estimated at a Run II luminosity of 5×10^{31} cm^{-2}s^{-1} for various FPS trigger parameters (E_{iso} and spatial EC–FPS match) and as a function of EM trigger tower thresholds, E_T, described in the text. Results adapted from [61]. 66

4.2 Results from MC studies of efficiencies for electrons from b decays and from dijet background sample using reconstructed clusters in the calorimeter (row a) and the FPS (rows b–c), and the algorithm described in the text. The estimated background rate, at the luminosity of 5×10^{31} cm^{-2}s^{-1}, is also given in parantheses. Results adapted from [61]. 69

6.1 Summary of basic particle signatures in the upstream (forward) and downstream (backward) layers of the FPS detector used for particle tracking and identification. 98

6.2 Summary of important detector parameters of the FPS. . . . 109

6.3 Summary of parameters of the FPS modules. 110

7.1 Number of different modular species in each layer of a FPS detector. 127

7.2 Nominal distance required for each lead surface epoxied to its steel support plate relative to the radial edge of the steel as a function of r–z. 150

7.3 Number of sections, optical connectors and channels corresponding to the three different FPS module species. 162

8.1 Outer Mounting Hardware for FPS and ICD: the quantity, material and method of attachment for installation are provided. 179

8.2 Final inner pin deviations for each FPS detector from nominal specifications. The average of all eight pins per cryostat head is determined. Note: cw = clockwise ϕ-rotation and ccw = counterclockwise ϕ-rotation taken from the interaction point. 183

8.3 ϕ-position of anchoring holes drilled on FPS Layer 3 inner ring to accomodate Luminosity Counter installation. Note: a) Hole numbering is needed for installation purposes, and b) 0° is taken at the 12-o'clock position (local FPS coordinates), rotating cw (ccw) for FPS-N (FPS-S). 193

9.1 DØ software release versions for generating and processing J/ψ signal samples for Level 3 studies. See text for a discussion of comments. 200

9.2 Summary of local changes and/or modifications made to L3 filtering tools during event processing under DØTrigSim. A detailed description of each package and corresponding parameter definitions is given in [111]. 202

9.3 QCD background samples available for L3 studies: The p_T range for each event sample is given with the cross-section as obtained using a Gaussian fit to the weighted MC event distribution provided in the DØTrigSim ntuple. Each QCD sample has been generated with on average 0.7 minimum bias overlay expected for a luminosity of 3.2×10^{31} cm^{-2}s^{-1}. 203

9.4 Summary of the L1 and L2 triggers for L3 event pre-selection. 218

9.5 Number of events in signal and QCD background samples passing the L1 and L2 triggers specified in Table 9.4. Values in parentheses indicate the corresponding rates in kHz at the input of L1 and at the output of each trigger level (see also Sec. 9.3.6). 219

9.6 Basic selections applied to calorimeter clusters at Level 3. . . 219

9.7 Definitions of an electron match for identifying (a) tracks and (b) CPS clusters with the calorimeter, as needed by the algorithm described in the text. 221

9.8 Number of electron cluster candidates for both J/ψ and QCD background events passing various trigger conditions in Type 1 after L1 and L2 triggers have been applied. The values for (a) correspond to the basic selection cuts given in Table 9.6, performed prior to the Type 1 requirement in (b). Variables in (c,d) correspond to the two tighter cuts studied in a Type 1 category; these together yield the final "regular" cut (e) imposed on a Type 1 candidate. Those cuts in (f)-(h) are shown only to compare their rejection capability with (e) on QCD samples and are not used in the final analysis. The corresponding values for the J/ψ electron efficiency and QCD rejection, $\mathcal{R}$, (per candidate) with statistical errors are given. 223

9.9 Number of electron cluster candidates for both J/ψ and QCD background events passing various trigger conditions in Type 3 after applying L1 and L2 triggers. The values for (a) correspond to the basic selection cuts given in Table 9.6, performed prior to the Type 3 requirement in (b). The variables in (c,d) provide the tighter conditions studied in the Type 3 category; these together yield the final variables (e) used on a Type 3 candidate. The corresponding values for the J/ψ electron efficiency and QCD rejection, $\mathcal{R}$, (per candidate) with statistical errors are given. 229

9.10 Summary of Type 2 and 4 electron selection requirements. . . 232

9.11 Total number of clusters passing electron Type 1 and 3 for R_{cone} = 0.2 and 0.4. 233

9.12 Number of events in the J/ψ sample passing various mass conditions listed in the text. The events have been grouped according to electron pairs of Type 1 (T1) and/or Type 3 (T3). Results for both $R_{cone} = 0.2$ and 0.4 are given as is the final estimate of the L3 signal efficiency. 237

9.13 Summary of the L3 QCD background rate for (a) Type 1, (b) Type 1 and Type 1 or 3, and (c) Type 3 pairs passing the trigger requirement of two opposite-sign (os) electrons, i, j, contained within a mass window, M_{window}, of $1.2<M(ee)<4.0$ GeV. For comparison, the basic selection rate with the QCD 2 GeV sample is also given. The L3 Observed columns are based on the output of the L3 algorithm, whereas the Estimate represents the QCD 2 GeV rate determined from Eq. 9.10. The values in parentheses denote the number of events passing the trigger. 240

9.14 Summary of signal efficiencies and QCD background rejection at each trigger level using triggers described in Tables 9.4 and 9.5 for L1-L2 and in Table 9.13 (triggers (a,b)) for L3. For the J/ψ, the overall efficiency considers MC generator-level effects. For QCD, the rejection capability at each stage is listed. Here, the L3 acceptances for QCD 2, 5 GeV are estimated from Eq. 9.10, whereas for QCD 10, 20 GeV, the values represent the rates observed with the L3 algorithm. All results correspond to $\mathcal{L}=3.2\times10^{31}$ cm^{-2}s^{-1}. 241

9.15 Summary of yields for tagging the electron in the semi-leptonic decay of the b using the J/ψ signal sample with $R_{cone} = 0.2$ and 0.4. Included with the tagging efficiency is the overall performance from the potential method. See text for definition of variables. 246

10.1 Summary of the Level 3 J/ψ trigger for DØ using preshower information described in the thesis. Details on the exact definitions and requirements for each variable as well as for Type 1 and 3 are presented in Chap. 9. 250

Acknowledgements

Working on a large experiment could not have been possible without the encouragement, support, and guidance from a number of people. First and foremost, I would like to thank members of the DØ collaboration at Fermilab. This exciting experiment would not be possible without the contributions and endeavors of all the individuals and institutions involved.

I would also like to express my sincere gratitude to Drs. Sebastian White and Wlodek Guryn at Brookhaven National Laboratory, New York, for encouraging me to pursue experimental high energy physics. Their advice and recommendation influenced my decision to enter the field. I will always be grateful for the guidance they have given me.

I am deeply indebted to my dissertation advisor, Professor Michael Rijssenbeek. His guidance and enthusiasm has allowed me to achieve a degree that I once thought would be impossible. Likewise, I would also like to thank my "co-thesis advisor", Dr. Jonathan Kotcher. Jon's support and willingness to entrust me in co-managing a major subsystem for DØ has proved to be an invaluable experience during my graduate program. He has given me a deep appreciation and understanding of the level of effort needed in developing a final, deliverable product. From the outset, both Jon and Michael have been concerned with the timely completion of my Ph.D. and future career, providing every level of assistance during my development as a physicist. Working with them has indeed been a pleasure.

I would like to thank all my colleagues at the Stony Brook high energy group. In particular, Professors Paul Grannis, John Hobbs, and Research Scientist Dean Schamberger. They have not only provided for a pleasant work atmosphere but have offered valuable advice and direction throughout my graduate career. Indeed, it has been a privilege to be a part of the Stony Brook group.

I wish to acknowledge a number of my colleagues at DØ with whom I have closely worked with and who have assisted me throughout my years as a graduate student: Wendy Taylor, Sailesh Chopra, Satish Desai — for careful reading and useful suggestions of the manuscript; Anatoli Gordeev for many of the design and engineering figures embedded in this document; Anna Goussiou, Mrinmoy Bhattacharjee, Levan Babukhadia, Sonya Wright, Arnaud Lucotte, Dhiman Chakraborty, Don Lincoln, Jianming Qian, Drew Alton, Volker Buescher, Juan Estrada, Rick Van Kooten, Kin Yip, Bill Freeman, and Jerry Blazey. Also, I would like to thank André Turcot who has been instrumental with the physics studies presented in the final chapters of this dissertation. His pedagogy and assistance with the analysis has helped develop an algorithm for identifying low-p_T electrons at DØ in Run II.

My stay in New York during the first four years of graduate school will always be memorable. I would like to thank Josh and Lisa Grossman, Ashfia Huq, Onur Mentes, Scott Bogner, Todd and Amy Clatterbuck, Aaron and Sasha Stein, James Dickerson, and Barry Winn for all the enjoyable times.

I would also like to acknowledge the support of a number of close friends with whom I've either grown up or made along the way — and certainly enjoyed the company of: Shama, Yasir, Natasha, and Tariq Aleemuddin; Kamran, Rummana, Almas, and Ruby Hussain; Shumoon, Zeruck, and Manahil Khan; Farozan Islam, Michael Premsagar, Jacqueline Salam, Anjum Siddiqui, Afroz Khan, Saleem and Afshan Siddiqui, Ashir and Seema Hai, Nazish Faruqi,

Wendy Glogoza, Shamsheer Gir, Rizwaan and Dilshad Naimathullah, Shakeeb Alam, Ejaz Shamim, Kiernan May, Khalid Baig, Hiam Hammad, Shaheen Syed, and Latha Molakala. Without their friendship, my life would follow a very different path.

Finally, a special thanks to my family: my parents Abdussattar and Saleha; sisters, Ruksana and Shakira; brother-in-laws, Afsar and Masood; and nephews, Ajmal, Akram, and Ihsaan. Both my mom and dad, from Day I, have supported and encouraged me to pursue every level of education possible, and at the same time, provided for my happiness. Today, words alone cannot express the gratitude I have for them and the entire family. I can only continue to thank them, for it is through their support that I have come this far.

– Abid M. Patwa
Stony Brook, New York (USA)
February 2002

Chapter 1

Introduction

During the past half century, the field of experimental high energy physics has introduced compelling new questions and guided our understanding of fundamental physics. The interplay of experimental and theoretical particle physics has gradually provided us with a coherent view of the basic constituents of matter and the forces and interactions governing them. At the same time, efforts to study and measure these interactions to greater detail (*i.e.,* high-energy) and greater precision have led to larger and more sophisticated instruments in the form of colliders and detectors, allowing experimenters to penetrate deeper into the understanding of the structure of matter. The time, cost and effort needed to design, construct, commission, run, and analyze an experiment with such a capability has also grown accordingly. The challenge in developing such an experiment and the exciting physics it will address continues to attract resources and promises to offer great scientific opportunities.

This dissertation describes the design, construction, and installation of the Forward Preshower detector, an integral subsystem for the DØ detector. DØ is one of two large collider detectors located at the Fermi National Accelerator Laboratory in Batavia, Illinois (about 40 miles west of Chicago, Illinois). The DØ detector has been designed to study constituent products of high

energy proton-antiproton ($p\bar{p}$) collisions provided by the Fermilab accelerator complex. This thesis discusses the activities associated with the preshower system including the conceptual design, R&D of the primary detector components, detector design, construction, installation and alignment, and physics studies for which the detector has been built to address. A description of the performance and expectations from the preshower system is also given. The entire program outlined in this document has been carried out during a period of over six years and has largely been concentrated at the State University of New York at Stony Brook, Brookhaven National Laboratory (Upton, New York), and Fermilab.

After presenting a general overview of the Fermilab accelerator facility and the DØ detector, the physics motivation for instrumenting DØ with the Forward Preshower is given, outlining the various signatures the detector is capable of studying. A chapter on the properties of the preshower, namely its detection principles and readout, follows. A description of the detector design and relevant geometry is presented in Chapter 6. Subsequently, Chapter 7 discusses, in some detail, the techniques implemented during construction and assembly of the detector. Chapter 8 outlines the method for installing and aligning the preshower directly on the DØ detector.

The final part of this thesis concentrates on physics simulation results of electrons from b-quark decays, in particular those originating from the J/ψ meson. In the simulation studies, emphasis is placed on the contribution of the DØ preshower system to the electron identification and background rejection for a potential J/ψ measurement. Initial performance results for identifying soft leptons and how this can aid in data collection, trigger, and calibration is presented in Chapter 9. Chapter 10 concludes with a brief summary of and future prospects for DØ and the preshower detector.

Chapter 2

Theoretical Overview

A number of experimental discoveries and theoretical insights have significantly advanced the understanding of elementary particles and their interactions. The theory relating the strong and electroweak interactions, called "The Standard Model", has become a paradigm for particle physics. The model continues to be tested with a wealth of experimental data and precision measurements, and each time the data satisfies well its detailed predictions.

A comprehensive review of the Standard Model is beyond the scope of this thesis; however, a number of standard textbooks and review articles [1, 4, 5, 6] provide a descriptive framework on which the theory is based. Given here is a brief overview of the model, followed by a discussion of some of the important open questions in particle physics that help guide the physics topics studied by the DØ experiment.

2.1 The Standard Model

The Standard Model (SM) collectively incorporates the strong and electroweak interactions of elementary particles. It is a Quantum Field theory based on the principle of local gauge symmetry under transformations

that forms the group $SU(3)_C \otimes SU(2)_L \otimes U(1)_Y$. $SU(3)_C$ is the symmetry group of strong (color) interactions, Quantum Chromodynamics (QCD), and $SU(2)_L \otimes U(1)_Y$ represents the symmetry group describing the unified weak and electromagnetic (EM) processes. The model classifies all particles within two broad groups: a) fundamental fermions with intrinsic spin $\frac{1}{2}$, and b) the gauge vector bosons with integral spin 1.

The fermions, or matter particles, are further subdivided into colored quarks[1] and non-colored leptons. The lowest member in the fermion family is copied into two more generations of remarkably similar properties but increasing mass: (u,d), (c,s), (t,b) for quarks and (e,ν_e), (μ,ν_μ), (τ,ν_τ) for leptons. The SM provides no prediction for the total number of fermionic generations, but it does require that both leptons and quarks appear in left-handed doublets and right-handed singlets for purposes of electroweak interactions. Indeed, this particular aspect helps motivate the search for new heavy quarks and leptons. Tables 2.1 and 2.2 summarize the different generations of fermions and some of the properties associated with each.

Particle name	Symbol	Electric Charge	Mass (GeV)
Up	u	$+\frac{2}{3}$	$1.5 \sim 5 \times 10^{-3}$
Down	d	$-\frac{1}{3}$	$3 \sim 9 \times 10^{-3}$
Charm	c	$+\frac{2}{3}$	$1.1 \sim 1.4$
Strange	s	$-\frac{1}{3}$	$0.060 \sim 0.170$
Top	t	$+\frac{2}{3}$	174.3 ± 5.1
Bottom	b	$-\frac{1}{3}$	$4.1 \sim 4.4$

Table 2.1: Quark family in the Standard Model and some individual properties. The quarks have been divided in terms of their generation with the mass values and ranges obtained from [7].

[1]Quarks participate in the strong interaction and are believed to come in three colors: RGB for red, green, and blue, respectively.

Particle name	Symbol	Charge	Mass (MeV)
Electron	e	-1	0.511
Electron Neutrino	ν_e	0	$< 7.3 \times 10^{-3}$
Muon	μ	-1	105.7
Muon Neutrino	ν_μ	0	$< 0.17 \times 10^{-3}$
Tau	τ	-1	1777
Tau Neutrino	ν_τ	0	$< 18.2 \times 10^{-3}$

Table 2.2: Lepton family in the Standard Model and some individual properties. Similar to Table 2.1, the leptons are divided in terms of their generation.

Force Carrier	Force	Mass (GeV)	Electric Charge	Spin	Color Charge
Gluon (g)	Strong	0	0	1	R G B
W^+	Weak	80.417 ± 0.035	1	1	Neutral
W^-		80.417 ± 0.035	-1	1	
Z		91.187 ± 0.007	0	1	
Photon (γ)	EM	0	0	1	Neutral

Table 2.3: Gauge bosons and their basic properties in the Standard Model. The bosons are divided in terms of the force they transmit. Further, the mass of the W and Z are world average results which include indirect measurements.

The fundamental fermions interact by the exchange of gauge bosons. In total, there are twelve such bosons: a) eight massless, colored gluons[2], which mediate the strong interaction, coupling to the color $SU(3)_C$ charge, b) two W bosons ($W^\pm$) and a Z° boson for weak interactions, and c) the massless photon (γ) for the electromagnetic force. The $W^\pm$, Z°, and γ mix and form the gauge fields of the $SU(2)_L \otimes U(1)_Y$ sector of the electroweak interactions. Table 2.3 lists these force carriers in terms of their interaction type.

[2]Conventionally named g_i, where $i = 1...8$ and corresponds to the 3^2-1 generators of the $SU(3)$ symmetry group.

An exact local gauge invariance (under $U(1) \otimes SU(2)$) would require all four electroweak bosons to be massless. However, this appears not to be the case, and thus, the electroweak gauge symmetry must be broken [5, 8] providing known and observed masses for the $W^{\pm}$ and Z° bosons, while leaving the photon massless. In its simplest form, this can be accomplished through the Higgs mechanism [1, 5] which introduces a new spin-zero field, called the Higgs field, permeating the universe, and an associated massive, spin-zero elementary particle, H, known as the Higgs boson. Quarks and leptons, as well as the W and Z, each couple to this field and consequently, acquire a mass proportional to the coupling strength. On the other hand, the photon and gluons have no interactions with the field and remain massless. To date, the Higgs boson has failed observation by any physics experiment. Indeed, the mass of the Higgs is not predicted in the SM, but a lower bound, at 114.1 GeV (95% CL), is established through its non-observation from present experimental searches [8], while an upper bound, at about 800 GeV, is set through theoretical arguments [9].

The Higgs mechanism is the simplest scheme that generates the masses for the quarks, leptons, and the $W^{\pm}$ and Z° bosons. The ability of the Standard Model to predict the masses and indirect neutral currents of the $W^{\pm}$ and Z° combined with the direct experimental observation of each of these particles at CERN [10, 11, 12, 13] in 1983, established the integrity of the model. The discovery of the top quark by the DØ [14] and CDF [15] collaborations at Fermilab in 1995, and the direct observation of the ν_{τ} by the DONUT collaboration [16] in 1998, further completed the picture of the three generations of leptons and quarks required by the SM. In the framework of the SM, a precision measurement of the top mass and of the W and Z masses leads to strict experimental constraints on the Higgs mass, as indicated in Fig. 2.1. At the present energy regime accessible by particle physics facilities, the model con-

tinues to be an extremely effective approximation to the physics of elementary particles. However, theoretical considerations hint that it may only be a subset of a more fundamental theory, requiring it to be replaced at energy scales above the Planck scale, $M_P \simeq 10^{19}$ GeV [2]. Here, quantum gravitational effects become significant, and a much more complete theory incorporating gravity is required. Additionally, the theory does leave a number of issues unresolved — *e.g.,* the reason behind the exhibited large number of elementary particles with their observed pattern of masses, the origin of mass, the origins of electroweak symmetry breaking, as well as the predominance of matter in the universe. Each of these open questions urges experimenters to continue stringent tests of the SM and thereby, allows a search for (or constraint of) possible extensions to the model. It is therefore believed that at high energies, deviations from the existing framework will appear.

At present, the limits set by existing facilities on the Higgs mass and for possible supersymmetric particles prompt the need to construct machines of higher energy and luminosity, as well as detectors that implement newer, advanced detection methods. In particular, such searches have helped motivate the construction of a Run II upgraded Fermilab-DØ complex. For example, precision studies of SM parameters from existing facilities favor a light Higgs (of less than ∼222 GeV at 95% CL [17]), placing it within the sensitivity range of anticipated experiments during the next decade. Moreover, the number of speculations associated with the SM can only be resolved through experimental data, which in turn lends an opportunity to complete the theoretical picture of elementary particles and their observed behavior. Each of these aspects guides and governs a major portion of the physics program at DØ.

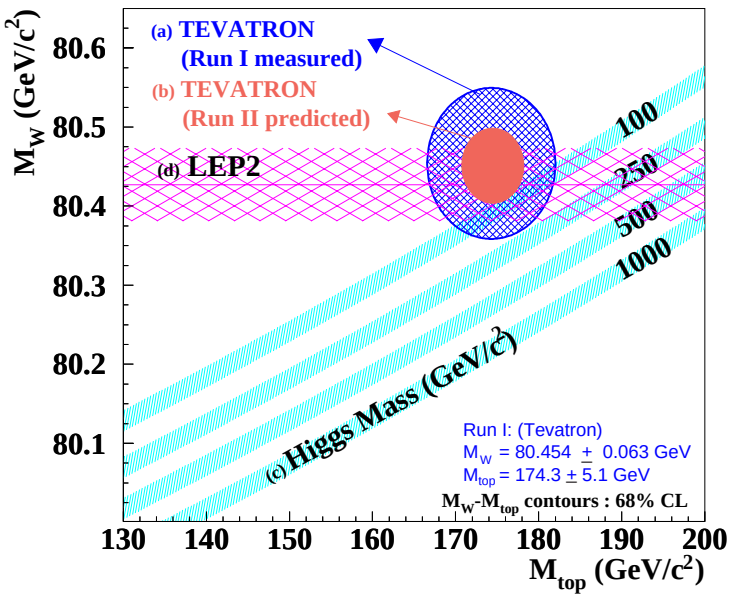

Figure 2.1: Measured Run I Tevatron W boson mass vs. top quark mass, shown by (a) cross-hatched oval, in addition with W mass band from LEP2, CERN (d). The four shaded bands (c) represent expected values for a specific Higgs boson mass in the SM, where the 1σ-width in each band is due to $\alpha_s(M_Z^2)$. The solid oval (b) shows a predicted Run II Tevatron measurement (using Run I central values) and is given for comparisons. Adapted from [17].

2.2 Physics Signatures

The control of systematic uncertainties is critical in high precision measurements of the top and W masses, in the identification of B meson flavors for B-physics processes, and for direct searches of Higgs and new physics phenomena. Many of the events studied by experiments contain signatures that require efficient lepton identification and background rejection, precise energy and momentum measurements, as well as large geometrical acceptance for signal detection. The need to extract signals from typically large backgrounds in high-energy $p\bar{p}$ collisions motivates the development of improved filtering algorithms. The inclusion of spectator quarks in $p\bar{p}$ collisions causes a large

Process	Particle	Dominant Decay Modes (Branching Fractions)
1	W	i) $l\nu_l$, where $l = \{e, \mu, \tau\}$ (at 1/9 each) or: ii) $q\bar{q}$ (jets: 2/3)
2	top $(t\bar{t})$	$W^+bW^-b \rightarrow$ i) all-jets: $q\bar{q}'\ b\ q''\bar{q}'''\ \bar{b}$ ($\simeq$36/81) ii) lepton+jets: $q\bar{q}'\ b\ l\bar{\nu}_l\ \bar{b} + \bar{l}\nu_l\ b\ q\bar{q}'\ \bar{b}$ ($\simeq$12/81 per l) iii) dilepton: $\bar{l}\nu_l\ b\ l'\bar{\nu}_{l'}\ \bar{b}$ ($\simeq$4/81) (and $b \rightarrow$ jet with possible μ- or e-tag)
3	SM Higgs (H)	bb (if $m_H < 140$ GeV; BR(m_H)$\simeq\mathcal{O}$(90%)) WW (if $m_H > 140$ GeV; BR(m_H)$\simeq\mathcal{O}$(40%+))
4	J/ψ	i) $q\bar{q}$ (87.7 $\pm$ 0.5 %) ii) virtual $\gamma \rightarrow$ *hadrons* (17.0 $\pm$ 2.0 %) iii) e^+e^- (6.02 $\pm$ 0.19 %) iv) $\mu^+\mu^-$ (6.02 $\pm$ 0.19 %)

Table 2.4: Major decay modes of certain high-p_T (W, top, Higgs) and low-p_T (J/ψ) signals. Adapted from [7].

fraction of energy to escape detection down the beam pipe, preventing momentum balance to be readily applied along the beam direction. Therefore, any application of momentum and energy conservation usually tends to be restricted to the plane transverse to the incoming $p\bar{p}$ beam. Studying kinematic variables along this plane provides one additional and useful means of reducing large backgrounds.

Processes of particular interest are those that provide critical tests of the Standard Model — *e.g.*, study of the W, top, and Higgs. Some of the dominant decay modes of these particles are summarized in Table 2.4. Many involve final states that contain mixtures of high-p_T leptons, b-quarks (which frequently can be tagged by the presence of low-p_T leptons, μ or e, from their decay), and/or considerable jet activity. Detecting any presence of neutrinos in many of these interactions requires the ability to infer missing transverse momentum ($\not{p}_T$) by a measurement of the total transverse momentum imbalance in the event.

Therefore, a detector that is hermetic (*i.e.,* with full 4π solid-angle coverage) is of utmost importance.

The major background for almost all signals of interest arises from QCD interactions, which give rise to multi-jet final states, effectively masking the signal in all-hadronic final states. One method for a precise measurement is to exploit the leptonic decay modes of the given process. A detector with a full 4π solid-angle muon coverage, a calorimeter highly segmented with forward electromagnetic layers, and a tracking volume with a fine granularity can identify charged leptons (usually e or μ) with high efficiency. Discriminating between electrons from $\pi^\circ \rightarrow 2\gamma$ conversion(s) can be done through a study of track information. *E.g.,* the partial absence of tracks for γ's converting inside or beyond the tracking volume provides a rejection of that background. Additional rejection is possible by differentiating between the tracking system's energy loss mechanism (*i.e.,* dE/dx response) for singly-ionizing electrons (say from W decays) and doubly-ionizing tracks from photon ($\gamma \rightarrow e^+e^-$) conversions. A requirement of e- or μ-isolation, expected for electrons produced in decays of massive particles (*e.g.,* W, Z), further separates signal from background.

Significant improvements in discrimination can be made by use of the event topology (*i.e.,* event shape) and a study of the production dynamics. For massive objects such as top, instead of being forwardly boosted, the decay products are concentrated more centrally (*i.e.,* about η=0) than the QCD-dominated background originating from qq, qg, and gg scattering. Here, improved tracking and calorimetry in the central region, in addition to the use of strong event shape discriminating variables in the analysis, can benefit. Moreover, physics studies can benefit greatly when particle tracking and energy measurements in the forward region is emphasized. In fact, certain SUSY signatures such as the associated production of charginos-neutralinos (*i.e,* $\tilde{\chi}^{\pm}\tilde{\chi}^{\circ} \rightarrow 3l + \not{E}_T$) have multibody decays with at least one lepton in the forward region. An effective

means for lepton identification at larger rapidities can help probe the presence of SUSY.

Top as well as a low mass SM Higgs ($m_H < 140$ GeV, see Table 2.4) are characterized with b-quark jets, and thus, prompt the need to identify and tag b-quarks with a high efficiency. Top signatures, in particular, are to be compared with a relatively low heavy flavor content in the background[3]. Nevertheless, one conventional and yet, powerful method in distinguishing such a signal from background is by tagging the b-quark using the b's inherent secondary (displaced) vertex extrapolation and/or the presence of a soft-lepton from the decay. Such techniques can easily be accomplished by the presence of a high resolution silicon vertex detector with a large fiducial acceptance, complemented by charged particle tracking within a central magnetic field, and/or subsequent downstream lepton identification. A tagging capability can also reduce jet combinatorics by a factor of 2 (3) for single (double) b-tagged jets in reconstructed events indicating the presence of a $t\bar{t}$ pair. This, in turn, can help improve the sensitivity of the top mass measurement. Moreover, observing a $b\bar{b}$ decay in the associated production of a Higgs and a W boson urges the use of efficient and pure b-tagging algorithms to help overcome the basic "W+flavor" background [19].

Within the SM, the three quark generations (see Table 2.1) couple to one another such that the level of mixing can be quantitatively described through elements comprising a 3×3 unitary mixing matrix known as the Cabibbo-Kobayashi-Maskawa (CKM) matrix [4]. The CKM matrix contains four independent parameters of which one can be chosen to represent a complex phase that gives rise to the phenomenon of CP violation in the SM. Further, each

[3]Primary backgrounds in top events include W+≥3-jet events, which are observed to have at least an order of magnitude less b-quark content than the signal [18].

of the nine matrix elements must be determined experimentally. Studying the level of mixing between the three quark generations allows for related searches for CP asymmetries [4] among the different generations. While CP violation is small ($\mathcal{O}(2 \times 10^{-3})$) in the $K^{\circ}\bar{K}^{\circ}$ system, indirect evidence indicates it is significant, $\mathcal{O}(1)$, in the B system. The B mesons that are directly produced in $p\bar{p}$ interactions tend to appear uniformly in pseudorapidity. Further, those produced centrally give rise to decay fragments that contain low-p_T leptons distributed in both the forward and central directions. Detection of these leptons requires uniform track coverage incorporating: a) an ability to measure displaced vertices from the long b-quark lifetime ($c\tau \sim 450\ \mu m$), b) a magnetic tracker to measure momentum and tag the sign of electrons and hadrons, as well as c) an efficient identification for muons and electrons downstream of tracking. Further, at hadron colliders, a golden channel for studying CP-violation is in the B-system through $B^{\circ} \rightarrow J/\psi K_s^{\circ}$ samples, in which the J/ψ subsequently decays leptonically to relatively low-p_T (≥ 1.5 GeV) leptons; $J/\psi \rightarrow \mu^+\mu^-$ or e^+e^- pairs (see also Chap. 9). The ability to trigger on and measure these dileptons demands efficient and pure low-p_T lepton triggers using a combination of tracking and calorimeter information. In such processes, a preshower detector designed to enhance electron identification and reduce QCD backgrounds, in addition to a reconstructed invariant mass of the lepton pair, may help to significantly reduce backgrounds.

The above are only a few in a series of physics signatures that probe the Standard Model. Nonetheless, they represent a large portion of the studies presently being performed at existing collider detectors. One such facility is the DØ experiment, whose detector is described next. Further, an integral element of the DØ detector (and the topic of this dissertation) is a preshower system, instrumented in both the central and forward region. This system is primarily intended to boost the capability to identify electrons and single

photons in the DØ detector by rejecting backgrounds from QCD processes at both the trigger level and offline. Second, this system aids in energy and tracking measurements for many of the final states outlined here. An extended discussion of the physics justification and the topics that are addressed with the preshower is given in Chap. 4.

Chapter 3

Experimental Apparatus

This chapter describes the Fermilab Tevatron $p\bar{p}$ accelerator complex and the DØ detector during its second operating period, Run II. Both the accelerator and the DØ detector have recently completed a major upgrade in preparation for an extended run that began in early March, 2001. Emphasis is placed here on these upgraded components.

3.1 Definitions and Conventions

A few definitions and conventions used in the experiment are given below. Unless otherwise specified, these definitions will be assumed for the remainder of the thesis.

3.1.1 Coordinate Systems

A right-handed cylindrical coordinate system (r, ϕ, z) is the convention used to describe interactions occurring at DØ. The origin is taken at the nominal interaction point: (x, y, z) = (0, 0, 0). The direction of the proton beam defines the polar axis (*i.e.,* the z-axis, θ=0) with the positive y-axis pointing vertically up. In certain instances, spherical coordinates (r, ϕ, θ) are

used. The angle θ defines the polar angle relative to the beam direction, and ϕ defines the azimuth about the beam direction with respect to the positive x-axis. The rapidity, y, is defined as:

$$y = \frac{1}{2} \ln \left(\frac{E + p_z}{E - p_z} \right) \tag{3.1}$$

and the pseudorapidity, η, is defined as:

$$\eta = -\ln(\tan \left(\frac{\theta}{2} \right)) \tag{3.2}$$

where m is the invariant mass $m^2 = E^2 - p^2$; in the limit $m \ll E$, $\eta \approx y$. Consequently, the rapidity variable y (or η) is often used in place of the polar angle, θ, because it contains convenient transformation properties under Lorentz boost along the beam direction. Thus, the spatial vectors of the detector are usually denoted by (r, ϕ, η).

Additionally, in $p\bar{p}$ collisions, the momenta along the beam of the constituents are not known since many of the collision products may escape detection down the beam pipe. As a result, another physically important quantity (which is also proportional to the "intensity" of the interactions) is the transverse momentum, p_T, of the secondary particles and is defined as the momentum vector projected onto a plane perpendicular to the beam axis. Since the transverse momentum of a particle is zero (or negligible) when compared to its momentum along the beam direction, momentum conservation can be applied in the transverse plane. Therefore, in reconstructing events it becomes convenient to use:

$$p_T = p \times \sin \theta \tag{3.3}$$

and similarly, a transverse energy, E_T, whose direction is taken to be the same as the p_T vector:

$$E_T = E \times \sin\theta \tag{3.4}$$

3.1.2 On Luminosities and Cross Sections

Any measurement of the reaction rate is often expressed in terms of a *cross section*, σ, the interaction probability per unit flux. The particle flux is known as the *luminosity*, $\mathcal{L}$; for colliding-beam machines, it is proportional to the square of the number of particles passing through a unit area per unit time. Luminosities are typically given in units of $\mathrm{cm}^{-2}\mathrm{s}^{-1}$, whereas cross sections are often expressed in *barns*, where 1 barn = 10^{24} cm^2. The product of the luminosity and cross section subsequently yields the reaction rate, R, expressed in units of hertz:

$$R = \sigma\mathcal{L} \tag{3.5}$$

A luminosity within a range of 0.4–50 $\times$ 10^{31} $\mathrm{cm}^{-2}\mathrm{s}^{-1}$ is expected at the Tevatron during Run II. Further, in order to prevent saturation, the rate for an experiment is often limited to a specified bandwidth and is established by event filters or triggers (see Sec. 3.4) made possible through a combination of detector and software selection algorithms characterizing a desired physics signature. Within any interval of time during which an experiment operates, the number of expected events, N, of a specific type is determined by integrating the rate with respect to time:

$$N = \sigma \int \mathcal{L} dt \tag{3.6}$$

The quantity $\int \mathcal{L} dt$ is referred to as the *integrated luminosity*. A goal at 2 fb^{-1} of total integrated luminosity is expected for Run IIa, at which time

additional upgrades to portions of the DØ detector will extend the run to 15 fb^{-1} and beyond. This latter operating period has been classified as Run IIb.

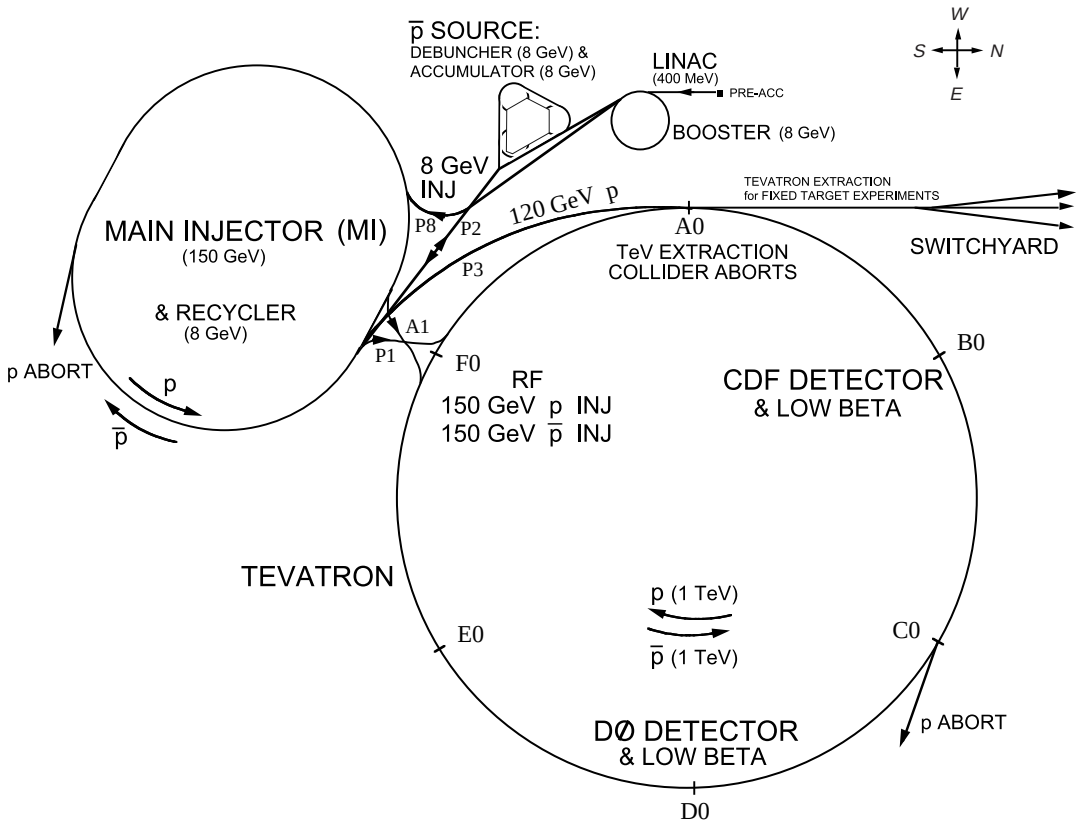

Figure 3.1: Schematic of the Run II Fermilab accelerator complex. Adapted from [20].

3.2 The Tevatron Collider

The DØ detector is located at the Fermilab Tevatron, which provides proton-antiproton collisions at a center-of-mass energy of 2.0 TeV [21, 22]. The Tevatron facility continues to be the world's highest-energy hadron collider. A general layout of the accelerator complex is shown in Fig. 3.1.

The Tevatron primarily consists of two basic components: superconducting magnets and radio frequency (RF) cavities. Protons and antiprotons complete many cycles in opposing directions around the accelerator ring, each time being appropriately bent into a circular orbit by the magnets and receiving a small boost of energy at a RF cavity. The final beams are made to interact, colliding at two experimental areas: B0 (*i.e.,* Collider Detector at Fermilab, CDF) and D0 (*i.e.,* DZero, DØ). However, the overall process leading to collisions at each of these two points is much more complicated, requiring detailed considerations and demanding a number of performance specifications be met. A general outline of the collision process is given here, but the reader is directed to consult additional references [23, 24] for a more technical overview. The process does require completing several acceleration stages, which can be separated into eight basic components:

- Pre-accelerator: a Cockroft-Walton
- Linear Accelerator: The Linac
- The Booster synchrotron
- The Main Injector
- The Antiproton Source: production and extraction
- The Debuncher, Accumulator

- The Recylcer
- The Tevatron Ring synchrotron

All of these stages must be integrated to yield the desired beam energies and/or luminosities and thereby, provide the physics signals for study.

The beam originates with H^- ions formed with an "ion source" and released into an electrostatic Cockroft-Walton accelerator. There, the H^- ions are accelerated by an electric field to 750 keV. After leaving the Cockroft-Walton, the ions are injected into a 500-foot-long Linac where oscillating electric fields boost the negative hydrogen ions to 400 MeV. The ions subsequently pass through a carbon foil, which strips both electrons from each ion, leaving only protons. The extracted protons are then steered into the Booster, a 1570-foot-circumference fast-cycling synchrotron ring. Here, the protons are constrained to a closed circular orbit by a series of bending magnets with quadrupole focusing fields that prevent the beam from diverging. At each revolution around the ring, the energy of the particles steadily increases by acceleration through a set of RF cavities. As the particle's momentum increases, both the magnetic field and RF frequency must increase in a synchronous manner in order to confine the particles to the same orbit. The protons travel around the Booster about 20,000 times until they reach an energy of 8 GeV. A pulse train of approximately 5 to 7 bunches, each containing $5\text{–}6\times10^{10}$ protons are subsequently delivered from the Booster to the next stage of acceleration: the Main Injector.

The Main Injector consists of a 120–150 GeV synchrotron ring, located tangentially next to the Tevatron ring at the F0 straight section (see Fig. 3.1). It was constructed expressly for the Run II upgrade at the Fermilab facility and significantly enhances the Tevatron collider program. In Run II, the Main Injector replaces the Main Ring, which operated during the accelerator's first

running period (Run I). In general, the Main Injector has been built to perform, with improved capabilities, all the duties that were available with the Main Ring. Roughly 2 miles in circumference, the Main Injector is capable of delivering three times as many protons to the Tevatron than were possible with the Main Ring. With the removal of the Main Ring from the Tevatron enclosure, beam halos and backgrounds seen in the colliding detectors (such as DØ) during Run I are reduced. The primary function of the Main Injector is to coalesce proton bunches exiting the Booster into a single high intensity bunch of approximately 5×10^{12} protons; a parameter which depends largely on the nominal performance of the Booster and the Main Injector. After reaching an energy of 150 GeV in the Main Injector, the protons are transferred to the Tevatron.

The Main Injector also extracts proton bunches at 120 GeV and allows these to impact on an external nickel/copper target for a continuous antiproton ($\bar{p}$) production cycle (at a rate of once every 1.47s). The secondary antiprotons are produced with a range of momenta and production angles and are focused through a lithium collector lens, which carries a large pulsed current (peak at 670 kA) flowing in the direction of the beam to generate an azimuthal magnetic field. The emerging antiprotons are collected into the first of two antiproton storage rings.

The first ring is the Debuncher, which applies complex computer-controlled RF techniques to rotate the antiproton beam into as compact a phase space as possible (*i.e.,* a continuous band with a very narrow momentum spread). The antiprotons are further stochastically cooled in order to restrict their transverse oscillation. This is done by applying correction signals to the particles to minimize their deviations from an ideal orbit. Once a coherent beam is achieved, the 8 GeV antiprotons are transferred to the Accumulator ring where they are further cooled. Here, stored antiproton bunches are produced with stacking

rates of up to 10^{12} antiprotons/hour. The Debuncher and Accumulator are in the same tunnel, which is roughly 1700 ft. in circumference. The beam from the Accumulator is transferred to the 8 GeV Recycler ring, which is located in a tunnel shared with the Main Injector.

The Recycler is a 8 GeV permanent magnet storage ring utilizing stochastic cooling systems. It is capable of delivering more antiprotons to the Tevatron and thereby, proportionally increasing the beam luminosity. The main function of the Recycler is to operate as a recovery channel (or post-Accumulator) for antiprotons left at the end of a previous collider store. The Recycler accumulates and re-cools dilute $1\text{–}6\times10^{11}$ antiprotons, every 0.5 to 3 hrs., up to a total stack of about 3×10^{12} antiprotons. Once the accumulated antiproton beam reaches 8 GeV, it can be extracted into the Main Injector, where the energy of the antiprotons is raised to 150 GeV.

The 150 GeV proton-antiproton bunch from the Main Injector are delivered in opposing directions into the Tevatron collider. Here, the final phase of acceleration is accomplished. The proposed plan in Run II is to initially deliver 36×36 $\bar{p}p$ bunches with a 396 ns bunch spacing and ultimately at a reduced 132 ns interval. Within the Tevatron's approximate 4 mile circumference tunnel, superconducting magnets (operating with cold compressors and upgrades to cryogenic controls) produce fields of 4 Tesla, allowing the beams to reach a maximum energy of 1 TeV each. Once accelerated to this energy, the beams are squeezed to small transverse dimensions through the use of low-beta quadrupole magnets at the interaction points, initiating collisions at: B0 (CDF) and D0 (DØ). The Tevatron normally operates with an expected mean lifetime of about 72 hours between intermittent failures that frequently arise by the random loss of stores. However, this rate depends largely on the day-to-day performance of all stages and components in the collider facility.

3.3 DØ Detector

The DØ detector is a general purpose detector, designed and constructed to study interactions originating from $p\bar{p}$ collisions at a center-of-mass energy of 2.0 TeV in the Tevatron collider [25]. The detector has been optimized to measure final states that contain electrons, muons, jets, and neutrinos from a number of key processes occurring during these collisions. It is particularly suited for the study of high mass states and large transverse momenta (high-p_T) phenomena. Commensurate with the improvements to the Tevatron, DØ has recently completed a major upgrade program; the new Run II detector continues to detect these important physics signatures, but at the same time, aims to extend the physics reach to lower-p_T final states. The detector is shown in Fig. 3.2 and consists of three main components:

- Inner Tracking System: The innermost system at DØ provides enhanced particle trajectory and tracking measurements over a broad range in pseudorapidity. The system is composed of four tracking subdetectors. Immediately surrounding the Tevatron beam pipe is a Silicon Microstrip Tracker (SMT), designed to reconstruct both primary and secondary vertices. This is radially followed by a finely segmented Scintillating Fiber Tracker (CFT), which provides efficient tracking in the central pseudorapidity region and, jointly with the SMT, provides track reconstruction and momentum measurements for all charged particles. Both the SMT and CFT are enclosed within a central magnetic field provided by a 2.8 m-long 2 Tesla superconducting solenoidal magnet. Directly downstream of the solenoid (and within the inner bore existing in the DØ central calorimeter), a Central Preshower (CPS) system aids in electron- and photon-ID as well as samples energy of particles traversing the solenoid coil. Similarly, a Forward Preshower (FPS), employed to serve a role

nearly equivalent to the CPS, occupies the forward pseudorapidity region.

- Calorimeter: Three finely segmented (*i.e.,* one Central and two Forward-End) sampling calorimeters surround the tracking volume, providing accurate measurements of the energy of electrons, photons, and hadronic jets. Together, they also allow the ability to measure the total transverse momenta of neutrinos and other non-interacting particles. Through a measurement of the energy cluster's centroid (within any particular calorimeter cell(s)), the calorimeter provides an additional tool in determining the position of electrons and/or photons and thereby, enhance particle identification in the DØ detector.

- Muon System: Immediately surrounding the calorimeter, an iron toroid spectrometer combined with central (forward) proportional (mini-) drift chambers and scintillation counters provide muon identification and additional muon tracking information.

Although the detector is highly compact, the full assembly is large and the hardware associated with the different subsystems is quite complex. The entire assembly approximates to about 13 m-high $\times$ 12 m-wide $\times$ 20 m-long and weighs roughly 5500 tons [18, p. 35]. The inner tracking system alone consists of approximately 1 million channels (distributed among its individual subdetectors). Many of these channels are read out via customized electronics located in rack spaces below the detector's support platform, as shown in Fig. 3.2. The detector and its platform are mounted on mechanical rollers that allow the detector to move from the assembly area (*i.e.,* detector construction and installation stage) to the collision hall (*i.e.,* detector operation and data acquisition stage).

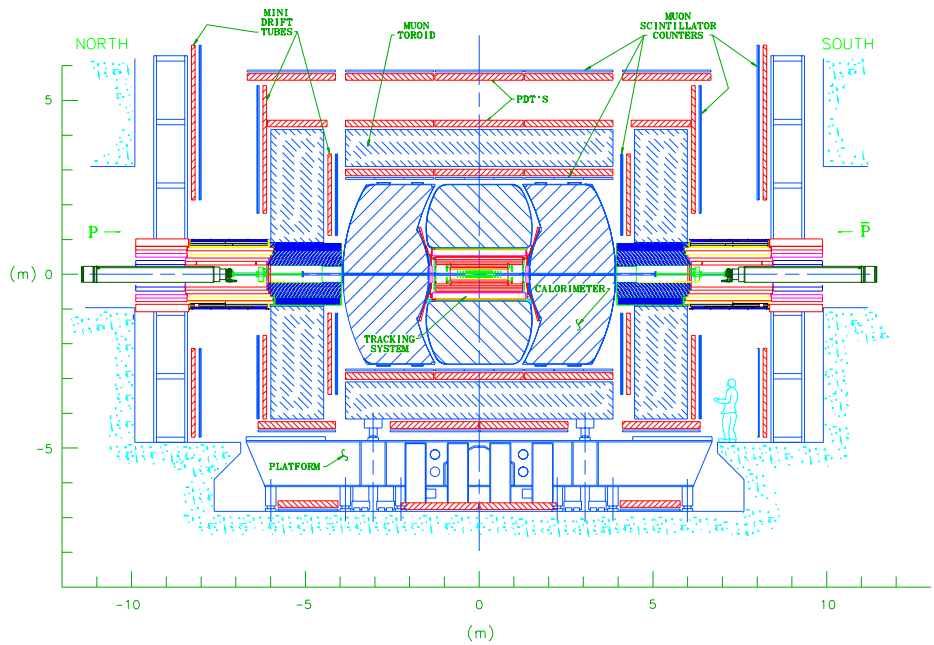

Figure 3.2: Two-dimensional view of the Run II DØ detector, showing the three integral systems outlined in the text.

The following sections provide a brief overview of each of the elements in the Run II DØ detector. For a much more complete treatment, the reader is referred to the many existing write-ups, design reports, and publications on the individual systems (see Ref. [26]).

3.3.1 Silicon Microstrip Tracker

The innermost tracking subsystem and the component closest to the Tevatron's beryllium beam pipe is the Silicon Microstrip Tracker (SMT) [27], illustrated in Fig. 3.3. The primary function of the SMT is to provide precision tracking and vertex information from the interaction point (IP) in $p\bar{p}$ collisions as well as to identify and reconstruct vertices displaced from the primary interaction (see Fig. 3.4). These secondary vertices are characteristic signatures of relatively long-lived decaying particles containing b and c quarks.

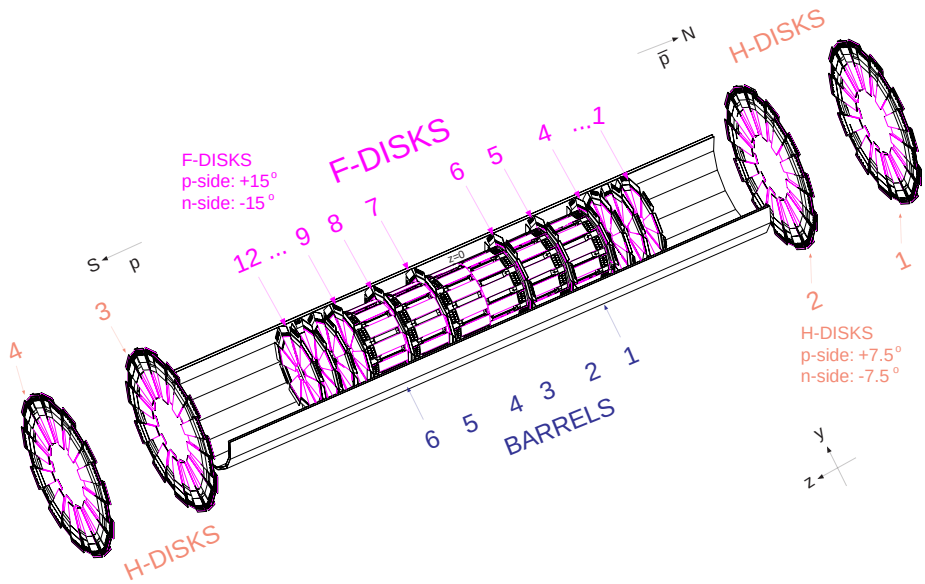

Figure 3.3: Three-dimensional view of the DØ silicon microstrip tracker.

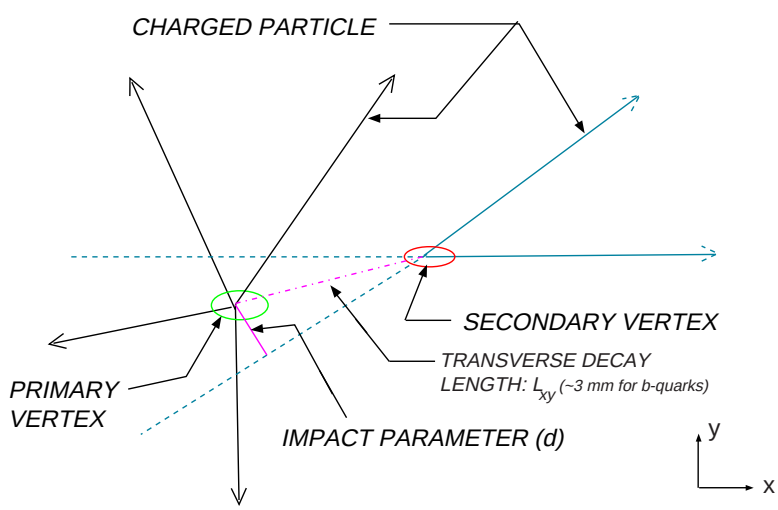

Figure 3.4: Schematic of an observed displaced vertex originating from b or c quarks in a silicon microstrip detector.

Mechanically, the tracker consists of two parts symmetric with respect to $z = 0$: the north-SMT ($z > 0$) and the south-SMT ($z < 0$). The primary vertices are distributed along z, over an extended interaction region (distributed according to a Gaussian centered at $z = 0$ with $\sigma_z = 25$ cm). This defines the length of the SMT detector and motivates a hybrid design of interspersed disk and barrel modules, as shown in Fig. 3.3. In this configuration, the barrel detectors measure primarily the r–ϕ coordinate while the disk assemblies provide r–z as well as r–ϕ track information. Consequently, the SMT is capable of three-dimensional track reconstruction allowing particles at small (high) values of η to be identified in barrels (disks). Additionally, the detector must be capable of providing z-vertex and transverse impact parameter resolutions to better than 30 μm and, concurrently, be radiation hard to operate efficiently in the high luminosity environment of Run II[1]. Likewise, a 132 ns bunch crossing interval expected in Run II sets the performance criteria for the associated electronics and readout of the SMT.

The main volume of the SMT is formed by six barrel units 12.4 cm-long in z, consisting of four concentric layers of silicon ladder detectors each. The layers extend radially from 2.7 to 9.4 cm. A ladder consists of two 300 μm-thick wafers at 6.0 cm $\times$ 2.1 cm, positioned end-to-end, with electrical micro-wirebond contacts. All barrel modules have double-sided small-angle (2°) stereo detectors in Layers 2 and 4. The central four barrels at low $|z|$ have double-sided large-angle (90°) stereo in Layers 1 and 3, whereas the two outer barrels have single-sided axial detectors in Layers 1 and 3. Interspersed within the barrels are twelve 8 mm-thick disks (*i.e.,* six disks symmetrically

[1]The silicon detector described here is expected to survive ~ 2 fb^{-1} and operate in Run IIa. For extended operation in Run IIb, an entirely new silicon will be implemented. For brevity, any discussion of the Run IIb silicon has been omitted, and the reader should refer to [28, 29].

located on each side of $z = 0$, known as F-Disks), each consisting of overlapping r–ϕ wedges to help improve tracking up to large η. The wedges of these central disks are double-sided with $\pm 15°$ stereo strips. Additionally, in the forward region (at high $|z|$), four H-Disk assemblies (*i.e.,* two symmetrically located on each side of $z = 0$) extend tracking out to $|\eta|$=3. These forward disks have back-to-back single-sided wedge detectors with an effective $\pm 7.5°$ stereo strips. Signals from the detector are read out by radiation-hard custom integrated circuits, called SVX-IIe chips, which perform signal pipelining and digitization. The chips are optimized for the Run II bunch crossing intervals.

Run II simulations and initial performance studies of the SMT during detector commissioning [30] have shown hits measurable to a precision better than 30 μm. Secondary vertex resolutions of about 40 μm in r–ϕ and 80 μm in r–z can be reconstructed. Moreover, Monte Carlo studies of top and Higgs generated final states measure a tagging efficiency (at $p_T = 50$ GeV/c) of $\sim$50% for b-quark and $\sim$10% for c-quark jets (with less than 0.5% fake tag rate from lighter flavor contributions). Each of these results are expected to impact a number of Run II physics studies.

3.3.2 Central Fiber Tracker

Directly surrounding the Silicon Microstrip Tracker is the DØ Central Fiber Tracker (CFT) [31]. The CFT complements the SMT in track reconstruction. With the 2 T solenoid magnet enclosing it, the CFT also measures the transverse momentum of charged particles. Indeed, as shown in Fig. 3.5, simulations suggest that a CFT momentum resolution, $\delta p_T/p_T \simeq 8\%$, can be obtained for normally incident electrons of relatively high-p_T ($\simeq$ 45 GeV). Such resolutions can be of importance during E/p calibrations between the tracker and calorimeter as well as allowing CFT information to be used in situations that require

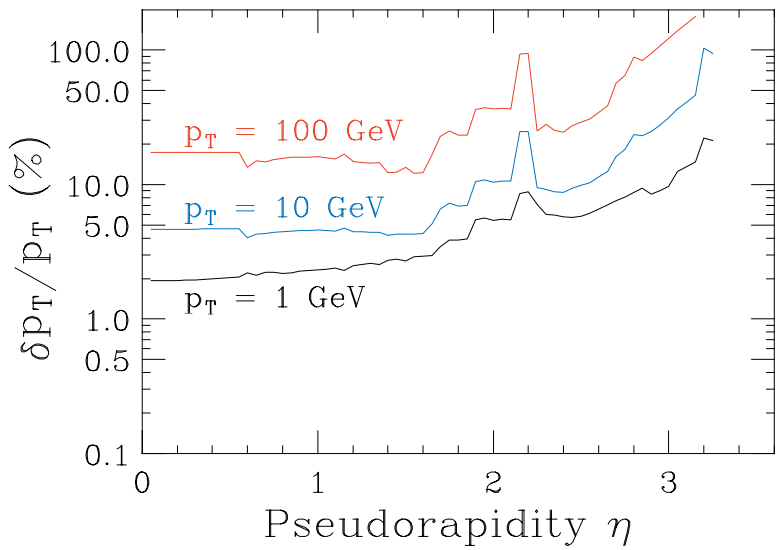

Figure 3.5: Simulation results for the momentum resolution with the Fiber Tracker as a function of psuedorapity (η) for three different p_T values.

charged sign determinations. Moreover, the detector is an integral element of the DØ trigger system (more on the trigger system will be discussed later in this chapter). The signal collection time from the CFT during an interaction is within the Run II bunch crossing interval. The CFT can thus, effectively coordinate with other subsystems to form first-level (*i.e.,* Level 1) electron and muon triggers with minimal dead time.

A schematic view of the CFT is shown in Fig. 3.6. The detector consists of closely packed ribbon layers of scintillating fibers mounted on eight concentric carbon-fiber support cylinders extending radially from 20 to 51 cm and providing full coverage in the central region up to $|\eta| < 1.7$. The inner two cylinders are 1.7 m long while the outer six are 2.5 m long in order to accommodate the silicon H-disk detectors located at high-η. A barrel supports alternate scintillating-fiber doublet layers (*i.e.,* two rows of interlocking fibers, as shown from the r–ϕ end-views in Figs. 3.6 and 3.7). The first layer of doublet fibers are parallel to the beam line while the second layer is at a constant pitch of

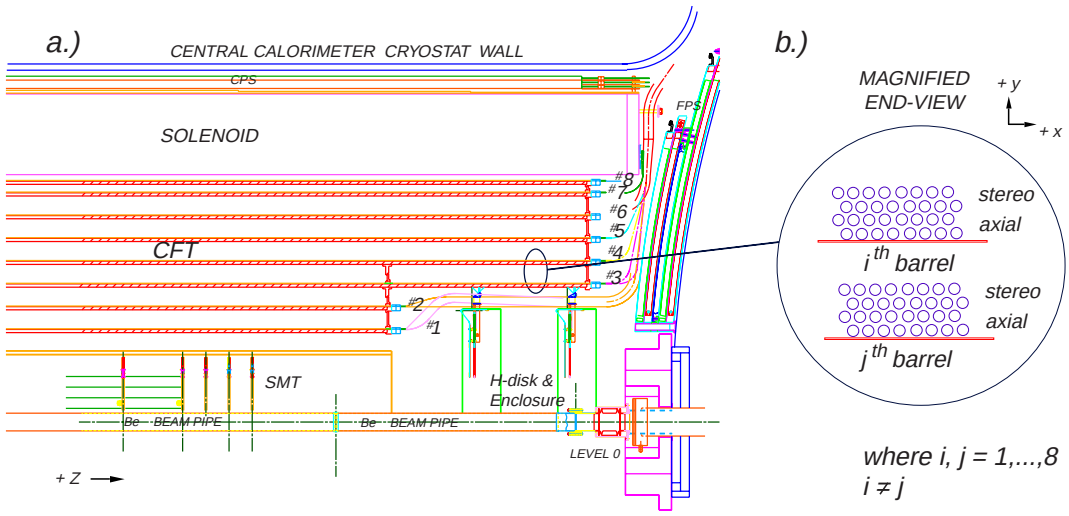

Figure 3.6: Quarter r–z view of CFT detector as installed at DØ. Shown is a) the nested eight barrel configuration of the device, A magnified r–ϕ end-view of the two ribbon doublet layers per barrel is also given in (b).

$\pm 3^\circ$ stereo. Each fiber is 835 μm in diameter and of Kuraray multiclad S-type comprised of a polystyrene core doped with 1% pT and 1500 ppm 3HF [32]. Fibers within a doublet are offset from fibers in the partner layer by half a fiber spacing. This minimizes dead regions and improves the spatial resolution of the tracker. During assembly, fibers are grouped into 256-channel ribbons and mounted with an accuracy better than 40 μm [33]. This helps preserve the detector resolution and also provides enough granularity for detecting tracks and triggering in complex event situations. In fact, as evident from Fig. 3.7, studies with representative CFT ribbons in a cosmic ray system test indicate a doublet position resolution of $\simeq$ 100 μm for single muons [31].

A total of 76,800 channels instrument the CFT. Fibers from a ribbon are routed to custom-machined optical connectors, which transfer light from the scintillating fiber into 8 to 11 m-long clear fibers. The clear fibers are grouped into 256-channel lightguides and transport the optical signal to highly sensitive arsenic-doped silicon avalanche photodiodes, known as visible light photon

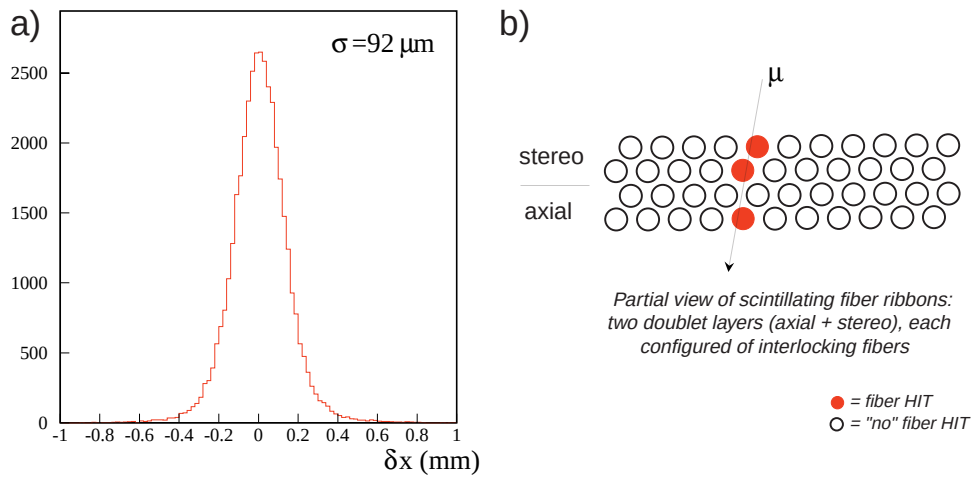

Figure 3.7: a) Distribution for the position resolution measured in the Fiber Tracker for single muons traversing b) an interlocking ribbon doublet configuration.

counters (VLPCs). Here, the signal is converted into electrical charge and pipelined to an SVX-IIe chip for digitization. The VLPCs with their front-end readout electronics are all situated below the DØ detector, on the readout platform. Tests with the CFT read out through VLPCs and SVX-II chips have measured doublet light yields of about 14 photoelectrons (p.e.) for a minimum ionizing particle (MIP) traversing the detector. These responses are more ($\sim \times$ 3–4 higher) than that needed for efficient tracking [34]. Further, a doublet efficiency greater than 99.9% has been measured for an established $\simeq 2$ p.e. (*i.e.*, $\simeq$ 10 fC) charge threshold, yielding signals well above the electronic noise levels in the tracker readout [35]. The reader is directed to Chap. 5 for an extended discussion of VLPCs as well as the process of scintillation light propagation and detection.

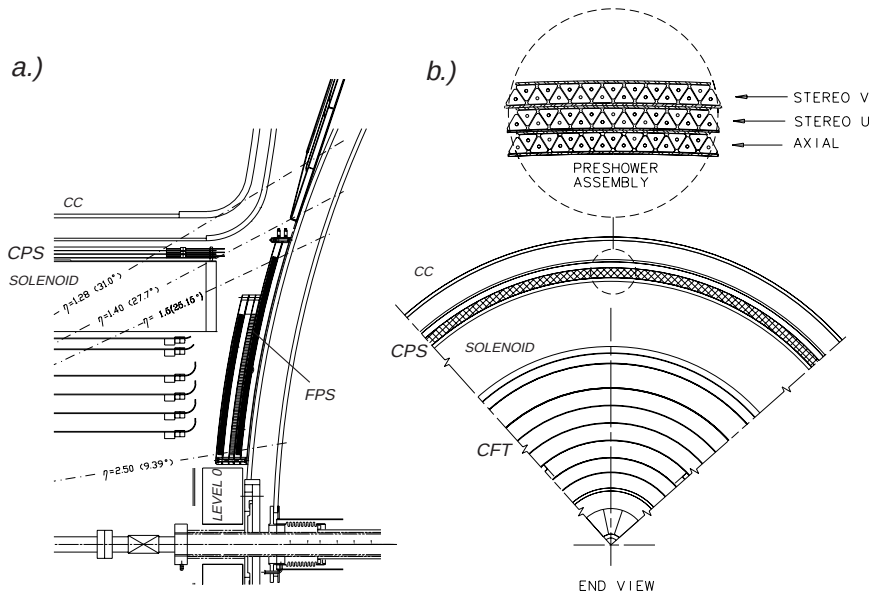

Figure 3.8: Central Preshower detector shown in: a) r–z semi-quarter-view and b) cross-sectional (r–ϕ) end-view of the DØ tracking system. The inset in (b) gives a magnified view of the triangular strip nesting and layer configuration.

3.3.3 Central Preshower

The Central Preshower (CPS) for DØ is based on a similar scintillator-fiber technology as the CFT. The detector, as shown in Fig. 3.8, is cylindrical in shape and is mounted in the nominal 51 mm gap that exists between the solenoid and central calorimeter. This location allows the detector to play a dual role in DØ's detection capability. First, it functions as a calorimeter element, participating in the early energy sampling of the particles traversing the solenoid and entering the central calorimeter. Additionally, it can be employed as a tracker by precisely measuring in η, ϕ, and z the position of traversing particles, thereby adding to the track information from the SMT and CFT.

The detector is made up of three concentric cylindrical layers, each accom-

modating an array of nested $\simeq 6.1$ mm base extruded triangular plastic scintillator strips with co-axially embedded 835 μm-diameter wavelength-shifting (WLS) fibers (see cross-section in Fig. 3.8b). Strips in the innermost layer are oriented axially while those in the two outer layers are arranged in a u, v-stereo configuration with $\pm 22.5^\circ$ crossing angles with respect to one another [36]. Each strip is about 2.6 m long, with the WLS fiber split at the center of the detector to effectively double the segmentation along the beam direction. The saw-tooth of one strip is nested with the saw-tooth of a neighboring strip to improve the position resolution when light-sharing information between adjacent strips is used. Directly surrounding the $1X_\circ$-thick solenoid coil is an additional $1X_\circ$ layer of lead radiator (at $\eta = 0$; *i.e.,* normal incidence) so as to initiate showers for electromagnetically interacting particles.

A circular $\simeq 1$ mm-diameter hole is located at the center of each extruded triangle allowing a 0.835 mm-diameter wavelength shifting (WLS) fiber to run longitudinally through the scintillator. The end of the WLS fiber opposite the readout is aluminized for optimal collection of light. Moreover, each strip is wrapped in aluminized mylar for optical isolation. Light from the scintillator-WLS fiber assembly is allowed to exit through optical connectors and, similar to the CFT, is propagated through 8 to 11 m-long clear lightguides to VLPCs and SVX-IIe readout.

The CPS is one of two preshower detectors (the other being the Forward Preshower) in DØ. The two are based on identical scintillation-fiber technology. However, since they occupy different regions in the DØ detector, they differ in a) geometry (*i.e.,* the shape and orientation) and b) the number of layers comprising each detector. However, since the focus of this dissertation is the Forward Preshower for DØ, any detailed discussion of the system is deferred to later chapters.

3.3.4 DØ Calorimetry

The DØ detector was designed to measure with high resolution the energy and direction of electrons, photons, and jets over a broad range in pseudorapidity. Furthermore, the detector is required to distinguish efficiently electrons and shower patterns characteristic of hadronic jets as well as to provide with sufficient resolution missing transverse momentum information needed to infer the presence of neutrinos and other non-interacting particles. Such measurements are possible through the use of calorimetry. Here, incident particles are made to interact in a large detector mass to yield a large number of secondary particles, which in turn generate tertiary particles and eventually produce a cascade or 'shower' of lower energy particles. The entire process measures the ionization loss of the secondaries. Since the number of secondaries is proportional to the incident particle's energy, the amount of energy the parent particle deposits can be determined.

The DØ calorimeter is a fundamental component of the DØ detector, playing a dominant role in the detection of key signatures from $p\bar{p}$ interactions. The entire system is hermetic (*i.e.,* provides full coverage about the beam axis and also in η) and is separated into three different cryostats: one central (CC) and two symmetric end (EC) calorimeters. Each calorimeter is further subdivided into three sections: the electromagnetic, fine hadronic, and coarse (or outer) hadronic modules. A cross-sectional view of the calorimeters including these separate components are illustrated in Fig. 3.9. The following sections discuss each of the calorimeters.

Electromagnetic Calorimeter

The innermost layer of the DØ calorimeter, closest to the interaction point, is optimized for precision measurements of electrons and photons, and is re-

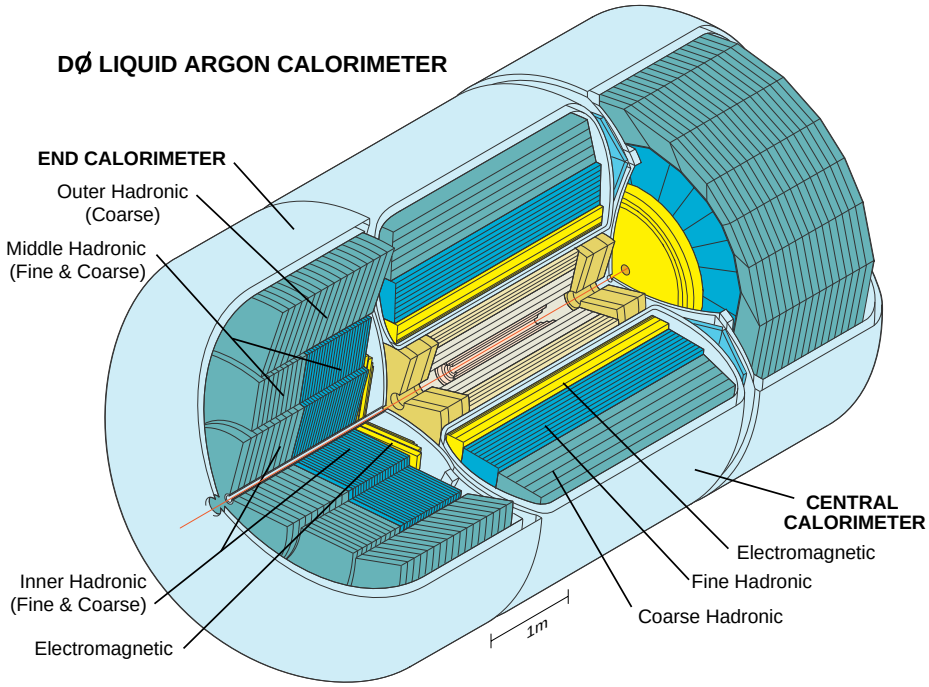

Figure 3.9: Cutaway view of the DØ calorimeter.

ferred to as the electromagnetic (EM) calorimeter. The calorimeter is a sampling calorimeter composed of a depleted uranium absorber and a liquid argon (LAr) sampling medium. LAr was chosen as the sampling material for several reasons: a) it provides uniform gain over the entire calorimeter, thereby allowing for a channel-to-channel response stable over time and only dependent on gap and absorber thicknesses, b) is highly flexible in segmenting the calorimeter volume into readout cells, c) is radiation hard, and d) is relatively straightforward to calibrate. Meanwhile, the high density of uranium not only allows for an inexpensive, compact detector but improves the e/π ratio. The need to operate the calorimeter at liquid argon temperatures imposes restrictions on the detector design. Construction and installation concerns as well as the necessity to access the inner tracking volume dictate the central calorimeter (CC) to exist as a separate unit from each of the two end calorimeters

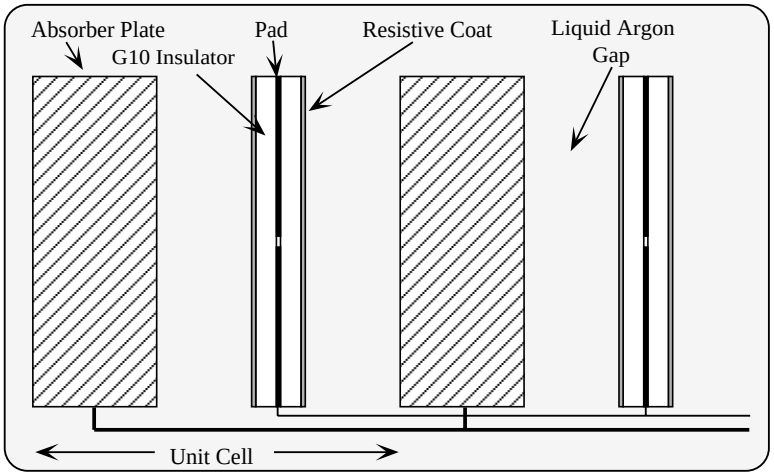

Figure 3.10: Schematic view of a representative calorimeter unit cell. The gap structure, grounded absorber plates, and signal boards are shown.

(EC-North and EC-South). The CC covers the central region of DØ within $|\eta| < 1.2$, whereas each EC extends the coverage from $\eta = 1.3$ to 4.2 for measurements near the beam line. At $|\eta| < 1.5$, Inter-Cryostat detectors (ICD) based on a scintillator-fiber technology are mounted to instrument the 1.5 to 3 inch gap between the CC and ECs (see also Sec. 3.3.7).

The EM calorimeter is 21 radiation lengths deep and is divided into a large number of mechanically self-contained modules, each composed of alternating layers of uranium absorber plates and signal boards (as shown in Fig. 3.10). A 2.3 mm LAr-filled gap separates the signal boards from the absorber plates. The absorber plates are 3 (4) mm-thick in the CC (EC). The signal boards are printed circuit boards made of two 0.5 mm-thick layers of G10 sandwiching copper-clad readout pads; the outer surface of the circuit boards is coated with a resistive epoxy coating. This results in a positive high voltage of 2.0–2.5 kV with respect to the grounded absorber plate. A drift field across the LAr gap is generated allowing a shower traversing the gap to produce ionization tracks as it crosses to the next absober plate. The liberated electrons drift toward

the signal board, producing a current that induces a signal onto the copper readout pads. Readout pads at the same η and ϕ and consecutive in depth are grouped together to form readout cells.

The EM portion of the calorimeter consists of four layers of cells. The first two layers measure the initial longitudinal development of a shower and are about $2X_o$ each into the CC (and about $2.3X_o$ each into the EC). The maximum of an EM shower is expected to occur within the third layer and thus, measures $7X_o$ thick. The final layer contains the shower within an additional $10X_o$. The calorimeters are transversely segmented into a pseudo-projective geometry in which the cell boundaries are non-projective but the towers they form point to the nominal interaction point. The transverse segmentation in $\Delta\eta \times \Delta\phi$ is 0.1×0.1 in all layers except for the third, which is twice as finely segmented in both η and ϕ with cells of size $\Delta\eta \times \Delta\phi = 0.05 \times 0.05$. This granularity allows an accurate measurement of the shower's transverse position. The segmentation of the calorimeter system is given in Figs. 3.11 and 3.12.

Hadronic Calorimeters

Hadronic calorimeters directly surround the EM calorimeter (in both the ECs and CC) and are 7–9 nuclear interaction lengths deep and divided into four (CC) or five (EC) layers. The transverse segmentation of all hadronic modules is $\Delta\eta \times \Delta\phi \approx 0.1 \times 0.1$. The CC has two different types of modules: a) 16 fine hadronic (FH) modules, and b) 16 coarse hadronic (CH) modules. The FH modules make up the first three out of the four CC layers (of depths of 0.9λ, 1.0λ, and 1.3λ) and radially exist directly behind the EM layers. The FH consists of 6 mm-thick uranium-niobium alloy absorber plates and primarily measure the hadronic shower shape. The CH, on the other hand, consists of

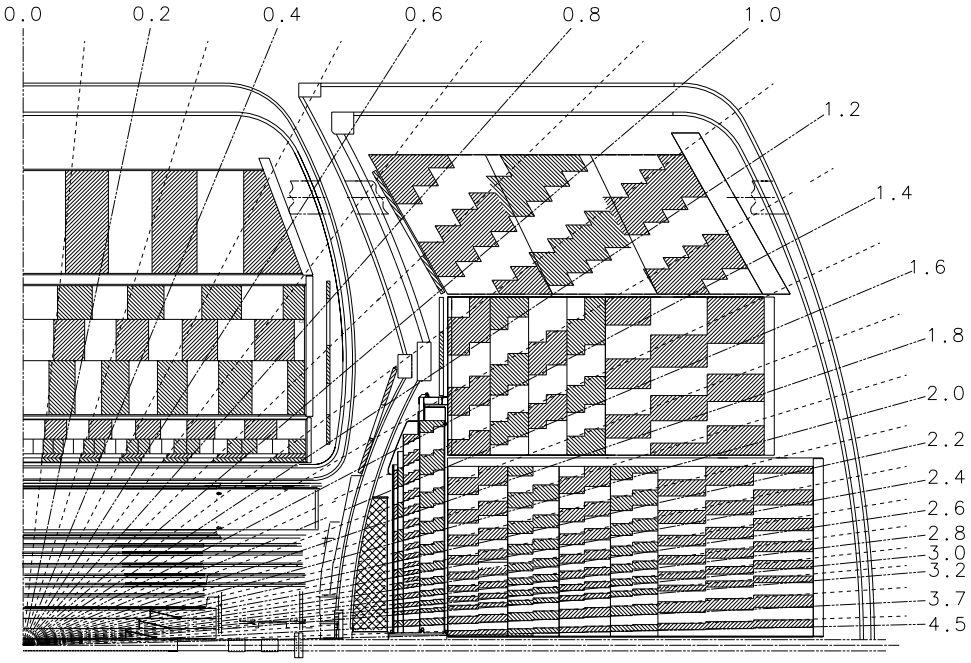

Figure 3.11: Side-view of one quarter of the DØ calorimeter system, showing segmentation and tower definitions (see text). The lines extending from the center of the detector denote the pseudorapidity coverage of cells and projected "towers".

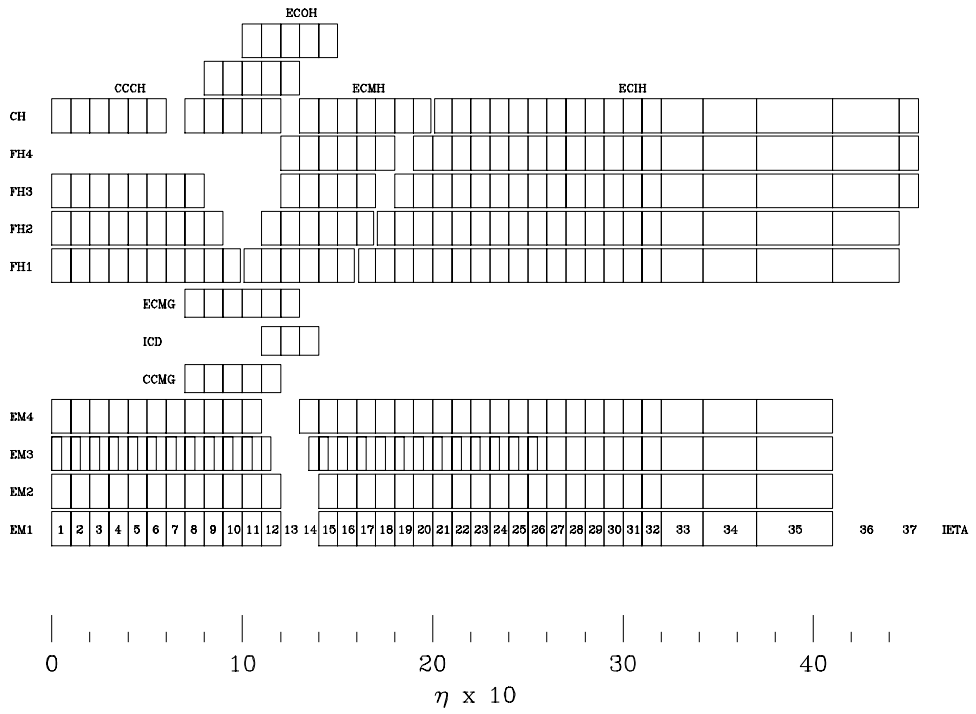

Figure 3.12: Calorimeter channel configuration in terms of depth and η.

a single layer at 3.2λ deep with 46.5 mm-thick copper absorber plates. These modules help contain the longitudinal development of a shower.

Like the CC, the EC hadronic calorimeters contain a fine and coarse modular assembly. However, the geometry is different. Here, the FH and CH module segmentation exists with a slightly different ordering scheme from that of the CC. Directly behind the electromagnetic layers is a cylindrical fine and coarse inner hadronic module, which is radially followed by a ring of fine and coarse middle hadronic modules, and subsequently another ring of coarse outer hadronic modules. Similar to the electromagnetic sections, most of the hadronic modules use depleted uranium as the absorber material because of its high density and compensating e/π response.

3.3.5 Calorimeter Readout

The improvements to the Tevatron collider in Run II require a modification of the Run I readout electronics of the calorimeter. The higher instantaneous luminosity with the shorter bunch crossing interval of 132 ns (compared to a Run I bunch crossing interval of 3.5 μs) forces a faster readout time (*i.e.,* shorter signal shaping time) as well as an analog buffering capability to pipeline data until a first level (L1, see Sec. 3.4.1) trigger decision is available. At the same time, a low-noise performance and minimal channel-to-channel variations must be maintained, thereby preventing any degradation to the calorimeter's performance. Given here is a brief outline of the Run II calorimeter readout chain [37]. A schematic of the electronics is shown in Fig. 3.13.

The signal from each calorimeter readout cell is taken to a feedthrough port via 30 Ω resistive coaxial cables. The impedance-matched cabling maintains a low-noise transfer of the signal to preamplifiers. The integrated circuits in the preamplifiers convert the charge to voltages that are proportional to

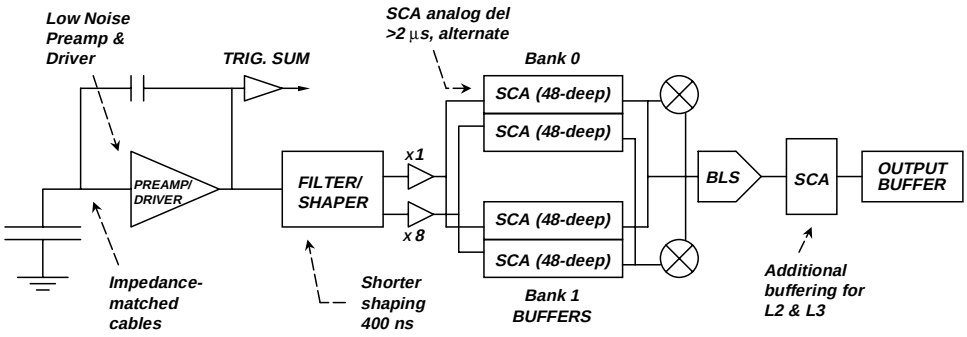

Figure 3.13: Schematic of the primary elements for the DØ calorimeter electronics.

the input charge. In order to minimize electronic noise stemming from the shorter shaping times, the preamps incorporate a dual FET input design. The output voltage is stored in an array of capacitors called the Switched Capacitor Array (SCA). The SCA is a 48-element-deep storage device that provides a buffer zone for saving analog information from a calorimeter channel until it can be processed through analog-to-digital converters (ADCs) after an event has occurred and a trigger has been received. A pulse from the SCA is delivered to baseline subtractor (BLS) modules, which further shape the analog signal and remove slowly-varying offsets in the input voltage. A second SCA can be filled while the first one is being processed, avoiding any deadtime. Once the event has been accepted by the first level trigger, the ADCs digitize the sampled output. Additional SCAs are used after the BLS to store data while awaiting higher level (L2, see Sec. 3.4.2) trigger decisions. The data is ultimately transferred to a host computer for storage and analysis. All three calorimeter cryostats together contain a total of 47,800 channels.

3.3.6 Calorimeter Performance

The performance of the DØ calorimeter has been studied extensively in test beams as well as during the detector's initial operating period, Run I [38, 39, 40, 41] (and see also [25, 18, 37]). The measured response to single electrons and pions has been observed to be linear to within 0.5%. It is believed that comparable resolutions are expected during Run II.

The energy resolution is parameterized as:

$$\left(\frac{\sigma}{E}\right)^2 = C^2 + \frac{S^2}{E} + \frac{N^2}{E} \tag{3.7}$$

where C, S, and N denote calibration errors, stochastic fluctuations of shower development, and noise contributions, respectively. For electrons, the resolutions are:

$$C = 0.003 \pm 0.002, S = 0.157 \pm 0.005\ (\mathrm{GeV})^{\frac{1}{2}}, N \approx 0.140\ \mathrm{GeV} \tag{3.8}$$

and for pions,

$$C = 0.032 \pm 0.004, S = 0.41 \pm 0.04\ (\mathrm{GeV})^{\frac{1}{2}}, N \approx 1.28\ \mathrm{GeV} \tag{3.9}$$

The position resolution of the EM calorimeter varies as $1/\sqrt{E}$ and is found to be 0.8–1.2 mm for 100 GeV electrons.

Test beam results with the calorimeter yield an e/π ratio of about 1.11 at a beam energy of 10 GeV, dropping to ≈ 1.05 at 150 GeV [42].

3.3.7 ICD

Particles traversing the region in the calorimeters occupying $1.1 < |\eta| < 1.4$ (see Fig. 3.11) will pass through several layers of central and endcap calorimeter support structures that contribute to dead regions with none or minimal

energy sampling. To allow measurements in this area, an Inter-Cryostat Detector (ICD) is mounted on each face of an end-cryostat wall [43] (see also Chap 8, Sec. 8.3). This scintillating tile array not only allows for the sampling of particles exiting the solenoid and CC cryostat walls but enhances the measurement of hadronic jet energy. It further allows calculating the missing transverse energy ($\not\!\!E_T$). Each ICD (*i.e.,* north or south) consist of 16 trapezoidal-wedges[2], 22.5° in ϕ. A groove within a scintillating tile carries a WLS fiber, which transmits light via optical connectors to clear fibers exiting the outer edge of a tile module. These clear fiber ribbons transport the light to photomultiplier tubes that are controlled and read out from crates mounted outside the endcap calorimeter walls. Much of the readout electronics for the ICD is similar to that of the DØ calorimeters.

3.3.8 Muon System

Muons do not readily initiate electromagnetic showers at Tevatron energies and can penetrate several layers of matter, depositing only ionization energy in the process. Therefore, an accurate determination of a muon and its momentum can be made by a matched CFT track with a separate muon system, situated furthest from the DØ interaction region. The muon detector is the largest physical subsystem within DØ. For sake of brevity, only the major components are highlighted here, and the reader is referred to [44, 45, 46] for a thorough description.

The DØ muon system consists of central and forward detectors, as shown in Fig 3.14. These sub-detectors are each separated into three detection layers, increasing radially outward and conventionally labeled: A, B, and C. The

[2]Existing services from the solenoid magnet require truncating the ICD array to only 15 ϕ-wedges on the south-EC for mechanical clearance when the detector is in its running configuration.

A-layer is separated from the B- and C-layers by a 2 T toroidal iron magnet. The toroid is subdivided into three magnetized regions: a) a central iron (CF) magnet, covering the angular range $|\eta| < 1$, and b) two end-iron (EF) magnets, covering the region from $|\eta| = 1$ to about $|\eta| = 2.5$. The azimuthal field generated by the toroid causes deflections in the r–z plane such that the muon's trajectory and momentum can be determined by measuring how much a B- and C-layer's track bends with respect to the matching A-layer track. The resolution is improved through a global fit of the A-layer track with an associated minimum ionizing trace (MIP) in the calorimeter and a matching track in the CFT and preshower.

The central muon region covers $|\eta| < 1$ and consists of the three layered (A, B, C) Wide Angle MUon System (WAMUS) — *i.e.,* proportional drift tube (PDT) chambers — and cosmic ray scintillation counters implemented for timing. The WAMUS PDTs (filled with a 80% Argon, 10% CF_4, and 10% CH_4 gas mixture) provide a coordinate determination by producing for each hit: a) the drift-time perpendicular to the anode sense wire, b) the difference in the arrival time of the hit at the two ends of the sense wire, thereby approximating the distance along the wire, and c) the charge deposition on chevron-shaped vernier pads for a more accurate measurement of the distance along the wire in combination with the coarse measurements from timing. The cosmic ray scintillating counters (known as the "Cosmic Cap") are mounted outside of the WAMUS C-layer PDTs (see Fig. 3.14). Here, for each PDT chamber, eight counters each composed of scintillator sheets with embedded WLS fibers are read out by two 1.5 inch-diameter phototubes [44]. Additional coverage of the Cosmic Cap is extended to the underside of the DØ detector to assist in trigger and track matching with the CFT (see Sec. 3.4 for a discussion on the DØ trigger framework).

In order to determine a match in ϕ with the DØ central tracking sys-

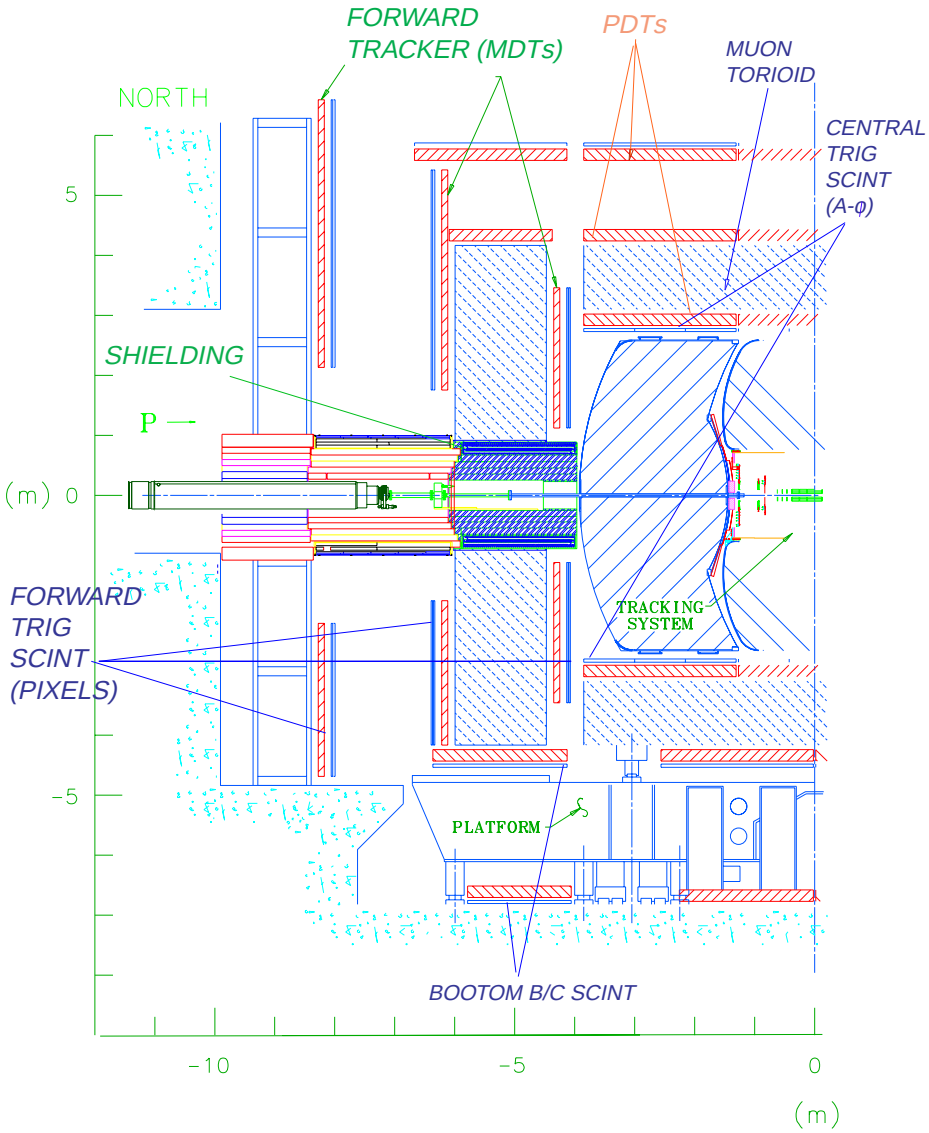

Figure 3.14: r–z half-view of the Muon System. Components of both the Forward and Central systems are shown.

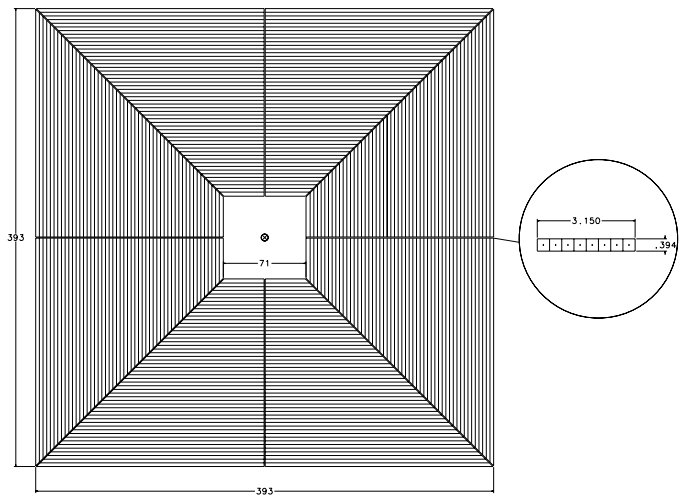

Figure 3.15: Illustrative view of one r–ϕ plane in the muon mini-drift tube. The insert shows the cross section of a single Iarocci tube, which consists of eight 1×1 cm^2 cells.

tem (*i.e.,* for high- and low-p_T muon triggers), a layer of "A-ϕ" scintillation counters are placed between the CC outer-wall and WAMUS central A-layer PDT. These counters also serve to reject out-of-time backgrounds at/near the calorimeter's exit. A scintillator-fiber and PMT technology is used for these counters [44].

The detection coverage is extended from $1.0 < |\eta| < 2.0$ by the forward muon system. Instead of PDTs, Iarocci mini-drift tube (MDT) chambers are arranged in three planes (A, B, C) with (4, 3, 3) layers of tubes per plane. As shown in Fig. 3.15, the tubes are oriented in a r–ϕ geometry and contain square 1 cm-wide (internal) cross-sectional cells. At the center of each cell, a 50 μm anode wire is strung, providing coordinate information of forward muons. Three layers (A, B, C) of scintillation pixel counters (also in a r–ϕ geometry) segmented in $\Delta\eta \times \Delta\phi = 0.1 \times 4.5^\circ$ (see Fig. 3.16) are installed to optimize tracking and detect low-p_T ($\simeq$ 3 GeV) muons, characteristic of a number of physics signals. Each counter serves similar functions as the

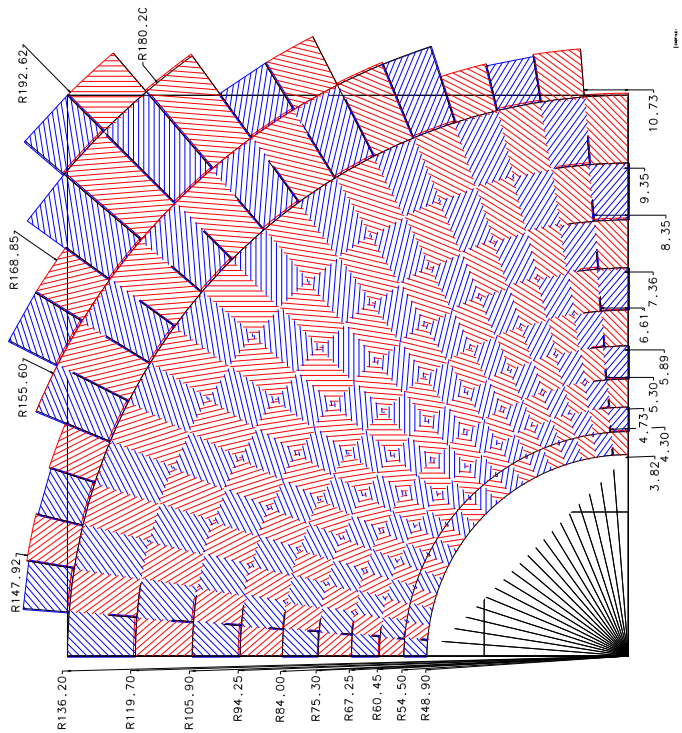

Figure 3.16: r–ϕ segmentation of the muon scintillator pixel counters.

central A-ϕ counter by providing a coincident hit in all three pixel layers in conjunction with a CFT/FPS forward trigger-track match.

Finally, as shown in Fig. 3.14 (and Fig. 3.2), the muon system contains a series of iron (50 cm-thick) and polyethylene (15 cm-thick) shielding with lead skins (5 cm-thick) that surround the accelerator beam pipe in the forward direction, behind the endcap cryostat wall (at about $2.5 < |\eta| < 3.6$). The shield is expected to reduce background fluxes interacting in the quads and beam pipe and from beam halo by a factor of 2 to 4 [47].

As described earlier, the muon momentum is measured by reconstructing the trajectory before and after the particle passes the iron toroid. If possible, the hit in the A-layer (*i.e.,* before the magnet) is matched to tracks in the inner tracking volume and to minimum ionizing traces in the calorimeter in order to

help improve the measurement. Of course, the momentum resolution not only depends on the quality of information available from the inner tracker but also on the position resolution of the muon system and multiple scattering in the toroid. These latter effects limit the resolution to 18% of the momentum (P). In general, the resolution is parameterized in terms of the inverse momentum $k = 1/P$ and is expected to be [44]:

$$\sigma\left(\frac{1}{P}\right) = 0.18(P - 2\text{GeV/c})/P^2 \oplus 0.005 \tag{3.10}$$

3.4 DØ Trigger System

The high luminosity ($\mathcal{L} = 2 \times 10^{32}\text{cm}^{-2}\text{s}^{-1}$), high rate environment (7 MHz or 132 ns beam crossing) in Run II requires an advanced data acquisition system for the DØ detector. Since recording every event from every crossing is impossible, only the fraction of events that show signs of interesting physics are selected for permanent storage. This type of selection is referred to as *triggering*, and a summary of the process is given below.

The trigger framework, as summarized in Fig. 3.17, is implemented as a hierarchy of three distinct selection stages: Level 1 (L1), Level 2 (L2), and Level 3 (L3) [49]. In the first two of these levels, a decision is made based on the raw detector information and simple algorithms in Field Programmable Gate Arrays (FPGAs), while the third uses software filtering algorithms running on a set of high performance commercial processors. An initial Level 0 (L0) trigger also exists and detects interactions from colliding beam crossings at DØ. It basically yields the non-diffractive inelastic collision rate that is converted into a luminosity. This measurement is available from two Luminosity Monitor (LM) counters, each composed of plastic scintillator-WLS fiber array read out

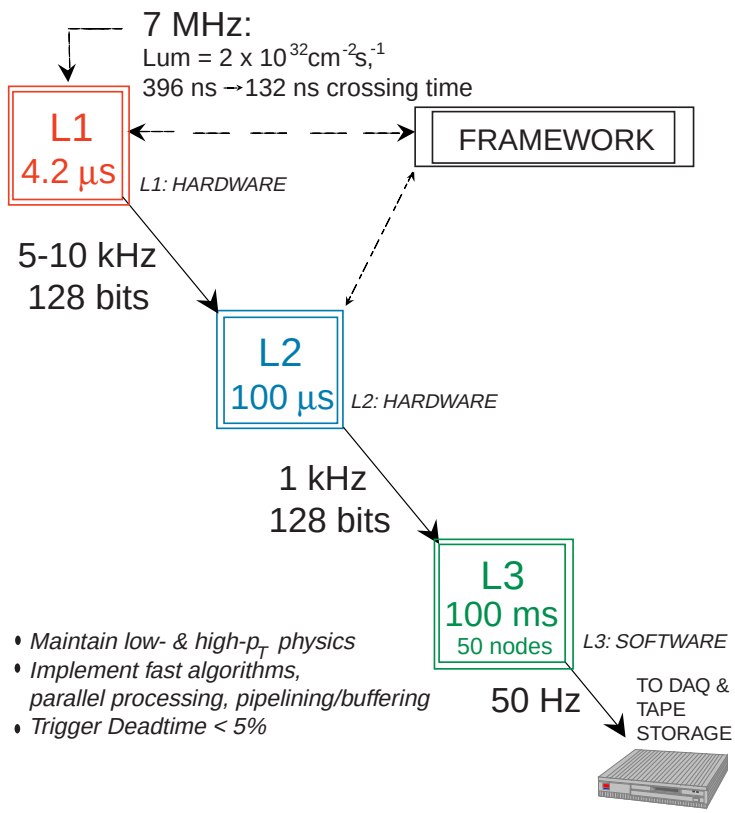

Figure 3.17: Summary of the three-level DØ Trigger System for Run II with the decision time and bandwidth allocated to each level.

by PMTs. Each counter is mounted in a circle on the end-cryostat head, in-between the beam pipe and FPS detector, covering $2.7 < |\eta| < 4.4$ [50] (see for example, Fig. 3.6). Time-of-flight measurements of charged particles incident on the LM also allow the detector to determine the primary vertex position for crossings containing a single $p\bar{p}$ interaction. A single trigger term from the LM is passed on to the Level 1 trigger.

3.4.1 Level 1 Trigger

The first stage (L1) is a hardware trigger system that compiles a list of candidate events obtained from the CFT, preshower detectors, calorimeters,

and muon scintillation counters. The information pathway for the L1 and L2 triggers is shown by the block diagram in Fig. 3.18. The calorimeter, fiber tracker, and preshowers provide electron identification and triggering for $|\eta| < 2.5$. Muon triggers are possible by matching tracks from the CFT axial layers and muon chambers within a fiducial $|\eta| < 2.0$ volume.

Each L1 processor examines its corresponding sub-detector on the basis of trigger terms. These detector-specific triggers include, for example, the candidate's: a) trigger tower E_T above a preset threshold, total energy, and $\not{E}_T$ in the calorimeter; b) hit pattern consistent with track momentum above a threshold, charge, and azimuth in the last axial layer for the CFT; and/or c) energy deposition above threshold, track isolation and match using the forward and central preshowers (see Ref. [48] for a complete list of L1 triggers). Each term indicates a specific condition has been met for the given event.

The results from individual L1 processors are sent to a L1 Framework (L1FW) capable of supporting 128 unique L1 trigger bits. The L1FW is pre-programmed to require a specific combination of trigger terms in order to form global L1 decisions. The list of terms collected from each L1 trigger subsystem is processed through a series of FPGAs located on VME cards to determine if a specific L1 bit has been satisfied. A L1FW logical "accept" digitizes the event, and the trigger is pipelined to 16 event buffers for temporary storage and thus, to reduce deadtime arising from pileup. The L1 trigger decision is subsequently passed up to the L2 system. L1 provides a trigger decision in 4.2 μs with an accept rate of 5–10 kHz [49].

3.4.2 Level 2 Trigger

The L2 system correlates the L1 trigger information from the different sub-detectors. As shown in Fig. 3.19, two stages are distinguished at L2: the

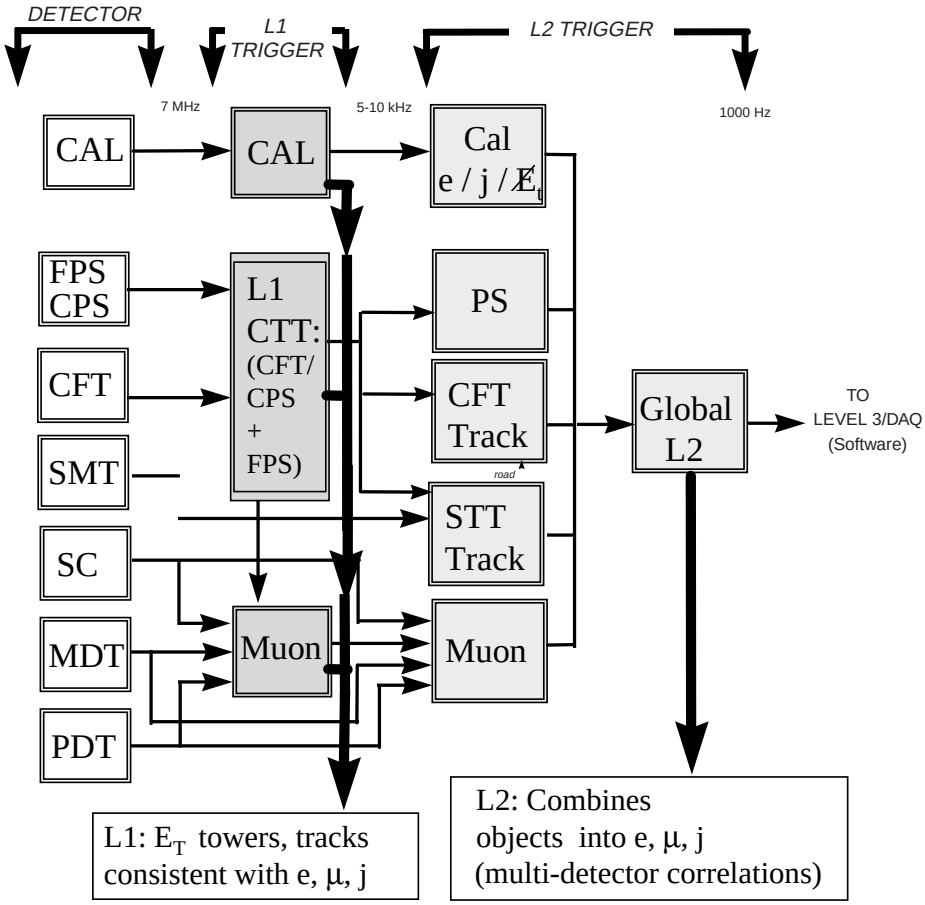

Figure 3.18: L1 and L2 trigger data pathway. The arrow indicates the direction of data flow. Multiple arrows from a particular subsystem are present for parallel processing of detector information and thus, to permit fast trigger decisions and sophisticated physics filters.

preprocessor phase and the global processor. In the first stage, each subystem uses correlation algorithms to build (in parallel) a list of trigger objects available from the L1 detector-specific trigger information. Particular correlations include the energy of clusters in the calorimeter (or preshower) or the azimuth or rapidity of an electron or muon in the central tracker. An expanded list of these objects is summarized in Table 3.1. The time allotted to the formation of these preprocessor objects is less than 50 μs and is limited to a few hundred to a thousand bytes of information for each trigger type.

The list is fed to the global processor via serial data highways of 128-bit (16-Byte) wide data buses (Magical bus, MBus), located on the backplane of the L2 VME crate. The information is transmitted with a nominal throughput of 320 Mbytes/s in order to make trigger decisions within 75 μs [49].

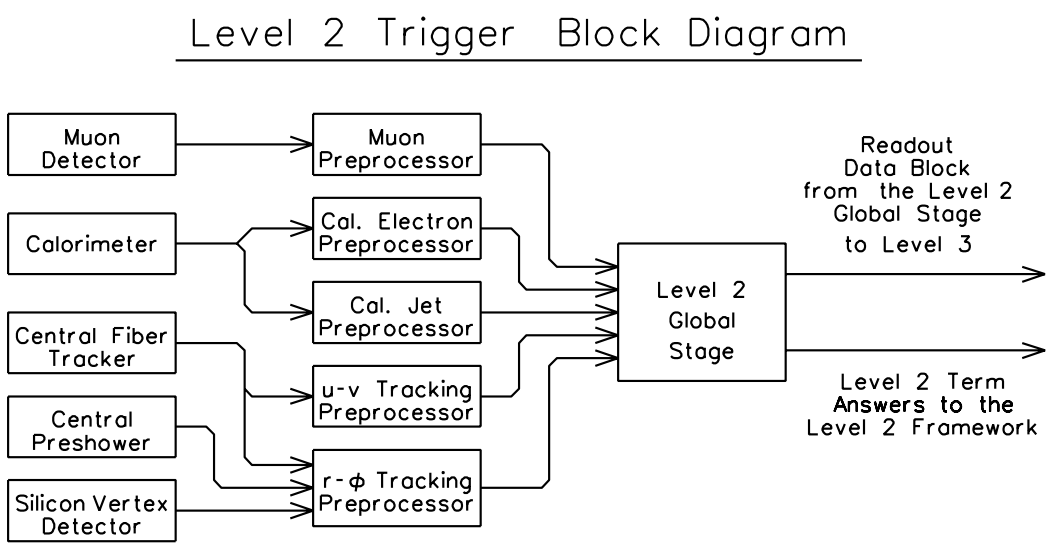

Figure 3.19: Configuration of L2 trigger components.

The global processor considers the correlations among the various detector subsystems, combining the information to form measurable quantities. Exam-

Detector	L2 Preprocessor Objects
Calorimeter (EM)	EM cluster: E_T, η, ϕ, track quality
Calorimeter (Jet)	Jet cluster: E_T, η, ϕ, track quality
CFT	Track: p_T, ϕ, track quality (no stereo $\rightarrow$ no η)
FPS	PS Hit: E, η, ϕ, track quality (MIP vs. Shower)
Muon	Muon track: p_T, η, ϕ, track quality

Table 3.1: Various detector-specific L2 preprocessor objects, for electrons, muons, and/or jets.

ples of such correlations include a) spatial distributions of candidates based on a match between the calorimeter and tracker, b) preshower and calorimeter matches and energy depositions, c) inclusion of preshower information with hits in the fiber tracker, d) determination of jet parameters using jet cone definitions for the calorimeter, and e) the estimated mass of dileptons, dijets, or lepton-jets. The algorithms implemented by the global processor are based on distinct physics signatures studied for a variety of processes and decays of interest with the DØ detector (see Chap. 2, Sec. 2.2). The output from the global processor feeds to a L2 Framework (L2FW), which using a similar FPGA logic as the L1FW, coordinates trigger decisions to L3. The overall L2 system is designed to operate with minimal deadtime ($< 1\%$), providing a factor of 10 rejection. It is required to make a trigger decision in 100 μs at an accept rate of 1 kHz [49].

3.4.3 Level 3 Filter and DAQ System

The L3 trigger and data acquisition system incorporates a farm of high-performance processors operating under a joint Windows NT/Linux environment. Each processor runs event filtering (software) algorithms using "physics tools" that search for physical objects (*i.e.,* for reconstruction of electrons,

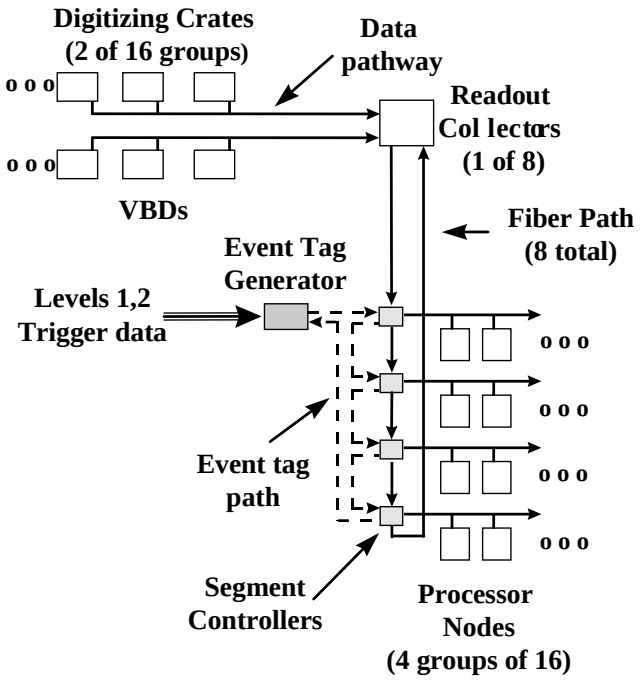

Figure 3.20: L3 trigger framework. Data flow is indicated by the direction of the arrow.

muon, and jet candidates) and relations between them such as event topologies or the invariant or transverse mass distribution. The system relies heavily on a number of parallel processors in order to manage the high event rate as well as to provide a high degree of reliability.

The data acquisition pathway is shown in Fig. 3.20 and consists of a number of parallel paths that use VME buffer drivers (VBD) to feed the L2 information via high-speed data cables to an Event Tag Generator (ETG). Here, a link between the lower level trigger and the data acquisition and L3 nodes is made. The ETG directs the flow of data on the basis of a specific event class and assigns the data block to an available L3 processor node for single event construction. The output from each L3 node goes to another VBD and data cable system consisting of a host interface node that transfers the data to data-logging and monitoring cluster nodes using standard ethernet con-

nections. The filtered events passed by L3 are stored on a robotic tape unit accessible for offline event reconstruction and data analysis. The L3 system provides a trigger decision in 100 ms with an accept rate of 50 Hz [49].

Chapter 4

Physics Motivation for DØ Preshowers

Preshower detectors have increasingly become a popular choice in high energy physics experiments to provide efficient electron and photon identification as well as to enhance the matching between tracking and calorimetric measurements. Rapid advances in technology have allowed them to become much more compact, and thus be easily adapted over broad pseudorapidity ranges, within the confines of a typical inner tracking volume immediately upstream of calorimeters. In general, they serve as a) a particle tracking device for triggering and identification of electrons (and photons) and b) an energy sampler for losses induced by the presence of the large amount of material comprising the inner tracking volume (*i.e.,* readout connectors and cables, detector services, and solenoid coil). In fact, as indicated from Fig. 4.1, simulation studies of the electromagnetic energy resolution of the DØ calorimeters have shown that the calorimeter resolution can degrade by the presence of such material [51]. The studies suggest that the absolute response from the CPS (FPS) must be known to within 10% (15%) to help restore the overall energy resolution without the upstream material. These numbers set the scale to which objects must be measured with the preshowers and prompt the need to include preshower information during event reconstruction. Likewise, the opportunity to capi-

talize on a number of physics processes that probe the SM (see Chap. 2) help motivate the presence of a Central (CPS) and Forward Preshower (FPS) at DØ. An overview of the physics that can be addressed is given below.

4.1 Physics Topics

The full coverage, in addition to the fine granularity and segmentation of the central and forward preshowers, contribute to an enlarged acceptance for low-p_T electrons and photons and, in particular, improve the triggering capability, background rejection, and offline identification of all EM signals. The high rate and large backgrounds, particularly those from QCD processes expected during the upgraded Tevatron run, require some means to reduce data samples by a considerable factor in order to meet the bandwidths of the DØ trigger framework and data acquisition (see Sec. 3.4). The dominant backgrounds for electrons include charged hadrons that overlap spatially with π° decay photons as well as "fakes" originating from jets that fragment with a leading energetic π° or charged pion with a subsequent early charge exchange. Pulse height cuts as well as coarse position-matching algorithms using the FPS (and CPS) with CFT tracks applied at Level 1 ensures rejection and reduces the L1 output rate to Level 2 by a factor of 2 to 4 (3 to 7 at Level 2), dependent on p_T [53]. A preshower trigger combined with a calorimeter trigger at Level 1 and other subsystem tracking triggers at higher levels permits cleaner triggers with lower p_T thresholds.

4.1.1 γ/π° Separation

Major backgrounds such as photons from π° conversions can be rejected using information on the lateral shower shape available from the preshowers

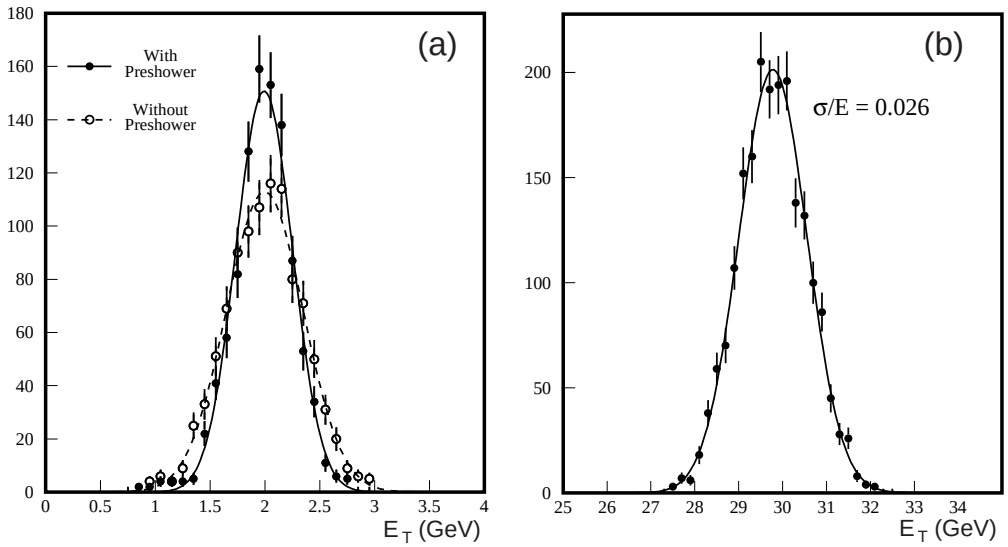

Figure 4.1: Simulation of the Run II DØ calorimeter measuring a) the response to $E_T = 2$ GeV electrons at $\eta = 1$ for the cases with (solid-line) and without (dashed-line) a preshower detector. The resolution with calorimetry alone is shown to be about 18% and improves to 13% when preshower information is included. Also shown is b) the response to $E_T = 30$ GeV electrons with a preshower detector.

and matching calorimeter cells. Further rejection is obtained from the degree of spatial separation between the two photons. In fact, preliminary studies with the CPS have shown that the shower centroid from π° decays are registered in two different scintillator strips/doublets for π° energies up to 10 GeV [54], indicating an important preshower contribution in γ/π° separation. In all cases, however, the level of discrimination depends strongly on combining the preshower hit information efficiently with information from both tracking and calorimetry subsystems.

4.1.2 Low-p_T Phenomena

Physics topics where the contribution of the preshowers is particularly needed are those which have a substantial cross-section and large backgrounds in both the forward and central region. Examples include Drell Yan (W/Z) and a variety of B-physics processes, namely ones that have a low-p_T electron final state. These final states are useful in the study of B semi-leptonic decays, J/ψ, Υ, and χ-state production [55]. In fact, collecting large $J/\psi \to e^+e^-$ samples during detector operation opens the potential for calibrating the response of preshowers in the low energy region on the basis of the dilepton invariant mass. Physics topics such as CP violation also require these and similar samples with as low background as possible. For the J/ψ, dielectron triggers[1] requiring two EM depositions in the calorimeter confirmed by the presence of preshower signals and upstream track candidates can help improve the sensitivity in measuring the sin2β angle of the unitary triangle and thus, determine the CP asymmetry in the B system. Moreover, low-p_T states such as $b \to e + X$ are important for B-mixing studies and B-hadron lifetime mea-

[1]The reader is also referred to Chapter 9 for a detailed example of a J/ψ trigger using the preshower and the DØ detector.

surements.

The FPS provides an additional tool for identifying electrons in the study of much favored extensions to the SM. These include signals of supersymmetric (SUSY) origin, many of which have low-p_T leptons in the final state. For example, a promising channel for a SUSY discovery entails chargino-neutralino pair production, whose signature contains forward decaying trilepton final-states coupled with substantial missing energy (*i.e.*, $\tilde{\chi}^{\pm}\tilde{\chi}^{0} \rightarrow 3l+\not{E}_T$). The presence of at least one soft electron ($p_T \geq 5$ GeV) detectable with a combination of low-p_T FPS tracking and calorimeter triggers motivates the preshower as an integral component of SUSY searches.

4.1.3 Precision Measurements

As described in Chapter 2, the validity of the SM can be tested through precision measurements of W, Z, and top production. In each of these processes, the decay channels needed for the measurement involve final state electrons that require precision tracking and high resolution energy measurements with good rejection of backgrounds. For top samples, where the decaying electrons frequently appear centrally, a CPS certified electron cluster provides additional electron-ID and rejection of the large $W+$ multijet backgound, thereby complementing the silicon detector's b-tagging capability. W mass determinations depend crucially on the accuracy of the EM energy measurements. Although previous analyses (see for example, Refs. [56, 57]) focus on M_W using calorimeter information alone, this measurement will suffer slightly with the addition of the solenoid coil material in Run II, and benefits from an extra energy sample with the preshowers. Such samples would help lower energy scale systematics, a dominant uncertainty for the W-mass. Likewise, a measurement of the $W \rightarrow e\nu_e$ charge asymmetry fixes the u/d ratio as a function

of the momentum fraction x, and provides strong constraints to parton distribution functions [56]. This, in turn, can improve the W mass resolution, whose systematics is dominated by uncertainties in the structure functions.

Other precision electroweak parameters such as the weak mixing angle, θ_W, or more importantly $\sin^2\theta_W$, can also be measured[2]. It can be determined, among others, by the experimental forward-backward asymmetry (A_{FB}) in $Z \to ee$ events. Such a measurement is ideal with the forward coverage enhanced by the FPS. In fact, preliminary Run II studies for the DØ detector indicate that systematic errors on $\sin^2\theta_W$ are small compared to the statistical error [53], indicating a need for larger data sets and signal detection that makes use of the coverage within this region. A preshower included $\sin^2\theta_W$ extraction should help lower the error and improve the sensitivity in the measurement[3].

4.1.4 QCD and Electroweak Processes

The Run II Tevatron facility offers the opportunity to test the non-abelian self-couplings of the W, Z and γ (*i.e.*, WWV, $V = \gamma$, Z, $WW\gamma\gamma$, etc.) originating from the $SU(2)_L \otimes U(1)_Y$ gauge symmetry in the SM [58]. These trilinear vector boson couplings can best be studied through diboson production processes such as $q\bar{q} \to W^+W^-$, $W\gamma$, $Z\gamma$, WZ. A precise measurement of the coupling parameters provides a crucial test of the SM, while any observable anomaly can signal the presence of new physics. Experimental values and/or limits on the couplings can be obtained by comparing the shape of the

[2]The value of θ_W (or $\sin^2\theta_W$) provides insight on the $V - A$ coupling of light quarks and leptons in the theory of the SM. However, since the SM provides no prediction, the parameter must be determined experimentally. For an extended discussion, see for example Ref. [52].

[3]It is important to note that $\sin^2\theta_W$ also contributes to radiative corrections (or higher-order effects) in the SM. Therefore, any discrepancies from an ensemble of precision measurements are hints of violations of the model.

measured and theoretically predicted distributions, such as the p_T of the W, Z or photon. In Run I, diboson data samples such as those for $W\gamma$ obtained by both the DØ and CDF collaborations were dominated by W/Z + jet(s) background, in which one of the jets fakes an isolated photon [58]. Isolation requirements using preshower triggers as well as kinematic cuts and fits made to the $p_T(\gamma)$ spectra may reduce the background within data samples. Use of the transverse shower profile of the photon from both preshowers and calorimeters can further improve the selection.

The subprocesses $q\bar{q} \to W\gamma$, in which $W \to l\nu$ ($l = e$, μ), are particularly interesting due to a presence of a predicted zero in the helicity amplitudes. In such processes, all SM helicity amplitudes vanish at a particular scattering angle, θ^*, of the W-boson taken with respect to the quark (q) direction in the $W\gamma$ rest frame. Moreover, the zero is a consequence of factorizing the SM gauge theory amplitudes into a factor that contains the gauge couplings and another containing the spin dependence. It has been suggested to correspond to the absence of dipole radiation by colliding particles with the same charge-to-mass ratio (see [58], Pg. 105-106 and Ref. therein) and is therefore commonly referred to as "radiation zero". Ambiguities resulting from the unobserved neutrino from the W-decay, however, complicates the reconstruction of the parton center-of-mass frame. Instead, as shown in Fig. 4.2, a study of these reactions can be done using the invariance of rapidities under boosts, and thus measure the rapidity correlations between the final state leptons and photons directly in the laboratory frame. Any radiation zero would be evident from a resulting dip in these distributions. At the Run II Tevatron, simulations [58] have shown that a conclusive determination of radiation zero requires sufficient rapidity coverage and forces the use of electrons and photons in both the central and forward regions to obtain enough statistics. The improved triggering capability of electrons and photons with the preshower

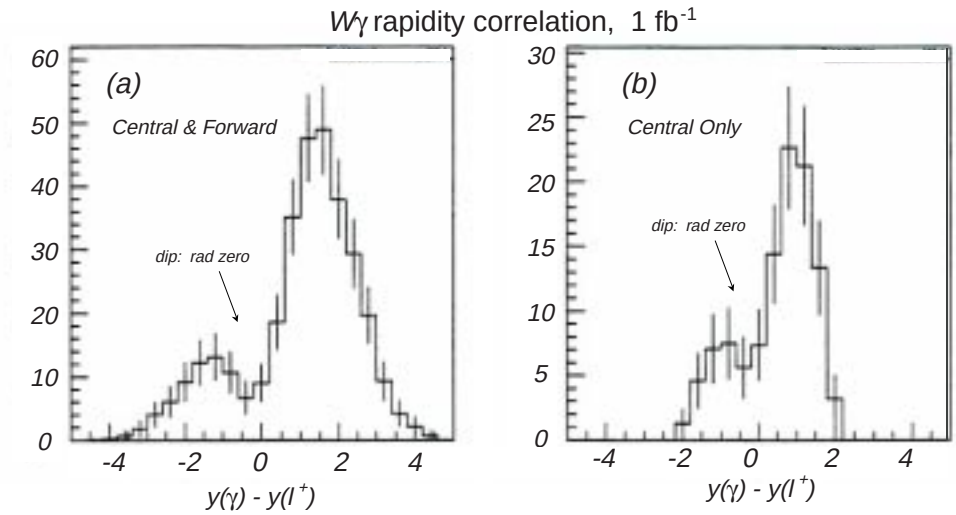

Figure 4.2: Simulations of the photon-lepton rapidity difference distribution for $W\gamma$ production for 1 fb^{-1}, using a) central and endcap photons and electrons, and b) central photons and electrons only. Adapted from [58].

and DØ calorimeter, in addition to the full solid angle coverage, can indeed benefit in such studies.

The functionality of the preshowers can be expanded to assist in a number of other studies, which are needed prior to obtaining final physics results. These include a supplementary position measurement for muons to help improve reconstruction of the muon trajectory and p_T resolution. Effective π° and photon measurements help in establishing the jet energy scale (see Ref. [59]) and thereby, lower systematic errors for a number of important studies — *e.g.*, top, W, as well as Higgs searches. Advanced photon separation algorithms allow an understanding of backgrounds from signals as well as provide a tool to study higher order QCD calculations [60].

4.2 Case Study for Inclusion of FPS at DØ

The detection of electrons plays an indispensable role for a number of Run II physics processes that are of interest and need to be studied at the Tevatron collider. The ability for a detector to efficiently identify electrons and distinguish them from other particles such as hadrons (pions, kaons, etc...), muons, and photons — both online (*i.e.,* at the trigger level) and offline — is crucial to the physics program outlined for Run II. Given the high luminosity expected at the Tevatron and the limited trigger bandwidth available with the DØ detector, good background rejection is required. The detector and its front-end readout must also process signals quickly enough so that results are delivered well within the specified decision time for a trigger. For these purposes, the Forward Preshower system has been designed and implemented in the DØ detector. In fact, as alluded to in the previous section, the FPS is designed to enhance DØ's capabilities in several physics studies:

- the identification of electrons in the forward region for high-p_T final states: $Z \to ee$, $W \to e\nu$, and/or $t\bar{t} \to e + X$,
- the identification of non-isolated, lower p_T electrons: in the study of SUSY signatures, a variety of B-physics processes such as $J/\psi \to ee$, $b \to e\nu c$, and also in final states of Z and top (which contain b),
- γ–π° separation (prompt γ production, $W + \gamma$, $Z + \gamma$).

In view of the above discussion and to illustrate more concretely the necessity and the performance of a preshower at forward rapidities, two quantitative examples, involving a physics simulation [61] of the end calorimeters (EC) and the FPS, are given here. The first study measures the background rejection with the inclusion of the FPS at the trigger level for dijet events, which dominate the background for inclusive electron triggers. The QCD background is

E_{iso} (FPS)	Location of trigger tower	Cross-Section in μb (and Trigger Rate) for EM trigger tower thresholds, E_T		
		E_T = 5 GeV	E_T = 10 GeV	E_T = 15 GeV
none	EC only	18.5±2.9 (0.925 kHz)	1.34±0.32 (67 Hz)	0.22±0.04 (11 Hz)
∞	EC	4.6±0.7 (0.230 kHz)	0.6±0.2 (30 Hz)	0.14±0.03 (7 Hz)
15 MeV	EC	4.4±0.7 (0.220 kHz)	0.5±0.2 (25 Hz)	0.12±0.02 (6 Hz)
15 MeV	EC matched to FPS	2.5±0.5 (0.125 kHz)	0.4±0.2 (20 Hz)	0.08±0.03 (4 Hz)

Table 4.1: Dijet cross-sections and corresponding rates (in parantheses) estimated at a Run II luminosity of 5×10^{31} cm^{-2}s^{-1} for various FPS trigger parameters (E_{iso} and spatial EC–FPS match) and as a function of EM trigger tower thresholds, E_T, described in the text. Results adapted from [61].

generated with $10 < p_T < 500$ GeV and includes in addition, on average, one minimum bias interaction to correspond to a luminosity of 5×10^{31} cm^{-2}s^{-1}. Further, the trigger is modeled as a function of calorimeter E_T threshold in order to observe the level of reduction in the trigger rates for low- and high-p_T processes. The reduction is studied on electron candidates (as defined by calorimeter and tracking) as function of various FPS selection criteria: a) an isolation requirement in the FPS, and b) a spatial match in η and ϕ between the preshower and a trigger tower in the EM calorimeter. Here, the preshower trigger candidates are coarsely matched with six calorimeter trigger towers in pseudorapidity and two towers in azimuth (*i.e.,* $\Delta\eta \times \Delta\phi = 1.2 \times 0.4$). The isolation criterion is tested in terms of the energy deposited by electrons in the FPS using a pure, MC generated $Z \to ee$ sample and requiring the energy in a local region (within a $\Delta\eta \times \Delta\phi$ of about 0.04×0.4) on either side of the electron shower be below a given limit, E_{iso}. A value of $E_{iso} = 15$ MeV is taken as it yields an 85–90% efficiency for electrons from Z decays.

The results are given in Table 4.1 and are catergorized as follows: row one yields the cross-section and corresponding trigger rate measured for an EM tower above threshold, E_T, in the EC; row two in addition requires the FPS energy term and row three the FPS isolation term. Finally, the fourth row includes, in addition to the isolation requirement, the spatial match between the EM trigger towers and FPS. Given the trigger bandwidths that are established for the DØ trigger system (see discussion on Trigger in Chap. 3), it is observed that for low calorimeter thresholds, needed to trigger on low-p_T processes, calorimeter information alone is insufficient. In fact, the addition of preshower information enables the rates to be lowered to a much more manageable level for Level 2.

At higher calorimeter thresholds (and hence, for high-p_T signals), where the rates tend to be lower, the FPS plays a supplemental role in the reduction. Although the degree of rejection appears less than that observed for lower calorimeter thresholds, the preshower ensures that the rates stay within the allocated trigger bandwidth; in particular at Level 3. Nonetheless, it is expected that for these processes, the FPS will mostly contribute at the offline stage, where much more sophisticated algorithms are used to improve the identification of electrons from the QCD background.

It should be noted that the projections given here are based on a collider luminosity expected during the initial operating period of DØ in Run II. Indeed as the run progresses and higher luminosities are achieved, preshower information will increasingly become necessary and tighter correlations between subdetectors will be needed in order to appropriately respond to the trigger bandwidth constraints for both low- and high-p_T states. However, the above projections do indicate that the proposed FPS enables a reduction by a factor of about 3–7 and illustrate the potential for rejection of fake electrons from an integrated preshower system at DØ.

A second study examines the improvement in background rejection due to the preshower with electrons from b decays in $p\bar{p} \to b\bar{b} + X$ (direct b-pair production). Processes such as $b \to e + X$ are of particular importance as they are useful for b-tagging in top, in Higgs samples, as well as for a variety of b physics analyses — all of which are central to the physics program of DØ in Run II. The electrons from b decays in direct b-pair production tend to be of low energy, typically non-isolated, and emitted at forward rapidities. Such electron signals tend to be dominated by large backgrounds and thereby require an additional rejection of background.

The study uses a MC generated sample of $p\bar{p} \to b\bar{b}$ with $5 < p_T(b) < 20$ GeV, in which the b-quarks are forced to decay electronically to $e\nu c$. As a background sample, MC generated dijet events with $2 < p_T(jet) < 100$ GeV are used. The algorithm reconstructs electromagnetic energy clusters in the end calorimeters above a E_T threshold of 1.5 GeV. A tight spatial match between the preshower and EC is made such that FPS energy clusters that line up with the shower centroid in the calorimeter and the reconstructed primary event vertex are required. Further, to ensure electromagnetic showers, the clusters must pass a minimum 10 MeV ($\simeq$ 8 MIPs) energy threshold in the FPS fiducial volume, appropriate for electrons signals.

The results from the algorithm are given in Table 4.2. The efficiency is determined by the fraction of clusters in the signal that are accepted, verified as electrons from the MC information. The rejection against background clusters is taken as the fraction of clusters from the dijet sample that are rejected by the algorithm. The method shows that about 99% of background clusters can be rejected, while 70% of the electron clusters can be reconstructed in the FPS. Although the study is simple, it again demonstrates the capability of the preshower to reduce backgrounds to electrons in the forward region.

Sample	Signal: $b \to e + X$	Background: dijet (Estimated Rate in kHz)
a) # of EC clusters	300	808 (60)
b) with FPS charged track	250	94 (6.9)
c) with FPS shower + (b)	205	9 (0.72)
efficiency (≡c)/a))	68.3%	1.2%

Table 4.2: Results from MC studies of efficiencies for electrons from b decays and from dijet background sample using reconstructed clusters in the calorimeter (row a) and the FPS (rows b–c), and the algorithm described in the text. The estimated background rate, at the luminosity of 5×10^{31} cm^{-2}s^{-1}, is also given in parantheses. Results adapted from [61].

4.3 Summary

The discussion presented here clearly illustrates the wide variety of physics processes that will benefit from and even require a preshower measurement. The example quoted: semi-leptonic b decays in direct b-pair production represents the case for an efficient and clean trigger on low-p_T electrons that is much enhanced and made feasible by the addition of a preshower detector. Similar low-p_T electron signals are found in a variety of high-interest topics: $H \to b\bar{b}$, $p\bar{p} \to t\bar{t}$, CP-violation in the B system, SUSY searches, etc... For high-p_T isolated electrons, the FPS provides additional rejection and cross-checks. Finally, the FPS will enhance the single photon and pion identification. Further, offline analysis with the FPS and CPS provides additional rejection of backgrounds as well as allows understanding efficiencies, performing cross-checks, and identifying correlations between selection cuts in many of these topics. In conclusion, the preshower system offers a direct opportunity to augment the physics program at DØ.

Chapter 5

Properties of Scintillation-based Detectors

Many high-energy experiments require precision multiple track reconstruction in high-rate, high-luminosity environments. A device must be highly segmented to yield good spatial resolution ($\sigma_x \sim 100\ \mu m$) as well as capable of operating with fast response times ($\sigma_t \sim$ 1–10 ns) in order to handle the short bunch spacings at existing colliders. To build such a detector over a large area warrants a technology that is simple, inexpensive and suitably reliable for operation over extended periods of time. All these requirements can be met with a system consisting of a scintillation strip array with fibers for light-collection and transport to a photodetection readout. The system of choice presents itself as a technically viable way for constructing a compact, flexible detector capable of measuring not only the particle's trajectory but sampling its energy as well.

5.1 Scintillation Principles

The basic photochemistry on which scintillation counters operate differs for inorganic and organic materials. However, in this thesis only organic scintillators used within the DØ preshowers are considered, and the reader is directed

to Ref. [62] (and refs. therein) for a disscussion on other compositions.

As ionizing particles pass through a scintillator, the electron structure of the scintillator solvent molecule is excited from its ground state to a higher energy level (*i.e.,* singlet states of molecules – see Fig. 5.1). Through thermalization or internal non-radiative processes, the molecule de-excites to the first excited state S_1. A subsequent transition to the ground state, S_0, follows with the emission of light, known as *fluorescence*, with the wavelength usually in the UV region (peaking at $\lambda \simeq 320$ nm). The fluorescence (see Fig. 5.1) is the chief ingredient in the detection of particles. The entire process, however, is complicated by the fact that a small overlap exists in wavelength of the absorption and emission spectra[1]; the inherent attenuation length of the scintillator scales inversely with the area of the overlap [62]. The overlap region can be minimized by doping the solvent (*i.e.,* those molecules generating the original fluorescence) of the scintillator with a high concentration of a primary fluor and a much lower concentration of a secondary fluor. The multi-step process facilitates the shift in the emission spectra from a shorter to a longer wavelength. The secondary dopent absorbs (through a non-radiative energy transfer resulting from the well-matched energy levels) the emission of the primary fluor, and instead, through its own molecular transition (S_{10}), fluoresces at a longer wavelength where the system's absorption is minimal. The concentration limits of the primary and secondary dopents are set such as to yield an efficient energy transfer between solvent and fluors, while at the same time maximizing the light output from the scintillating mechanism.

The entire process yields light usually in the blue wavelength region (peaking near $\lambda \simeq 420$–450 nm) with an extremely fast response, on the order of

[1]The two spectra are shifted according to Stokes Shift [62], involving a change in the interatomic spacing after excitation of the molecule's electronic states.

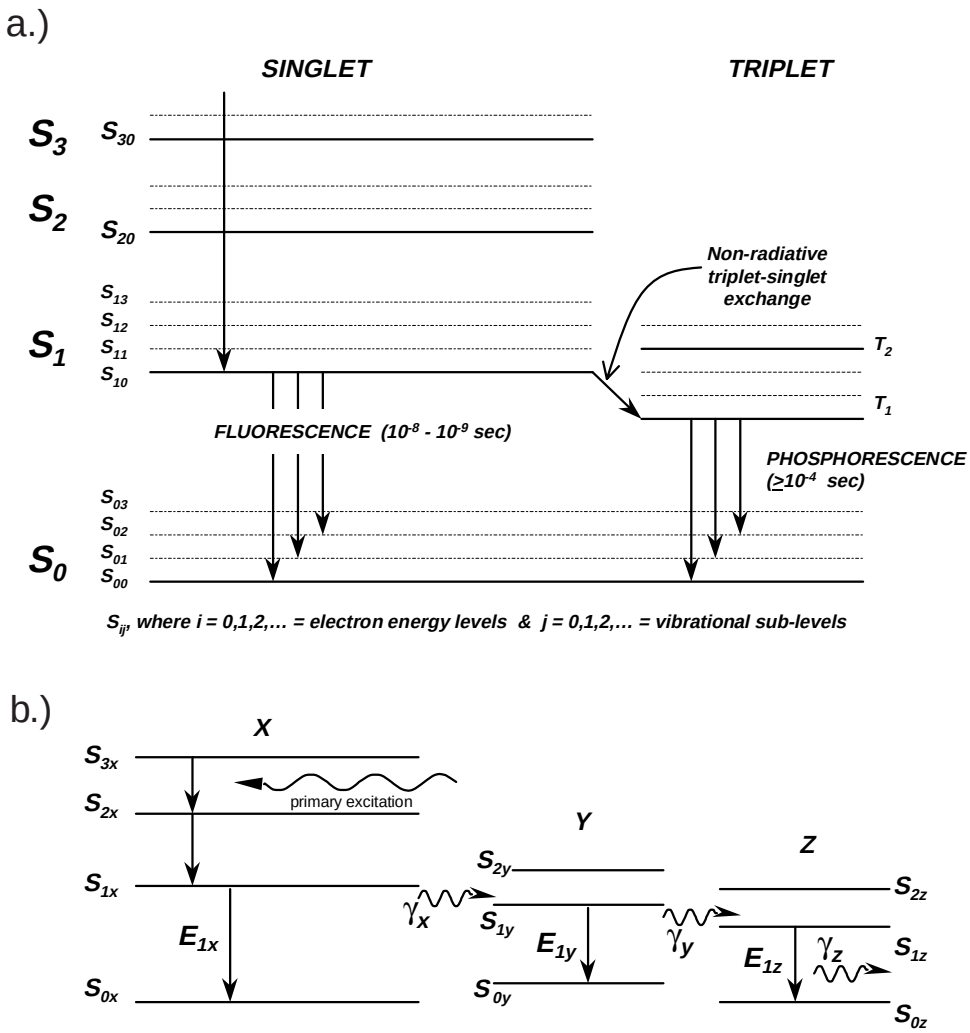

Figure 5.1: Representation of energy levels indicating the fluorescence mechanism in a scintillator. Shown are: a) the π electron energy levels participating in scintillation light and b) the energy transfer process in a scintillator from a solvent (X) with two fluors (Y & Z). Adapted from [62].

10^{-9} seconds, characterized by the S_{10} lifetime of the scintillator. Both the wavelength and time must be well-matched to the spectral range of solid-state photodetectors (such as PMT or avalanche photodiodes) that perform the signal readout. Most devices have efficiencies in the visible region (λ within 480–540 nm), requiring the wavelength of the scintillator to be further shifted to higher values. To do so, a wavelength shifting (WLS) mechanism is added to the scintillation detection system. The WLS element not only serves to absorb and re-radiate the primary scintillation light near the required wavelengths but is also used to transport the signal over necessary distances in large detectors. Further, WLS are used to prevent a loss of the signal while light is pumped from a scintillation counter to a photodetector that is smaller in cross section. Here, waveshifters overcome the limitation by surrounding a scintillator block on one (or more) side(s) with a thin sheet of WLS and allowing the light from the scintillator to be absorbed effectively in the WLS. The light can not only be re-emitted at desired (longer) wavelength but also be transported efficiently into a detector of comparable cross section as the thin WLS sheet.

Given the above principle, one should note that scintillators can themselves be termed "waveshifters" considering the fact that the overall process involves a series of wavelength shifts. However, tradition dictates that scintillators be considered distinct from WLS fibers, although a complete detection system usually requires an optimal combination of both.

5.1.1 WLS Fibers

Optical waveshifting fiber coupled to a plastic scintillator is the technology used for the DØ preshowers. The shift in wavelength relies on the addition of dopents to the base material and follows the same principles outlined above

for scintillators. Moreover, such fibers are primarily available with either a circular or square cross-sectional geometry; for the DØ preshowers, circular fibers (O.D. of 0.835 mm) are adapted and briefly discussed here.

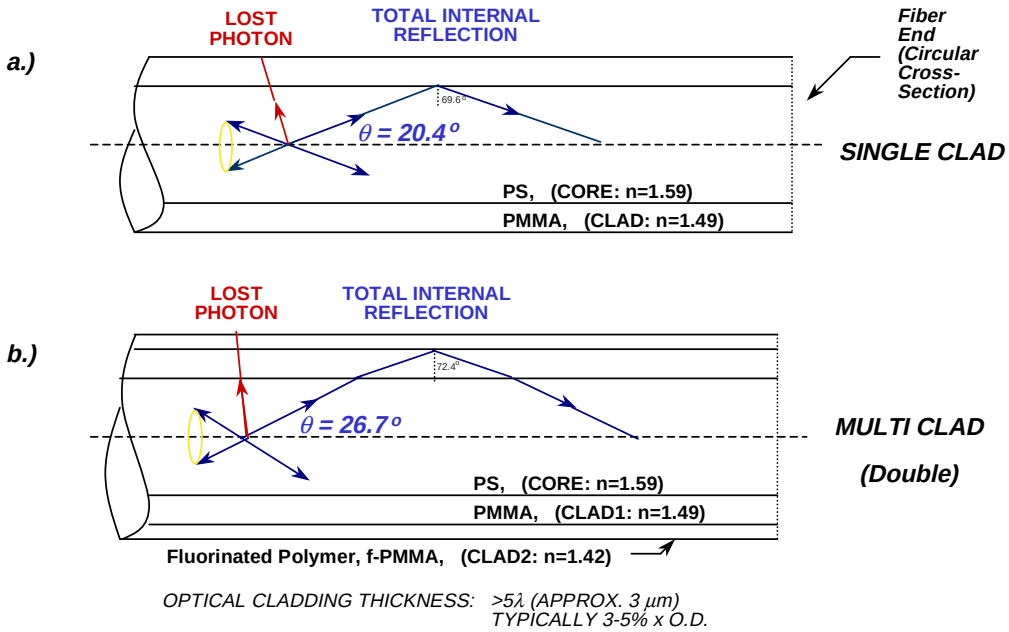

Figure 5.2: Schematic configuration of a typical WLS fiber: a) single clad and b) double clad fibers are shown. Adapted from [62, 32].

The principle of light transmission through the fiber is based on the concept of total internal reflection in optical fibers [63]. Most fibers are fabricated from plastic polymers and are of a "step-index" configuration composed of a) a doped inner polystyrene (PS) core of refractive index, n_{core} =1.59 followed by b) one (singleclad) or more (multiclad) outer co-axial layers of acrylic cladding; one outer layer being the most common configuration. A schematic is given in Fig. 5.2. Normal thicknesses for the cladding are in the range of 3 to 4% of the fiber's outer-diameter [62]. Typical WLS fiber arrangements consists of polymethylmethacrylate (PMMA, with index, n_{clad1} =1.49) as the innermost clad layer, and if a double layer is implemented, fluorinated-PMMA (with

index n_{clad2} =1.42) over the inner cladding[2]. It should be mentioned that the use of plastic fibers as opposed to other types (*e.g.* glass) generally improves photon transmission and provides longer light attenuation and faster response times [64]; all of which are desirable for particle detector applications.

To first-order, the presence of a cladding serves to protect the fiber core against deteriorations at its outer cylindrical surface. Further, the absence of cladding introduces light loss and lower yields. In fact, using the different indices of refraction at the core-cladding interface, the fraction of the isotropically emitted light, Ω, which is contained within the solid angle of the core and is propagated to its end can be determined. From simple optics (*i.e.,* an application of Snell's Law[3]) and the definition of solid-angle, the fractional amount of light delivered with double clad fibers relative to single clad ones can be calculated using:

$$\Omega = \frac{1 - n_2/n_1}{2} \tag{5.1}$$

where n_1 refers to the PS core and n_2 to the outermost cladding layer [66]. Inserting the values for refractive indices (see Fig. 5.2), one notices that double clad fibers improve the light yield (5.34%) over comparable single clad ones (3.14%), resulting in ~70% more light to undergo total internal reflection. Additionally, any fraction of untrapped light, n_2/n_1, eventually escapes from the outer fiber coating at such an angle that makes it difficult for any adjacent fiber to retrap it and instead, allowing it to disappear after a fiber length of about 50 mm. This effect helps suppress cross-talk [64].

The structurally large detectors for high energy physics experiments require

[2]The inclusion of the PMMA as an intermediate cladding layer is required due to the fact that a direct contact of the PS core with the fluorinated-PMMA would result in a mechanically incompatible interface.

[3]The law describes the angle of refraction, θ_i, at an interface with two different refractive indices, n_i, with $i = 1, 2$ by the relation: $n_1 \sin\theta_1 = n_2 \sin\theta_2$.

the use of fibers of several meter lengths. The detection efficiency and overall performance of these devices depend heavily on the light attenuation in the fiber, which scales with the length used. As light propagates through the fiber, a portion of it will be absorbed by the system. Quantitatively, the amount of absorption can be determined by measuring the average signal propagated through the fiber, I, as a function of the axial distance, z. The loss follows an exponential form given by the relation:

$$I = I_{\circ} e^{-z/\lambda} \tag{5.2}$$

The quantity λ is commonly known as the "attenuation length" of the particular fiber and is defined as the distance where the signal has been reduced and fallen off to $1/e$ of its original intensity, $I_{\circ}$. In order to obtain the maximum light output, fibers with a large λ are desirable[4], allowing one to spatially cover large detection regions with minimal light loss. The amount of attenuation depends on a number of factors and include a) the concentration and type of the primary fluor used, b) the addition of an appropriate lower concentration secondary fluor, c) the overall quality of the plastic and its surface, and/or d) geometrical effects. Moreover, the attenuation length also depends on the wavelength of light being pumped along the fiber.

One immediate way of increasing the light output is by applying, through vacuum deposition, an aluminized, mirror-like reflective coating on the (polished) non-readout end of the fiber [65]. Doing so not only allows the light that would normally escape the end to be reflected back into the fiber (and eventually measured at the photosensitive readout) but adds a second term to Eq. 5.2:

[4]Typical attenuation lengths for fibers available through commercial vendors (such as [32, 69]) for detector applications can span values near and between 4–12 meters.

$$I = I_{\circ}(e^{-z/\lambda} + Re^{-(2L-z)/\lambda}) \tag{5.3}$$

Here, R is the reflection coefficient of the aluminized end and L is the length of the medium [54, 65]. One can also replace λ in Eq. 5.2 with an effective attenuation length λ_{eff}. However, since one end is now aluminized, the effective attenuation length does not give the "true" attenuation length of the WLS fiber, but instead provides the level of uniformity over the full coverage length, incorporating the effects of attenuation and reflection. Typically, one can perform fits to fiber attenuation curves using Eqs. 5.2 and 5.3 to obtain the effective attenuation length for the fiber. In fact, using independently measured values of R=0.7 and λ=4.5 [54] with the range of fiber lengths used in the DØ preshowers, the method has shown to increase λ_{eff} by a factor of two or more for silvered fibers over non-silvered ones

One method of coupling WLS fibers to a scintillator is by fabricating small grooves within the scintillator to allow the fiber to be embedded in the scintillator material. Since one end is not readout, a reflective coating at this end is made, while the opposite end gets routed towards the photodetector. Usually, a more efficient means of signal propagation over considerable distances can be facilitated by optically coupling the WLS fiber to conventional (*i.e.,* non-shifting, optical transmission) clear fibers. The effect introduces some (typically 10% or less) light loss [68] at the WLS-to-clear fiber interface. This loss, however, remains lower than that from using WLS fiber alone over lengths larger than some minimum length. Additionally, for the scintillator-fiber mechanism comprising the DØ preshowers, geometry alone would introduce about a factor of 3 loss in light yield if the use of WLS fibers was avoided, and the scintillator was coupled directly via clear fibers to photodetectors.

5.2 Application: DØ Forward Preshower detector

A number of considerations motivate the choice in technology for the Forward Preshower (FPS) detector. Electron identification is enhanced in a device that is highly segmented. Since cost scales proportionally to the channel count, a suitably inexpensive detection system is also called for. Triggering requirements dictate the technology be suitably fast as well. The preshower is designed to distinguish between minimum ionizing signals from hadronic (and muonic) single particle tracks and the comparatively large signals originating from electron showers. Since the preshower is mounted directly upstream of the forward electromagnetic calorimeters (on the end cryostat walls), the existing electromagnetic energy resolution with the calorimeters must not be compromised. In order to prevent any degradation, the energy measured in the preshower must be added, with proper weights, to that measured in the corresponding calorimeter tower(s) for electron candidates. This necessitates the FPS readout be linear over a relatively wide range of energies and stipulates an absolute energy calibration to a sufficient level of accuracy. The desired spatial resolution (for low- and high-p_T signals) also requires the detector be constructed of fine granularity. Finally, another more practical concern is the severe spatial constraints existing in the area between the central tracker and end cryostat walls. Such a situation dictates that the detector be compact and thus, constructed to conform to the spherically-shaped DØ end-cryostat inner head on which it mounts.

In order to satisfy the above criteria, both the CPS (see Chap. 3, Sec. 3.3.3) and FPS detectors are based on a scintillation strip with embedded wavelength-shifting (WLS) fiber technology. The WLS fibers are connected to

several meter (∼10 m) long clear fibers, whose signal is read out by visible light photon counters (VLPCs). Both detectors incorporate identical front-end and trigger electronics, achieve similar light yields, and use similar scintillator fabrication and assembly techniques — introducing modifications as warranted by technical and geometrical considerations. The decision to use such a technology is extensively described in Refs. [53, 55] and has been based on a number of R&D studies, physics requirements, and cost issues. For brevity, only the main characteristics are given here.

5.2.1 Preshower Scintillator and Fiber

The scintillation layer for the preshowers (both FPS and CPS) are comprised of custom extruded triangular-shaped strips of plastic scintillator. During extrusion, a circular co-axial hole is created in the strip. The material is of polystyrene (PS, refractive index n_{PS}=1.60), doped with the same fluorescent compounds as a commerically available scintillator from Bicron Corp. [69], BC-404. BC-404 is a polyvinyltolulene (PVT, refractive index n_{PVT}=1.58) based scintillator with p-terphenyl (pT) and di-phenyl-stilbene (DPS) as the primary and secondary dopants, respectively [54]. For proprietary reasons, the precise concentrations of each dopant in BC-404 are unavailable. The WLS fibers are purchased commercially, from Kuraray International, and are 0.835 mm in-diameter of multiclad Y11 type fiber [32]. The Y11 wavelength shifter is made of a proprietary K27 dopant, with a different and again unknown concentration. The fluorescence spectrum of both the BC-404 (including the emission peak of pT and DPS) as well as K27 have been measured by illuminating either the scintillator and fiber with a 313 nm light source [54]. Results are shown in Fig. 5.3.

BC-404 scintillator is usually available in sheets of 5 mm-thick panels of

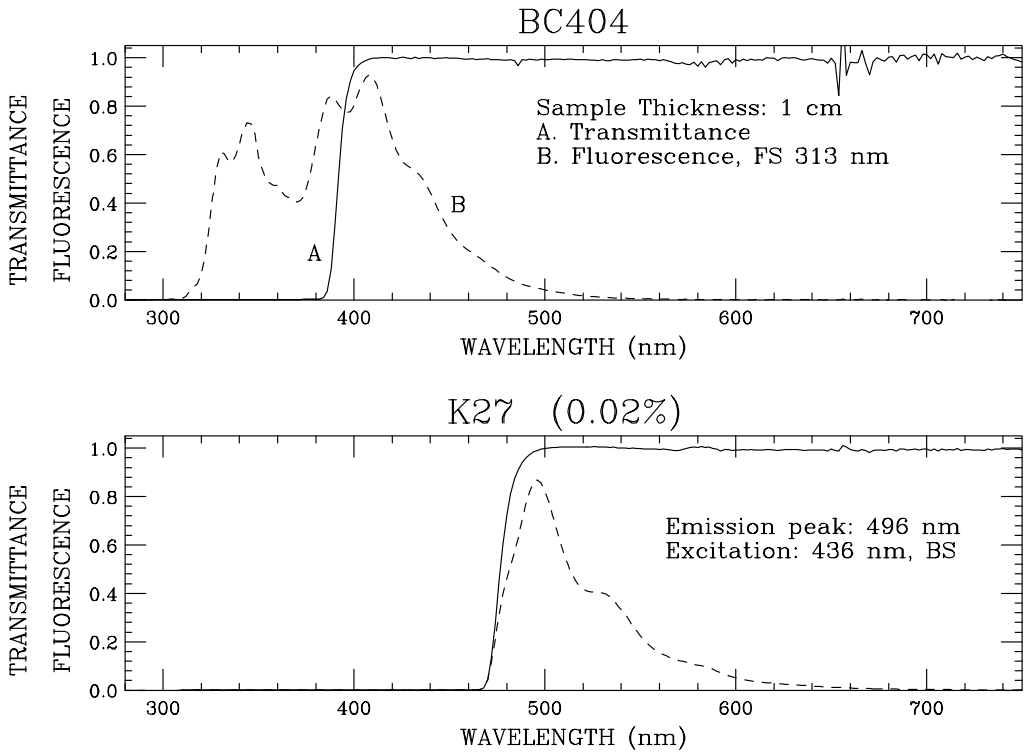

Figure 5.3: Fluorescence spectrum of BC-404 (top) and K27 (bottom). For BC-404, the two peaks near 350 (400) nm are from pT (DPS). The light transmission curve is also given. The light output from BC-404 is a convolution of the emission and transmission curves. For K27, the emission peak includes the effects of self-absorption and is at ∼500 nm. Adapted from [54].

variable lengths that have tolerances ranging around +0.56/-0.45 mm [54] (dropping off with increased dimensions). BC-404 has been used extensively in detectors which require high light yields, long-term stability, and are exposed to high radiation environments. Although it can be adapted for the DØ preshowers, the desire for improved tolerances as well as the need for a triangular strip with central hole motivated alternative approaches. DØ has opted to manufacture its own scintillator through the process of extrusion. One notes that the intrinsic light yield of PVT is ∼ 10–15% greater than strips extruded using PS [54]. However, as described in the previous section, the actual yield

is highly dependent on both the relative and absolute level of the primary and secondary fluor concentrations. R&D studies indicate concentrations of 1% pT and 150 ppm DPS [54] for the extruded option give a spectral yield comparable to BC-404 (see Fig. 5.4).

The extrusion of the scintillator strips has been pioneered by researchers at Fermilab and performed at a commercial vendor [70]. Small cylindrically-shaped pellets of polystyrene ($\approx$3 mm in diameter and $\approx$5 mm in length) are impregnated with the scintillating fluors, yielding pellets of scintillator. These pellets are gradually heated to their melting temperatures ($\sim$ 180–185°C), allowing for an uniform temperature to be achieved along the entire length of the extruded strip. The resulting fluid-like mixture is channeled through an extrusion die, designed according to the cross-section of the strip. Subsequently, the scintillator is cooled through a bath of water, allowing the strips to harden. A sharp, computer-controlled cutting blade truncates the strips in 2–3 meter long pieces. Strip are stored in proper humidity-controlled containers. For the preshowers, a triangular geometry with a circularly-shaped central WLS fiber hole is required with nominal dimensions given in Fig. 5.5. The temperature and extrusion speed of the scintillator flow are varied to guarantee that individual strips are within $\pm 0.010''$ and $\pm 0.003''$ of their nominal dimensions for the sides and fiber insertion hole, respectively. Since the production speed is on the order of $\sim$10–15 ft/min, any *in situ* QC by visual inspection is difficult to perform for every single strip. Only every 10th or so strip can be inspected directly at the plant to verify that specifications are being met. This includes insertion of a WLS fiber to guarantee that the axial hole is not plugged-up. After extrusion, each strip is sent to Fermilab and wrapped by a reflective mylar tape. Moreover, the open ends of the strips in a module are manually painted with a white reflective coating. The entire process will guarantee zero cross-talk between adjacently nested strips in the detector.

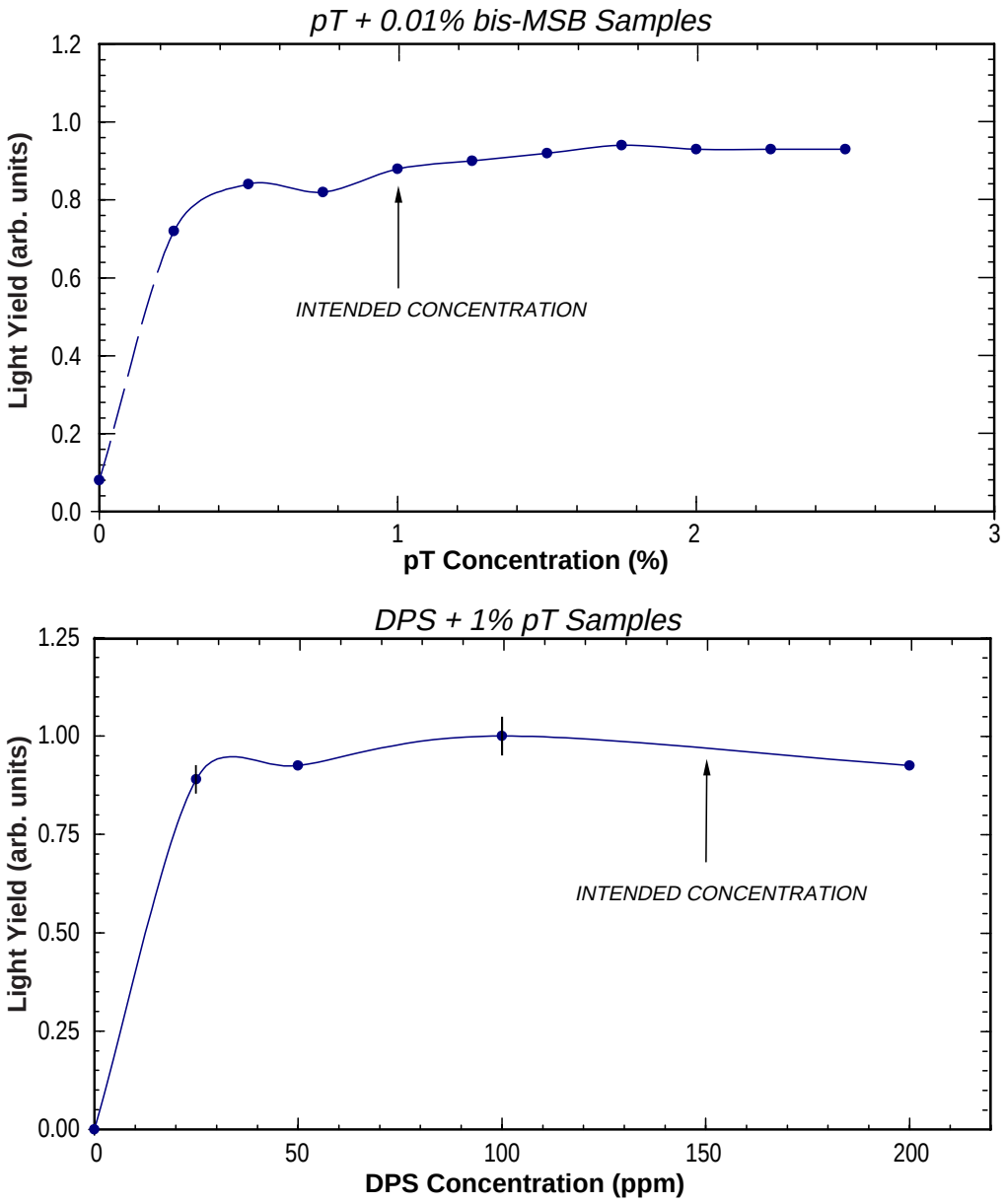

Figure 5.4: Chosen concentrations of scintillating fluors, pT (top) and DPS (bottom) for extruded scintillating strips. The concentration mixtures are determined on the basis of approximating BC-404 scintillator as well as aiming to minimize light re-absorption. Adapted from [67].

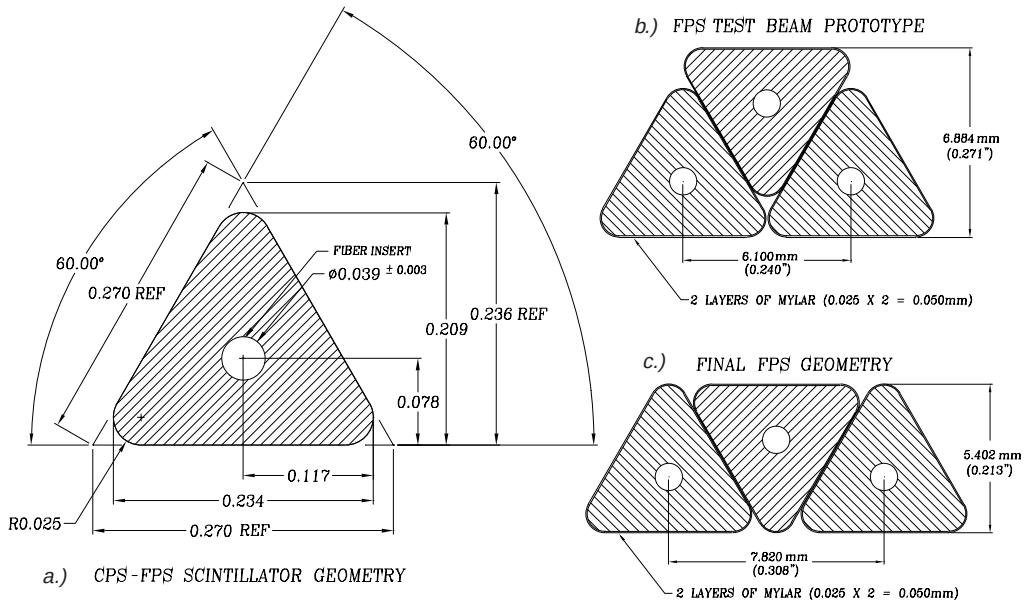

Figure 5.5: a) Detail of the scintillator dimensions used for the preshower detectors. Dimensions are in inches. Also shown are the scintillator spacing for the (b) preproduction prototype modules and (c) representative modules in the FPS detector. The nesting of each strip, and hence, a layer's thickness is different in the two methods.

Nature of Triangular Strip Geometry and Intra-layer Nesting

The preshower detectors are composed of strips of a triangular cross section. As shown in Fig. 5.5(b,c), these strips are interlocked together so as to form cylindrical (CPS) and wedge-shaped modular layers (FPS). Several other geometries, namely a square cross-section, have been considered. However, for any precision tracking detector, such a design would only provide the position at the center of the strip for a perpendicular crossing minimum ionizing particle. Strip-by-strip interpolation would be impossible, and this would degrade the resolution of the detector. On the other hand, a triangular geometry allows one to use the ratio of signals appearing in neighboring strips, 1 and 2, to determine the position of a traversing particle with greater accuracy. Such a two-strip configuration that contains tracks passing through

both strips is usually known as a doublet. This is to be distinguished from a singlet configuration in which tracks only register hits in one strip. For normal incident charged particles crossing two adjacent strips, the reconstructed position follows from the observed strip signal as [71]:

$$x_{position} = x_\circ \pm a \frac{S_2/S_2^{max}}{S_1/S_1^{max} + S_2/S_2^{max}} \tag{5.4}$$

where $x_\circ$ is the position of strip 1, $2a$ is the triangle's base-length, and S_1 and S_2 are the signal strengths normalized to S_1^{max} and S_2^{max} in strips 1 and 2, respectively.

In practice, systematic shifts between two strips in a layer are possible and must be corrected for. Nonetheless, the spatial resolution has been determined using representative preshower scintillating modules irradiated with cosmic rays [78]. The cluster position within the preshower fiducial volume is measured with respect to tracks identified by PDTs mounted above and below a module. As shown in the residuals given in Fig. 5.6, a doublet resolution of 510 $\pm$ 50 μm can be achieved with single muons traversing a triangle with a base-length near 6.0 mm [78]. The dominant sources for errors arise from multiple scattering and alignment uncertainties. The resolution does establish a level at which the preshower can perform as a granular tracker.

The manner in which contiguous strips are nested with one another should be noted. Fig. 5.5(b) and (c) show two such methods for strip registration. In order to provide a region between strips for epoxy to flow, an additional space must be added between the strips. From R&D studies [55], this space has been determined to be about 100 μm between each strip. Since the extruded strips are not exactly triangular in cross section, but instead rounded at the three vertices, the amount of additional space may prevent the tip of the upper nested triangle to lie along a sphere. This type of nesting, shown in Fig. 5.5(b),

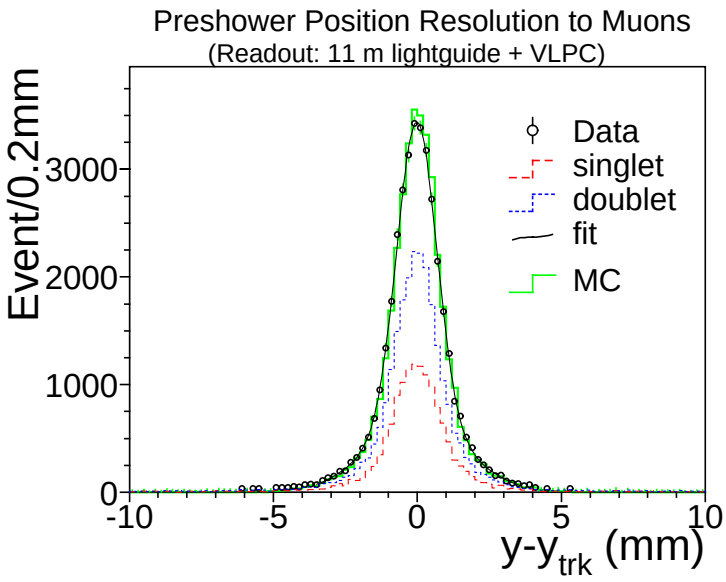

Figure 5.6: Residuals for preshower cluster position relative to a PDT track used to measure the spatial resolution for MIPs in a module readout by 11.0 m lightguide and VLPCs. Shown are distributions for both singlet (dashed) and doublet (dotted) tracks (see text for definitions) as well as the data (circles) fitted to double-Gaussian (solid). MC simulations are shown in histograms.

has been implemented for the FPS prototypes used for testing, prior to final detector production. The geometry — and hence, the overall thickness of the detector — can be adjusted by varying this additional inter-strip space during construction. The minimum thickness for a layer, however, corresponds to the strip spacing that allow the triangles to nest perfectly, as shown in Fig. 5.5(c). Comparing the two, one should notice that the prototypes are made slightly thicker than the possible minimum; however, it has been studied [55] that either arrangement will yield signals of comparable resolution. Therefore, to achieve compactness, the nesting indicated in Fig. 5.5(c) has been chosen for the final FPS detector.

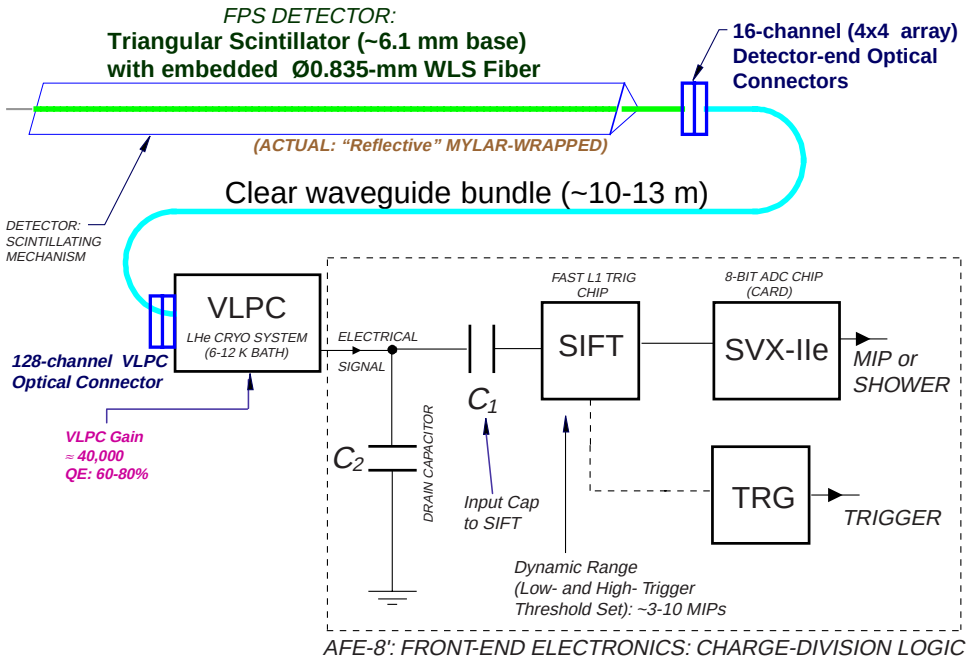

Figure 5.7: Schematic of the FPS readout system.

5.2.2 FPS Readout Scheme

The FPS readout system is designed to identify and characterize both minimum ionizing tracks and electromagnetic showers and is thereby capable of handling signals over a reasonably large dynamic range. The data flow for the system is shown in Fig. 5.7. It should be noted that both preshowers, central and forward, implement similar electronics. Differences, however, originate from the particle rates and energy spectra in the two regions, and consequently require changes in certain parameters for the layout of the front-end boards in the two systems. Moreover, a similar approach for the readout as shown in Fig. 5.7 is used for the DØ Fiber Tracker (see Chap. 3, Sec. 3.3.2) — with differences only in the trigger electronics for the detector (see Ref. [72] for further discussion).

The primary elements of the readout system for the preshowers consist

of Visible Light Photon Counters (VLPCs), the Scintillating Fiber Tracker trigger chip (SIFT), and the SVX-IIe readout chip. Light from the detector's scintillating mechanism is shifted from the blue (λ=430 nm) to the green (λ=510 nm) and optically transported through clear fibers and converted into electronic signals by the VLPCs. The output charge from the VLPC is digitized by the SVX-IIe. Since the SVX-IIe digitization speed is too slow to produce the required Level 1 trigger decision, an intermediate SIFT chip provides the fast trigger signal by generating a TTL discriminator output that is sent to Field Programmable Gate Arrays (FPGAs) used to implement the trigger logic. The discussion for the operation of the VLPC is beyond the scope of this thesis; the reader is referred to Refs. [35, 73, 74] for a more complete treatment. Instead, only a brief overview of the VLPC as well as the signal processing scheme for the preshower is given below.

VLPC Characteristics

DØ has chosen to use the Visible Light Photon Counter (VLPC) as the photosensitive device for signal readout from the preshowers and fiber tracker systems on the basis of its high performance. VLPCs are arsenic-doped silicon diodes, originally developed at Rockwell International [75] and subsequently produced by the Boeing Company [76]. They exhibit high quantum efficiency ($\sim$ 60–80% at visible light wavelengths) for single photon detection, high gain ($\sim$40,000 electrons per converted photon), low noise occupancy (<0.1%), excellent individual photoelectron resolution, and are capable to operate at high rates of at least 10 MHz with a very fast response (*i.e.,* rise time of $\sim$40 ps). In order to arrive at this performance, the device must be cooled with liquid helium (LHe) to temperatures near 8–9 K and operate at a bias voltage of 6–7.5 V.

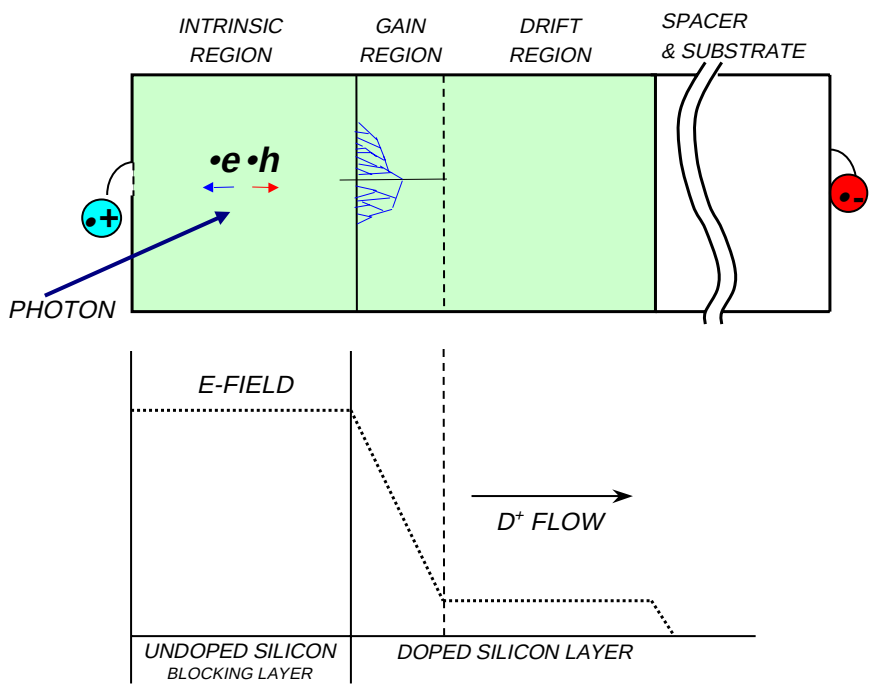

Figure 5.8: Cross-sectional illustration of VLPC operation (top) and corresponding electric field profile (bottom).

The operation of the VLPC is illustrated in Fig. 5.8. It is based on impurity band conduction [77], created by the heavy (light) doping of one of the two silicon layers with donor (acceptor) atoms. Such heavy doping causes the impurity atoms to be arranged close to one another, allowing for electrical charge transport from one impurity site to the next. For the VLPCs at DØ, the active silicon gain layer is heavily (lightly) doped with arsenic donor (boron acceptor) atoms. The arsenic atoms form an impurity band 50 meV below the conduction band while the boron atoms shape the electric field. The standard 1.12 eV valence band in silicon is used to absorb photons, thereby creating an electron-hole pair across the valence-to-conduction band gap of the intrinsic undoped silicon layer. The hole drifts through the "gain region" and into the "drift region," colliding with neutral donors to free electrons and start an

electron avalanche. The small 50 meV gap is used to feed the multiplication. A bias voltage applied across the device divides the doped silicon layer into a gain (*i.e.,* linear field) and drift (*i.e.,* constant field) region, thereby allowing the drift region to behave as an internal resistor in series with an ideal VLPC. The presence of the small band gap reduces gain dispersion ($< 2\%$) and requires low fields to create the electron avalanche.

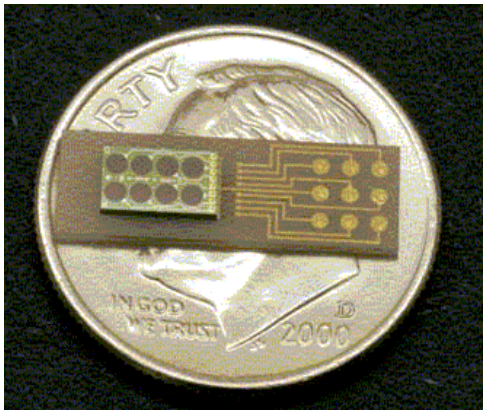

Figure 5.9: Picture of a VLPC chip. The chip has 8 pixels of 1 mm diameter mounted on an aluminum-nitride substrate. The gold-plate conduction pads on the substrate are contacts for the 8 signal outputs and the bias.

The VLPCs are grouped on the surface of a chip in a 2×4 array of circular pixels of 1 mm-diameter (see Fig. 5.9). The chips are mounted and wire-bonded to an aluminum-nitride substrate, which provides electrical contacts to the VLPC via conducting pads. The chips are manufactured epitaxially on 3.5″ diameter silicon wafers with a total of 176 chips/wafer. Each pixel is centered on a chip to accuracies within 10 μm using high-resolution videography. This guarantees that readout fibers and connections are properly aligned and axially matched upon hookup. Including ∼10% spares, the three VLPC subsystems at DØ incorporate about 75 total wafers. It is important to note that the use of VLPCs for both the CFT and preshower subsystems makes DØ the first detector to incorporate these devices at such a massive channel scale.

Preshower Signal Processing

The signal flow in the readout system for the preshowers is motivated by a number of considerations. The system has been designed to measure effectively small, MIP-like signals such as those observed in the CFT. However, the preshowers must not only identify and characterize MIPs but also EM showers, and therefore, be adapted to measure large shower energies and wide pulse height distributions. Further, in order to extend the physics scope of the detector, the system must be capable of handling trigger terms for both high-p_T signals, such as those from decay electrons of W, Z, or $t\bar{t}$ pairs; as well as electrons produced in lower p_T processes as in b-tagging, J/ψ, and SUSY. The resolution must also be fine enough so that single MIPs, expected for use during detector calibration runs, can be resolved.

A number of studies (*i.e.,* cosmic ray, test beam, and MC simulations) have indicated that the charge expected at the output of the VLPC is on the order of 15 fC for MIPs while a factor of $\approx$10 higher for energetic electron showers [79]. Such large differences imply that appropriate high- and low-p_T thresholds be established for electrical signals exiting a VLPC channel and being processed for triggering and digitization by the SIFT and SVX-II readout, respectively. These thresholds must be set at such values that enable both low- and high-p_T preshower triggers. However, it has been suggested that initially calorimetry alone may suffice to control trigger rates for higher p_T processes until reaching much higher luminosity conditions. Therefore, a decision to operate with relatively low threshold ranges ($\mathcal{O}$(3–10 MIPs)) has been made. The range is believed to retain much of the low-p_T physics capability with the detector as well as provide some flexibility in conditions which require a control on trigger rates [80].

The readout utilizes capacitors (on the order of a few pF) soldered onto

the preshower front-end readout boards (see Fig. 5.7). The nominal values chosen for the capacitance are such that the chain can handle as much of the dynamic range for the system as possible, subject to the constraint that it will not introduce saturation at high frequencies. Since the maximum amount of charge at the output of the VLPC exceeds the maximum input level of the SIFT, some of the charge must be drained through capacitor, C_2, in Fig. 5.7. The remaining fraction of charge that flows to the input of the SIFT depends on a number of factors; these include the random noise in the SIFT chip and any expected degradations in the readout chain (*i.e.,* radiation hardness, signal variations in the clear lightguides, etc...). However, the capacitances, in addition to the ability to systematically control the bias voltage settings on the VLPC chip itself (*i.e.,* hence tune VLPC gain, quantum efficiency, and/or noise), largely define the low- and high-thresholds used for any Level 1 preshower related trigger. Nonetheless, such signal processing techniques ensure the capability to finely resolve MIPs while maintaining a dynamic range wide enough to measure shower depositions with minimal saturation.

Preshower Light Yield

The above discussion of the preshower readout and trigger requirements is largely driven by the absolute light yield given in terms of the number of photoelectrons (p.e.) per MIP traversing the detector. The value constrains the design of the trigger logic board and operating parameters (*e.g.,* trigger thresholds and dynamic range) of the preshowers. The discussion on the logic and design of such a trigger is beyond the scope of this thesis, and thus, only the results for the yield are given here (see also Ref. [78] for a complete discussion). The magnitude of the MIP charge can be determined from the detector's response to cosmic rays using representative elements of the detector readout

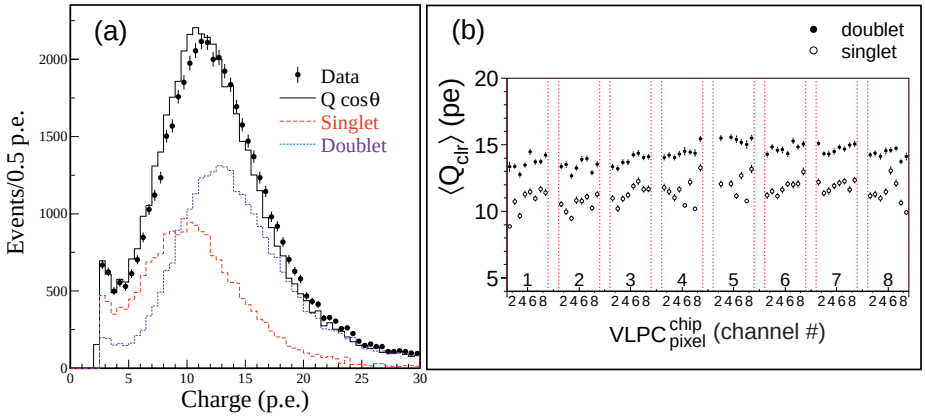

Figure 5.10: Measurement of preshower light-yield for MIPs (a) in a cosmic ray system setup. Shown are data corrected for $\cos\theta$ (solid line) as well as singlet (dashed) and doublet (dotted) extrapolations. Charge uniformity, mean charge vs. channel number, is given in (b). Distributions represent results using final scintillator strips, WLS fibers, 11.0 m clear lightguides, and VLPCs.

by clear fiber lightguides and VLPCs. Shown in Fig. 5.10 is the response from the preshower for a muon passing through one (singlet) and two (doublet) triangular strips. Since the charge depends on the cosine of the incident angle, θ, of a traversing particle, the analysis must incorporate angular effects.

Measurements indicate a ratio of approximately 14 (12) p.e./MIP for doublet (singlet) track configurations. Further, the data fluctuates by only 5–10% across the area of the module (see Fig. 5.10b), and thus, shows a relatively uniform strip response. It should, however, be noted that the ratio is dependent on a number of factors, which include the overall lightguide length and operating parameters of the VLPC. In fact, increasing the lightguide from 11.0 to 13.0 m can result in a $\sim 20\%$ drop in the ratio. Nonetheless, the 14 p.e. translates to $\simeq 100$ fC/MIP of charge at the output of the VLPC[5] (or equiv-

[5]The value of the charge is dependent on the gain of the VLPC. For the results given here, a gain of 40K is taken as it represents the nominal value assigned for much of the FPS readout.

alently, at the input to the trigger framework). The amount of light from the detector is more than adequate and well above noise levels ($\mathcal{O}(10)$ fC) in the front-end electronics.

Chapter 6

Forward Preshower Design

Two basic requirements define the design of the Forward Preshower system for DØ. The detector must be sufficiently granular to function as an efficient tracker for charged leptons and photons, and it must sample energy of particles traversing into the calorimeter. The higher luminosities expected during Run II will diminish the ability to trigger on and identify electrons and photons using calorimeter information alone — in particular, in the forward direction and in the proximity of jets. The FPS exploits the wide coverage of the DØ calorimeters and assists in identifying and triggering on key electron and photon signatures in the face of large background levels. At the same time, the signal from the detector should be available quickly enough to be used in a Level I trigger decision. These issues, in addition to the many spatial and geometrical constraints of the DØ detector itself, ultimately drive the design of the FPS subdetector. Given below is a brief discussion of the conceptual design of the detector, which is followed by a general technical overview of the various elements composing the FPS. The items addressed here have undergone extensive R&D, testing, and technical reviews. For reference, the reader is referred to [31, 36, 54, 55, 81, 82], and references therein, for a more detailed explanation of the design, assembly, and readout of the detector.

6.1 Conceptual Design

One FPS detector mounts on each of the spherical heads of the end calorimeter (EC) cryostats, covering as much of the forward electromagnetic calorimetry as possible. The primary constraint that limits the coverage of the FPS to $1.5 < |\eta| < 2.5$ is the presence of other subdetectors occupying the end-cryostat head at the inner- (Level Ø-Luminosity Counter) and outer- (Inter-Cryostat Detector) radii of the FPS. At $|\eta| < 1.5$, only partial electromagnetic coverage is available with the end calorimeters and thus, any additional coverage with the FPS in this region will not significantly improve the electron measurement. Further, as observed during Run I and expected again in Run II, in the forward regions at $|\eta| > 2.5$, resolving electron trajectories in tracking becomes increasingly difficult [55]. Therefore, the design of FPS has been optimized to cover regions that maintains the DØ electron and photon detection capability for the physics processes of interest.

As illustrated in Fig. 6.1, the FPS detectors consist of two finely-segmented active layers of scintillation material capable of charged particle tracking. Directly sandwiched in-between each of these layers is a total of two radiation length ($2X_o$) bonded lead-stainless-steel absorber plates that initiate showers of electrons and photons traversing it. The upstream active layers (*i.e.,* closest to the interaction point) are known as the minimum ionizing particle, or *MIP layers*, while the downstream layers (*i.e.,* directly behind the lead) are termed as the *Shower layers*. This terminology is based on the type of signatures produced by each of the charged hadrons, muons, electrons, and/or photons traversing the detector. All charged particles that pass through the detector will register a minimum ionizing track in the forward MIP-detecting layer, and therefore yield a space point (in η, ϕ and z). Electrons will readily shower in the lead absorber, generating a collimated cluster of energy in the

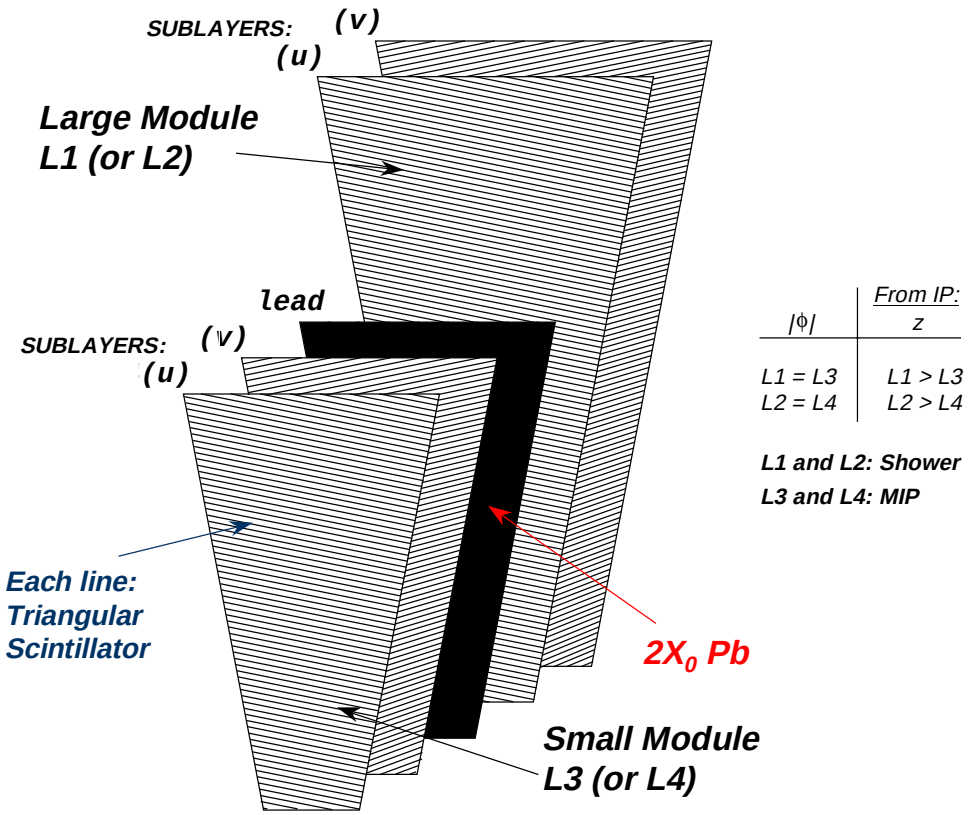

Figure 6.1: FPS module's azimuthal geometry with joint u-v MIP and Shower sublayers, each separated by a lead absorber.

Particle	MIP deposition (FPS Layers 1,2)	Shower cluster (FPS Layers 3,4)
electron	Yes	narrow ($\approx$ 3 strips-wide)
pion π^o	No	wide (two photons)
pion $\pi^{\pm}$	Yes	little energy (space point)
muon μ	Yes (MIP/space hit)	No (MIP/space hit)

Table 6.1: Summary of basic particle signatures in the upstream (forward) and downstream (backward) layers of the FPS detector used for particle tracking and identification.

Shower layer with a spatially matched hit in the MIP layer. Heavier particles such as charged pions and muons, however, may not generate any type of shower. Instead, only another minimum energy space point in the Shower layer will be identified, in coincidence with a MIP deposition in front of the lead. Photons, on the other hand, will not register in the forward MIP layer, but the shower induced by the lead will generate a cluster of electromagnetic energy similar to that of electrons in the Shower layer. The different types of hits or energy clusters in the forward and back scintillation layers of the FPS allows identification of key signal and background processes with the detector. For clarification, some tracks produced through Monte Carlo simulations for 50 GeV e and π° (*i.e.,* 2γ conversions) candidates are shown in Fig. 6.2. The various signatures in the FPS described above have been summarized in Table 6.1 [90].

A number of important issues contribute to the overall geometry and coverage of the lead absorber element. First, the absorber must be densely constrained. Moreover, the region of the FPS is partially in the shadow of the solenoidal magnet coil. This is a relatively large amount of material (*i.e.,* $\approx 3X_o$ at $|\eta| \approx 1.5$) and may readily induce showers by particles penetrating the coil, thereby registering a shower-like cluster in the upstream layers of the

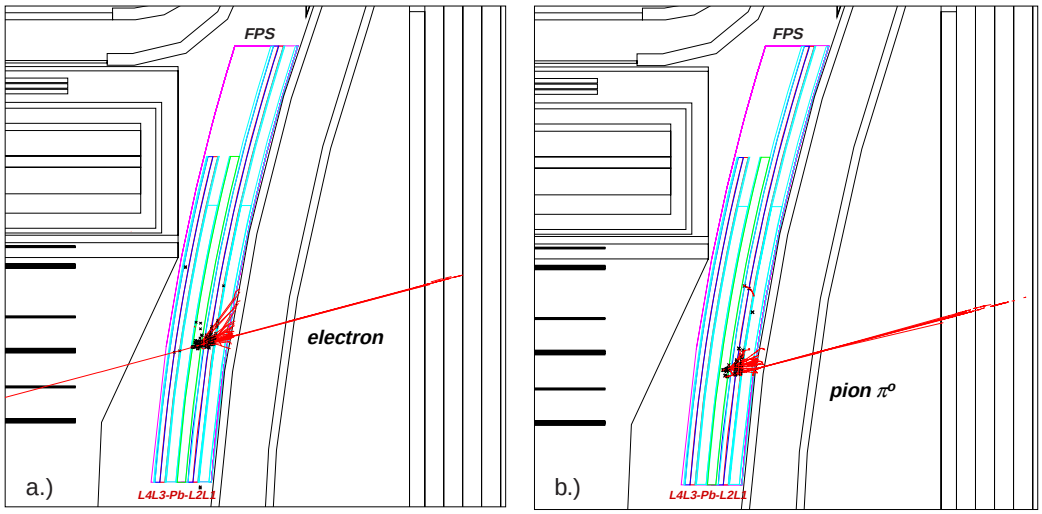

Figure 6.2: Typical GEANT simulated signature of 50 GeV a) electrons and b) neutral pions traversing the FPS detector.

FPS. Since the upstream layers are intended primarily for a MIP determination, extra absorber material is not required. Therefore, the lead converter is truncated radially near the boundary of the coil, restricting its coverage to $1.65 < |\eta| < 2.5$. The presence of the coil further lends itself in segmenting the rest of the detector into two distinct regions in pseudorapidity. The layers behind (*i.e.*, downstream of) the lead can be used to provide shower information throughout the entire range of pseudorapidity, and therefore cover the entire available area of $1.5 < |\eta| < 2.5$. The (MIP) layers in front (*i.e.*, upstream) of the absorber are limited to that pseudorapidity range in which there is no coil upstream: $1.65 < |\eta| < 2.5$. These η contours are given in Fig. 6.3.

The geometry of the FPS system has been designed to complement the rest of the DØ detector by maximizing the active coverage at DØ while maintaining as compact a detector as possible. The geometry impacts the technical design of the FPS, significantly contributing to how parts of the detector are assembled and readout. The following sections give an overview of these issues.

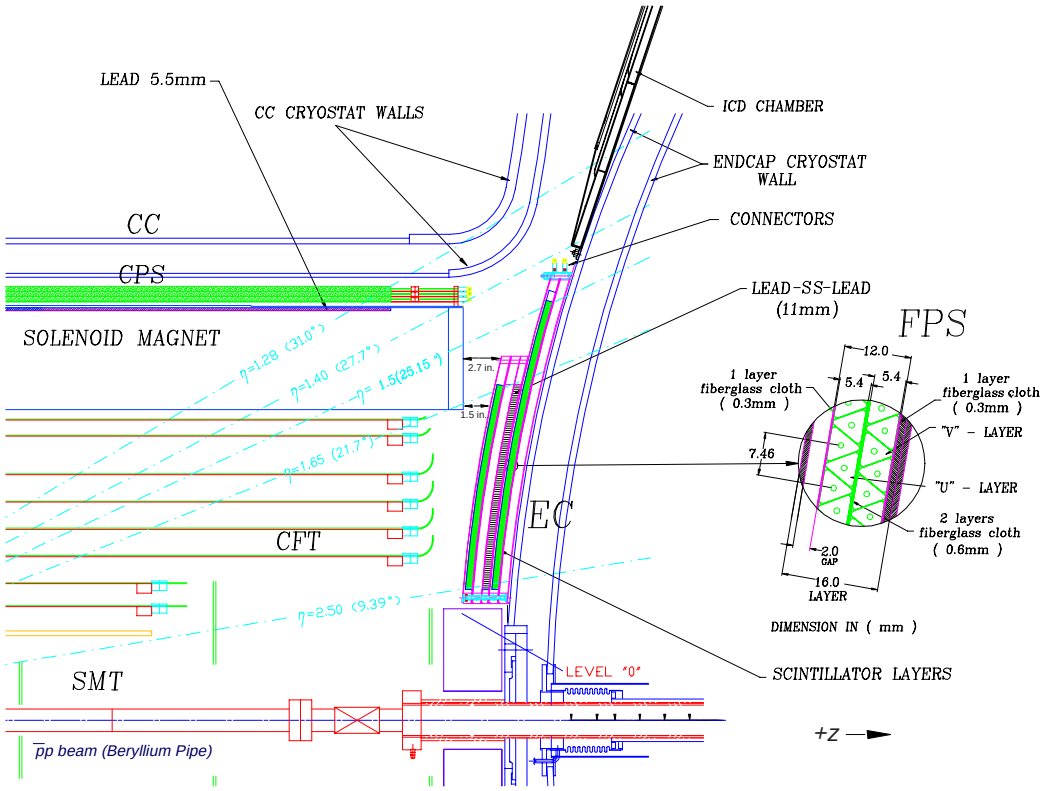

Figure 6.3: Cross-sectional r–z view of the FPS detector at DØ. Given within the inset is a module's triangular strip nesting configuration.

6.2 FPS Geometry and Technical Design

A cross-sectional view of the FPS detection layers mounted on the EC head is given in Fig. 6.3. The detector is composed of four successive layers from 1 to 4 and identified as follows: the layer furthest (closest) from the interaction point is Layer 1 (4), labeled L1 (L4). This convention will used for the remainder of the thesis. Further, since the method for detector assembly and installation has a number of geometry and design issues itself, any detailed discussion of the assembly components has been deferred to Chapters 7 and 8.

A major concern in design and construction is the severe spatial constraints that exist within the DØ detector. As mentioned earlier, the FPS is radially

limited on the EC by the existence of the LØ Luminosity Counter and ICD at the inner and outer radii, respectively. Similar constraints exist within the intercryostat (ICR) gap region between the central- and end-calorimeter cryostats. The DØ detector designed to be as hermetic as possible limits uninstrumented dead regions, requiring the ECs to be as close to the CC outer-wall as possible. However, enough space must remain for services and readout cables from the silicon and fiber tracker (a total of about 900,000 readout channels), which are routed through this region prior to their respective DAQ electronics located outside the ICR gap. Many of these cables consists of delicate fibers, which require strain relief at regular intervals to avoid damage. Likewise, the FPS itself requires cabling and adds to the total space requirement. A compact detector layout is, therefore, essential. Given these constraints, the design for the detector conforms directly to the spherical shape of the end cryostat wall — a geometry that requires spherically shaped detector components difficult. A detector built with any other geometry (for *e.g.,* conical or flat) would severely interfere not only with the cables but also with other detection components (*i.e.,* SMT, CFT, CPS and solenoid coil).

The FPS detector is composed of 32 ϕ-modules, trapezoidal in outline, each independently housed in a wedge-shaped aluminum support frame, as shown in Fig. 6.4. Eight modular frames assemble into a single, structurally distinct FPS layer and form a spherical disk that conforms to the face of the end calorimeter cyrostat. Two successive layers are offset by one module to make a hermetic detector. The first two layers are separated from the last two layers by a bonded lead-stainless steel absorber element. The four layers, with the lead radiator in-between, form a FPS detection unit. Two such units exist. The module boundaries (see Fig. 6.5) are oriented such that the modular regions spatially match the ϕ geometry of the EM calorimeter modules. A frontal view of the detector showing the layered configuration is

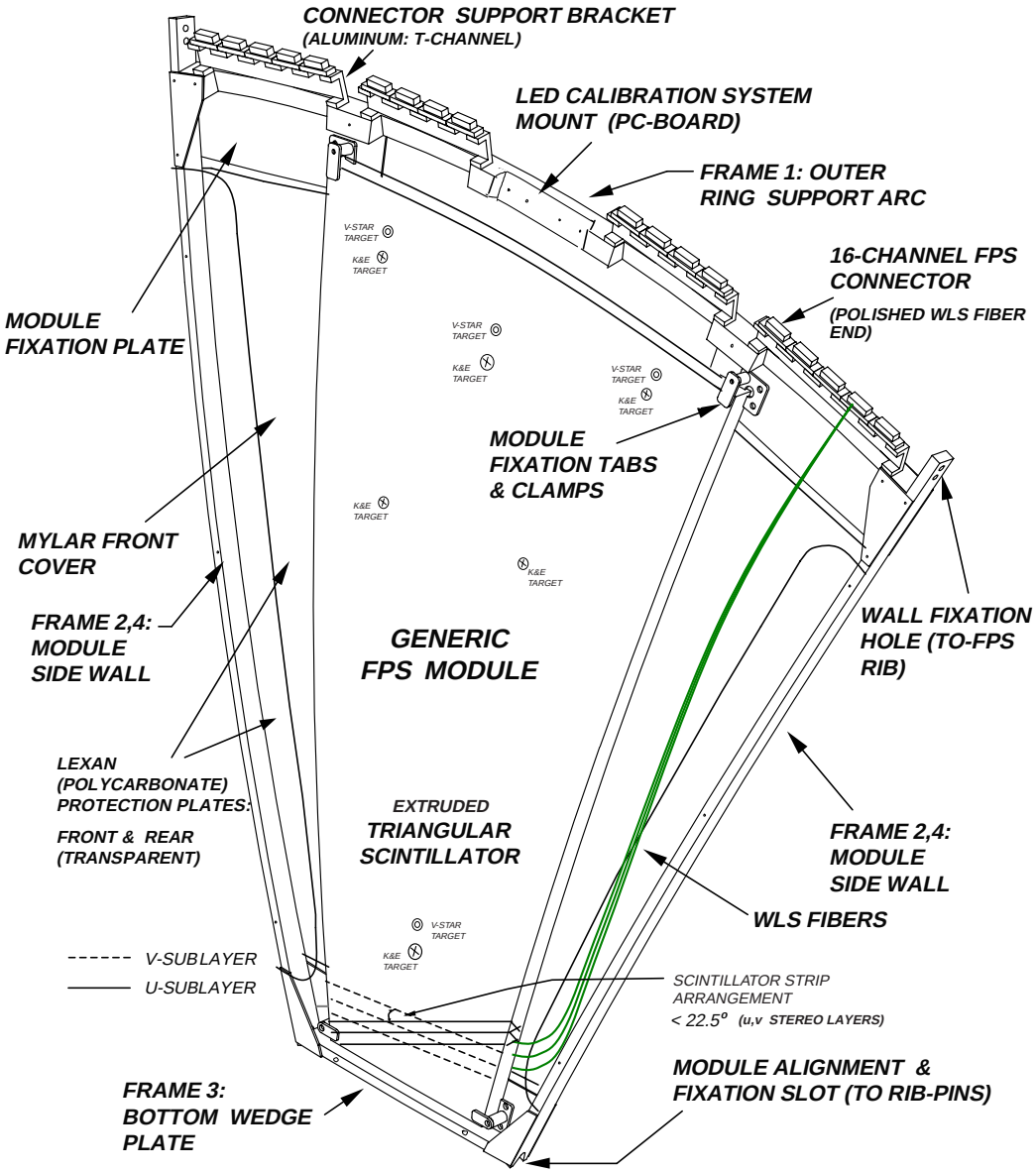

Figure 6.4: Three-dimensional view of a trapezoidal shaped FPS ϕ-module in its supporting frame. Shown are the main elements including WLS fibers, optical connectors and brackets, surveying targets, and protective clear frame-covers. See text for complete description.

given in Fig. 6.6. All the main elements of the FPS detector — modules, lead absorber, and support housing — are each individually bent to the spherical (nominal 100″ radius) shape of the EC cryostat head.

The ϕ-modules are primarily composed of extruded scintillator-strips with embedded wavelength-shifting (WLS) fibers. Each module consists of two sublayers of nested strips that form a crossing ("stereo") angle of 22.5° with respect to one another to provide space point (x,y,z or r,ϕ,z) measurement capability. The strips in the two stereo layers (u and v) are oriented perpendicular to one of the edges of a module and form an angle of 78.75° with the vertical bisector of a module. Each scintillator strip is wrapped in reflective mylar tape after extrusion (and prior to module assembly) for optical isolation. The blue light emitted by a strip is strongly absorbed (maximum at λ=430 nm) by the coaxial WLS fiber, and re-emitted in the green (λ=510 nm). The WLS fiber is coupled to clear fiber lightguides at the ϕ module's outer radius. These lightguides are subsequently routed to readout electronics (see summary in Fig. 5.7, Chap. 5).

As shown in Fig. 6.5, the active area of each module subtends 22.5° in ϕ (1/16 of the full 2π ϕ coverage). The successive layer follows it in z and is offset by 22.5° in ϕ to contain modules that cover alternate ϕ sections. A full 2π angular region in ϕ is therefore covered by a pair of adjacent layers with modules that are staggered in ϕ. The staggered modules have a total overlap region of one inch ($\pm 1/2''$) with respect to one another. This staggering eliminates any projective cracks. The modularity of the FPS system is especially convenient during detector assembly and installation: a module which needs replacement from installation damage or failure can easily be removed and replaced without affecting other modules.

The central hole in each triangular scintillator strip (as shown in Fig. 5.5, Chap. 5) accommodates a WLS fiber, which axially runs along the scintillator

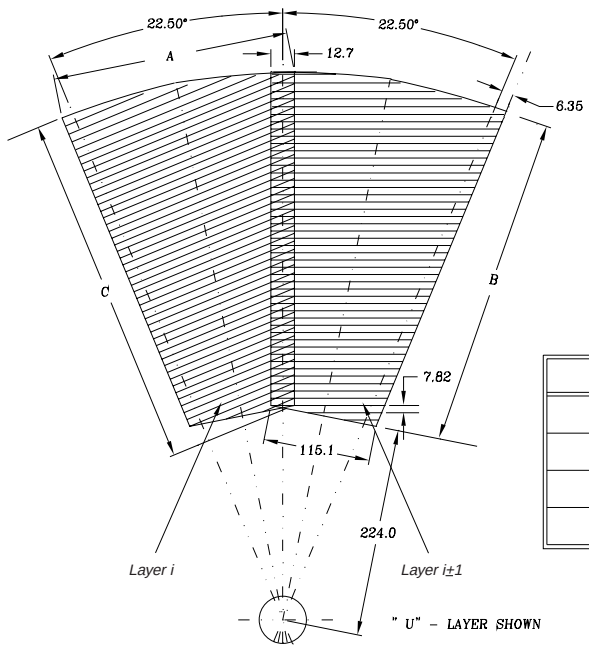

MODULE TYPE	DIMENSION (in mm)		
	A	B	C
SPECIAL	214.9	250.9	278.3
SMALL	255.3	352.3	381.7
LARGE	312.6	496.6	528.7

Figure 6.5: Module orientation within two successive FPS layers. Given is the $1/2''$ overlap region between two adjacent ϕ-modules as well as dimensions of the active area of each module type (see text for description).

strip to the edge of the module. The fibers are then grouped in batches of 16-channel strips and run radially to the perimeter of the detector frame to optical connectors mounted for light transfer. The azimuthal edges of a support frame in a given layer lie along lines of constant ϕ, between the modules, at 45° ϕ intervals. The space between the frame and the active area of a module provides the necessary space for routing the WLS fibers. The optical connectors that couple the emerging WLS fiber to the clear fiber are mounted on aluminum brackets that are fixed to the outer perimeter detector's support frame (see Fig. 6.4 or Figs. 7.5 and 7.6 in Chap. 7). Installation, cabling, and space considerations require these connectors be located at the outer periphery. The set of clear fibers are routed over the EC cryostat head, radially outward and then around in ϕ directly towards the Visible Light Photon Counter (VLPC)

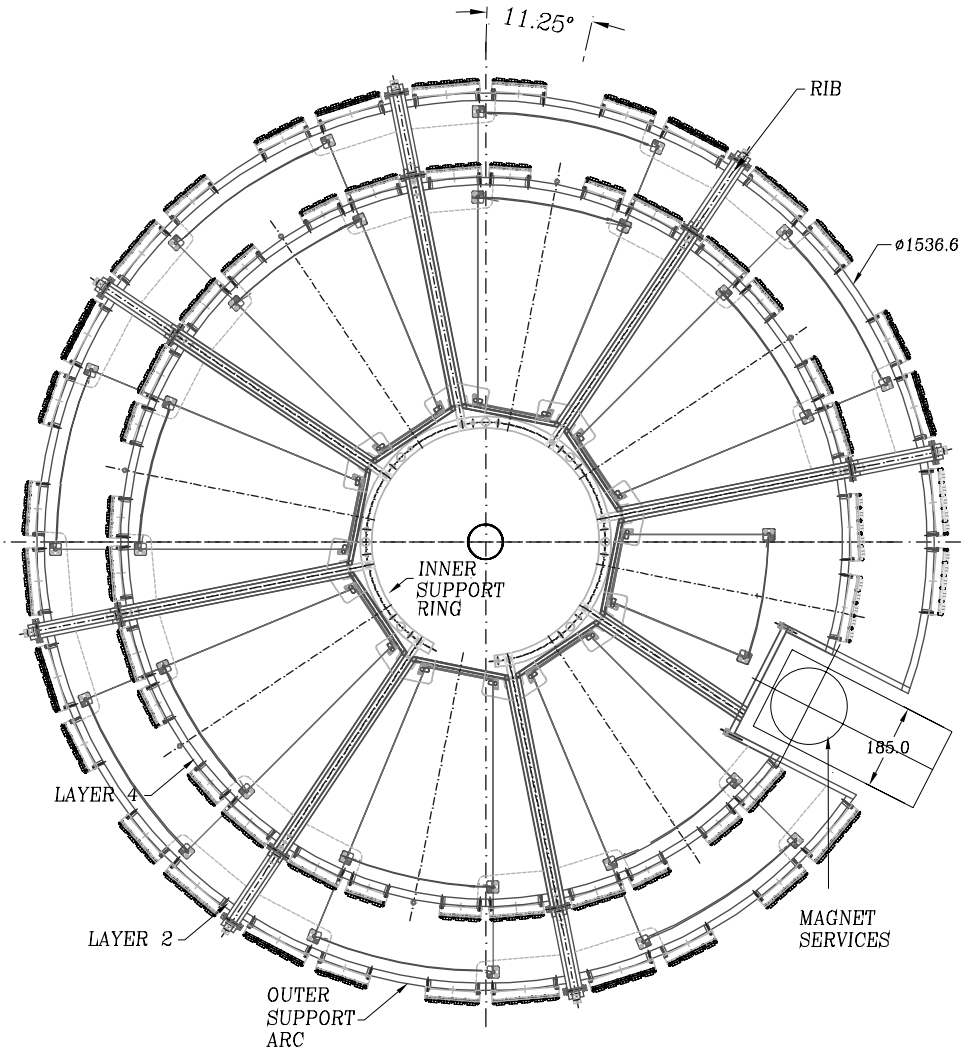

Figure 6.6: r–ϕ view of the North-FPS detector. For brevity, only (nested) Layers 2 and 4 are shown; Layers 1 and 3 are rotated by 22.5° in ϕ with respect to these layers. Also, the South-FPS is not given here, as it is a symmetric, mirror-image of the north detector.

readout system housed on the platform, below the DØ detector.

As discussed earlier, the lead absorber layer covers the pseudorapidity region of $1.65 < |\eta| < 2.5$. The entire absorber layer is divided into 48 individual (and precisely constructed) wedge-like segments[1], each subtending 7.5° in ϕ. Each segment gets mounted between inner and outer absorber support rings. A segment contains two lead absorber elements mechanically epoxied on a 1/8″ thick stainless-steel surface (*i.e.,* a Pb-SS-Pb sandwich). Each steel plate is radially longer than the lead units — by approximately 1/2″ on either side — to provide a means for mechanical fixation onto support rings that are nested within the overall FPS layers. The total thickness of a bonded lead-stainless-steel unit measures 11 mm, or $2X_o$. During construction, the 7.5° wedges are bent into a cylindrical shape before bonding so that the 48 elements comprising a full layer form a closed circular unit (*i.e.,* 2π in ϕ). A 7.5° wedge angle has been chosen so that the complete layer closely approximates the overall spherical geometry of the rest of the detector. Moreover, the ϕ-edges of each side of a bonded wedge segment are beveled in so as to allow nesting of adjacent absorber elements with minimal and non-projective gaps (or "leakage") in-between them.

As is evident from Fig. 6.6, each detector (north and south) contains a limited ϕ-slice for which the ϕ-symmetry of the design is broken. Modifications in two 22.5° sectors[2] are needed in order to allow the coexistence of the FPS with the magnet support services at $\phi = 332.946°$, or 27.054° below the $+x$-axis in the DØ coordinate system (see Sec. 3.1). The presence of the magnet services forces the detector to be truncated in this region, resulting in four "special" detector modules per side (i.e., one per layer), which cover only

[1]The construction of the lead layer also has detailed design issues, and thus, an extended discussion of the lead absorber has been deferred for Chap. 7.

[2]The modified channels in the FPS sectors occupy the same angular ϕ-slice on both sides — north and south — of the detector.

$1.8 < |\eta| < 2.5$. A similar truncation is needed for the lead absorber elements in the region.

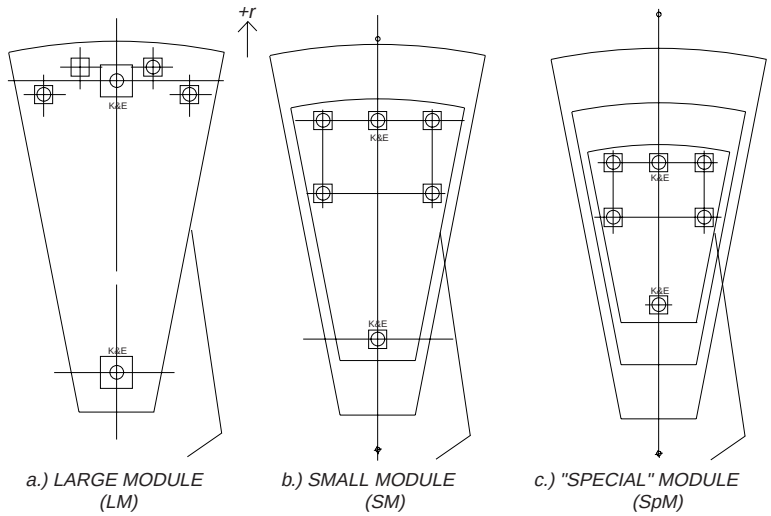

Figure 6.7: The three different types of representative FPS modules: a) Large Module (LM), b) Small Module (SM), and c) "Special" Module (SpM).

This completes the introduction and overview of the layout, mechanics, and introduced terminology and notation in describing the different module species of the FPS detector. The Shower layers (*i.e.,* FPS Layers: L1 and L2), in each detector, consist of 14 "large" modules (LM) as well as the 2 "special" modules (SpM) near the region of the magnet services. The MIP layers (*i.e.,* FPS Layers: L3 and L4), in each detector, consist of 14 "small" modules (SM) with the 2 "special" ones. For completeness, the different types of modules are illustrated in Fig. 6.7. A MIP layer ϕ-module in L3 (L4) matches precisely the ϕ interval with a Shower layer module in L1 (L2) — see Fig. 6.1, lending itself to a natural single FPS triggering segment or "unit". This unit is often referred to as a FPS "readout sector". Each detector then consist of 16 such sectors. For reference, some of the important design parameters for the FPS, including the geometric acceptance and total channel yield, are given in Tables 6.2 and

6.3. Many of these parameters have been determined from simulations and tests prior and/or *in situ* of the FPS construction (see Refs. [61, 78, 91, 92] for further discussion).

Item	Description
Number of detectors	2 (one on each end cryostat: North & South)
Inner (outer) radius (mm) [inch]	200 [7.880] (1536.6 [60.542])
η-coverage of FPS	$1.5 < \|\eta\| < 2.5$
Active material	nested scintillator strips of triangular cross section
Readout	WLS fibers, clear waveguide, VLPCs, SVXIIe
Estimated length (min, max) of scintillator strip per module	MIP Layer: (0.01 m, 0.22 m) Shower Layer: (0.01 m, 0.3 m)
Length (min, max) of WLS fiber	MIP Layer: (0.5 m, 0.8 m) Shower Layer: (0.7 m, 1.2 m)
Length (min, max) of clear fiber	(9.5 m, 13.7 m)
λ_{attn} of WLS fiber	4.5±0.5 m (UV region)
λ_{attn} of clear fiber	9–11 m
Calibration/Monitoring System	blue surface-mount LED pulsers
Quantity of LEDs (North+South)	968 (one per FPS optical connector)
ϕ-segmentation	32×2 trapezoidal ϕ-wedges
z-segmentation	4 (two u,v) layers per side
Strip geometry	22.5° stereo
Total channel count (MIP layer)	3168 (per detector)
Total channel count (Shower layer)	4316 (per detector)
Total channel count	$2 \times 7{,}484 = 14{,}968$ (both detectors)
Absorber	bonded lead-stainless steel-lead sandwich, Total: $2X_\circ$
η-coverage of absorber	$1.65 < \|\eta\| < 2.5$
Weight of absorber	approximately 127 kg (280 lbs.) per side
Weight of detector	approximately 222 kg (495 lbs.) per side
MIP Light-yield (using 11 m-long clear fibers)	Singlet: ∼11 pe (∼75 fC) Doublet: ∼14 pe (∼90 fC)
Estimated VLPC Gains (for FPS)	FPS Upstream: 38–41K FPS Downstream: 29–31K

Table 6.2: Summary of important detector parameters of the FPS.

	Large Module	Small Module	"Special" Module
η-coverage	1.50< $\|\eta\|$ <2.5	1.65< $\|\eta\|$ <2.5	1.80< $\|\eta\|$ <2.5
ϕ-coverage	$\pm$(11.25° +12.7 mm)	$\pm$(11.25° +12.7 mm)	$\pm$(11.25° +12.7 mm)
# channels ($u+v$)	288 (144+144)	206 (103+103)	142 (71+71)
# modules per side	14	14	4
Radial coverage (mm)	496.5	352.3	250.9

Table 6.3: Summary of parameters of the FPS modules.

Chapter 7

Forward Preshower Construction

The design that has been outlined in the previous chapter establishes the groundwork in constructing the FPS detector subsystem. The construction, which began in March 1998 and continually progressed until April 2000, has introduced a number of *in situ* procedures that have been implemented at various stages of the assembly. Likewise, since many aspects of the construction require quality control and warrant meeting established specifications, additional procedures have been developed. The systematic, reproducible means of fabricating accurate modular active elements as well as the techniques used for module assembly, support frame alignment and assembly, support of the lead absorber, module installation and testing, layer alignment, and detector installation and alignment must each be understood and studied. The following sections discuss many of these topics.

7.1 Module Construction

The main element of the FPS is a scintillation module. Module construction is possible through the implementation of number of sequential steps, each of which require care and precision in order to achieve the granularity needed

for particle tracking. Such procedures are presented here.

7.1.1 Spherical Template

As described in Sec. 6.2, the volume of each FPS detector must conform to a spherical geometry of the EC cryostat wall. In order to achieve this, aluminum domes, cut to the radius of the EC head via a digital programmable cutting machine, are used. These domes serve as a "template", providing the spherical surface on which all module construction is performed.

The domes are machined by fixing a thick ($2''$) solid aluminum sheet on a cutting table and allowing it to spin about a vertical axis oriented perpendicular to the plane of the sheet. While spinning, a sharp cutting blade, programmed to walk radially about the surface of the plate and varying in height along the vertical axis, carves out a spherical shape. Rough passes are first made over the entire surface to approximate much of the desired shape. Additional passes using a finer blade provide a smooth, finished surface with the proper radial tolerances. Five such "template" domes are constructed, each of which are cut to a sphere with a radius of 100.42 ± 0.010 inch, and hence, consistent with the radius of the EC cryostat head. The two larger (smaller) domes each measure 36 (30) inch in diameter along their length and allow preparation and construction of a large (small, special) module. One additional large dome is also constructed to facilitate multiple day-by-day module production, and thus, shorten the time period for FPS module fabrication.

7.1.2 Scintillator Strip Preparation

Chapter 5 presented an overview of the extruded triangular scintillator strips used in the preshower detector. Directly after extrusion, each of these strip must undergo a labor-intensive process that prepares it for module as-

sembly. Here, the strips are initially taken to Fermilab (Industrial Building #3 facility) where they are carefully quality controlled: individually cleaned with alcohol and visually inspected along their length for cracks and/or stress fractures that may have resulted from intermittent extrusion failures and/or mishandling. Each strip is subsequently machine-wrapped with reflective mylar tape at relatively high speeds — on the order of 1 ft/sec and $\approx$ 4 ft/min, respectively — and stored in humidity-controlled shipping containers. The boxes contain roughly 800–1000 strips, each 3 m-long, which are all shipped to SUNY, Stony Brook and Brookhaven Lab where additional preparatory work is performed.

Upon arrival from Fermilab, the mylar wrapping of the strip is visually inspected. Next, a 0.835 mm-diameter fiber is axially inserted through the entire length of a strip to verify that blockages that may have arisen from extrusion failures do not exist. This step is critical as it prevents losses in active detector channels, allowing one to continue further with module production.

Subsequently, each strip is pre-cut using a sharp hand-cutting tool. Care is taken to avoid cracking and/or developing stress fractures in the scintillator material. A 1:1 "template" drawing is used to define the length needed for a strip in the module as well as to ensure proper lengths are being cut. An extra distance of about 1″ from the scintillator edge is added to the length (which eventually is cut-away) to help ensure blemishes will not be present in the strips occupying the final module. Because the scintillator is already wrapped in mylar when the cut is made, a thin ($\simeq$ 1 mil) mylar tape is placed along the edge, prior to making the cut, to prevent the mylar from unraveling afterwards. Care is taken in applying as little tape as possible as large thicknesses may cause stress distortions and misalignments during module assembly. The tape, of course, is only temporary and is removed (as waste) during the final stages of module fabrication. Next, each strip is numbered to register the spatial

position it occupies in the module.

Once the strips are cut, taped, and numbered, they are uniformly laid in an alignment jig mounted on the spherical dome. Here, the array of strips is pre-bent ("slumped"), heated to about 170°F in an oven for about 2 hours under a vacuum. This helps maintain the strip's relative concavity (convexity) of the module's lower (upper) layer. The slumping continues by allowing the strips to remain in the warm oven environment overnight. Studies have shown that heating the scintillator during this stage results in no short- or long-term degradation in the detector's response [55].

One additional step must be fulfilled before module assembly can take place. Extensive R&D studies have indicated that during module assembly (outlined in the next Sec. 7.1.3), the epoxy used to fix scintillation strips together can easily creep up into the extrusion hole, partially (or fully) blocking the holes, and prevent the insertion of a fiber. The blocking can occur not only at the edge of a strip but also 1 to 2″ axially inward. Since a border of about 1″ is provided for prior to module cutting, the plug must not extend farther than this (a 1/4″ creeping of the glue from a strip edge is allowable, as this portion is cut-away from the active portions of the module). Moreover, some of the holes within a module can be cleared up by a thin ($\approx$ 1 mm diameter) drill bit. However, the use of such a bit can easily lead to blemishes on the inner-surface of the strip material, corrupting the scintillator in a considerable way. Precautionary measures are taken to prevent such a blockage from occurring. One method conservatively applies a bead of five-minute epoxy on both ends of the cross-sectional face of the strip prior to module gluing. Care is taken in applying the bead of glue only on the surface: covering the complete hole. At the same time, the epoxy must not "leak" onto the strip's outer triangular sides, as this introduces extra material between adjacent strips, and thereby, compromises the intra-strip alignment during module assembly. Moreover, the

difficulty in controlling the depth of the epoxy, in addition to the difficulty in visually inspecting whether the fiber-hole has been fully covered, frequently results in modules with channels that still must be reamed out ($\approx$ 5–10% of a module's to strip count) or which are treated as either spares or simply discarded. In fact, the first 15 modules produced have used the five-minute epoxy technique. However, out of these 15, at most 10 have been accepted as representative units for the FPS, and the remaining 2 (3) labeled as spares (discarded). In order to improve these yields, an alternative approach has been taken, which considers heating the edges of a strip to temperatures well above 200°F by laying the strip-edge flush on a hot-burner plate. The high temperature is beyond the melting point of the scintillator and allows enough plastic about the scintillator's hole to melt, wick about 1/8″ up into the hole, and naturally plug-up. The depth of the plug falls well within the extra 1″ length provided for during individual strip cutting. The process proves to be much simpler, cleaner, and considerably quicker than applying five-minute epoxy. Since this method has proven to be successful, the remaining FPS modules have been subsequently fabricated in this fashion.

Once the scintillator strips are pre-cut, taped, labeled, slumped, and appropriately plugged, they are ready for module assembly. This is preformed using a set of alignment hardware mounted on the spherical "template" domes, all known as the "jig". A final pass is made from strip-to-strip to ensure that the array of scintillator is properly prepared for the next stage.

7.1.3 Module Fabrication

The modules are structurally independent units, composed of wrapped scintillator strips, epoxy, laminated fiberglass cloth, and precision-mounted optical K&E survey targets, which are necessary for detector installation and

alignment. Each is constructed on the spherical aluminum domes described in Sec. 7.1.1. Any particular assembled module consists of a doublet set of u and v ("stereo") layers (*i.e.,* two sets of nested pairs). The u and v layers are mirror images of one another and are each glued separately on independent domes. Once the glue is allowed to cure, the two layers are mated together and re-glued on a single dome. In order to maintain correct strip and layer positioning, the nested strip array must be glued on the domes with the aid of certain strip alignment and registration hardware. The hardware guarantees modules can be repeatedly assembled, in a consistent manner, from module-to-module. The logic is described next.

Strip and Layer Alignment

The primary means of maintaining strip position within a stereo layer is by the use of a pair of aluminum lateral alignment bars that are placed vertically on either side of a module using slots milled into the bar's edges (see Fig. 7.1). These slots anchor the ends of the first and last scintillator strip with every other strip in-between for the bottom-half of the stereo layer surface (u or v) under construction. Roughly $1/4''$ from the strip edge is accommodated within a slot. For the remainder of this thesis, these particular strips will be called "registration strips." The alignment bars are first pre-bent into the required spherical radius and subsequently fixed onto the dome at threaded-holes pre-existing in the dome accessed through four countersunk through-holes in the alignment bar. The bars are kept thin enough (in the transverse dimension) to allow bending in only two dimensions, and thus, lay flush on the face of the dome. Every alternate strip that comprises the upper-half of the stereo layer, which is nested into the lower sawtooth during epoxying, is free to move since it is not held to either of the alignment bars or to the lower strip in any way.

However, its registration is constrained by those strips which are fixed into the bars as well as from the high vacuum pressure applied during assembly.

The pair of alignment bars control the overall strip-to-strip alignment, and hence, define the alignment of an entire stereo layer within a module. Therefore, the position of the two bars must properly (and consistently) be established on a dome for all subsequent module construction. Two fiducial endpieces are used (as shown in Fig. 7.1) for such an alignment. A straight line is scribed into the dome across its diametric center. The set of alignment pieces — two lateral alignment bars with the pair of fiducial endpiece — are mounted, and the scribed line is centered on the central fiducial hole in each endpiece. The angle formed by the scribed center line and the lateral alignment bar is iteratively adjusted until a 11.25° angle is achieved between the two bars and the scribed line. At this point, the location of the fixation holes in the bars marks the proper assembly location on the surface of the dome. These positions are transferred onto the domes, the bar-endpiece tooling removed, and appropriate holes that will be used to fix the alignment hardware on the domes are subsequently drilled and tapped via a digital programmable CNC. Here, the fiducial endpieces are used only once: to register the precise position of the lateral alignment bars. Once this has been determined, they are removed and are no longer a part of module fabrication.

Each stereo layer will be epoxied together and subsequently placed under vacuum, allowing each strip in the layer to position itself to the constraints of any existing alignment hardware until curing. The dominant component of the force (on the order of 5 psi, Ref. [87]) in such a technique is radial — *i.e.,* in a direction along the radius of the spherical dome on which the assembly is constructed. The upper scintillator layer is forced into the lower layer into which it nests during the vacuum procedure, implying that any piece of scintillator at the outer periphery (*i.e.,* upper and lower boundaries)

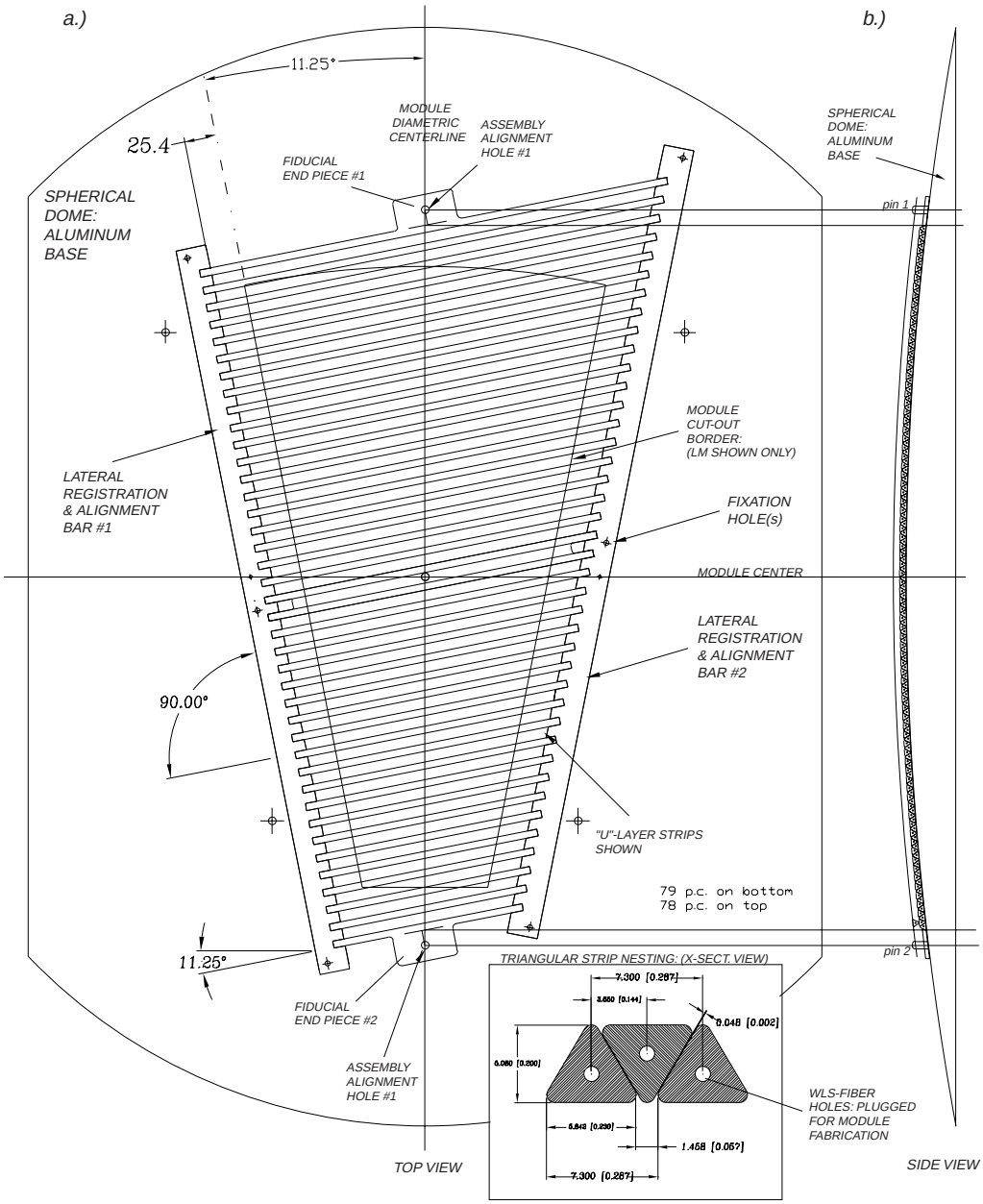

Figure 7.1: Schematic of module fabrication: strip-by-strip layout, registration and alignment on the spherical template dome is shown. Given are a) top r–ϕ modular view including the "nested" triangular strip cross-section and b) side r–z profile of assembly.

of a module can easily "bow" away from the inner volume of the layer, if left unsupported at either end. Therefore, two additional precision-milled, thin aluminum bars or "stops" (see Fig. 7.2) are each placed at the upper- and lower-most strips of each layer during the gluing and assembly. These stops are screwed directly into central pins that exist on the domes in order to maintain correct scintillator spacing. The sides of the stops that abut the scintillator are milled with the appropriate angle so that they nest with the edge of the outermost scintillator strip, ensuring a flush fit. Additionally, a soft $1/4''$ long $\times$ $1/2''$ diameter coaxial rubber cap is placed on top of each central pin in order to avoid tearing of the mylar sheet used to cover the full layer and help seal the vacuum from air leaks. The use of such tooling does not, in any way, introduce major systematic alignment biases during assembly [86].

Once such alignment details have been addressed, module construction can begin. The procedure consists of the following steps:

1. Lay a thin ($\approx$0.005$''$) plastic backing material on the surface of the domes.

2. Fix lateral alignment bars to the domes at the positions and in the manner described above. These positions will maintain the proper angle of the strip axis with respect to the module edge. The bars must be sprayed with a mold releasing agent in order to facilitate the removal of the scintillator strips from the alignment bars after curing as well as of the bars from the surface of the aluminum dome.

3. Place a thin $0.012''$ (300 μm) Fiberglas cloth — cut into the shape of the u- or v-stereo module layer — in the region between the two bars.

4. Uniformly apply EPON epoxy with a paint-roller over the cloth. Enough epoxy must be applied (*i.e.,* about 0.010–0.015$''$ thick coat) to penetrate both the matrix of the cloth and the pre-determined inter-strip spaces.

5. Place the appropriately prepared strip, one-by-one, onto the cloth in the correct "numbered" position. Verify that every alternate "registration" strip is anchored into the alignment bar slot. If such an inspection is not performed, neighboring strips may misalign and, since the spatial location of all strips is strongly coupled, the alignment to the rest of the layer will be compromised.

6. Liberally apply more epoxy, in a similar manner, to the upper-side of the first layer of scintillator.

7. Place each strip in the upper sawtooth of the stereo layer at its proper "numbered" position. Note that none of these strips are anchored to the alignment bars (see Fig. 7.2: steps (a) and (b)).

8. Place a layer of Fiberglas cloth on the top of this scintillator layer and coat it with a final layer of epoxy.

9. Place another thin plastic covering sheet on top of the Fiberglas cloth.

10. Use a thick ($0.032''$) mylar sheet and vacuum bag the entire assembly. A rubber sealant must be placed about the perimeter of the dome to attach the bag to the dome's surface and help prevent vacuum leaks. Vacuum pump the entire assembly and allow it to cure for at least 24 hours at room temperature.

The u- and v-stereo layers are mirror images of one another and are constructed in-parallel on independent domes. The two layers are then mechanically mated to form the complete two-layered module. Again, prior to mating, the alignment of each layer relative to one another must be established. The mating of these layers is illustrated in step (c) of Fig. 7.2 and is described next.

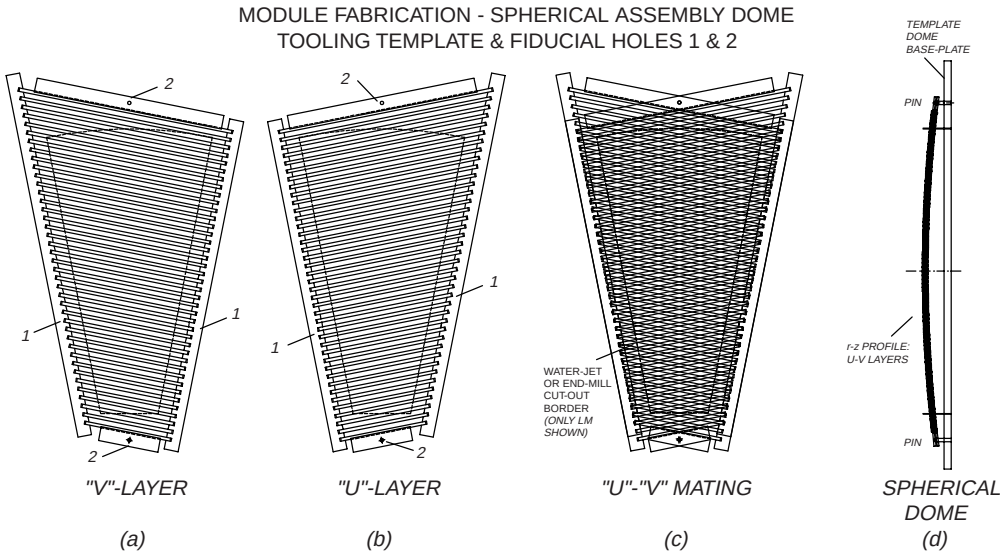

Figure 7.2: Strip-by-Strip layout using lateral alignment bars (1) and alignment stops (2) for module fabrication. Shown are a) v-layer, b) u-layer, and c) mated u–v layer, all assembled on d) the spherical (r–z view) "template" dome. The fiducial holes in (2) serve to reference the module's position during water-jet and/or end-mill cutting.

Alignment of $u - v$ stereo mating

The two lateral alignment bars each contain one hole that accommodates an $1/8''$ diameter dowel pin. The two dowel pins are inserted into the holes, which are in cattycornered positions on the two alignment bars. A thick ($1/8''$) aluminum alignment plate with through-holes at the position of these pins is slipped over each of the layers. The plate also contains two precision-drilled holes at the top and bottom which are used to position fiducial drilled holes in the aluminum stopping bar at the top of each layer. The holes are made perpendicular to the alignment plate and are drilled into the upper and lower aluminum stopping bars on each layer independently. They establish the positioning of the two stereo layers relative to one another during the mating process. They also orient the absolute position of a module in space during the actual cutting of the fabricated module.

After the aluminum alignment plates are removed, the stereo layer is freed from the dome. The mating surfaces of each of the layers are gently sanded to encourage adhesion. Epoxy is uniformly applied on the lower layer, and the upper layer is laid on top. The constructed upper (or upstream) layer is labeled as the u-layer, while the lower (downstream) layer becomes the v-layer. Such a convention is used for all constructed modules and is followed in the software framework (*i.e.,* FPS geometry, RECO, etc...) developed for the FPS system. Pins are placed through the upper and lower holes to establish the layer-to-layer alignment. Before the assembly is pumped down, copper shims (0.005–0.010$''$ thick) are placed at any overhanging area of the upper layer to prevent buckling of this layer from the vacuum forces. R&D studies have indicated that shims must be placed to prevent noticeable misalignments during the mating procedure. Finally, the mated assembly is placed in a vacuum and allowed to cure for at least 24 hours. After curing, the module can

be cut into the required wedge-like trapezoidal shape. The cutting also enables the lateral alignment bars and aluminum stops to be recycled for subsequent module production.

7.1.4 Module Cutting

Many techniques have been studied to determine a precise, reproducible means of cutting the boundaries of a module to its required trapezoidal shape. Some of the R&D details are presented in Ref. [55]. For the representative FPS modules, two methods have been used: a) precision water-jet machining, and b) digital end-mill routing. Each is an effective technique but has inherent limitations. Details of both are described below.

The water-jet technology is commonly used in aerospace engineering as well as other modern industries in cutting metal, plastic, and other materials to size. To a large degree, it has yielded desired results for accurate FPS module cutting. A very thin jet of water is driven from a small nozzle at approximately 50,000 pounds-per-square-inch (psi). The module to be cut is placed on a digitally programmable table that uses the holes drilled in the upper and lower support bars as fiducial reference points. The form is cut relative to these holes according to design prints made for the FPS module. A tolerance of $1/32''$ ($\simeq$30 mils) is guaranteed by the vendor [83]; accuracies of better than half this have been observed using the technique. Additionally, in order to facilitate cutting and ensure a reasonably clean edge, an abrasive media (*i.e.,* sand or grit) is traditionally added to the water prior to pumping. The size of the grit begins at about 80 grits and can be varied according to ones needs. The sand helps improve the cutting mechanism. However, the sand does remain inside the WLS fiber hole of the scintillator and is removed by an air-gun prior to fiber insertion. Further, the modules must each be dried

by a similar air-gun, upon return from the vendor.

Although the technique can prove to be clean, accurate, inexpensive, and reproducible, exposure of damp modules to humid and high temperatures (*i.e.,* above 90°F) during processing and shipment can oxidize the strip's reflective mylar wrapping and aluminized coating. This immediately results in light sharing and crosstalk with neighboring strips, defeating the purpose of wrapping mylar on each scintillator strip. Historically, many modules (mainly large) were fabricated and cut during fall-winter seasons (*i.e.,* low temperature and humidity environment), and the effect was not readily observed. However, the first batch of 8 production small modules were made during warm, humid summer temperatures and failed all quality inspections upon return. Thus, the water-jet method was quickly abandoned for all subsequent modules (small, special, and spares). Instead, an alternative technique incorporating a digital programmable end-mill router was used.

The end-mill procedure is a standard technique available in most machine shops, such as the BNL Central Shop. A sharp routing (about 1/4–1/2″ in diameter) drill is mounted on a digital programmable CNC. Each module is clamped into an aligned position on the table-bed of the CNC. The existing, centered holes on the aluminum stops of each fabricated module serve as markers for such an alignment. The setup is then programmed to walk and cut the trapezoidal shape to dimensions established by the design prints. However, in order to achieve a tolerance comparable to the water-jet technique, a "two-pass" cutting procedure is used. Here, the first pass of the routing drill establishes a rough shape for the module, taking away most of the material but leaving an extra 1/16″ border about the desired module perimeter. The second pass uses a sharper drill to remove this excess border and is made at much lower speeds than the first to provide a clean, smooth finish. Indeed, comparisons of the quality and tolerances achieved by the technique show that

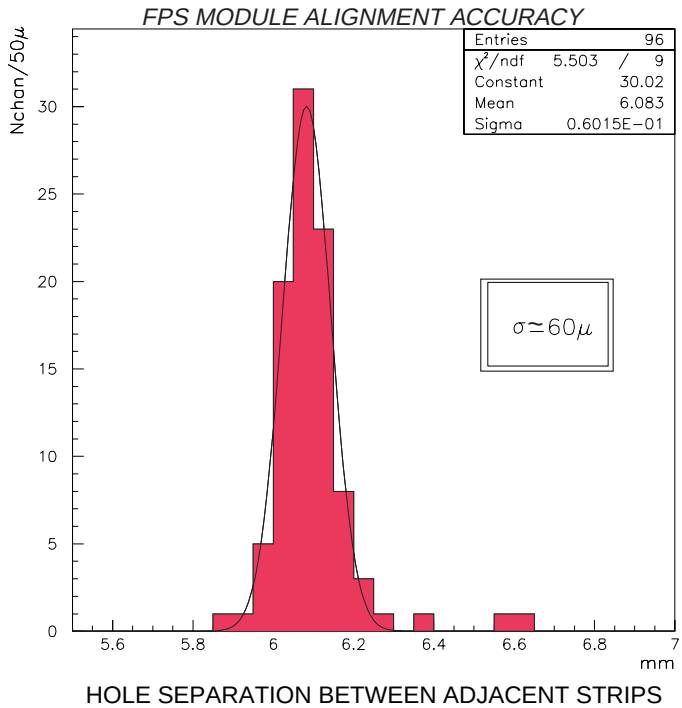

Figure 7.3: Result for channel-to-channel alignment accuracy measured using a CMM for a FPS module. A narrow distribution with an accuracy of about 60 μm is achieved and well within design specifications.

the end-mill is similar to the water-jet option, and at the same time, requires little attention to the type of atmosphere where modules will be exposed to.

7.1.5 Strip-to-Strip Alignment Study

The procedures developed for module fabrication requires an understanding of the level of accuracy achieved in the strip-to-strip alignment of a module. This study must verify that the techniques are reliable, reproducible, and hence, can be continued with the full complement of modules comprising the FPS detector.

As a benchmark, simulation studies suggest that the level of accuracy in channel-to-channel alignment be on the order of 20% (or 200 μm) of the 1

mm position resolution for tracking electrons in modules constructed with 6 mm-wide triangular strips [84]. It is believed that an accuracy at or below this value is sufficient for efficient particle identification with the detector. Once a module has been fabricated, a CMM instrumented with a high-resolution optical magnifier can be used to measure the strip-to-strip alignment. Here, the cross-hairs of the magnifier are centered on a strip's fiber-hole and stepped from strip-to-strip to measure the distance of separation from one nested channel to the next. For the example given here, a total of 96 measurements are made. The results appear in Fig. 7.3. A narrow distribution yielding a 1σ width of 60.8 μm is observed, indicating the complete technique constructs modules to well within specifications. Such a value indicates that significant contributions to the alignment of the detector are not from the nesting of strips, but instead, on the overall method in positioning a module in its support frame, and in turn, the frame's assembly into the FPS support structure. These procedures are outlined next.

7.2 Detector Support Structure and Assembly

Once a module is built and cut, it remains to be WLS fiber cabled and mounted into a structural support frame. Since the detector has been designed to be "modular", allowing each FPS (north and south) to be divided into 16 $\times$ 2 independent but equal module elements, the two items can be addressed separately. Further, the modularity allows the cabling to proceed in-parallel to the construction and alignment of the support frame assembly. The following section describes the frame and detector assembly; the reader is directed to Sec. 7.3, which outlines the cabling procedure.

	Large Module	Small Module	"Special" Module
Layer 1: Shower	7	0	1
Layer 2: Shower	7	0	1
Layer 3: MIP	0	7	1
Layer 4: MIP	0	7	1

Table 7.1: Number of different modular species in each layer of a FPS detector.

7.2.1 Detector Structure — General Principles

As discussed in Chap. 6 and listed here for reference, the distribution of modules within each layer in each detector is given in Table 7.1. Each of these modules sits in its respective position of the layer by means of an aluminum supporting frame. The frame provides the structural integrity of the detector. The frame itself in a given layer consists of eight radial ribs spaced at 45° intervals in ϕ and are fastened at one end at the inner support ring (see Fig. 7.4). For L1 and L2, the outer periphery-end of the rib is subsequently fixed by stainless steel mounting brackets, which are aligned and welded on the EC head *in situ* during installation (see Chap. 8). On the other hand, for L3 and L4, the ribs are fixed to an outer support ring used to support the lead layer, which itself is mechanically anchored to the ribs in L2. The rib's profile is water-jet cut [83] in two dimensions to conform to the spherical curvature of the EC head. Each layer's inner ring contains eight milled slots located 45° apart in ϕ — corresponding to the rib-to-rib angular spacing — to accommodate the placement and attachment of the ribs. Each rib is also machined at its inner radius to facilitate a proper ring-to-rib connection. The ribs are milled in such a way that the two support elements fit securely together, being mounted so that the entire layer of the support frame is at equal height in z from rib-to-rib (see Sec. 7.2.3 for extended discussion).

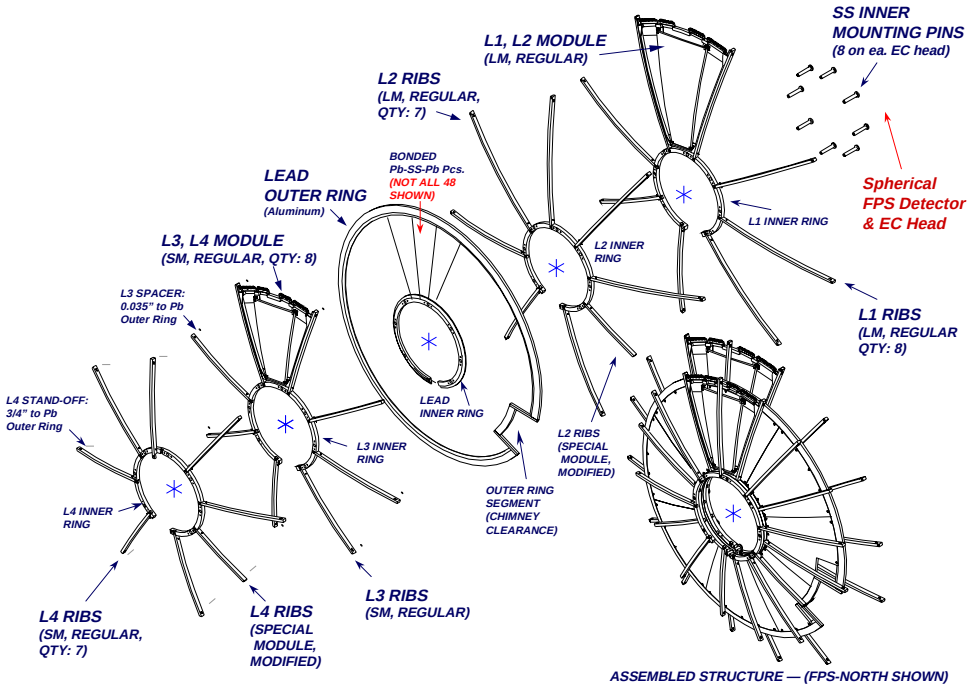

Figure 7.4: Three-dimensional view of the layered FPS support structure assembly. For brevity, all modules and lead pieces are not shown.

A fabricated (and cabled) module sits within a separate trapezoidal-shaped module frame "box". Each box consist of two side-walls mechanically held together at the inner radius by a bottom-wedge support and at the outer radius by a 45° outer support ring/arc (see Fig. 6.4 in Sec. 6.2). Each of these boxes can be freely inserted (or removed) into the inner ring-rib frame housing. The two units: module's frame box and rib are mechanically coupled to one another at each frame's side-wall. Similar to the ribs, the profile of each component in the module's frame: side-wall, bottom-wedge, and outer support arc are also water-jet cut to the spherical radius of the EC head.

As shown in Fig. 7.5, each frame's outer support arc is further machined to contain milled slots through which the wavelength shifting (WLS) fibers pass as they exit the edge of the scintillator module and are routed to the outlying

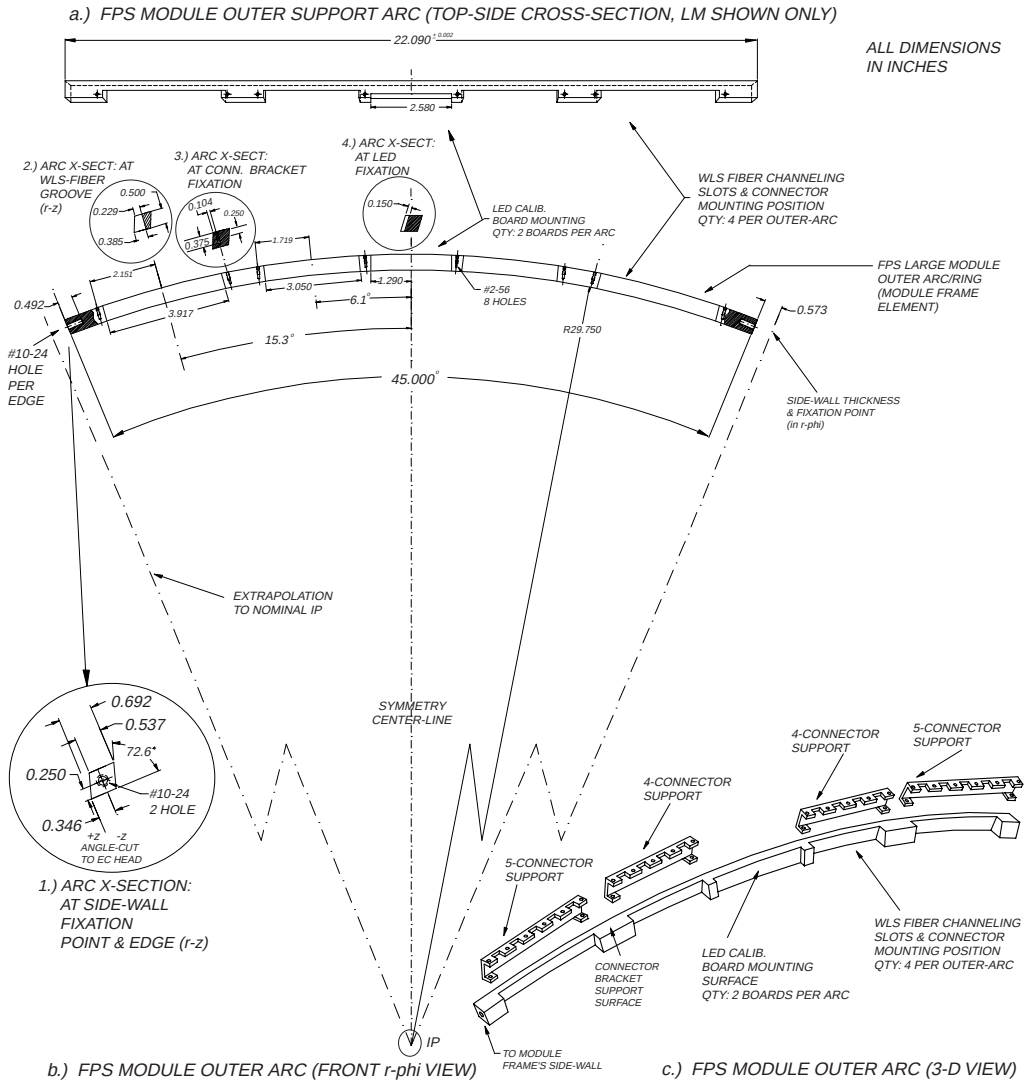

Figure 7.5: Production print of the outer support arc in a large module/frame unit. The arc is precisely machined with angles on both the $\pm z$-surfaces to conform to the spherical EC head. For completeness, r–z cross-sectional views along the arc are shown in circles #1–4. The geometry for the SM and SpM arcs is designed and constructed similarly.

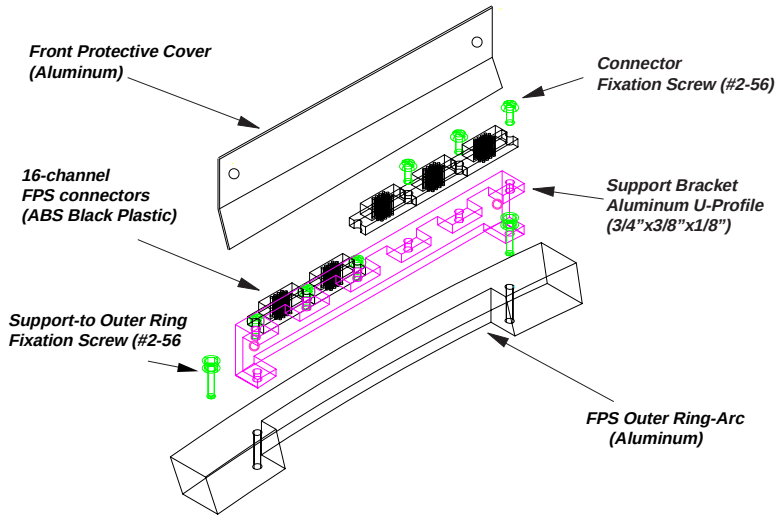

Figure 7.6: Section of FPS outer arc supporting optical connectors and required brackets, all protected by a 1/16″-thick aluminum covering plate.

optical connectors (see also Fig. 7.6). The connectors are mounted to brackets that are, in turn, anchored to the outer arc. Additional slots are milled at the center of each arc to allow attachment of two small (each $1.0'' \times 1.25''$) pc-boards carrying surface mounted LED calibration/monitoring systems. Since the FPS upstream and downstream layers are of different radial extent, the outer support arcs are cut to two different sizes. Moreover, assembly and installation concerns demand that the surfaces of the outer arcs at their inner and outermost $|z|$ position be machined in order to ensure that the frames in adjacent layers nest properly with one another.

The complete FPS unit mounts and is held to the EC at two radii: one at the inner support ring and another, using machined mounting brackets, radially at the outer perimeter of each support rib. The two not only provide the structural support, but also register the module's precise location on the cryostat wall. The following sections address, in more detail, this as well as the methods for construction, assembly, and alignment.

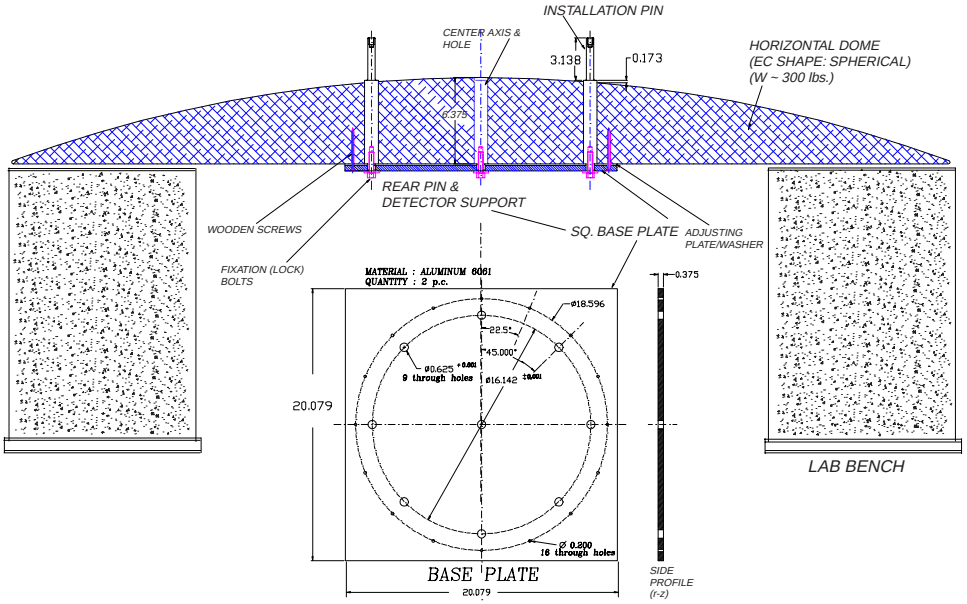

Figure 7.7: One-to-one assembly of DØ EC head for detector assembly during FPS construction. The eight stainless steel support pins mounted on the dome are supported by the adjustable rear base-plate aligned on the dome.

7.2.2 Assembly Hardware

Prior to the installation of the detectors at DØ, the full assembly for each half of the FPS is staged to ensure the installation procedures (described in Chap. 8) are performed in a systematic and logical manner. In order to mock such a scheme, a 1:1 "model" of the EC head is required. This permits a study of all pertinent assembly issues (*i.e.,* nesting, alignment, clearances, etc...) that inevitably will have to be addressed in the actual DØ detector.

A cross-sectional view of the model assembly is shown in Fig. 7.7. The main element consists of a 300 lbs., 6 ft. diameter, spherical-shaped wooden dome. Although the actual diametrical region of the EC heads is greater than 6 ft., the wooden dome built here is enough to accommodate the full FPS system including the optical connector volume that radially protrude an additional 2–3″ from the outer periphery of the support structure. Such a dome

is constructed on a spinning lathe with six 6 ft.×6 ft. particle boards, each 1.0″ thick, all glued together. A concentric through-hole, 1.375″ in diameter, is drilled perpendicularly through the entire thickness to allow the boards to be mounted vertically, through a 1.25″ diameter boring bar attached with the lathe. The total length of the bar is 100″, and hence, the desired radius of the EC spherical head. The entire unit is made to spin clockwise at about 10–15 r.p.m. about the axis defined by the boring bar. A separate routing unit is mounted next to the lathe, which contains a lateral swinging uni-strut bar that holds a routing tool at one end. Each time the particle board rotates, the routing tool steps in/out along the ϕ–z plane, carving out the 1:1 shape of the cryostat head. Local deviations of only 1/4–1/2″ from the 100″ radius are observed from such a setup; and consistent with the deviations in local regions of the actual EC heads. The assembly of the FPS must approximate conditions as close to the DØ environment as possible, and thus the dome must be mounted vertically to stage the installation of the detector in this position. Therefore, two such wooden domes are built: the first to study assembly and alignment issues horizontally, on a lab bench, and the second to address these same issues vertically.

Once these domes are constructed, eight circularly arrayed, oversized (0.6–0.75″ diameter) through-holes are drilled into each dome to accommodate eight stainless-steel pins that support the detector at the inner radius (see Fig. 7.8). Each pin is $0.550^{+0.000''}_{-0.001''}$ in diameter, protruding 3.138″ — the nominal thickness of each FPS assembly — from the surface of the dome and are mounted at 45° intervals about ϕ relative to one another. The first pin at ϕ=$\pi/2°$ (*i.e.,* local 12-o'clock) is located and subsequent pins are inserted. The location of each pin matches holes machined on a FPS inner support ring (see Sec. 7.2.3). For additional leverage in supporting the detector, the pins are held at the rear of the dome (*i.e.,* at its flat-surface) by a flat 1/2″ thick aluminum support

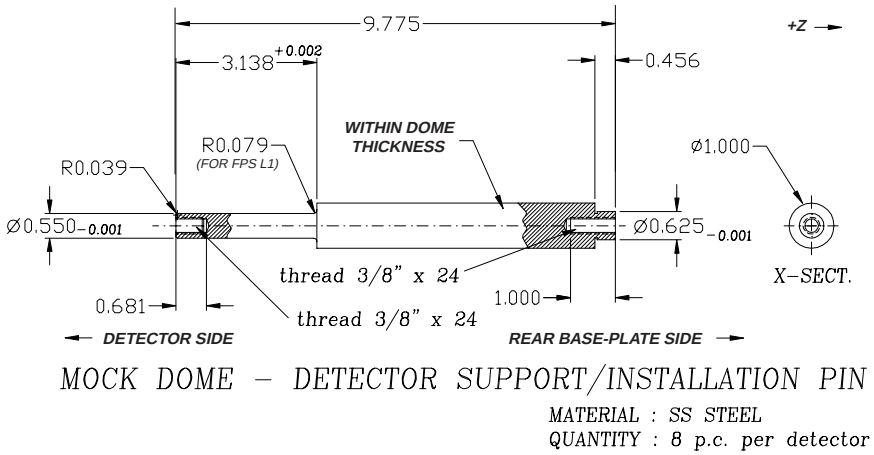

Figure 7.8: Detector inner support pins mounted within the wooden dome/base plate assembly. The pins support the FPS inner ring structure outlined in Sec. 7.2.3.

base-plate that has similar holes drilled to couple each pin.

The entire dome-pin assembly is placed horizontally on a lab-bench to align the pins to their correct height and verify that each pin is parallel to one another. To do so, a telescopic survey/leveling stand shoots the dome relative to the surface of the flat base-plate held at the rear of the dome. Next, 2″ thick aluminum shims are iteratively inserted about the outer perimeter of the dome to raise/lower the unit on the lab bench to an equal horizontal height. The optical stand then surveys the upper-edge of each pin relative to the surface of these leveled shims. The base-plate contains sixteen additional 0.300″ holes (see Fig. 7.7) that carry leveling screws to allow the surface of the plate, and consequently, the pins to be iteratively adjusted so that the height of each is within ±0.010″ relative to one another. Once the alignment has been established, the pins are bolted to the base-plate. Next, each layer's FPS inner ring is one-by-one inserted into the dome-pin assembly. This ensures that each pin is parallel to one another. EPON and five-minute epoxy are inserted into each of the oversized holes existing in the dome. Once the epoxy

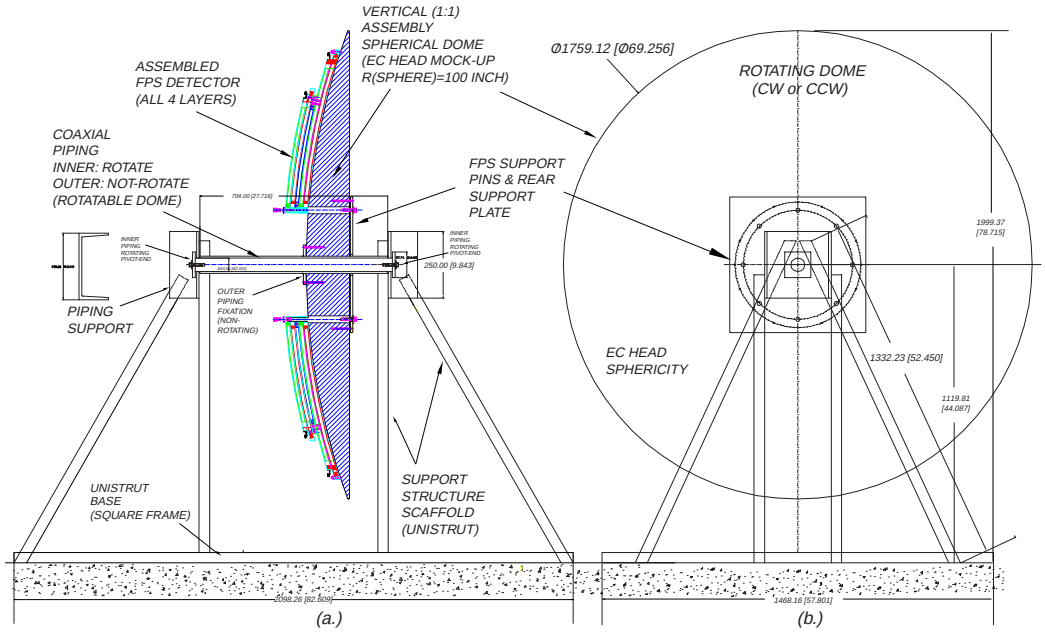

Figure 7.9: Vertical mounting of the mocked-EC head for final testing of the assembly procedures prior to installation at DØ. Shown are: a) r–z view and b) r–ϕ view. To facilitate module insertion and removal, the dome is made to rotate about a central axis.

cures, the pins are fixed in their proper orientation for the duration of the FPS assembly. One of the two domes is then tilted vertically and supported on a scaffold assembly made of uni-strut frames (see Fig. 7.9). The vertical dome is also free to rotate in $\pm\phi$ to help in the insertion of modules during assembly as well as to conveniently allow local regions of the detector to be examined.

7.2.3 FPS Inner Ring and Support Rib Structure

Each layer of the FPS detector contains an inner aluminum support ring that provides the main fulcrum in supporting the detector on the cryostats. As mentioned earlier, the FPS support rib matrix is bolted at this ring. The profile of these ribs is water-jet cut to the spherical geometry of the cryostat with tolerances of up to $\pm 1/32''$ (along the radial thickness). The rings, shown

in Fig. 7.10, are machined on a digital programmable CNC and contain three types of holes — each of which perform a specific function (see sets #1–3, Fig. 7.10b):

1. *Set #1:* The main set of holes is used to mount and support each detector. These consist of eight $0.565^{+0.002''}_{-0.001''}$ diameter through-holes, equally placed in ϕ at 45° with respect to one another and match the ϕ-interval for the stainless-steel support pins mounted (welded) to the wooden assembly domes (DØ cryostats) for installation of the FPS (see Sec. 7.2.2 and Chap. 8, also cross-section in Fig. 8.2). These are precision-machined through-holes that are slightly oversized with respect to the $0.550''$ diameter pins for articulation of the rings on/off the pins.

2. *Set #2:* Pair of threaded-holes for layer-by-layer "jacking" of the detector off the EC. These holes are located next to item (1) in all rings except that of L1 to allow raising (in z) of each cabled layer. They are anticipated to be used only when need arises such as during FPS installation at which time potentially damaged modules in L1 may require replacement without compromising modules from L2–L4 in the detector. Such jacking allows a synchronous movement of L2–L4 (in conjunction with the lead layer), by nominally $1.0''$ out in z, to provide access to modules in L1. The main pivot point is made at the inner ring.

3. *Set #3:* Eight #1/4-20 threaded-holes, each spaced 45° in ϕ, to anchor support ribs, and thus provide the skeletal framework of a FPS layer. This item is addressed further below.

As seen from Figs. 7.10 and 7.11, each ring contains eight machined slots to accommodate a rib. The connection is made by mating #1/4-20 × $3/8''$ long slotted screws that are nested inside the machined slots. The head of each

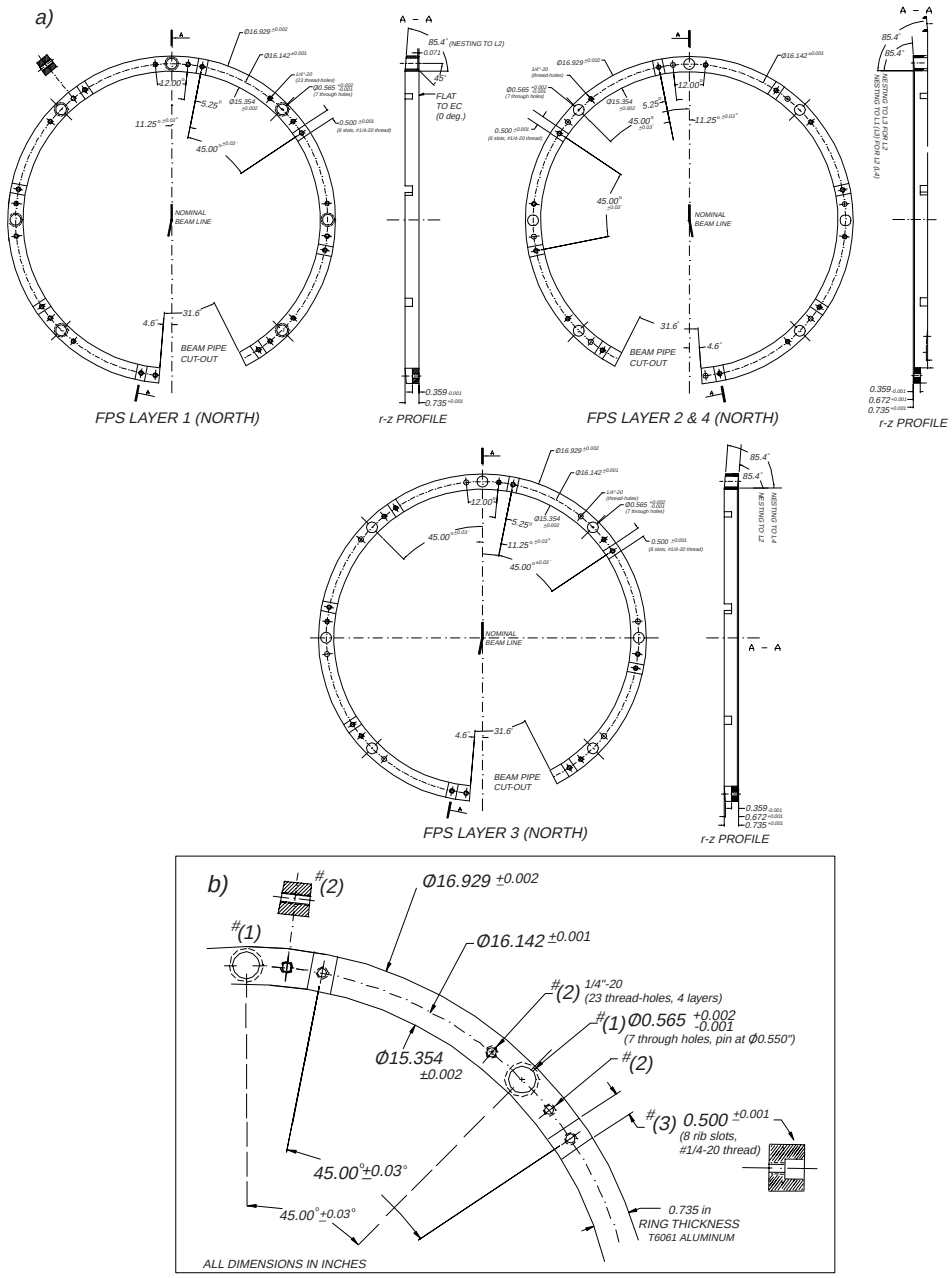

Figure 7.10: Inner support rings for Layers 1–4 (FPS-North). (a) gives each layer's ring and its respective r–z profile. The rings for L1 and L3 are geometrically similar and only differ in the nesting configuration in the r–z plane. (b) gives a limited, expanded r–ϕ view of the different sets of holes used for assembly and mounting, outlined in the text. Rings for FPS-South are a symmetric, mirror-image of the north half.

bolt must be manually machined so that it lies flush (or $\simeq 0.005''$ below) to the outer ($-z$) surface of the ring in order for the inner ring from an adjacent layer to sit abut the given ring without introducing mating gaps in z. Moreover, the outer and innermost surfaces ($|z|$) of each ring is radially machined with a beveled-cut so that it also follows the geometry of the cryostat head, and thus, guarantees the rings in adjacent layers nest compactly. Finally, the inner ($+z$) surface of the inner ring for L1 differs from the other layer's rings by having eight holes countersunk (to radius $0.080^{+0.002''}_{-0.000''}$) to allow insertion onto the inner pins. This type of hole matches the $0.079^{+0.000''}_{-0.002''}$ radius machined on the inside-edge of each pin (see cross-section in Fig. 8.2, Chap. 8) and thereby, ensures the detector will rest as close to the cryostat wall as required.

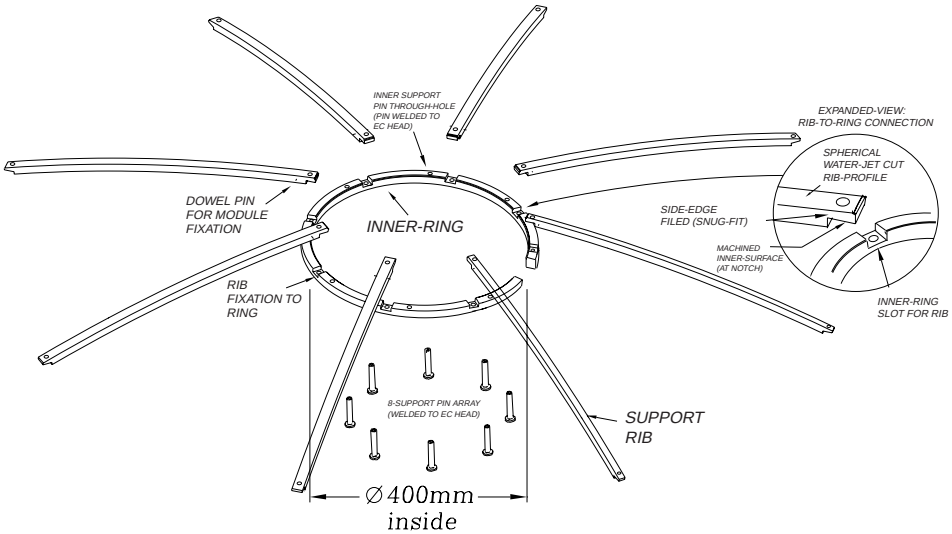

Figure 7.11: View of FPS supporting unit for independently constructed modular frames. Shown is an inner ring with machined slots to attach the support rib array. Modules for all subsequent active layers are supported in a similar manner.

The lower radii at each ϕ-side of a support rib contain dowel pins protruding $1/8''$ out from the edge. The dowel pins provide the first point of support to "v-notches" machined at the inner radius of each modular frame (see Fig. 7.12).

The second support point is made via precision-drilled threaded holes (#10-24) existing at each ϕ-side, at the outer perimeter, of a rib.

Although the rib's profile has been water-jet cut, the fixation notch at its rib-to-ring contact is machined (initially to $\pm 1/8''$). However, for each rib, the surface at this rib-to-ring fixation slot can cause more than $\pm 1/8''$ deviations in z (from rib-to-rib) at the rib's outer radius (given the large 2–3 ft. lever-arm existing from the pivot point made at the ring). Therefore, an optical survey is done to level (in z) the height of each rib's outer radius with respect to a reference point taken at the outer ($-z$) surface of the inner ring. In order to equalize the height to within $\pm 1/16''$, each rib in a layer is iteratively machined, at the rib-to-ring fixation slot, until the tolerance has been achieved. Once each rib has been fine-tuned, it is labeled and fixed to a particular slot in the ring. The process of equalizing the rib's outer perimeter in z guarantees that all layers will mesh compactly and exist in-parallel when assembled.

It should be noted that a segment on each inner support ring has been cut-out to negotiate the installation of the detectors with the $1.25''$ diameter beryllium beam pipe and beam-support flanges existing at DØ [85]. Historically, such a design had been chosen prior to production, during the initial periods of the technical design of the FPS. Here, it was believed that the FPS detectors would be installed at DØ while the detector was in the collision hall. This would require mounting the inner rings on the cryostat without removing the beam pipe. However, the early installation of the FPS (with respect to the actual Run II start date) allowed mounting the detectors on the cryostat without the presence of the beam pipe, thereby making the ring cut-out redundant. Nonetheless, the removal of this material from the ring does not compromise the structural integrity of the unit.

7.2.4 Modular Frame Box Assembly

As observed in Fig. 6.4, a module sits within a trapezoidal-shaped "modular" frame box. The components of each frame — *i.e.,* side-wall, bottom-wedge, outer support arc — must each be mechanically joined and aligned together to within $\pm 0.005''$. This tolerance guarantees that all boxes will be inserted and fixed into the rib support frame without inducing any stress to the overall structure.

Any particular frame is assembled by the aid of a digitally programmable CNC, which drills precision holes to within $\pm 0.002''$ on each component. The side-walls are first joined with the outer arc by two #10-24 $\times$ $1/2''$ long flat-head screws, one on each side-wall. The mating holes in the side-wall are countersunk so that the screws rest about $0.010''$ below the ϕ-surface of the wall. This ensures that screws will not protrude and interfere with the mating ϕ-edge of a support rib. For mechanical rigidity, a series of #2-56 holes are drilled and tapped on $(+z, -z)$ surfaces of the side-wall and outer arc, allowing four aluminum tab-plates, two per side-wall (see Fig. 6.4), to hold the units together at the frame's corners. These holes are made, again via the CNC, perpendicular to the surface of the wall in order to prevent distortions in the frame and the alignment during assembly. Also shown in Fig. 6.4, at the lower radius corners of a module, the bottom-wedge is mated to the pair of side-walls by four additional aluminum plates, two on each $(+z, -z)$ surface of the side-wall. Each aluminum plate uses four #2-56 $\times$ $3/8''$ long pan-head screws for mechanical fixation. One should note a nominal 2 mm ($0.0788''$) gap exists (in z) between the surface of each rib and the module (and their fibers) in the layer directly above or below it. The thickness of the plate ($0.0625''$) plus an additional $0.010''$ thickness from the head of each screw is therefore sufficient to prevent any interference.

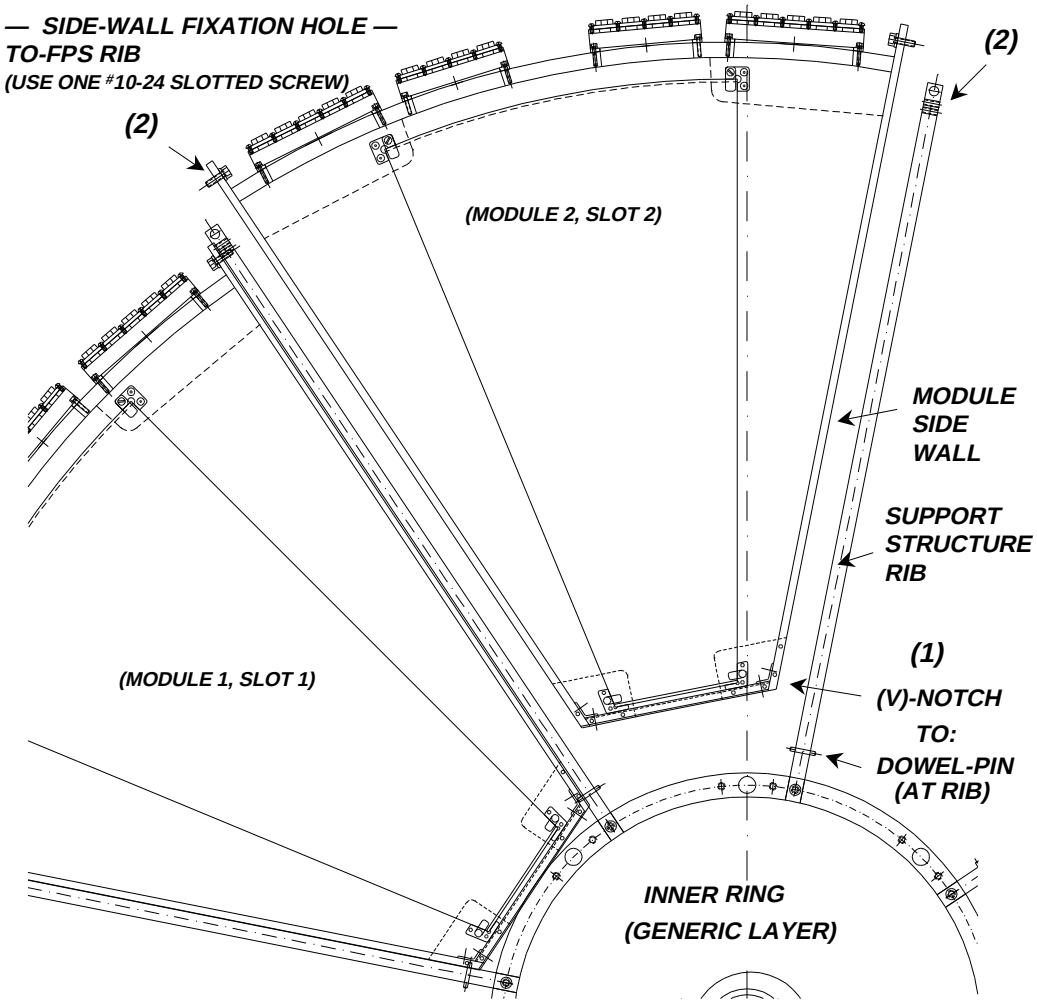

Figure 7.12: Module insertion process into FPS support structure. The lower radius of the module is inserted first until its v-notch rests on dowel pins attached to each rib (1), and the full unit is pitched about z for holes at (2) to be aligned and bolted.

Once all sides of a frame have been mechanically joined together, a precision reference "jig," as shown in Fig. 7.13, is used to verify the alignment of the entire unit. The jig models a generic module's "slot" in the actual FPS support structure by consisting of two support ribs on either ϕ-side, inclined to a height that maintains the spherical geometry. Every constructed module is required to fit securely and stress-free within the jig, thus guaranteeing that all modules have met specifications and will fit into the support structure during detector installation. The lower radius of the module is inserted first until the v-notch (see Figs. 6.4 and 7.12) in each side-wall rests on dowel-pins existing at a support rib. The upper-half of the module is then tilted in $+z$ until the side-walls are aligned and mechanically bolted with two $1/2''$ long (#18-8$\times$10-24 thread) stainless-steel head-cap screws at holes existing on each ϕ-side at the outer radius of a rib. One notes that these steps are equivalent to those performed during insertion into the FPS support structure.

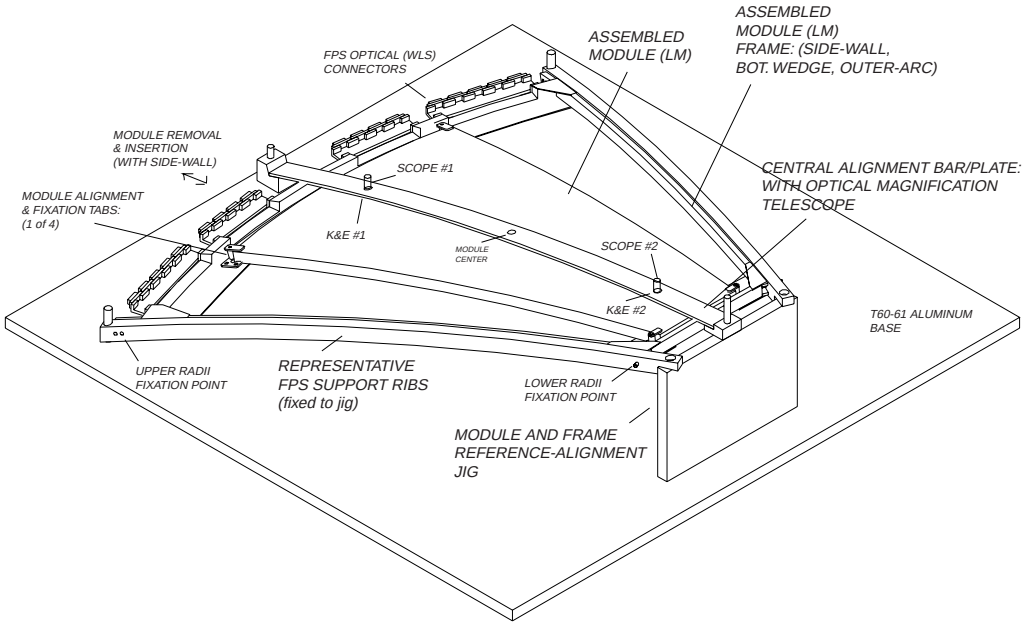

Figure 7.13: Three-dimensional view of alignment jig used to assemble and align module frames and each element. Details are given in the text.

The bottom aluminum plates not only provide rigidity to the frame but mechanically hold and fix the corners of a fabricated module. The jig in Fig. 7.13 is again used to align the module, and hence, the strips within the frame. Here, two optical magnification ($\times 10$) lens located on a spherically-bent $1/2''$ wide aluminum rod are mounted on the jig, directly at the center-line ($11.25°$) of the module's frame. The lenses pick up two of the six K&E survey targets placed on a module during fabrication (see Sec. 7.1.3). These targets have been precisely mounted using a CMM, and are positioned from module-to-module to within $\pm 0.002''$. The magnification lenses establish the distance between the central dots of each target to within $\pm 0.005''$ relative to the module's support frame housing. Once a module has been centered in the frame, the means by which it is fixed is shown in Fig. 7.14. Small aluminum tabs are placed via #2-56 $\times$ $1/8''$ long pan-head screws in precise positions at the four corners of the module, clamped into place on the surface of a fixation plate located at the r–ϕ corners of the frame. Each tab has a precision notch cut out allowing the corner of a module to nest. The thickness of the bottom surface of a tab is $1/16''$, preventing the tabs from covering the WLS fiber holes of the scintillator. An aluminum clamping bar ($1/16''$ thick) is screwed into a threaded stand-off tube, which itself is fixed to the bottom surface of the tab (see Fig. 7.14). The bar serves to hold the module in place. Once the module is aligned and fixed within the frame/box, it can be cabled (see Sec. 7.3).

7.2.5 Lead Absorber and Support

Extensive design studies and R&D efforts have been made to arrive at a suitable choice for the lead absorbing layer contained in the FPS detector. Several approaches were studied, and in general, each required a structurally rigid

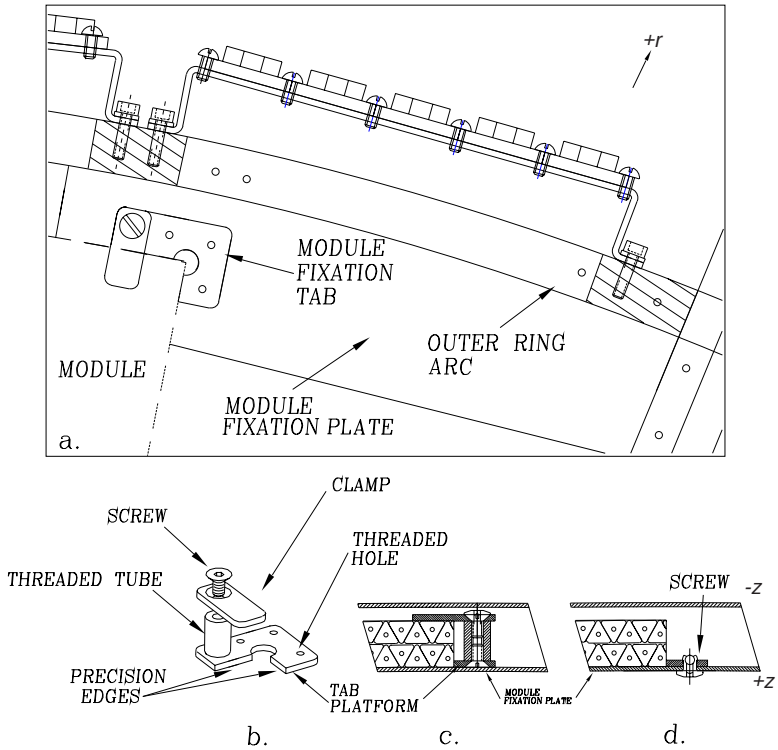

Figure 7.14: (a) An r–ϕ view of the outer edge of a layer, showing the means of module fixation within individual supporting frames using aluminum fixation tabs. Each module is held in place in an identical manner at each of its four corners. Also shown are b) and c) details of the fixation tab attached to the surface of a corner fixation plate with pan-head screws in (d). The threaded tube stand-off is held to the tab's platform using a flat-head screw on the $+z$ surface.

element that ensured proper coverage. An absorbing layer as one "complete" unit and of the size (and spherical geometry) necessary for the FPS would be extremely difficult to manufacture, handle, and install. Therefore, a wedge design seperated but nested along lines of constant ϕ has been determined. Moreover, care must be taken to ensure the nesting does not introduce any projective cracks. Thus, the geometry of the cut at the mating edges must follow a step-like or beveled surface. A straight cut machined to the radial extent of an individual wedge would inevitably produce visible gaps.

Two approaches were studied; each offering a variety of advantages and/or disadvantages during production and subsequent handling. The first, shown in Fig. 7.15, consisted of producing sixteen 45° ϕ-wedge absorbers, eight for each FPS detector. Each wedge would be 11 mm ($2X_\circ$) in thickness, casted to the 100″ radial spherical shape. The absorber would be procured with antimony-doped lead (6% Sb) thereby helping to maintain the rigidity of these large, reasonably heavy (*i.e.,* $\simeq$ 40 lbs. each) structures. The ϕ-edges of any two neighboring elements would be beveled, with a so-called *rabbit-cut*, at 45° angles with respect to its inner and outer (z) surfaces for proper meshing. Each piece would be tacked along its inner (outer) radius to an aluminum inner (outer) support ring. The outer ring would be fixed in ϕ at the proper radius to a support rib in FPS L2, as shown in Fig. 7.4. Connections to the support frame would help prevent any potential creeping of the absorber.

Although the above design provides one option for the FPS lead layer, it also introduces a number issues that must be considered during production and assembly. Each of the eight wedges must be appropriately casted to achieve the spherical geometry of the EC. Doing so with a thick lead sheet, over a large r–ϕ area can result in local regions of non-uniformity. In fact, after fabricating six prototype assemblies and subsequently measuring the thickness across the surface at 10–12 localized spots, non-uniformities on the order of 10–15% of the nominal 11 mm thickness have been observed. Re-casting after modifying the hardware used to fabricate each piece has improved the results by only 2–5%, but at the same time, has introduced several other effects, which include degraded (and cracked) edges and deviations from the 100″ spherical radius. The method can also pose a safety hazard during detector installation when mounting and precisely locating a heavy 40 lbs. object between the support rings, in a spatially constrained region between the EC-CC intercryostat gap, without compromising the safety requirements imposed

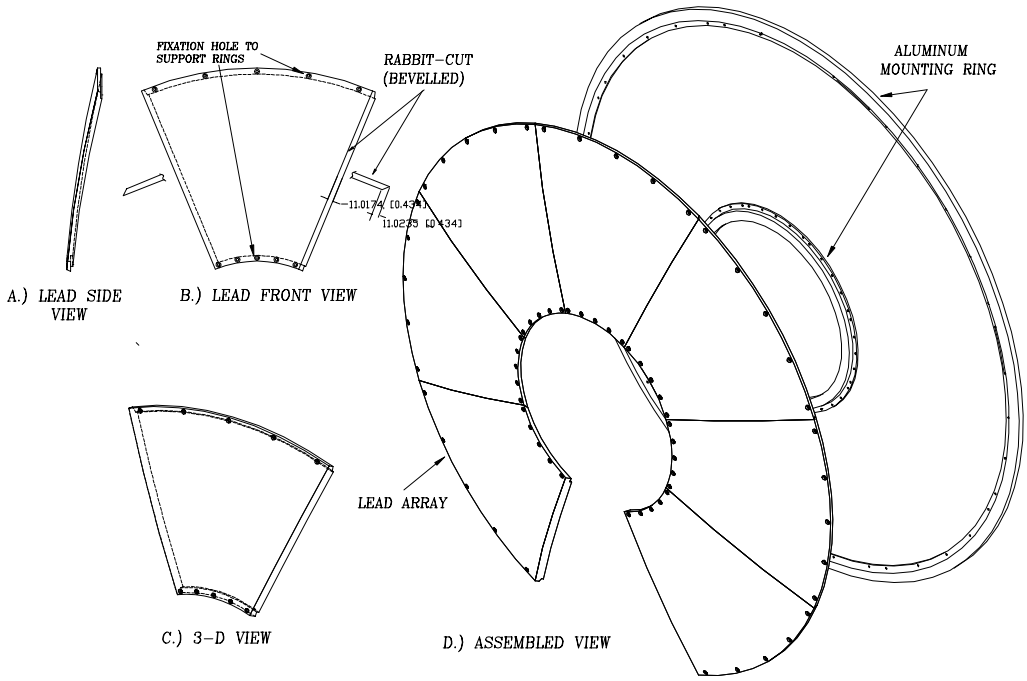

Figure 7.15: Lead absorber layer design with eight 45° wedge-like elements: (a), (b), and (c) showing the side, front, and three-dimensional views, respectively, including the beveled "rabbit-cut" on the ϕ-edges of each absorber. This ensures (d) nesting with adjacent pieces, and thus, full coverage.

in handling lead. The entire approach further requires retrofitting *in situ* of detector assembly; an aspect, which coupled with the above issues, dictates studying alternate designs and methods.

A second approach consist of utilizing small, 7.5° bonded lead-stainless-steel-lead (Pb-SS-Pb) sandwiches, totaling $2X_\circ$ in thickness, as shown in Fig. 7.16(c,f). Each detector contains forty-eight of such three-layered, lightweight (*i.e.,* each about 5–6 lbs.) elements arranged in a circle and independently mounted between the inner- and outer-support rings (see Fig. 7.20) at pre-existing holes drilled on the stainless-steel. The lead elements (see Fig. 7.16b) of one sandwich is malleable, allowing it to easily bend to the required geometric shape. However, when epoxied to the surface of an 1/8″ thick stainless-steel

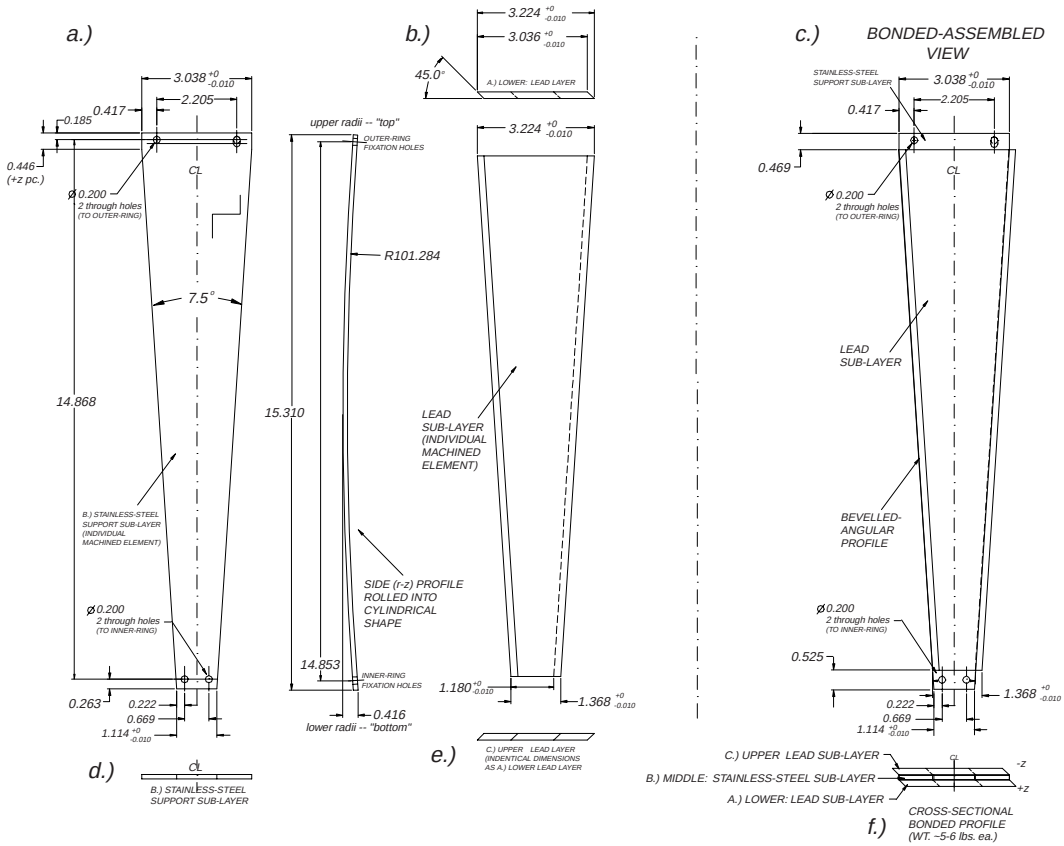

Figure 7.16: Lead absorber design using 7.5° wedge-like elements: (a) and (b) shows the front r–ϕ view of the stainless-steel support unit and lead sub-layer, respectively, as individual elements, while the assembled view is given in (c). A cross-sectional profile of each component is given in (d), (e), and (f), respectively.

support plate (see Fig. 7.16(a,d)), the complete Pb-SS-Pb unit results in a structurally rigid element incapable of creeping over time. Further, each steel plate is pre-rolled to form the desired shape. Similar to the 45° wedge assembly design, the ϕ-edge of each lead, prior to bonding, is beveled. The bonding of the lead to the steel, however, requires the ϕ-edge of the lead to lie flush to the ϕ-edge of the steel, and thus produce a step-like cross-sectional joint (shown in Fig. 7.16f). During installation, each ϕ-edge of the stainless-steel is forced to

butt against the adjacent steel neighbor in order to prevent projective cracks in the layer. Further, since all Pb-SS-Pb pieces are small in comparison to the 45° wedge design, regions of local non-uniformity over the surface are negligible (*i.e.,* $\mathcal{O}(<1\%)$). The size and weight of each piece also provides a straightforward installation procedure. Moreover, the tight tolerances required in the actual bonding process guarantees little (or no) retrofitting during assembly.

Lead-Stainless-Steel Bonding

The procedure used to bond the lead units with the stainless-steel support plate closely resembles steps taken during module fabrication (see Sec. 7.1.3). The entire assembly is performed on a 2 ft.×3 ft. cylindrical surface, 3/8″ thick aluminum "base-plate" machined on a digitally programmable bench with a nominal 100.722″ radius (shown in Fig. 7.17). Although the entire detector is spherical in geometry, the short 7.5° ϕ-interval defined for a wedge allows work on a cylindrical surface. Such a value for the angle, when arranged successively into forty-eight pieces, to form a complete 360° enclosure, approximates the desired spherical geometry, and at the same time, ensures a proper mesh of all bonded pieces. Further, a total of eight Pb-SS-Pb elements can be fabricated simultaneously, thereby allowing the entire bonding for the FPS to be completed within 2–3 weeks. As shown in Fig. 7.17, each successive bonded piece is arranged in an alternate (top-bottom) pattern to accommodate all eight absorber elements on one compact table.

For each piece, three sets of aluminum alignment hardware, illustrated in Figs. 7.17 and 7.18, are mounted on the base plate to register the position and alignment of the bonded assembly. The first two sets: (a) and (b) are small (1.0″×1.5″×1/8″) blocks, labeled "top" ("bottom") to define the position of the "upper-" ("lower-") radii of each Pb-SS-Pb element. Each of these two

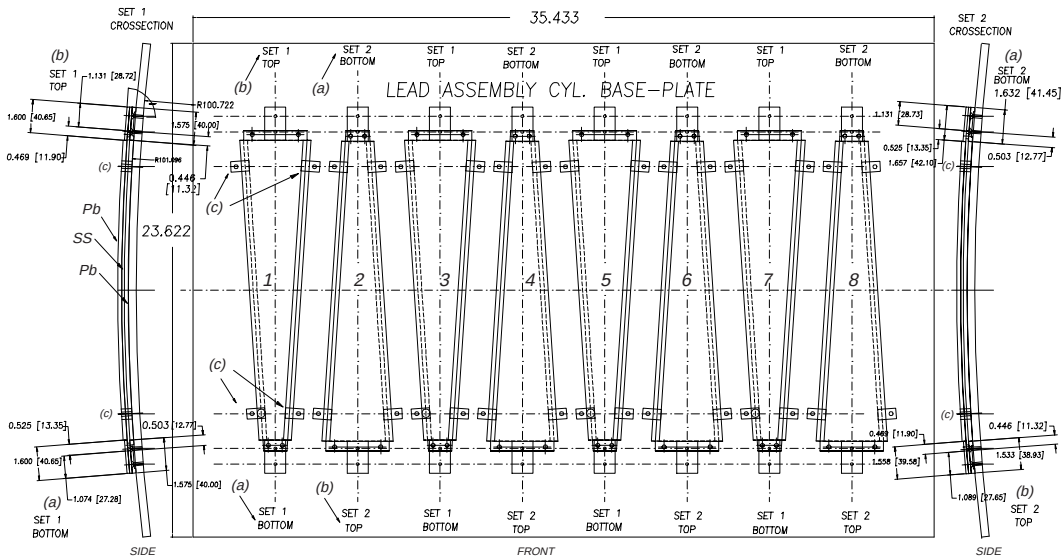

Figure 7.17: Lead base-plate and tooling hardware used for Pb-SS-Pb bonding and production. See text and Fig. 7.18 for description of tooling items (a), (b), and (c).

sets further comprise three different registration units to establish the relative radial positions of the three separate layers of one Pb-SS-Pb wedge (in decreasing z): a) "lower" lead surface (closest to cryostat head), b) "middle" stainless-steel supporting plate, and c) "upper" lead surface (closest to interaction point). Each of these three units are positioned and fixed on top of one another to constrain each wedge in r–z. Further, the "bottom" units are separated from the "top" ones by a polarity made by drilling two different size holes (*i.e.,* one at #8-32 and second at #10-32) for each respective unit. Similar fixation holes are also drilled on the cylindrical base-plate, perpendicular to its surface. Since the steel support plate is designed to anchor into the lead layer's inner- and outer-support ring, the "middle" registration unit in the "top" and "bottom" alignment set is made to shorter dimensions than the other two sublayer's registration units. The entire alignment set is positioned so that each lead piece rests relative to the edge of the steel plate. Since the

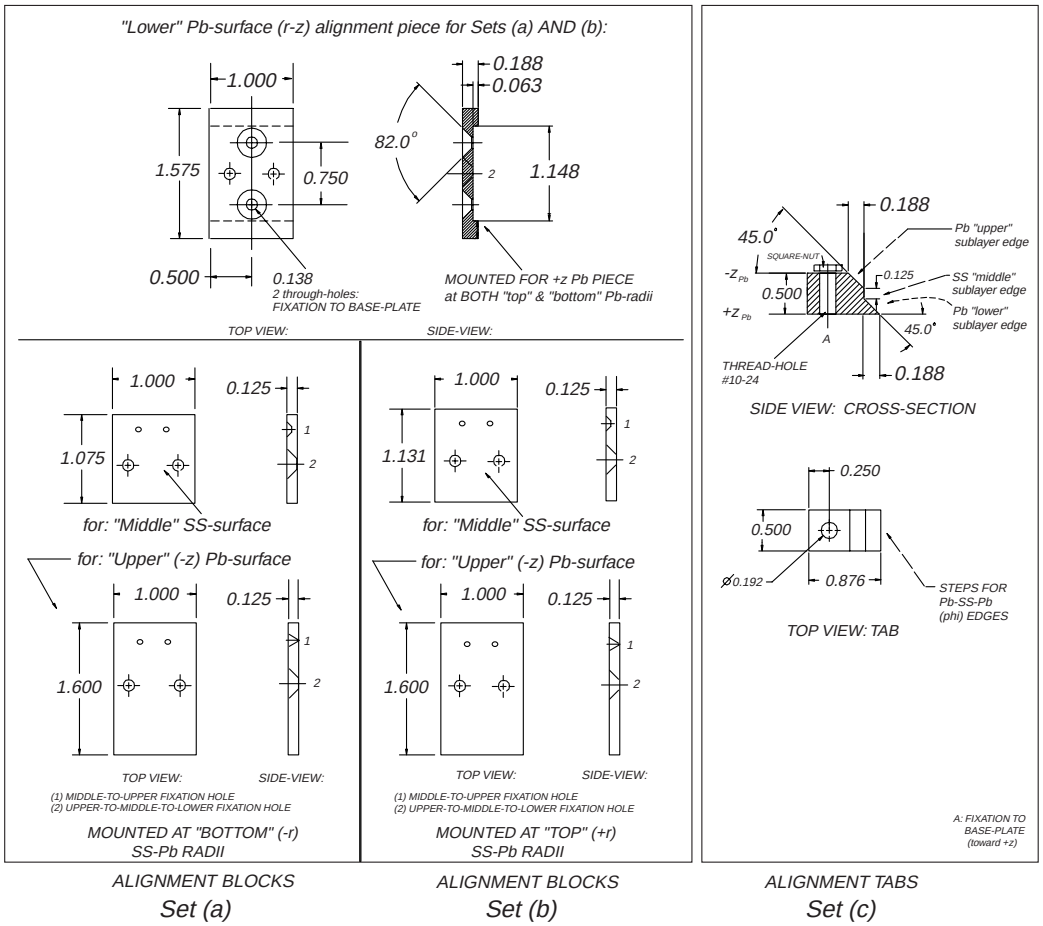

Figure 7.18: Registration hardware for lead-stainless-steel-lead pieces used during bonding. Items (a) and (b) control the r–z alignment of individual Pb-SS-Pb sublayers, whereas (c) defines the ϕ-positioning of each piece.

$100''$ cylindrical radius for each lead sublayer differs in z, the distance of the lead relative to the radial edge of the steel plate changes slightly at the lower- and upper-bonding surfaces. The nominal distances are listed in Table 7.2.

An additional set of alignment hardware consisting of four lateral aluminum alignment tabs establish the ϕ-position of each assembled Pb-SS-Pb element. As shown in set (c) in Figs. 7.17 and 7.18, each pair is located on either $\pm\phi$-edge of a bonded piece. A tab is made to follow, and thereby, abut to the

	Upper lead radii (labeled "top") $\eta = 1.65$ $\binom{+0.000''}{-0.005''}$	Lower lead radii (labeled "bottom") $\eta = 2.50$ $\binom{+0.000''}{-0.005''}$
$+z$-surface (closest to EC head)	$0.446''$	$0.503''$
$-z$-surface (closest to IP)	$0.469''$	$0.525''$

Table 7.2: Nominal distance required for each lead surface epoxied to its steel support plate relative to the radial edge of the steel as a function of r–z.

diagonal, step-like cross-sectional cut of the Pb-SS-Pb absorber. The height of the tabs are also designed to the overall thickness of the Pb-SS-Pb assembly. During vacuum-bagging, the four tabs together squeeze the multilayered absorber downward, toward the midline of each element. However, in order to prevent any small perturbations in ϕ, resulting from the strong vacuum forces, a $1/4''$ thick square-nut with #10-24 matching holes is added on all four tabs. The tab-nut array together with the two "top" and "bottom" units concurrently hold each Pb-SS-Pb downward, toward the surface of the base-plate, preventing any motion in r, z, and ϕ.

As evident in Table 7.2, one should note the tight, negative tolerances required in positioning the registration units on the base-plate. This type of precision is necessary to guarantee that projective cracks do not exist between neighboring elements. Moreover, each of the eight slots on the base-plate is made to be within $\pm 0.002''$ of one another so that reproducible elements are fabricated and little bias exists from one assembled Pb-SS-Pb element to the next.

Once these units are defined, the bonding process can be summarized in the following steps:

1. Pre-bend individual lead sheets on the spherical domes used during mod-

ule fabrication (see Sec. 7.1.1), prior to bonding. These sheets will then form the desired shape without inducing stress or fractures during production.

2. Attach the "lower" and "middle" units of the "top" alignment set at each of the eight slots on the base-plate without fixing the "upper" unit. This last unit locates the "upper" lead sublayer surface ($-z$) and must be put on after the "middle" steel sublayer is placed.

3. Next, locate the "lower" unit of the "bottom" alignment set at each slot on the base-plate. Insert the "lower" lead sublayer ($+z$) in each slot between the two alignment sets of Steps 2 and 3.

4. Liberally apply a thin (5–10 mil thick) coating of EPON epoxy over the front, convex surface of the inserted lead. For best results, apply less epoxy at the perimeter of the lead — as the glue will tend to squeeze outward from the middle during vacuum suction.

5. Place two of the four lateral alignment tab-nut fixtures at a given ϕ-side of each slot. Leave these tabs mounted but not tightened as further adjustments to all sublayers will be required.

6. Place the stainless-steel plate on top of the epoxied lead sheet. Note that no glue is applied on either surface of the steel plate.

7. Fix the "middle" unit of the "bottom" alignment set at each slot, thereby registering the radial position of the "lower" lead sublayer and stainless-steel. Next, place the "upper" alignment unit to both the "bottom" and "top" sets. Again, keep all screws loose as different sublayers may need adjustments.

8. Place the final two lateral alignment tabs (and nut) on the remaining, opposite ϕ side of a slot.

9. Repeat Step 4 to the bottom, concave surface ($+z$) of the "upper" lead sublayer and insert this last layer on each steel plate.

10. Individually tighten all screws, from one slot to the next, visually verifying that all edges of the lead and steel are flush with one another.

11. Cover the eight bonded assembly region with two thin (each $\simeq 1/16''$ thick) plastic wire-meshes to prevent potential vacuum leaks at sharp corners.

12. Vacuum bag the entire assembly. A rubber sealant must be placed about the perimeter of the base-plate for attaching the bag to the plate's surface and preventing vacuum leaks. Pump the entire assembly down, allowing it to cure for at least 24 hours at room temperature.

13. After curing, carefully use an alcohol-soaked sponge to clean any epoxy present on the face and ϕ edges of an absorber. This is due to epoxy being forced outward from each sandwich during vacuum suction (as alluded in Steps 4 and 9).

One should also note that the presence of the magnet services at DØ requires customizing three Pb-SS-Pb pieces in this ϕ-region by decreasing the radial coverage of the absorber. Here, for these three "special" elements, the above procedures are still used and full-sized elements are initially produced. However, the stainless-steel is carefully cut-away to the required radial extent. Next, the distance, as indicated in Table 7.2, for each lead sublayer from its top and bottom radial-edge with the steel, is cut-away with a sharp blade running in $\pm z$. The blade is made to stop as soon as it hits the ($|z|$) surface of the

steel support plate. A chisel, with alcohol applied to the region, can be used to pry-off the portion of the lead that needs to be removed. Correct mounting holes are re-drilled at the inner and outer radius of the exposed steel.

Lead-Stainless-Steel Support

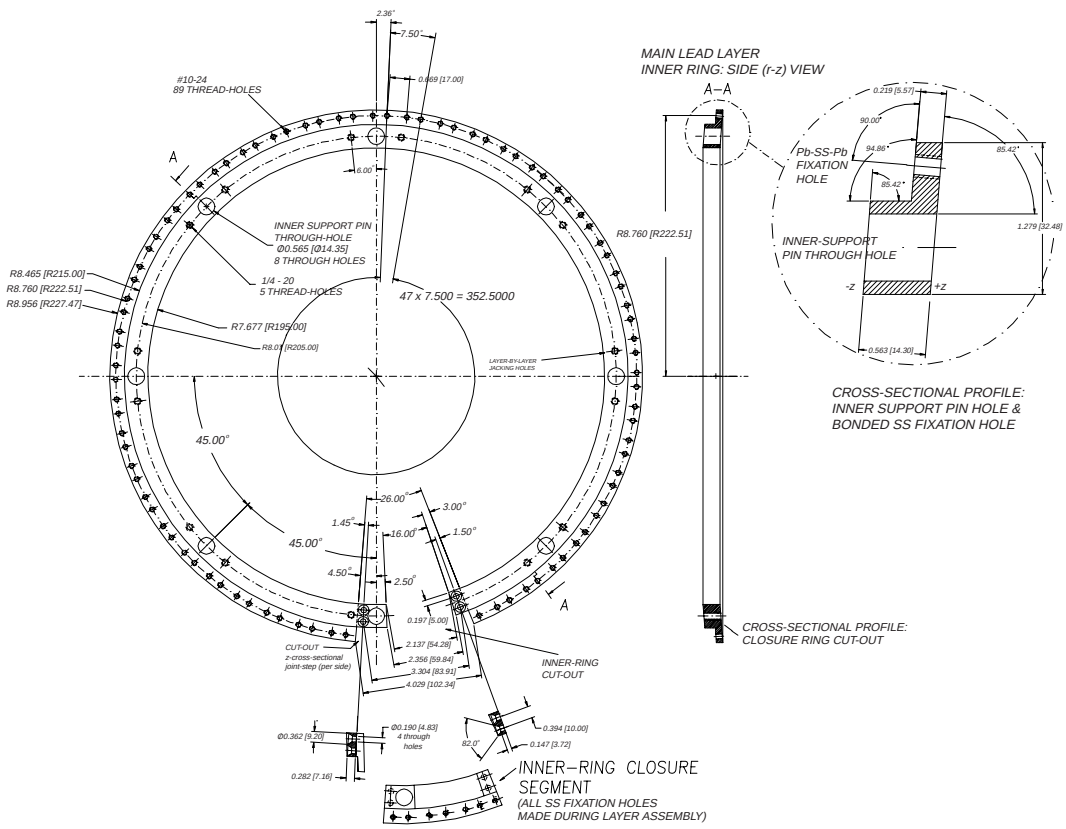

Figure 7.19: Precision-machined lead layer's inner support ring with closure segment. Shown are the eight through-holes that mate to supporting inner pins welded on EC wall as well as a cross-section (insert) illustrating the ring's r–z surface. In order to properly nest and anchor a cylindrically-shaped Pb-SS-Pb element, an angular profile is needed on the surface. Note: all fixation holes on the closure segment are made *in situ* during actual lead layer assembly.

The Pb-SS-Pb wedges are each supported at an inner- and outer-support ring by anchoring the steel to precision-drilled #10-24 mounting holes on the

rings. The inner ring, as shown in Fig. 7.19, is similar to the rings in other layers, being mounted through the eight welded pins on the cryostats. The ring, however, differs only in that it is made of two segments so as to close-up the designed ϕ cut-out needed in clearing the Tevatron beam pipe. The first segment consist of the main portion of the ring, cut-out at a ϕ=278.50° midline with a symmetric opening of $\pm 2.015''$ ($\Delta\phi$=13.00°) in either side. At each ϕ-edge of this gap, a step is made along z to join it with a second ("closure") segment machined to close-up the opening. The step aligns the two segments together. Such a complete 360° enclosure is required at the inner radius in order to mechanically anchor the bonded lead elements about this ϕ-interval, and at the same time, carry the heavy load of the complete layer. In fact, the location and opening of such a gap is based on the region of the inner ring that provides the maximum structural rigidity for the layer and also does not interfere with any fixation hole for the Pb-SS-Pb pieces.

The lead layer's outer ring, as shown in Fig. 7.20, is perhaps the most complicated (and expensive) unit machined for the FPS detector. The precision and structural rigidity that it has been designed with serves three useful purposes for detector assembly and installation:

1. *Bonded lead support.* The primary purpose of the outer ring is to provide, with the inner ring, the required connections for each bonded Pb-SS-Pb element.

2. *Support and alignment of FPS MIP Layers: L3 and L4.* These two layers do not have any outer fixation support directly on the EC cryostat wall, and therefore, differ in the installation scheme with the Shower layers. Instead, since the radius of L3 and L4 is matches the radius of the lead layer, each rib in these layers is fixed to the lead layer's outer ring. Precise mounting holes on the ring are drilled to establish the correct

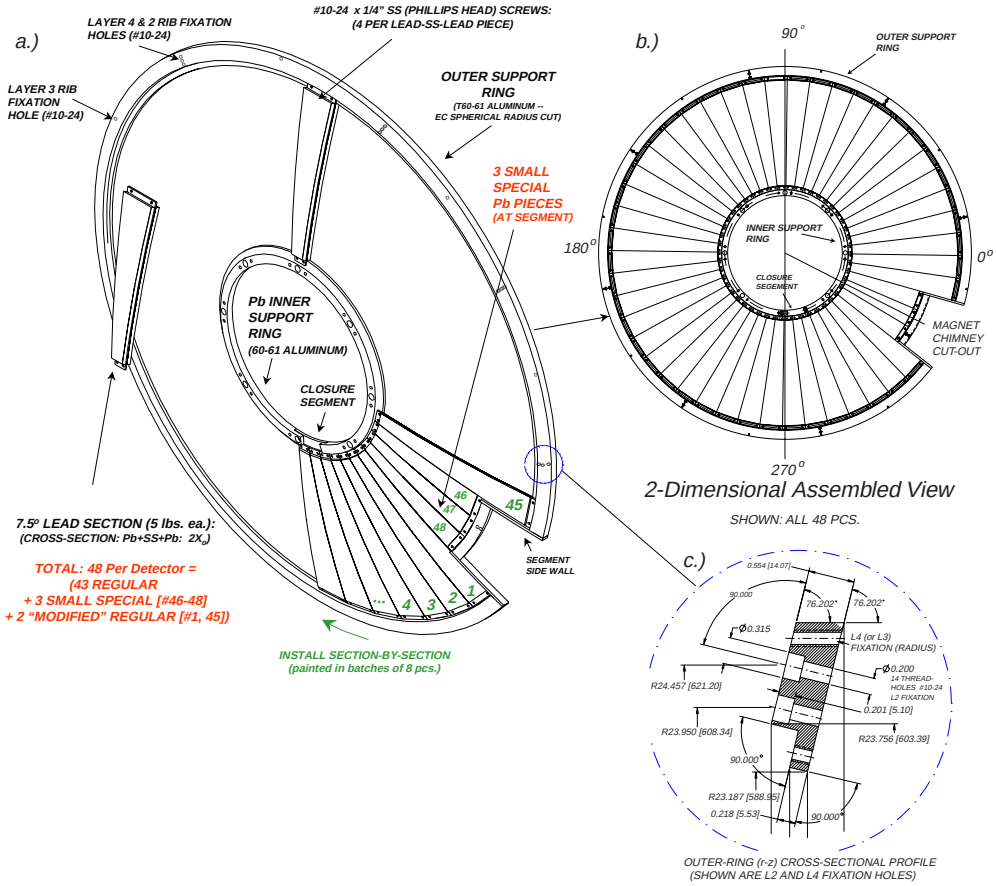

Figure 7.20: Lead layer support assembly showing bonded pieces mounted between inner- and outer-support rings. A 2-D projection of the completed layer (b) and a close-up of the outer-ring's cross-sectional profile (c), which follows the L2 rib's spherical profile are given.

ϕ-position of a L3 and L4 rib.

3. *Installation template for alignment of FPS Shower Layers: L1 and L2.* The outer ring is anchored to the each support rib of L2. The holes that exist on the ring must match threaded-holes on a L2 rib while maintaining the correct opening angle (in ϕ) for cabled modules to be inserted or removed stress-free. Since the outer-ring is a rigid element and constructed in a precision manner, it can be made as a "template" in aligning

the ribs in ϕ during installation. Also, the ribs in L1 are equivalent in geometry to those in L2[1], and for the given purpose, interchangeable. Therefore, by drilling similar holes in the ribs of L1, the ring can be used to align L1 as well.

Item (3) is discussed in the next chapter (see Sec. 8.1). Each FPS outer ring contains ninety-six #10-24 threaded-holes to allow two $1/2''$ screws to anchor the outer radius of each of the forty-eight bonded Pb-SS-Pb elements (*i.e.,* item (1)). The holes on are made via a digital programmable CNC with tight tolerances: $\pm 0.001''$. Each steel contains matching slotted holes to allow $\pm 1/8''$ movement in r. A slotted hole serves to align the bonded elements with their neighbors, and hence, maintain full coverage in r–ϕ. Moreover, the presence of the solenoid services require the outer ring to be modified at the proper $\Delta\phi$. A cut-out is made and subsequently closed by an arc segment of a smaller radius (see Fig. 7.20). The correct radius for this segment is determined by machining an entirely new outer ring of smaller radius and cutting the enclosure to the required arc-length. The segment can then be joined to the actual outer-ring with two aluminum side-walls used for an active modular frame (box). Since this segment must hold the three "special" Pb-SS-Pb elements, the mounting holes are manually drilled.

Extra holes are machined on the outer-ring to address item (2): the precision mounting and nesting of the FPS MIP layers. These holes are made with the CNC at correct ϕ-intervals. One should notice from Fig. 7.20c that both the lower ($+z$) and upper ($-z$) surfaces of the lead layer's outer-ring are machined to conform to the spherical geometry of the detector. The lower surface can thus mount and rest along the upper surface of a L2 support rib.

[1]They each only differ at the inner ring where extra machining has been done on the rib's mating groove to align the ribs to an equal z (see discussion in Sec. 7.2.3).

Similarly, the ring's upper surface allows a rib from either L3 or L4 to nest against it without introducing gaps in z. However, to establish the correct distance in z at the outer radius of a L3 (L4) rib, a $1/16''$ ($3/4''$) thick aluminum washer is placed between the rib-to-ring surfaces. A #10-24 $\times$ $1''$ ($1.5''$) long slotted-head screw is used to attach the L3 (L4) ribs to the outer ring.

7.3 Module Cabling and Certification

The cabling of individual FPS modules is divided into three categories: 1) Preparation of WLS fiber and connector assemblies, 2) Strip-by-strip fiber routing and module cabling, and 3) Installation of LED monitoring/calibration systems. The design and R&D of the optical connectors used to transmit light from WLS fibers to clear fibers is described, in length, in [55] and only briefly discussed here. The main procedures used to cable modules are summarized below.

7.3.1 FPS Optical Connectors – Design and Support

The preshower detector is read out through WLS fibers coupled to clear fiber waveguides, which transport light to remote VLPCs (see Chap. 5). The transfer between the two fibers is made at sixteen-channel optical connectors (see Fig. 7.21) located at the outer periphery of a FPS module. The connectors are injection-molded [88, 89] from black ABS plastic[2]. The injection-molding, quality-control, and measurement of light transmission (see Fig. 7.22 for a typical result from such tests) are done by the UIC DØ group [94], and the final product is delivered to Fermilab for fiber-connector preparation.

[2]pure ABS — Acrylonitrile Butadiene Styrene — polymer cylindrical pellets ($\sim$1 mm-diam. $\times$ $\sim$2 mm-long) have been used, manufactured at DuPont Corp. [93].

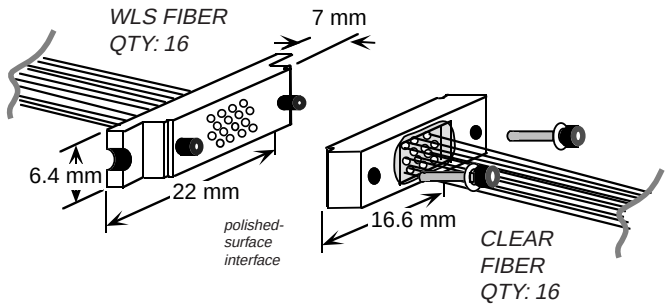

Figure 7.21: 3-D view of detector-side (mating) FPS optical connector assembly and alignment.

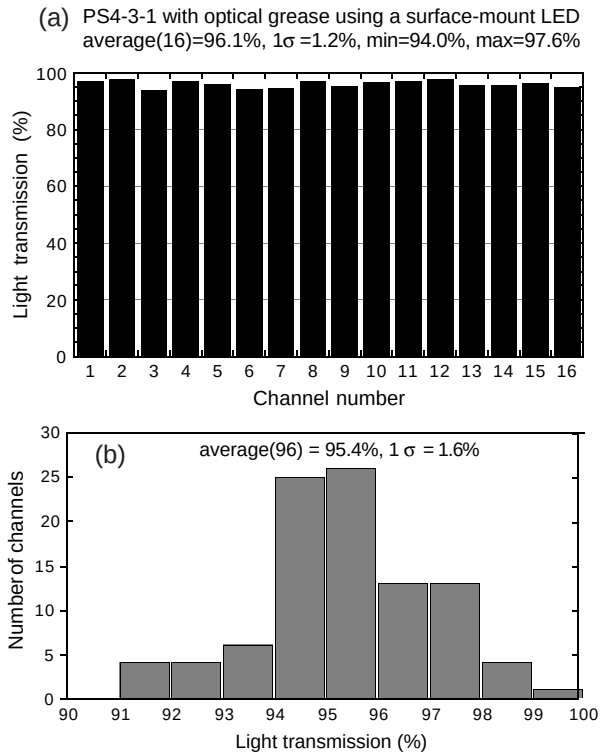

Figure 7.22: Observed light transmission for each channel in a 16-channel one-to-one mated connector assembly (a), and the measured distribution of fiber channel transmissions (b). Both distributions yield, on average, 95% light transmission through the fiber/connector interface.

The connector, shown in Fig. 7.23, has dimensions of 6.4 mm×22.0 mm×7.0 mm, and contains a matrix of 4×4 fiber channel grooves. Each groove holds a 0.835 mm-diameter WLS fiber. A pocket in the rear of the connector allows for convenient potting (and fixing) of fibers in a groove. Two pins of different sizes (large at 2.3 mm-diameter, small at 2.11 mm-diameter) mounted on the face of a connector, mate and align the WLS fiber side with the clear fiber side connector. The connections are made (see Fig. 7.21) and bolted to one another by custom-made #0-80 × 1/4″ hex-head screws inserted into the threaded alignment pins. Further, during module cabling and assembly, a convention is established to ensure the larger (smaller) of the two pins points away (toward) the center of a module, when the connector is mounted on the frame's outer arc. This polarity ensures a fixed orientation for all connections, as dictated by mapping concerns.

Connectors are mounted in a single row (in z) at the FPS outer-perimeter via machined aluminum support brackets (see Fig. 7.6). Each bracket contains square slots (in ϕ-z), 1/16″ wider than the connector's glue pocket for fibers to tunnel through to their required strips. For ease in assembly, the brackets support connectors in groups of three, four, or five. Moreover, two adjacent connectors are held on a bracket (in ϕ) by the same round-head #2-56 screw (see Fig 7.24). A single row configuration allows connectors to occupy a space as compact as possible. The clear fibers from the FPS must negotiate the run over the face of the outlying ICD, which requires the connectors to be positioned as far away from the cryostat face as possible. Thus, the brackets (and connectors on which they sit) in L1 and L2 are pitched at roughly 8–10° away from the cryostat head to clear (in z) the 1.0″ thickness of the ICD tiles at this radius (see Fig. 7.25).

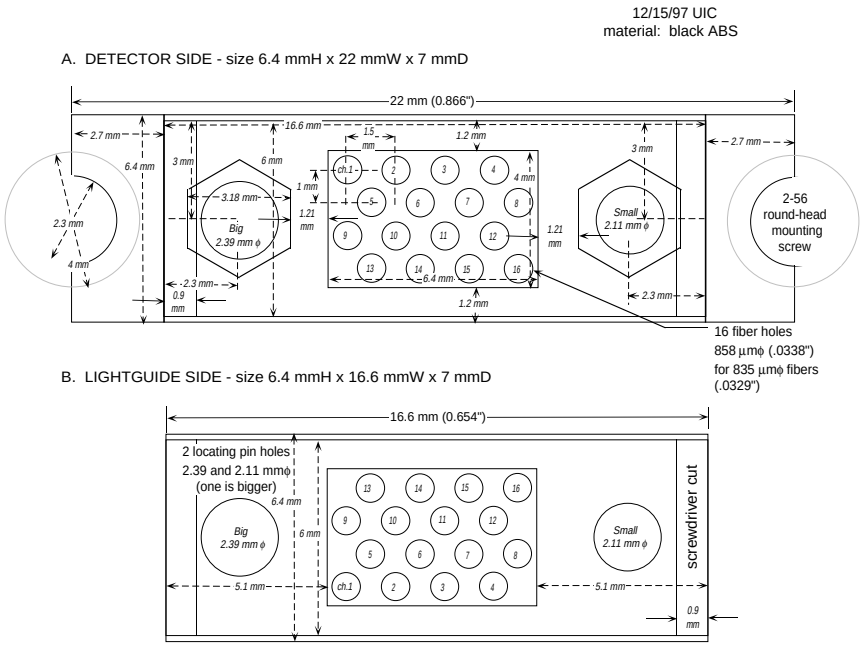

Figure 7.23: Front face of the 4×4 array, sixteen-channel FPS a) WLS-fiber (detector-side) optical connector and its mating b) clear-fiber (light-guide side) connector. All dimensions are given for completeness.

7.3.2 Preparation of Fiber & Connector Assemblies

The FPS modules contain a u- and v-layer, in which the strips in each are oriented perpendicular to one of the radial sides of the module. Within each strip, a 0.835 mm-diameter WLS fiber is inserted and protrudes approximately 10–12 mm on the end opposite the connector. In order to optimize the light output, each WLS fiber is silvered at this end. The fiber is held in place at

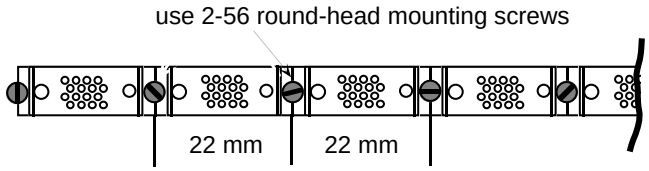

Figure 7.24: ϕ–z view of the single row connector mounting configuration in each FPS module.

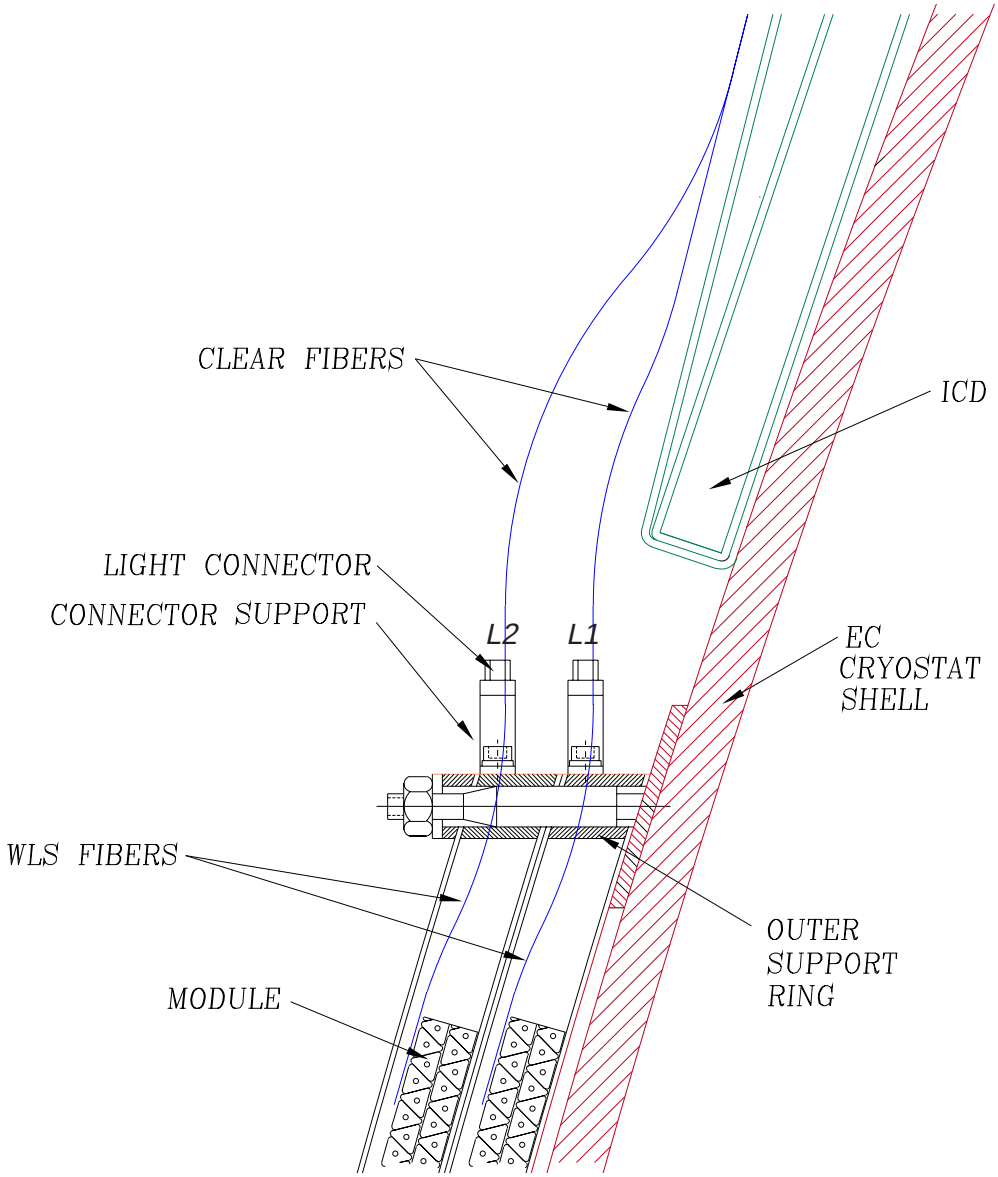

Figure 7.25: r–z view of FPS connectors at the outer periphery of Layers 1 and 2. An angular pitch to these connectors is made for waveguides to clear the existing ICD tiles at this radius.

	Large Module	Small Module	"Special" Module
Sections (regions)	9 (u) + 9 (v)	7 (u) + 7 (v)	5 (u) + 5 (v)
Strips per section	16 (section 1-9)	16 (section 1-6) 7 (section 7)	16 (section 2-4) 8 (section 1) 15 (section 5)
Optical connectors	9 (u) + 9 (v)	7 (u) + 7 (v)	4 (u) + 4 (v) + 1 (u+v: Sect. 1)
Channels (u-layer)	144	103	71
Channels (v-layer)	144	103	71

Table 7.3: Number of sections, optical connectors and channels corresponding to the three different FPS module species.

both exits of the scintillator strip by a small ($\simeq$ 0.9 mm-diameter) O-ring. The ring proves to firmly hold the fibers in-place and eliminates the need for glue (which can be very messy) as well as offers the advantage of being reversible: any mistake made during cabling can be readily undone and the proper connections easily re-established.

The WLS fibers are initially delivered from the manufacturer [32] in 3 m-long canes. They are pre-cut to lengths of 1.0 (1.5) m for the small (large) modules, and both ends are ice-polished and aluminized (by vapor deposition) at Fermilab's Lab 7 facility. Prior to insertion into the optical connector, the fibers are again cut in half (50 and 75 cm lengths), and the aluminized-ends are protected with a small dab of glue.

The trapezoidal geometry of the FPS modules dictates that only the two nested scintillator strips in each u (or v) sublayer have exactly the same length. This symmetry allows determining only the lengths in one sublayer, and use the same for the other. The length of the associated WLS fiber depends on a) the length of the strip it is coupled to, b) the strip position, c) the position of the connector, and d) on the detailed routing it is constrained to follow. As

summarized in Table 7.3 (and illustrated in Fig. 7.26), each u and v sublayer in the three different types of modules are subdivided into different sections (or regions), containing 16 consecutive strips[3] that correspond to a specific optical connector. A mock-up, using production modules and frames for each module type (*i.e.,* large, small, special), is done. Here, fibers are routed from strip-to-strip in an optimal (and "natural") configuration, inducing very little stress in densely-packed regions and respecting a minimum $2.0''$ bending radius [95] specified for the WLS fibers. Each strip's fiber lengths — from the face of the polished connector-surface to the aluminized fiber-end — is measured. The fibers in the mid-sections (about regions #3–5 in Fig. 7.26) of a large, small module follow a simple linear approximation in lengths. However, care is taken to measure those lengths at the upper- and lower-edges of a module where deviations from a linear behavior is observed.

Once the lengths are determined, a fiber-to-strip map is made for each connector in the module. The strip-by-strip channel numbers and connectors are labeled for each module type. A prescription outlining the method in assembling fibers into a connector for each module type is given to Fermilab for assembly. This includes: 1) cutting all fibers to the correct length defined in the map, 2) threading fibers one-by-one into: a) LED calibration system's cylindrical barrels (see Sec. 7.3.4 for more details) and b) optical connectors, 3) potting and polishing (via diamond-fly cutting) the connector [96], and 4) quality-control of all assembled fiber-connectors for blemishes and/or fractures. During assembly, one adds an extra $1.0''$ to the prescribed lengths so that fibers can protrude from the surface of the connector-end that is polished. This additional length is required in the assembly method used, and removed as

[3]The geometric η boundary defined for the small (special) modules coupled with the unique routing scheme dictates sections #7 (1,5) to contain only 7 (8, 15) fibered channels.

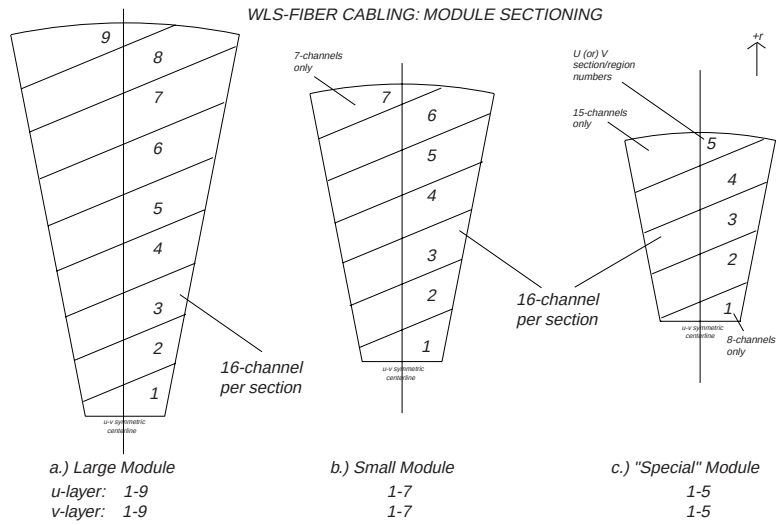

Figure 7.26: Sectioning of a) large, b) small, and c) "special" modules into regions with a given quantum of scintillator strip channels for WLS fiber and connector cabling.

waste, during connector polishing. The final product is shipped to Brookhaven Lab for module assembly.

The cable lengths for the four "special" modules in each FPS detector are determined in exactly the same manner outlined above. However, since the space allotted for fiber routing in their respective support frames (*i.e.*, between the scintillator and connector location) differs from one "special" module to the next, the lengths for each must be measured separately — in both the u- and v-layers. A similar prescription as that developed for regular-sized modules is made and given to Fermilab. Since the "special" modules exhibit a "detector-wise" symmetry from FPS-N to -S such that a strip in the FPS-N-u (v) layer is equivalent to the same strip in the FPS-S-v (u) layer, the cable lengths for the "special" modules are measured on one detector and are used again on the other. This symmetry reduces production times considerably.

7.3.3 Module Cabling

Once the completed fiber-connector assemblies are delivered from Fermilab, individual modules can be cabled. At this point, a fabricated module, aligned in its support frame (see Sec. 7.2.4) with properly secured connector support brackets (see Sec. 7.3.1), is used.

The connectors in a large (small) module are located in two groups of 9 (7) connectors on each side of the module, for a total of 18 (14) connectors per module. A given side allows cabling of the respective u- or v-layer, through the open space between the scintillator edge and frame's border (*i.e.,* side-wall), as shown in Fig. 7.27 for a typical large module. Most fibers cabled in this manner can thus exit a layer's strip at bending angles between 60° and 130° and be taken up to connectors in the same direction as the strip's orientation. The exception, however, is in the 16 fibers emerging near the outer radius of a module at regions 8 and 9 (large module) and 6 and 7 (small module) in Fig. 7.26. The close proximity of these strips to the connectors requires the fibers to exit, with a 290° fiber loop (of radius at about 2–3″) partially over the face of the module, and enter the connector closest to the bisector of the module.

The "special" modules in a layer contain the same number of channels (see Table 7.3) and only require 9 connectors, which are placed uniquely at the frame's outer-rim during cabling. The odd number of connectors forces one to share fibers from both a u- and v-layer. Moreover, the tight space in certain regions of a "special" module's frame dictates greater number of fiber loops than those visible on a large, small modular specie.

Once the routing plan has been defined, the cabling begins by inspecting the delivered assemblies for blemishes, fractures, as well as the quality of each fiber's polished- and silvered-end finish. Any degradations are immediately

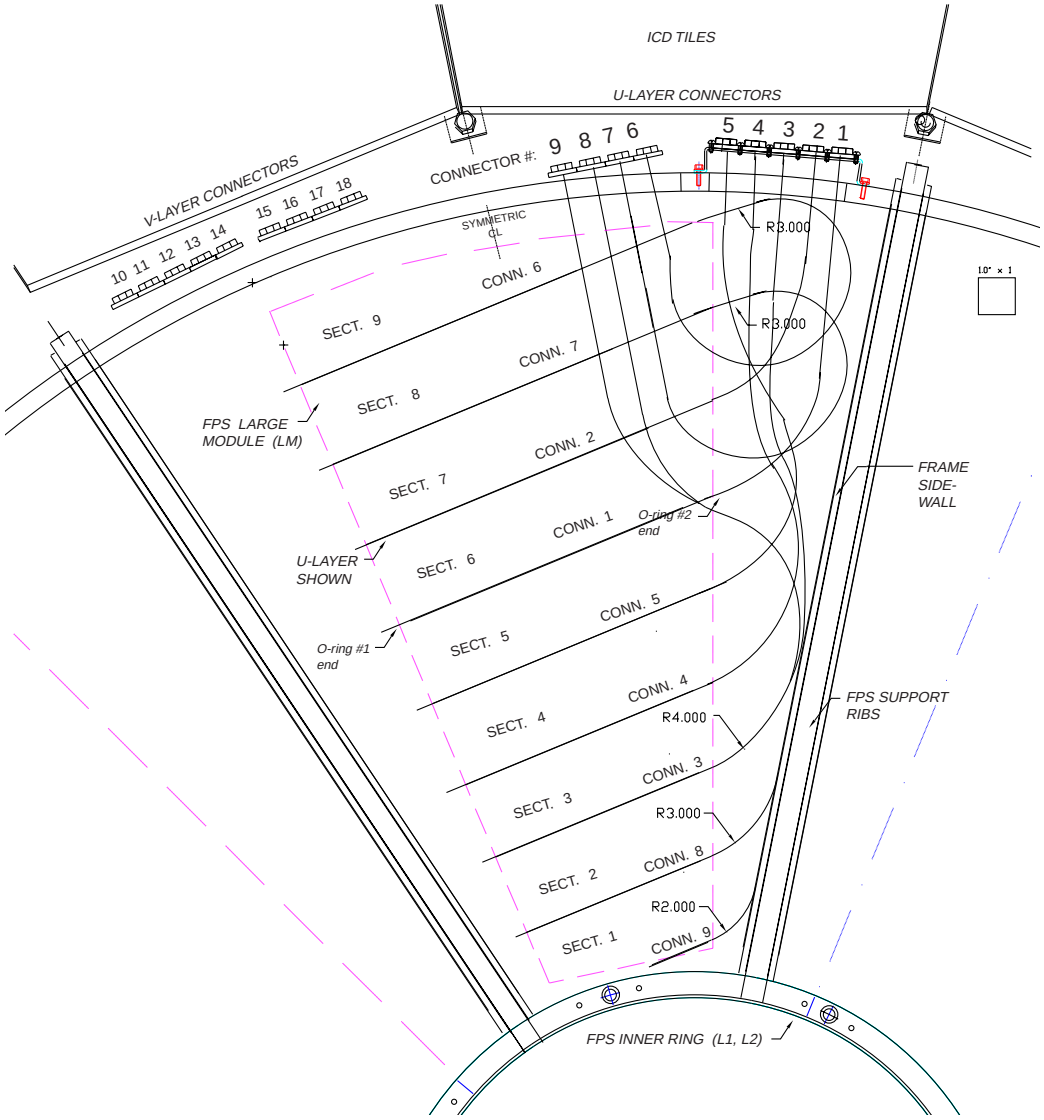

Figure 7.27: An r–ϕ view of a large module in L1 or L2 of the FPS, showing the WLS fiber/scintillation strip layout and connector-by-connector mapped routing. Individually labeled connectors are shown at the top and map to sections of 16 contiguous strips on a module's u- or v-sublayer. Cabling for the u-layer is only shown — the v-layer follows in a mirror-symmetric manner.

noticeable by shining an intense blue LED light on the connector's polished-end in a dark room and visually inspecting the resulting glow radiating from the fiber's outer-cladding. The connectors are thus sorted into two categories: 1) "accepted" for cabling, or 2) "rejected" — which requires recycling the acceptable fibers and re-making the given connector. The first set of O-rings is placed on each fiber and the fiber, one-by-one, is inserted into its defined strip. The process is repeated until all strips (u and v) have been fibered. Next, each connector is anchored to its support bracket. Meanwhile, the silvered-end of the fiber is permitted to protrude an equal 10–12 mm from the strip's edge and is fixed by a second O-ring.

Two additional steps are performed to complete the cabling. The first requires visually re-inspecting the cabled fibers for degradations: blemishes and silver scrapings — both of which can arise during the cabling procedure. Again, an intense blue LED light is used. If necessary, any degraded connector is replaced. Further, a dab of BC-620 [69] reflective paint is placed on any fiber surface showing the absence of its silver-coat. Measurements indicate that the paint can provide at least $\simeq 50\%$ [97] recovery in the light yield with respect to a complete silver finish. Finally, all fibers are checked for a correct map to their strips [98]. To do so, a 16-channel 1.0 m-long clear fiber bundle coupled 1:1 to an LED pulsing system is used. The LEDs are computer-controlled and programmed to successively step according to the correct channel ordering, thereby illuminating, one-by-one, a consecutive fiber-strips. A distinct pattern is observed in the strip-to-strip mapping. Any discrepancies are immediately noticed and corrected.

7.3.4 LED Monitoring and Calibration Systems

The FPS monitoring/calibration system serves to certify the proper connectivity and dead-alive operation of the detector channels. It further allows to monitor the response of individual channels over intermittent periods, providing a stability measurement in response over time. The system is composed of surface-mounted blue LED pulsers (Type: Nichia NSCB-100, λ_{max}=470 nm [99]) injecting light of a relatively calibrated amount into 0.835 mm-diameter clear fibers. The light gets centrally transmitted through the clear fiber onto a group of sixteen WLS fibers, uniformly embedded within a hollow, cylindrical barrel-cavity, which is installed on the fiber-connector assemblies made at Fermilab (see Fig. 7.28a). Each cavity holds the same group of WLS fibers that are mapped from their respective strips to optical connectors. The entire LED array is driven by pulsers located below the DØ detector, on the readout platform. A light uniformity to within 10% from connector-to-connector in a given module is possible with such a design [100].

Once modules have been WLS fiber cabled, two pc-boards[4], each supporting the 9 (7) surface-mount LEDs (and relevant electrical circuitry) for a large (small) module — *i.e.,* one board for each u or v layer connector — are mounted on slots machined at the center of a module's outer support frame's arc. Clear fibers are one-by-one inserted through 0.850 mm-diameter holes drilled into a machined black-ABS rectangular ($1.0'' \times 0.75'' \times 0.25''$) optical block, coupling the fibers to each LED (see Fig. 7.28b). The other end of a fiber is inserted into the central hole of the black cylindrical cavity. The output from the LED to each FPS optical connector is iteratively measured, and the distance, d (see Fig. 7.28(b)), between the clear fiber and LED is tuned *in*

[4]Since only nine connectors occupy a "special" module, one pc-board with nine mounted LEDs are needed for this particular module.

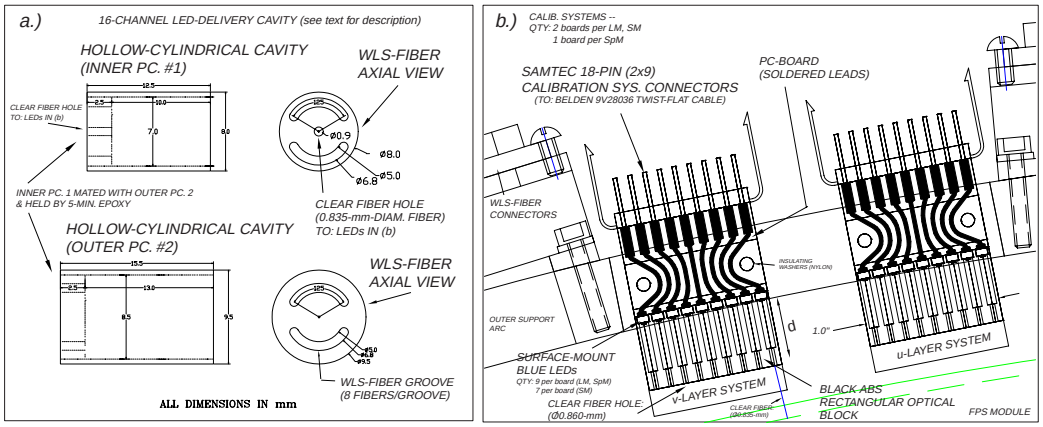

Figure 7.28: LED calibration and monitoring system. Shown are: a) a hollow-cylindrical cavity grouping sixteen WLS fibers and b) the surface-mounted LED pulser boards supplying the signal. Cavity 1 and 2 in (a) are mated and aligned together, being fixed with five-minute epoxy between their outer and inner cylindrical walls, respectively.

situ until the required amount of light is delivered into each cylindrical cavity. Once the 10% uniformity has been achieved, the clear fiber is five-minute epoxied to the ABS rectangular block. A second measurement is made on all LEDs, and the data stored for reference.

7.3.5 Module Certification and Integration

The above procedures — WLS fiber cabling, quality inspections, LED system installation, must all be performed sequentially. Once these steps have been completed, protective covers are cut to the geometric shape of the module. The covers are fixed to the borders of the module frame (*i.e.,* bottom-wedge, side-wall, frame's outer arc) with a series of #2-56 $\times$ 1/4$''$ long pan head screws. The covers are a means to hold the fibers within the space alloted to them and help prevent any potential damage during future handling. The thickness of the cover must comply with the nominal 2.0 mm gap existing between the module and the support rib directly (in $\pm z$) above or below it.

Therefore, two Plexiglas strips ($1/16''$ thick) are used on the bottom surface ($+z$) of a module, radially extending along each side-wall and overlapping $\simeq 1/2''$ with from the edge of a module (in ϕ). The top surface ($-z$) is covered with a similar (but smaller) Plexiglas strip ($1.0''$ wide $\times$ $1/16''$ thick) at edges of a side-wall. However, since many fibers (WLS and clear) are routed in local regions over the module's surface, the entire frame is covered with a $1/32''$ thick mylar, sandwiched between the module and Plexiglas strip. Additional aluminum ($1/16''$ thick) covers, bent to conform to the connector brackets (see Fig. 7.6), are placed to protect fibers entering the rear-end of the fragile fiber-to-connector joint.

Once all these details have been addressed (and properly documented), the protected, cabled module is inserted into the reference "jig," described in Sec. 7.2.4, to verify the structural alignment of the module-frame has not been compromised during handling. The module is then stored in strain-relieved storage/shipping containers until all modules for the FPS have been assembled. Likewise, it can also be mounted within its respective, aligned FPS support structure slot, and thus, one begins the installation phase of the detector.

Chapter 8

Installation and Alignment

A major aspect of the construction of the FPS involves staging the assembly of both north and south detectors as one complete unit prior to their installation at DØ. This includes the insertion of a cabled, certified module into its respective support frame slot, the nesting of one layer with the next, and the alignment of the detector to nominal design specifications. Once this is addressed, the modularity of the FPS allows dismantling the complete unit, properly packaging each component for transport to Fermilab, and again, reassembling the detector; this time: directly on the DØ end calorimeter-cryostat walls.

The alignment of the detector is a critical part of the FPS installation. The limited space within the EC-CC intercryostat gap requires the FPS to mount compactly and prevent any type of interference with other subsystems, cables, and services present in the region. Further, both the ICD and Level 0-Luminosity Monitor must anchor to the FPS detector at the outer and inner radius, respectively. This demands positioning the FPS as close to the nominal specifications as possible so that the alignment of any forward end-detector, in addition to the spatial constraints, does not get compromised in any way.

The installation of the FPS at DØ can be divided into two main categories:

1) welding of mounting hardware such as support pins and brackets onto the cryostat walls at the inner and outer radius of the FPS, respectively, for detector attachment, and 2) installation of the representative detector components, which include support structure elements, lead and corresponding supports, and modules. Such a division allows defining the location and alignment of the detector on the cryostat independent of making use of cabled modules that can potentially be damaged during any welding and/or *in situ* adjustments. The following sections discuss each category.

8.1 Installation and Alignment I: FPS Support Hardware

The FPS is held on the cryostat by mounting support hardware that are spot-welded at the inner and outer radii of the detector. These two points of support carry the main load of the FPS. It should be noted that, in general, the heads of each EC deviate from the nominal sphericity by some amount. This deviation can result in head distortions that are as large as about $1/2''$ (12.7 mm) — a non-negligible number, given a $0.0394''$ (1 mm) alignment accuracy that is desired in mounting each module. Although a few regions of the head can be measured, it is unrealistic to assume that the shape of the entire area to which the detector mounts is understood to any great detail prior to installation. The process of developing a full (1:1) contour map by surveying each head with the goal of obtaining local regions of spherical distortions has also been suggested. The results, however, can take many months to understand and, in the end, are usually not wholly unambiguous. Therefore, an installation procedure is used that presumes that the details of the shape of the heads are unknown, implying that the detector be installed on the

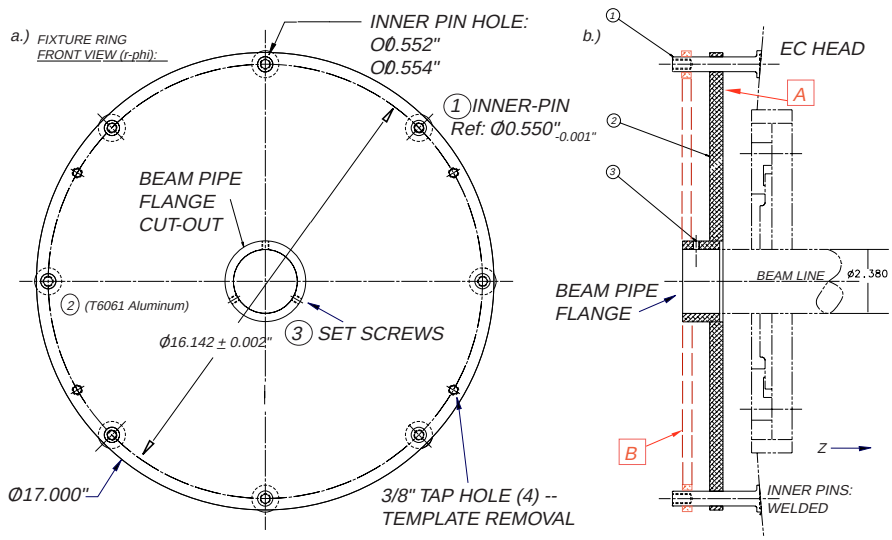

Figure 8.1: a) r–ϕ view of template used to align and weld eight stainless-steel inner pins for FPS support on EC heads and b) r–z view of assembly. Also shown is an inner ring (B) mounted in z with the template (A) to guarantee each pin is parallel to one another.

cryostat in a manner independent of the actual spherical geometry. Such a scheme requires an offset, by at most $1/8''$, to the FPS from the head onto which it mounts, and when necessary, the addition of appropriately sized shims to account for any local spherical deviations.

A precision installation template is machined to define the position of the inner support pins (*i.e.,* also called a "studs") on the cryostat. The template, as shown in Fig. 8.1, is a solid aluminum plate and contains the same fixation holes as those on the inner rings of the detector. It is used as a guide to weld the pins on the EC head. Each half of the FPS is mounted so that the detector is centered with respect to the beam line, which serves as the reference coordinate system for the alignment within DØ.

First, the eight machined stainless-steel[1] inner support pins (shown in

[1]Stock: 304SS is used throughout — thereby consistent with the type of steel comprising the DØ cryostat wall to enable a welded-contact.

Fig. 8.2, analogous to the "model" pins of Fig. 7.8), each $0.550^{+0.000''}_{-0.002''}$ in diameter are inserted into the circular arrayed holes of the template. The nominal length of each pin is $3.350''$ and thus designed to extend roughly an extra $1/8''$ from the measured z-thickness of all five nested layers of the FPS: $3.230''$. The head of the inner pin that touches the surface of the cryostat has been made with a circular cross-section to allow the full area of the pin to touch the cryostat head. A flat-beveled cross-section would only make a two-point contact with the wall's spherical surface, resulting in a structurally weak support. The thickness of this head (in z) further ensures the required $1/8''$ detector offset. The eight mating holes on the template for the pins have also been made to very tight tolerances, $0.552^{+0.002''}_{-0.001''}$, in order to achieve a snug-fit. One notes that such a pin-template assembly, when taken as a complete unit, will systematically shift all pins in a given direction and still allow the inner rings to be welded properly. Nonetheless, every step is taken to verify the full array is in its correct orientation.

The template and pin fixture is placed on the cryostat head over the existing $2.380''$ diameter beam pipe flange. With the help of four precision-mounted $1/4''$ survey balls (see also Sec. 8.1.1) fixed at a $10.000 \pm 0.005''$ radius from the template's center, the assembly is centered over the flange and clamped into place via three set screws. The ϕ-position of each pin, and hence, a ring is established — again, by survey — with the four balls.

Once the location of the pins has been determined, 2 to 3 inner rings are inserted over the plate assembly. This ensures that the pins will be aligned parallel to one another and the beam line. Next, the pins are tack-welded at local spots to initially adhere to the cryostat surface. One-by-one, the inner rings are removed and additional spots about the circular head of the pin (in ϕ) are welded. It is observed that the welding can create small perturbations to the parallel alignment of one pin relative to the next. Therefore, prior to

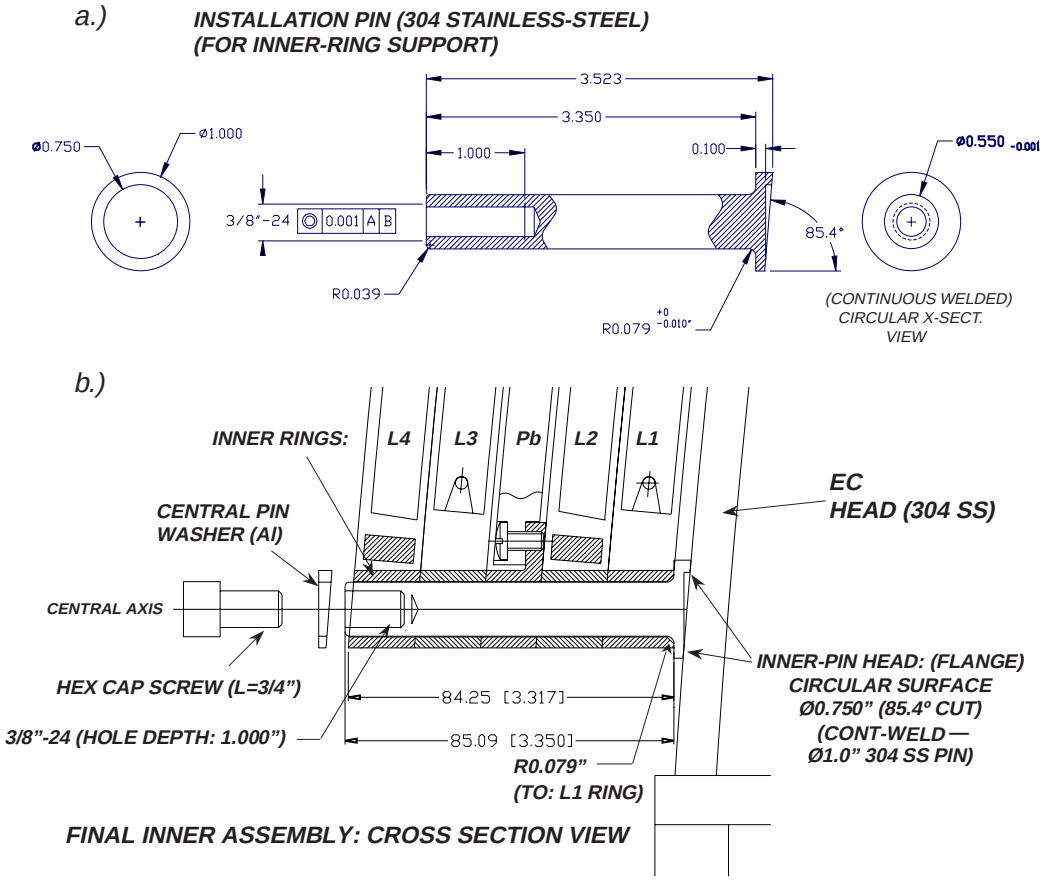

Figure 8.2: a) Stainless-steel FPS inner-support pin with dimensions and b) cross-sectional view of nested FPS layers and inner pin assembly. Eight such pins are aligned and welded on each cryostat head to support the detector.

achieving a continuous weld, the pins are re-surveyed after each spot-weld, and if deviations are noticed, a weld is applied at a point roughly 180° opposite of the initial one to force a pin back in place. The process iteratively continues, and the template is gradually displaced away in z from the cryostat until a continuous weld is made.

Next, FPS mounting brackets can be positioned and tack-welded at the detector's outer perimeter. Although the inner pins carry the main load of the detector, the outer brackets provide an additional point for support. The brackets are shown in Fig. 8.3 and consists of three elements for FPS and one element for the fixation of an ICD tile (see Sec. 8.3). The actual quantities needed of each element for installation on each of the two cryostats is given in Table 8.1. Here, a slotted-hole machined on a bracket (spacer) allows attachment through the ϕ-thickness of a L1 (L2) support rib by means of a #10-24 threaded-hole drilled into the rib. The slotted-hole permits *in situ* adjustments of the rib, in $\pm z$, during assembly with the matching hole centered on each rib so that symmetric adjustments in/away from the cryostat head can be made, parallel to the beam line. The sides of a bracket contains wings, which serve as the surface for the weld. Further, the use of a spacer for L2 allows modules that may potentially be damaged in L1 to be easily replaced. This requires translating the entire layer out in z and thereby letting the module clear the presence of any support hardware. Since a welded-joint might create complications for removing and re-welding a bracket after repair, the mounting hardware for L2 is designed with two pieces, offering a greater flexibility in requiring only the removal and re-attachment of a bolt on a L2 spacer with the bracket. It should also be noted that the symmetry of 8 equivalent modules with 8 equivalent support ribs is broken for L2 at the ϕ where the FPS must clear the magnet services. Since a radially shorter support rib must be used for a L2 module, the rib at this location cannot couple to any bracket welded

to the EC. Instead, it must attach directly to the lead layer's outer-support ring.

The FPS detector's skeleton support frame registers the mounting points of all outer brackets. In order to weld, the radial position is first determined by mounting the inner ring and rib structure for the given layer. However, since the rib is still free to move about ϕ at the location of a bracket (from its nominal position by approximately ± 1–2°), a means for locking a rib at a second point, namely at an outer radius from the inner ring, must be established. As shown in Fig. 8.4, the lead layer's outer ring provides a convenient template. The ring is a rigid element that has been precision-machined with a CNC and contains holes to allow attachment onto a L2 rib. These holes guarantee a correct ϕ can be established in order to insert modules and remove them from a layer. Since the location of these holes are transferred onto a L2 rib during construction, similar ones can be transferred onto L1, and thereby, "temporarily" use the outer ring for fixing the ribs in L1 as well. This approach offers the advantage of determining the ϕ for welding without making use of cabled modules. Here, the use of modules can damage delicate fiber connections and also cover the bracket, creating difficulties in welding.

From the above discussion, any outer bracket is welded by mounting the inner ring for L1 (L2) with the bracket (spacer) attached to the rib. For each layer, the lead's outer ring anchored to the skeleton frame locates the brackets for L1 (L2), and hence, establishes the r–ϕ coordinates of the detector. Since the load from the FPS is largely concentrated radially inward, toward the center of the FPS, a tack-weld at the corners of a bracket is sufficient. Moreover, the slots in a bracket (or spacer) allow final adjustments in z. However, this is done in the next phase of installation: the insertion of modules (see Sec. 8.2).

The installation and alignment of the inner and outer mounting hardware is completed by the following:

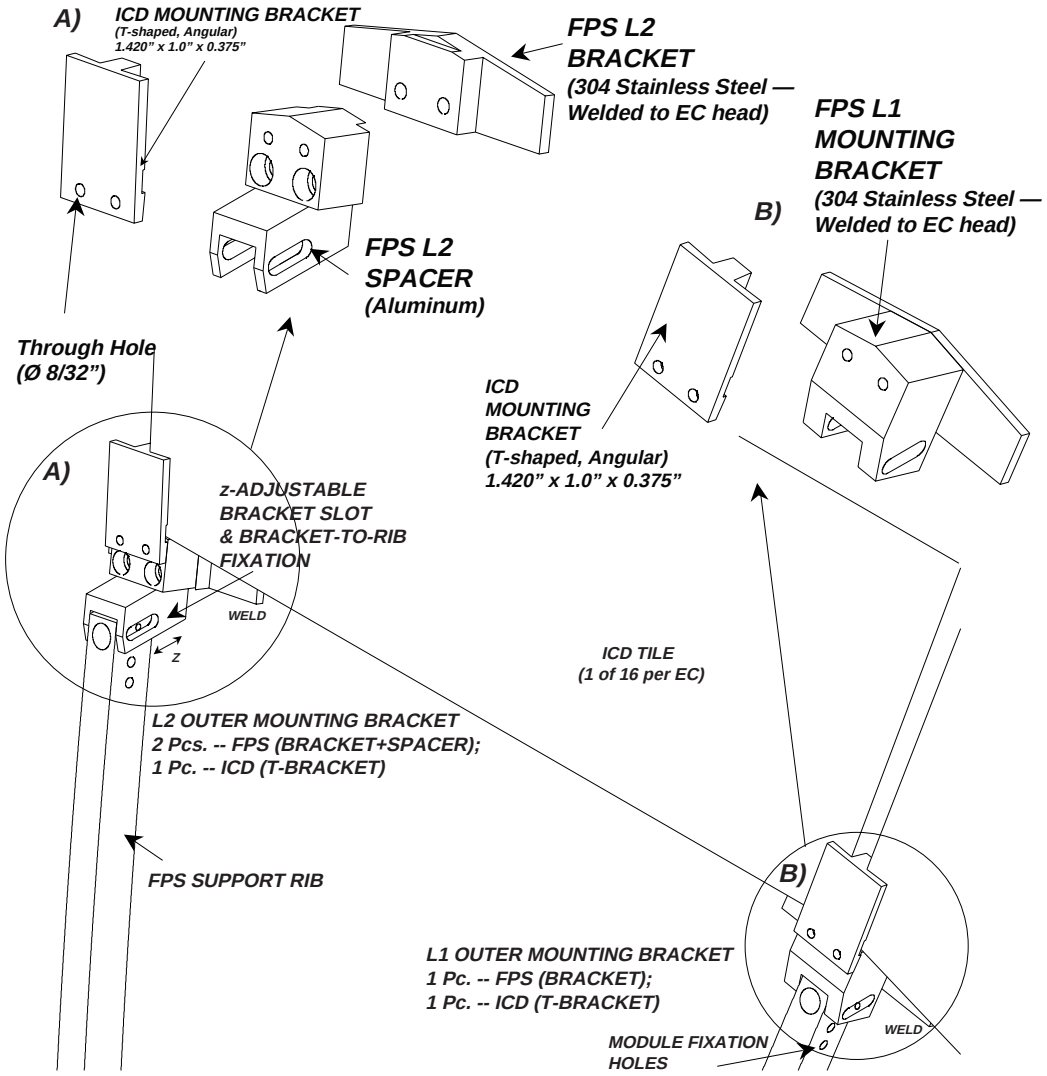

Figure 8.3: Welded stainless-steel brackets supporting the FPS support rib and detector structure at its outer radial periphery on the EC head. Shown are a) FPS L2's (two-piece) bracket and spacer as well as b) L1's (one-piece) bracket. At both L1 and L2, an equivalent T-shaped aluminum bracket (a) and (b) allows for a coupled ICD and FPS support.

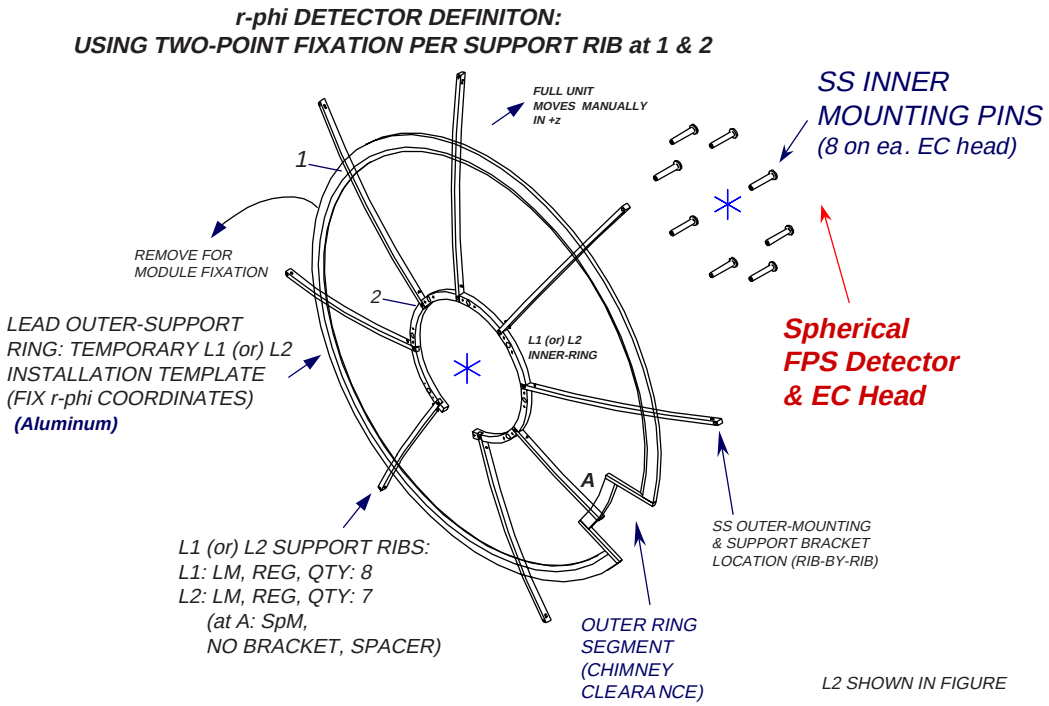

Figure 8.4: Lead layer's precision outer support-ring provides a convenient technique to establish the detector's r–ϕ coordinates on the cryostat head, prior to welding and module insertion.

	Quantity (per detector)	Material	Attachment
L1 bracket	8	304 stainless-steel	Tack-welded to EC
L2 bracket	7	304 stainless-steel	Tack-welded to EC
L2 spacer	7	60-61 aluminum	Bolted to L2 brackets
ICD bracket	15	60-61 aluminum	Bolted to FPS brackets

Table 8.1: Outer Mounting Hardware for FPS and ICD: the quantity, material and method of attachment for installation are provided.

1. Survey the position of the inner pin on the EC using the installation template and FPS inner rings.
2. Tack-weld the pins by iteratively displacing the rings and template away from the cryostat head (in z) until a continuous weld is achieved.
3. Mount L1 FPS inner ring with proper support ribs on the welded inner pins.
4. Temporarily use the lead layer's outer support ring as a template for registering the L1 ribs in ϕ.
5. Connect the stainless-steel outer support brackets to each L1 rib. If deviations from non-sphericity are observed on the cryostat wall, place shims of appropriate thickness until the bracket touches the cryostat head.
6. Tack-weld a L1 bracket. Note that a rib will still float in $\pm z$ — at the slotted-hole machined in the bracket — permitting future adjustments in z.
7. Remove the lead layer's outer ring from L1.
8. Repeat steps 3–7 for the FPS L2 brackets and spacers.

8.1.1 Inner Pin Surveying

The general method for determining the correct location of the FPS inner pin array on the north and south cryostat requires iterative survey of the fixture template that accommodates the pins. Such a survey is done by a "Laser Tracking System". Here, an integrated laser, interferometer, and motion-sensitive tracking unit provide highly accurate linear displacement and

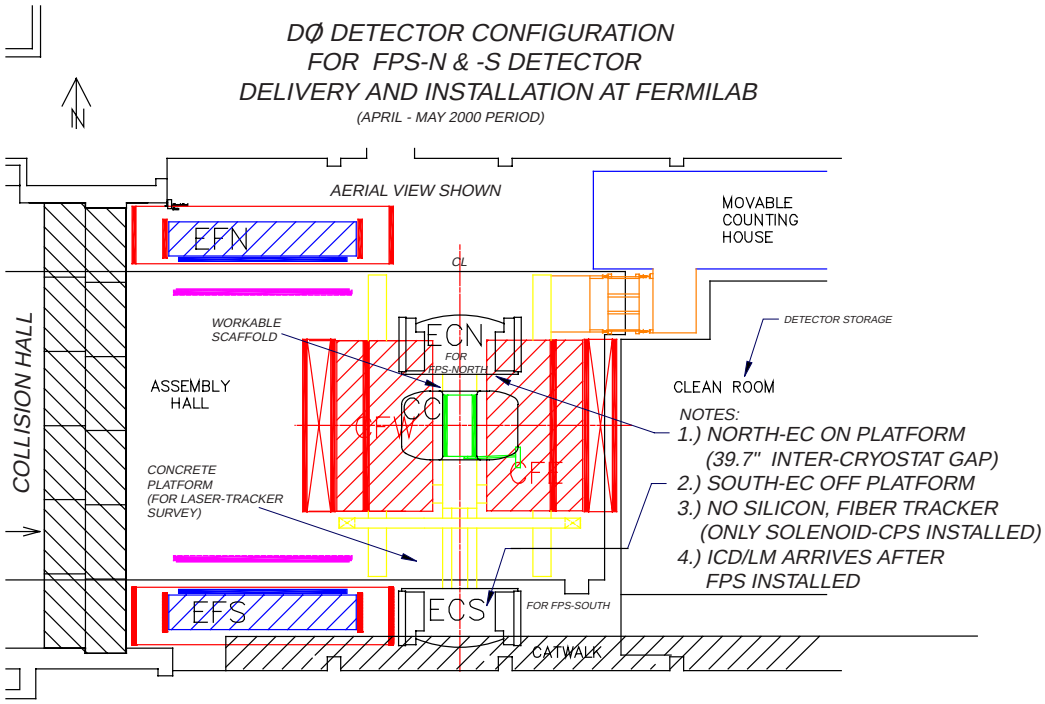

Figure 8.5: Configuration of the DØ Detector during the FPS installation period at Fermilab. See notes in figure and text for a description of the scenario available for preshower assembly and installation.

angular position measurements relative to a pre-determined reference point. The method has proven to be quite stable and reliable for aligning large sub-detectors at DØ, measuring coordinates to well within ± 0.1 mm. Further, the collection of data from each survey can be downloaded on the system's laptop computer, allowing results to be available *in situ* of detector installation, and thereby, correcting any observed discrepancy instantaneously.

During the FPS installation period (*i.e.,* April-May 2000), each EC at DØ is in its "opened" position some workable distance away from the CC. In this scenario, as shown in Fig. 8.5, the south-EC is located off the detector platform, roughly 10–12 ft. in z away from its running configuration. The north-EC, on the other hand, remains on the platform but maintains a $39.7''$

nominal gap with the CC wall. In order to mount a laser tracking system with a reliable field-of-view, one needs at least 4 ft. [101] of rigid, stable platform space. This amount is more than adequate for the south-FPS, as the equipment can be mounted on the existing concrete surface of the south platform, directly in-front of the detector. However, since the space to survey FPS-north is limited, the same equipment must remain on the south platform, and the north detector must be shot through the 2.73 m-long solenoid magnet opening [102]. The approach is only possible by the fact that the silicon (SMT) and fiber tracking (CFT) subsystems, which occupy the volume within the magnet, are to be installed after the FPS installation and alignment have been completed. Moreover, the solenoid's inner-diameter of 1.06 m is well within the visual range needed to measure survey targets located on the FPS inner pin's template.

The laser tracker system surveys the coordinates for each pin (and thus, the FPS detector) relative to the beam line. Here, the pins must be referenced to the DØ global reference frame, picked up by survey targets located on calorimeter feet and walls, and thus, at points where the position with the beam line is *a priori* known. In particular, for FPS-south, the laser system picks up the existing survey balls located directly below the platform, on the feet of the south EC, and builds a global network of additional "temporary" targets above the platform and on the south-EC head. This type of interpolation, from one target linked to the next, establishes the position of the entire south cryostat wall with the beam line. For FPS-north, survey balls existing on the face of the south-CC wall are used to link, through the solenoid, the north-pins with the beam line. Once the position of each survey ball on the FPS template is known with respect to the collection of these targets, the r–ϕ orientation of the pins is measured, and the targets are removed.

Although every step is taken to align the pins to their nominal position,

Detector	ϕ-clocking $\Delta\phi$ (mrad)	*wrt beam line at (x,y)=(0,0)*	
		Δx (mm)	Δy (mm)
FPS-South	1 mrad (cw)	+4 ($\pm$0.1)	-3 ($\pm$0.1)
FPS-North	$<$ 1 mrad (cw)	+4 ($\pm$0.1)	-2 ($\pm$0.1)

Table 8.2: Final inner pin deviations for each FPS detector from nominal specifications. The average of all eight pins per cryostat head is determined. Note: cw = clockwise ϕ-rotation and ccw = counterclockwise ϕ-rotation taken from the interaction point.

the welding can introduce certain deviations, which can be measured and corrected for through survey. Any information retrieved is entered into an alignment database and used offline during future data analysis with the DØ detector. Typical measurements include the average deviation of all eight pins on a cryostat with the DØ coordinate system (see Sec. 3.1), whose origin is defined with respect to the beam line: (x,y)=(0,0). The results for each FPS detector are given in Table 8.2. One will note that the deviations are small and well within alignment goals, and thus, no further adjustments to the pins are made.

8.2 Installation and Alignment II: FPS Detector

Once the inner and outer support hardware have been installed, detector assembly on the EC can begin. The modularity of the FPS makes the entire process straightforward. One must note, however, that the key layers for the installation are the FPS lead layer and Layers 2 and 1. Here, L2 registers the position of the lead layer's outer ring in conjunction with the lead layer. The lead layer, in turn, registers the final position of FPS Layers 3 and 4, which is

not adjusted during installation, and instead, defined by the manner to which each layer is held at the inner and outer radius. This alignment has been designed (and understood prior to the delivery of the FPS to Fermilab) within the lead layer's outer ring, and since last-minute adjustments are difficult to make within the DØ assembly hall, provisions are taken to mount and align L2 and the outer ring correctly. Moreover, L2 carries the primary load of the lead layer, which by itself makes up about 50% of the weight of an entire FPS detector. Since L1 sits downstream of L2, some fraction of the weight from the lead will transfer onto L1. Therefore, considerable care is needed to mount and anchor this layer as well.

The installation can proceed directly after all support structure elements that were used during the welding of the inner pin and outer support bracket array have been removed. Next, the first layer's (L1) inner ring is re-mounted. As described in the previous chapter, the ribs in each layer are made to fit uniquely at a given ϕ-position of an inner ring. These ribs have been labeled prior to installation and are now anchored to the L1 ring using #1/4-20 $\times$ 3/8″ screws. Only those screws with their heads machined to lie at or below the upper ($-z$) surface of the ring (and thus avoid L1-L2 nesting gaps) are used. Subsequently, the schematic given in Fig. 7.12 (see Chap. 7) is followed to insert the correct modules comprising L1 (see Table 7.1). Here, the module is: 1) directed radially downward until the 'v-notch' located on the module's frame nests within the pair of dowel pins located on a rib's ϕ-edge, and 2) pitched towards the EC until the side-wall aligns and anchors (use #10-24 socket-head screws) with a rib at the outer radius. These two steps are repeated until all eight modules in the layer have been installed. This defines a "natural" position of the modules in the layer, enabling each to rest without imposing any stress to the support structure. However, the ribs can still move in $\pm z$ within the slotted-hole of a support bracket. Although this degree-of-freedom

was needed to insert modules and to make last-minute adjustments in the alignment, it must now be fixed. A long (6 ft.), rigid stainless-steel leveling-bar is manually rotated, rib-to-rib, until each rib has been adjusted in z to a nominal value established during detector design and construction. Once adjusted, the rib is locked into place at the outer bracket. The entire layer is then surveyed (see Sec. 8.2.1).

After surveying L1, L2 can be installed following procedures similar to those for L1. Each rib is fixed to the welded outer bracket using the mating aluminum spacer listed in Table 8.1. Also, directly after the layer's position in $\pm z$ has been aligned with the leveling-bar, the lead layer's inner and outer rings are mounted. This is done prior to survey of L2, simply as a precautionary measure, to avoid perturbing the alignment of L2 when the rings are being physically installed. By design, both rings are located at a radius that still enables survey targets on a L2 module to be measured.

As described in Sec. 7.2.5, each half of the FPS accommodates a total of 48 bonded lead-stainless-steel (*i.e.,* Pb-SS-Pb sandwich) aborber pieces, tightly arranged in ϕ between the layer's inner- and outer-support rings. During production, each piece has been labeled with FPS-S and FPS-N to correspond with the detector on which it mounts as well as a number: 1–45 (46–48) to refer to a regular-sized ("special" — shorter radii — needed to clear the ϕ-opening of the magnet services) element. As indicated by Fig. 7.20 (see Chap. 7), each piece is bolted to the rings using four #10-24 $\times$ 1/4″ long phillips-head screws: two per outer and inner radius of the SS plate. Arranging approximately 46–47 pieces about the rings can create complications in mounting the 48th piece in its location, and therefore, the installation first requires the insertion of elements 1 through 45 and finally, the "special" absorber units. This technique is used so that any necessary retrofitting can be made to smaller elements, and thereby, prevent blemishes or stress fractures on regular-sized absorbers.

The final two layers (L3, L4) are assembled once the lead layer has been installed. Again, each of these layer's inner rings are mounted with their respective support ribs. For L3 and L4, the outer perimeter of the ribs is bolted directly into the lead layer's outer ring and no adjustments using the leveling-bar, as was the case for L1 and L2, is done. However, in order to establish the z for each layer, a $0.035''$ thick washer (machined $3/4''$ long aluminum stand-off) is placed at each rib in L3 (L4) at the fixation holes drilled into the lead layer's outer ring. A #10-24 $\times$ $1''$ long slotted-head screw is used. Subsequently, a MIP module is inserted, one-by-one, and each layer is surveyed. Finally, once the full unit (L1, L2, Pb-layer, L3, L4) has been mounted, eight $3/4''$ long hex-cap screws are bolted at the inner rings to complete the installation of one FPS detector at DØ; the entire process is repeated for the other half.

For completeness, these procedures are summarized below.

1. Mount L1 inner ring and support ribs and insert L1 modules.

2. Use a rigid vertical leveling-bar to adjust and align (in z) L1, rib-by-rib, to prescribed design value. Fix each L1 rib at the slotted-hole in its outer support bracket.

3. Survey the position of L1 modules (see Sec. 8.2.1).

4. Repeat 1–2 for L2 using the L2 outer support bracket with its mating aluminum spacer.

5. Mount the lead layer's inner-support ring and anchor the outer-support ring to a L2 rib.

6. Survey position of L2 modules (see Sec. 8.2.1).

7. Install Pb-SS-Pb pieces (#1–48), one-by-one, at appropriate ϕ-slots, in-between the layer's inner- and outer-support rings.

8. Mount the L3 inner ring and ribs. Fix each rib to the lead layer's outer ring using 0.035″ thick separation washers.

9. Insert and fix all L3 modules.

10. Survey position of L3 modules (see Sec. 8.2.1).

11. Repeat 8–9 for L4 using 3/4″ long aluminum stand-offs to fix and establish the z-coordinate of L4.

12. Bolt the entire FPS assembly at the inner pin using eight 3/4″ long hex-cap screws.

13. Survey L4 modules (see Sec. 8.2.1).

8.2.1 Module Survey

As a benchmark, the extent to which the spatial position of each module must be determined is on the order of the expected resolution of electromagnetic showers, or 1 mm. The position is found from survey measurements taken directly after each layer has been assembled on the EC head.

Survey Targets

During construction, two types of survey targets are placed on the uppermost (u)-layer of a module: 1) six optical K&E and 2) four retro-reflective coated V-star System targets (see Fig. 8.6). The targets are placed in such a manner that at least three lie non-colinearly and thus permit the x,y, and z spatial coordinates of a module to be measured. Extra targets of a given type are present merely for redundancy. Historically, the K&E targets have been mounted during the module fabrication process, directly on the module's

spherical template assembly dome by the use of a computer-controlled high-resolution CMM. The installation at such a stage allowed the central "dot" existing on the K&E to be centered radially with respect to the fiducial beam line as well as ensured the targets from module-to-module were placed in a repeatable fashion — to within $0.002''$. Moreover, each K&E was covered with the laminated layer of fiberglass used during the u-v mating step, being permanently embedded within the module. The full process ensured that any particular scintillator strip with respect to a K&E would be known and the same for every module. In fact, such targets have been the conventional way to measure the position of large detector objects; capable of being surveyed to within 0.2–0.5 mm (0.010–$0.020''$) accuracy [101], and thus, well within the desired goal. However, the $39.7''$ working space, in addition to the absence of any stable platform within the EC-CC intercryostat gap (on the north-end), creates difficulties in mounting any optical survey equipment capable of reading and extracting data from a K&E target. Therefore, an alternate solution is adapted, which use V-star targets. Such targets only require a digital hand-held CCD camera, allowing the data to be downloaded to a portable laptop and be done *in situ* of detector installation. This reduces the survey time considerably while achieving the same level of accuracy as the K&E.

Although V-star is highly desirable, the need to implement such an approach has been determined after detector completion. The lateness has forced the V-star to be "manually" installed on individual modules, and thus can only be placed "visually" from module-to-module. However, since the precise location of a K&E target is *a priori* known for every module, the (x,y) position of the $1/4''$ diameter circle existing on each of the four V-star targets can be measured with respect to an arbitrarily chosen K&E target. The position for the chosen K&E is, in turn, conveniently defined at (0, 0) — *i.e.,* see target #1, Fig. 8.6. Subsequently, a one-to-one map of the four V-stars relative to

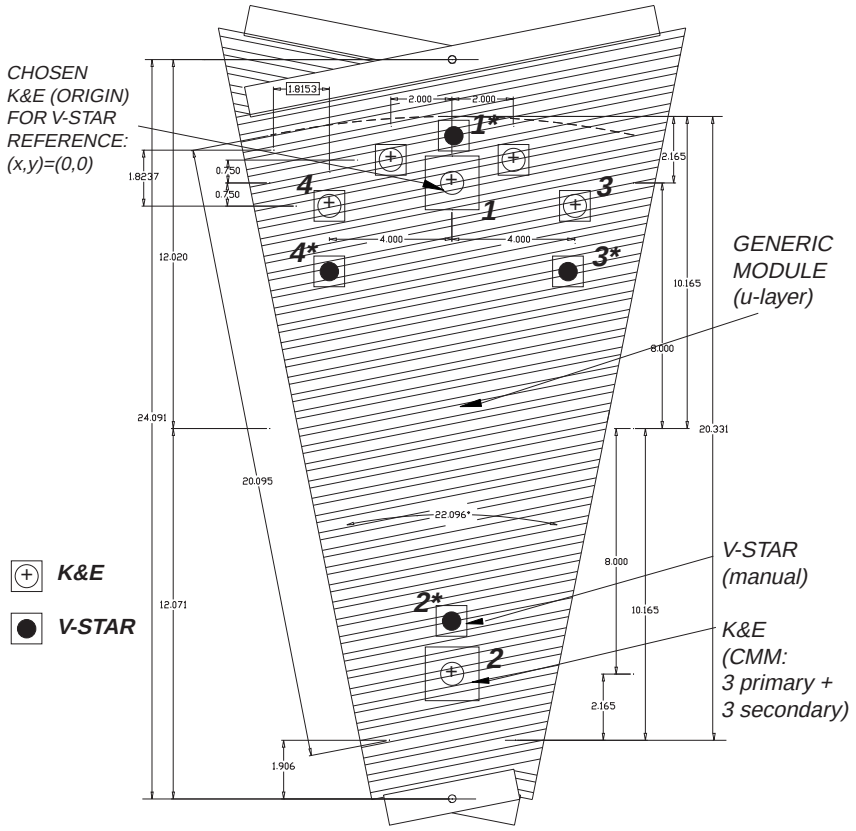

Figure 8.6: Generic FPS module illustrating the six (1-6) CMM installed K&E targets and four (1*–4*) manually placed V-star targets. K&E target #1 defines the origin and reference to which all other V-star mapping positions are made.

this K&E is measured using a CMM (to within 0.005″) for every module, prior to FPS installation. The method yields results unique for each module with the collection of data entered into a "look-up table" in terms of module and frame number. The random placement of all V-stars dictates the position of the detector (*i.e.,* the strip position) to be determined solely through the K&E targets. Therefore, after a V-star survey, the location of each K&E must be extrapolated from the information contained in the table.

Survey Measurements

Once modules are inserted and anchored into their support frame, the survey becomes straightforward. Since the FPS is installed by layers, the measurements naturally proceed "layer-wise". A total of four V-star targets exist per module, and thus, a total of 128 (x, y, z) coordinate data points are collected per detector.

Similar to the procedures implemented to install and align the support pins (see Sec. 8.1.1), the location of the detector, and hence, a V-star target must be referenced within the DØ global reference frame. This requires the creation of a global network of reference (V-star) markers on the face of the EC, with each marker linked from one to the next and eventually translating back to the nominal location of the beam line. Again, an intial reference point, one that is well-known with respect to the beam line, is needed. Here, for FPS-South, the east- and west-feet of the south end calorimeter are used; for FPS-North, the 1/4″ survey balls welded about ϕ, on the inside radial edge of south central calorimeter, are taken. Subsequently, the Laser Tracking System develops the network by temporarily mounting a series of rectangular (V-star) survey plates on the face of the EC. Several markers, incrementally increasing in radius outside the FPS fiducial volume, are placed in order to be visible when each FPS layer is measured. Such a complex network allows the collection of data by referencing any V-star on an FPS module simply with those on the EC.

The "look-up table" is used to extrapolate the location of the module's K&E targets. However, since the z-position of any K&E cannot be measured with the CMM during construction, a least χ^2 spherical fit to the (x, y, z) data obtained from the V-star survey yields a radius, which in turn can be used with the (x, y) information of the K&E to provide a fitted value of the

z-coordinate. Next, once the coordinates for the K&E have been calculated, a standard geometrical translation to any FPS strip position, module-to-module, is made. The data is entered into a hardware database for alignment studies and used during data analysis. For brevity, the collection of survey coordinates and calculations for each module (and layer) are not given here. Instead, a typical plot illustrating the coordinates of all K&E and V-star targets on eight modules in a given FPS layer is presented in Fig. 8.7.

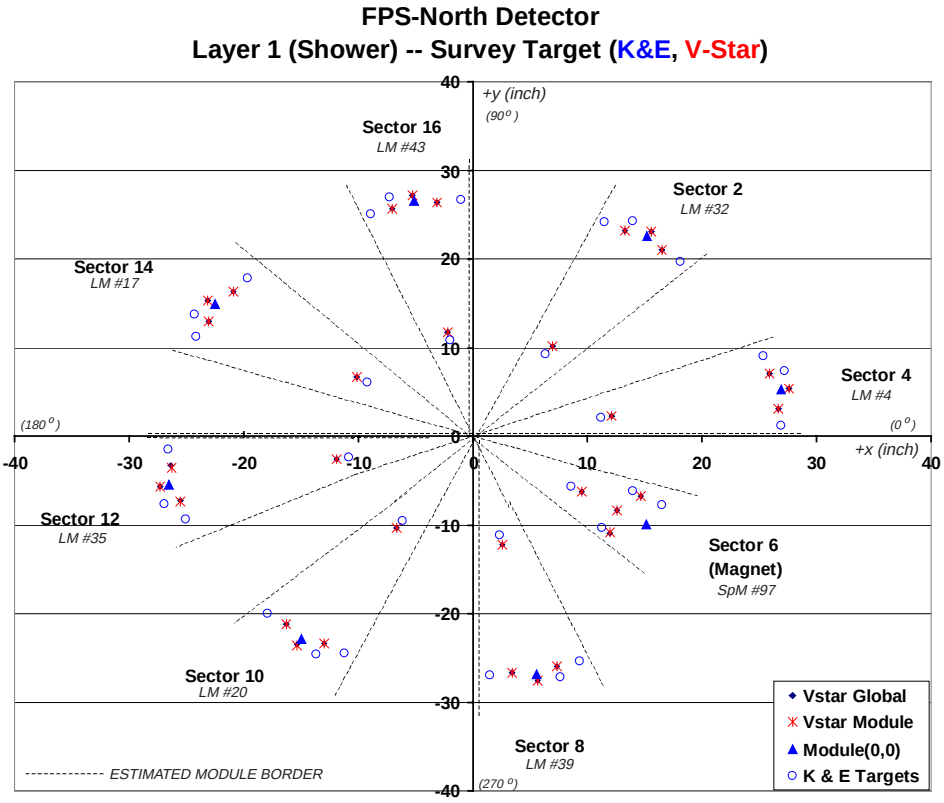

Figure 8.7: Graphical representation of survey target location for the eight modules installed in Layer 1 of FPS-North on the cryostat head. Shown are the actual V-star measurements (asterisk) extrapolated with the mapped K&E (open circle). As described in the text, the location of any V-star target is measured with respect to an arbitrarily chosen K&E (closed triangle), which is taken as the origin (0,0) for the module.

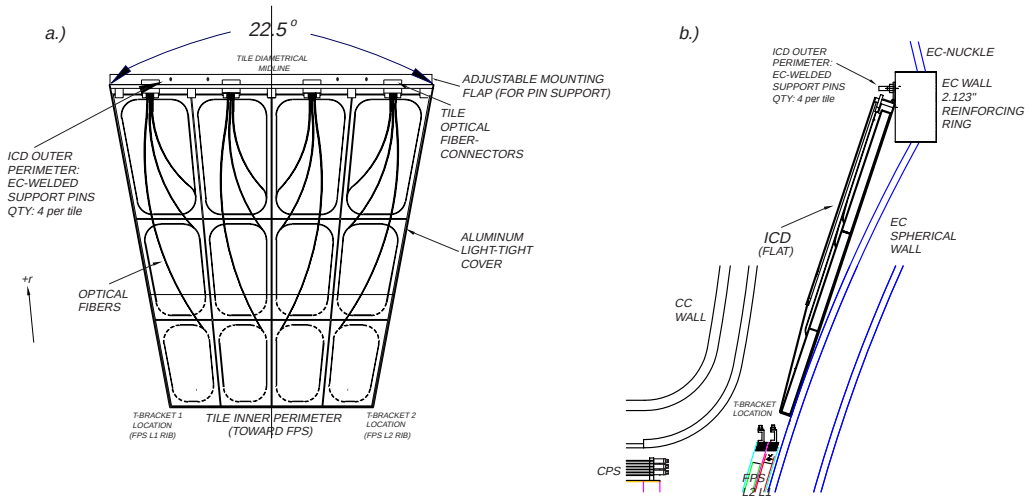

Figure 8.8: One of sixteen flat ICD panels mounted on each end-cryostat head. Shown are: a) r–ϕ view and b) r–z view of a tile.

8.3 Luminosity Monitor and ICD Mounting

The position of the FPS defines the location of both the ICD and Luminosity Monitor (LM) subsystems and requires the FPS installation to be completed prior to mounting either on the end cryostats. Moreover, neither the ICD or LM are surveyed. Instead, each is simply placed on the EC head, structurally anchored to hardware existing on the EC and FPS assembly, and thus, must rely on the alignment of the FPS[2].

The Luminosity Monitor is a circular assembly divided into eight octagonal sections [50]. Each counter is mounted on the inside faces of the end calorimeters, symmetrically constrained in-between the beam pipe and the FPS inner rings. The inner-diameter of the counter is at 2.540″ and fits directly around

[2]The Run I ICD was aligned relative to the EC, where ICD tiles were matched EC cells to within a few millimeters from their ideal position [103]. For Run II, positioning the ICD with the EC cells is done by extrapolating the position from the FPS alignment referenced to the beam line. The method is also expected to be within the same order of that observed in Run I.

Hole Number	ϕ-clocking (degrees)
1a	16.5
1b	28.5
2	112.5
3a	196.5
3b	208.5
4	292.5

Table 8.3: ϕ-position of anchoring holes drilled on FPS Layer 3 inner ring to accomodate Luminosity Counter installation. Note: a) Hole numbering is needed for installation purposes, and b) 0° is taken at the 12-o'clock position (local FPS coordinates), rotating cw (ccw) for FPS-N (FPS-S).

the beam pipe's 2.375″ outer-diameter [104]. The diameter increases to 6.132″ at a z of 1.080″ away from the surface of the counter that sits closest to the EC wall to clear a 4.0″ diameter wiper-flange, which is used to support, attach, and vacuum seal the beam pipe. The detector, however, is only positioned and not supported in any way about the beam pipe. Rather, all attachments are made to the FPS Layer 3 inner ring. Here, six threaded-holes, drilled at pre-determined ϕ-intervals [105] and listed in Table 8.3, are centered on the inner surface of the ring's z-thickness. A simple #10-24 slotted-head screw attaches the counter to the FPS via adjustable brackets on the LM. Since a counter is relatively light ($\mathcal{O}$(10–15 lbs.)), the six positions for support are more than sufficient.

The ICD is composed of 16 scintillating tiles per EC head, each housed in a light-tight, aluminum trapezoidal wedge support panel. Each unit is flat in geometry (see Fig. 8.8) and spans 22.5° in ϕ. The tiles mount, about ϕ, in the region between the outer periphery of the FPS detector and the 2.1″ wide flat reinforcing ring existing on the end-cryostat wall. The inner radius of each tile sits relative to an outer corner of a L1 and L2 FPS support rib. Since the azimuthal span of an FPS L1 rib with an L2 rib is also 22.5°, any tile can

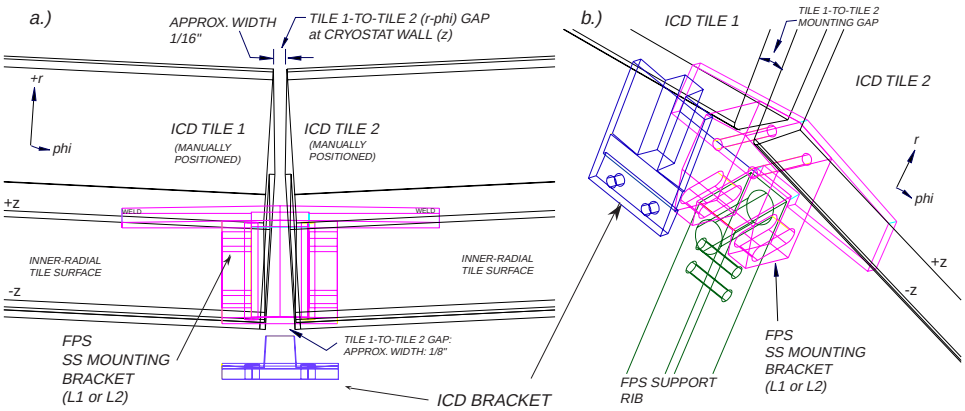

Figure 8.9: 3-D frame view in (r, z, ϕ) illustrating two ICD tiles nested on the EC wall. Shown are: a) a view from the innermost z-surface of two panels and b) a similar forward angular view. The brackets supporting the ICD are designed to securely fit within the gap existing between tiles.

be placed within this pair. Further, the flat geometry of an ICD tile, when arranged in a circular orbit on the spherical EC, forms a cone that creates a ϕ-gap between any two adjacent tiles. In fact, a three-dimensional model of the ICD clearly illustrates gaps on the order of $1/8''$ at the outer ($-z$) surface of an ICD wall, tapering inwards to about $1/16''$ at the surface ($+z$) that sits closest to the cryostat wall[3]. Such a view of the gap is shown in Fig. 8.9.

An ICD tile is manually mounted to the cryostat wall by the use of two aluminum "T-shaped" support brackets, shown in Fig. 8.3 and listed in Table 8.1. These so-called "T-brackets" are engaged to each FPS outer mounting bracket (or spacer) via $8/32''$ diameter through-holes located on the brackets. One notes that each of the L1 (L2) FPS bracket (bracket+spacer) has been designed with a $1.0''$ height (in z) in order to match the thickness of an ICD tile at its inner radius. While the pair of T-brackets provide support at the ICD's inner radius, four additional $1.0''$ long threaded-pins are welded on the EC's

[3]A precise value of the gap for each tile is not possible since the tiles are manually mounted and not surveyed. Thus, only estimates are quoted here.

reinforcing ring to anchor a tile at the ICD's outer perimeter. Each successive tile is mounted until all the required tiles have been installed on the cryostat head.

8.4 FPS Commissioning

The preshowers are instrumented with clear fiber waveguides transporting optical signals from the WLS fibers inside the detector to remote VLPC-SVXII electronics on the DØ readout platform. Each half of the FPS contains 32 such guides each composed of 256 fibers. Channels of this magnitude, in addition to the manner in which the preshower readout and trigger electronics are designed and built (see Sec. 5.2.2), requires the map from the scintillating strips to VLPC pixels be well-defined. A full layout of fiber channels to pixels in different η regions and FPS readout sectors is made [106], and the information stored in to a hardware database. However, during cable hook-up and prior to data taking, the integrity of the channel map must be verified. The LED-based monitoring/calibration system serves as a convenient check for the mapping and can indicate whether optical connectors have been mistakenly mismated, fibers broken, and/or relative (channel-to-channel) light yield degraded.

The LED system has been designed to operate within the dynamic ranges specified in the readout. Pulsing LED-by-LED can therefore check whether proper threshold settings are established, signals do not saturate, and proper downloads to the DAQ system are possible. Finally, reconstructed signals can help establish both the energy scale of the FPS as well as measure the alignment of the detector with DØ. Each of the above studies are to be gradually performed and understood as the Tevatron run progresses and form the basic outline for commissioning the FPS.

Chapter 9

Physics Studies with the Preshower and DØ

The upgraded DØ detector in Run II offers an unique opportunity to trigger on low-p_T electrons from J/ψ decays using the combined information of the preshower, calorimeter, fiber tracker, and silicon subsystems. Preliminary studies [107, 108, 109] have been performed investigating the possibility of this type of trigger, in particular using information from the central and forward preshowers. These described the performance of the Level 1 (L1) and Level 2 (L2) trigger and did not consider Level 3 (L3). The following addresses the Level 3 trigger as measured with a Monte Carlo sample of $J/\psi \to ee$.

For a complete understanding of the analysis, a brief description of the signal and background samples as well as the necessary software machinery used is given. This is followed with results on the resolutions of a) matching between subdetector units and b) invariant mass reconstruction. The final sections of the chapter provide a description of the algorithm developed for electron selection and background rejection as well as results expected for the performance of the J/ψ trigger.

9.1 Motivation and Constraints

The studies performed here are intended to a) develop an algorithm that optimizes the selection of low-p_T electrons and b) provide a fully functional $J/\psi \to ee$ L3 software trigger for the experiment. This is prompted by the desire to obtain large data sets for B-physics analyses. Such data samples provide extended opportunities to study a number of Standard Model processes; for instance, the determination of CP violation parameters. Further, an effective means of selecting electrons from the J/ψ, in addition to muons, can be used to address detector calibration issues at low energies. The precise measurement of two electrons from $Z \to ee$, $\Upsilon \to ee$, and/or $J/\psi \to ee$ decays allows a determination of relative electromagnetic calorimeter energy scales between the DØ central (CC) and end calorimeters (EC). In particular, the use of low-p_T electron triggers available with the preshowers can play an important role in calibrating the detectors with J/ψ in the low energy range, thereby providing an additional tool in establishing the jet energy scale and missing energy reconstruction. Proper electron triggers can also extend to other processes such as those from the associated production of charginos and neutralinos ($\tilde{\chi}_2^\circ$) containing soft-leptons. Finally, a direct reconstruction of the J/ψ signal peak constrains alignment uncertainties and monitors subdetector efficiencies.

Given the high energy physics program at DØ, any J/ψ trigger algorithm will be constrained by the accept rate and allocated bandwidth defined at the various trigger levels (see Chap. 3). At Level 1 (L1), the total acceptance rate is limited to 5 to 10 kHz, of which a J/ψ trigger can take at most 1.5 kHz in both the central and forward detection regions. The $J/\psi \to \mu\mu$ mode requires about 0.5 kHz of this bandwidth, leaving $\sim$1 kHz for a $J/\psi \to ee$ trigger at L1. Similar arguments suggest that at Level 2, the $J/\psi \to ee$ accept rate be kept

below ∼100 Hz, and at Level 3 within ∼3-5 Hz. Such constraints [109] guide the complexity of the algorithms used for the trigger and require a general study of the trigger efficiencies and rejection prior to implementation.

9.2 Software and Trigger Framework

The software and trigger framework is based on specific DØ event processing algorithms and procedures. The reader is directed to Refs. [110, 111] for a more detailed description of the software infrastructure as only a brief overview is given here.

9.2.1 Event Generation and Processing: J/ψ Signal

The present analysis utilized a J/ψ sample generated by PYTHIA [112], where the J/ψ's were forced to decay into electron pairs: $J/\psi \rightarrow ee$. The events were processed in two groups with a total of 200,000 $b\bar{b}$ events and were preselected by a standard selection criteria: a) $p_T(B) \geq 3.0$ GeV, and b) at least two electrons with $p_T(e) \geq 3.0$ GeV and -1.6 $\leq \eta \leq$ 1.6. A total of 1021 (1055) events survive in the first (second) group, yielding a sample of 2076 events for study.

The generated events were processed using DØ-specific tools that provide a full simulation of the Run II DØ detector and event reconstruction [113]. The procedure consists of a chain of processors such that the output of one must feed into another in an orderly, logical manner. The first package in the chain is known as the DØ GEANT Simulation of the Total Apparatus Response (DØgstar) and incorporates the detailed DØ detector geometry. The DØgstar output was then processed through DØSim which performs the digitization for each detector subsystem. DØSim also adds the appropriate number minimum

Generator or Processor	Version	Comments
PYTHIA generator	v. 6.161	–
DØgstar	p07.00.05a	Default version
DØSim	p07.00.05a	Default version
DØTrigSim	p06.00.01	Local modifications and L3 analysis
DØTrigSim	p09.07.00	L1-L2 Trigger Simulator

Table 9.1: DØ software release versions for generating and processing J/ψ signal samples for Level 3 studies. See text for a discussion of comments.

bias events with the hard scatter, accounting for the Run II luminosity. For the J/ψ signal sample presented here, an average of 1.1 minimum bias (Poisson distributed) was overlaid during processing. The DØSim output provides the input to the trigger simulator, DØTrigSim, which emulates an independent simulation of the L1, L2, and L3 DØ trigger. This last output provides the basis for the L3 studies presented here. It must be noted that although the DØTrigSim package is intended for an overall study of the trigger at all levels, the analysis was performed with two different releases: the first to perform a simulation of the L1 and L2 trigger, and the second to study the performance at L3. Such a division was required simply because the available software did not have a fully functional trigger simulator incorporating all three trigger levels in one package [114].

DØTrigSim produces a ROOT [115] file, which contains physics quantities from the L1, L2, and L3 simulations as reported by each trigger subsystem. The information is a result of processing the DØSim produced events with trigger conditions defined within the DØ Trigger List [116]. Information on the Monte Carlo generation (*e.g.,* particle-type, η, ϕ, event cross-section, etc...) is also contained within the DØTrigSim output.

The study was performed during a period when the DØ software was still under development, necessitating a number of private fixes and modifications. The simulation package used for the L3 studies described in this thesis is based on several production releases; the version for each processing component is listed in Table 9.1. A number of corrections and/or modifications were made in order to achieve optimal results. These modifications were primarily to the L3 filtering tools linked under DØTrigsim and are summarized in Table 9.2. The changes were the result of optimizing the performance of the different subdetectors from studies of low-p_T (J/ψ, Υ) and high-p_T (Z) dilepton decays under DØTrigSim.

The Monte Carlo cross-section corresponding to any generated sample is usually available from the DØTrigSim ntuple. However, for the 2076 event J/ψ sample, selections were made at the generator-level in order to improve the generation efficiency. Such a bias was introduced since, at present, the resources do not allow for large samples to be simulated. A production record was kept containing historical information for the generation run of the J/ψ sample [117]. This includes a corresponding value of the J/ψ cross-section according to PYTHIA. Thus, the total normalized cross-section becomes:

$$\sigma(B \to J/\psi + X \to ee + X) = \frac{1}{200000}(2076 \times 28.11\mu\text{b}) = 292\ \text{nb} \qquad (9.1)$$

The value quoted in Eq. 9.1 can be used to estimate the trigger rate for signal.

9.2.2 Event Generation and Processing: QCD background

The rejection of Level 3 for QCD background processes was studied using QCD background events produced by PYTHIA, overlaid with on average 0.7

L3 filtering package	Correction and/or Modification
l3fanalyze	Correct the track extrapolation from default radius 60.0 cm (solenoid radius) to 72.96 cm (CPS detector's radius).
l3fcps	Change maximum number of Single Layer Clusters (SLCs) from 31 to 63.
l3femtools	a) remove L3 call to CPS to use z-position information during cluster matching; instead, b) add L3 call to CPS to use log-weighted ϕ-position.
l3fcalcluster	Modify algorithm to compute all calorimeter cluster information (*i.e.*, η, ϕ E_T) wrt DØ detector's origin (0,0,0).
DØ Trigger List	Modify parameter to change electron p_T-threshold from a default 3.0 GeV to 1.0 GeV, and use global tracking information (*i.e.*, combined SMT and CFT information).
DØ Trigger List	Modify parameter R_{cone} used for the L3 calorimeter's Simple Cone Algorithm from R_{cone} = 0.4 to R_{cone}= 0.2.

Table 9.2: Summary of local changes and/or modifications made to L3 filtering tools during event processing under DØTrigSim. A detailed description of each package and corresponding parameter definitions is given in [111].

minimum bias interactions (Poisson distributed). The processing chain for these QCD samples was in many ways similar to those described for the J/ψ signal sample in Sec. 9.2.1. The samples are generated in p_T bins for efficient modeling of the relevant background with the signal that is under study. Once produced, they are stored in terms of their p_T thresholds in the DØ data repository for processing under DØTrigSim. The p_T range with the cross-section for each is given in Table 9.3 [118].

QCD Sample	σ (μb)	No. of Events
p_T >2 GeV	39529	15250
p_T >5 GeV	8280	13000
p_T >10 GeV	613	12750
p_T >20 GeV	35	16000

Table 9.3: QCD background samples available for L3 studies: The p_T range for each event sample is given with the cross-section as obtained using a Gaussian fit to the weighted MC event distribution provided in the DØTrigSim ntuple. Each QCD sample has been generated with on average 0.7 minimum bias overlay expected for a luminosity of 3.2×10^{31} cm^{-2}s^{-1}.

9.3 Level 3 Analysis

The ROOT file generated by the trigger simulator contains information on a variety of physics objects and their results. This study primarily utilizes: a) the results at the Monte Carlo (MC) generation level and b) the electron trigger tool incorporating the SMT and CFT inner tracking detectors, CPS, and calorimeter systems at Level 3. The variables and their definitions are listed in Refs. [119, 120].

9.3.1 Preliminary Studies: Matching and Mass Resolutions

Prior to attempting to model a J/ψ trigger and optimize the selection criteria, the inter-detector matching performance for electrons is studied. These resolution are based on a combination of the MC information provided by DØTrigSim and the detector measurements from the participating subsystems.

Electrons ($e^{\pm}$) with $p_T > 1.5$ GeV in the data sample are identified using the MC information. The value has been chosen lower than the p_T threshold originally set at the generator level for the two electrons from the J/ψ (see

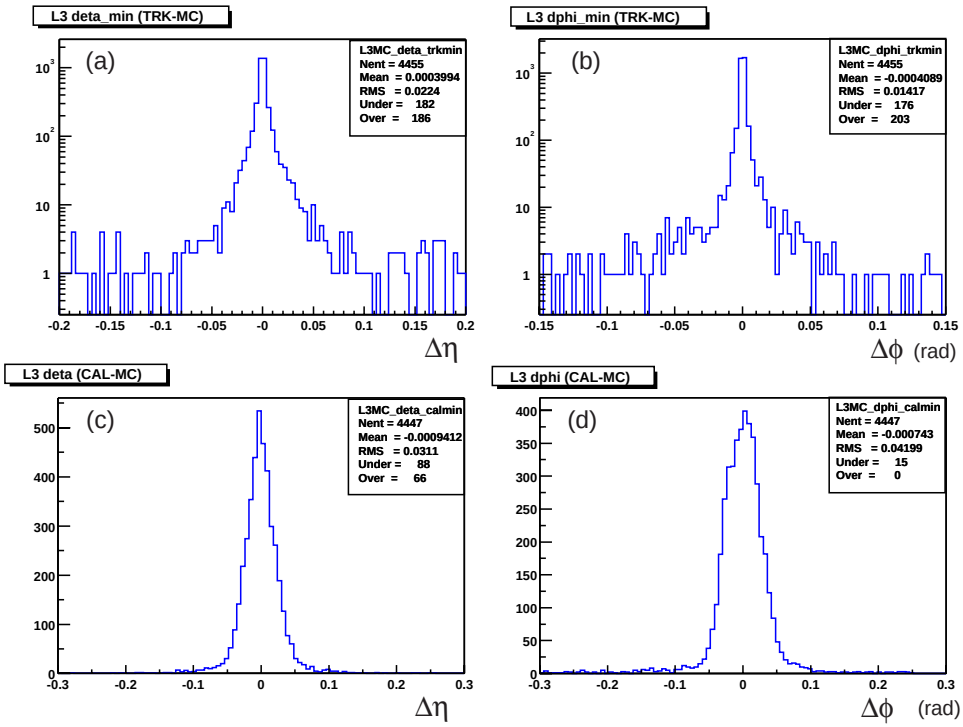

Figure 9.1: Matching resolutions in η and ϕ for MC electrons with (a-b) global tracking (*i.e.,* CFT and SMT) and (c-d) calorimeter, respectively.

Sec. 9.2.1) in order to study a possible online technique for tagging b-quark jets using electrons present in the semi-leptonic decay of the b. Since the calorimeter resolution is much poorer than that of the tracker, (see Fig. 9.1) matching information in azimuthal, $\Delta\phi$, and polar, $\Delta\eta$, coordinates for the MC electrons and tracker is used. Subsequently, the electron is "tagged" on the basis of a matched track within a radius, $\Delta R = \sqrt{\Delta\phi^2 + \Delta\eta^2} < 0.1$. With this requirement, each pair of detector subsystem (*i.e.,* global tracker: SMT-CFT, CPS, and calorimeter) is cycled, and thus, the $\Delta\phi$, $\Delta\eta$, ΔR, and/or axial, Δz, resolutions for the tagged electrons are determined.

L3 Calorimeter Clustering

For a better understanding of the results presented in this chapter, a brief description of the method used in defining calorimeter clusters at L3 is given. These clusters are based on the Simple Cone Algorithm (see Ref. [122] for further discussion). The technique involves reconstructing clusters based on the following three steps:

1. Define a list of seeds, initialized with the highest E_T calorimeter tower.

2. Calculate $\Delta R = \sqrt{\Delta\phi^2 + \Delta\eta^2}$ between unassigned tower with highest E_T and seeds.

3. Define the cone size variable of radius R_{cone} and add the tower to first seed in the list with $\Delta R < R_{cone}$. If there does not exist a match, add tower as a new seed to the list and proceed to apply 2 until all towers above a 1.0 GeV E_T threshold are processed.

A default value of $R_{cone} = 0.4$ is used in the algorithm and is specified in the DØ Trigger List. In an effort to improve the matching resolutions — and J/ψ efficiency (see also Sec. 9.3.3) — $R_{cone} = 0.2$ has been used. One should note that lowering this value also increases the number of calorimeter clusters reconstructed at L3. The minimum value, however, is constrained by the intrinsic calorimeter resolution. In addition, decreasing R_{cone} to arbitrary low values will degrade the trigger's rejection capability on backgrounds by increasing the number of fake trigger clusters and thereby, the background rate.

Matching Resolution I: Tracker and Calorimeter

Figure 9.2 shows the $\Delta\phi$, $\Delta\eta$, and ΔR distributions between the calorimeter clusters (using a 0.2 cone size) and "tagged" tracks. Similar distributions for $R_{cone} = 0.4$ are presented in Fig. 9.3. In each case, the ϕ-resolution between the calorimeter and track tends to exhibit a central core with a RMS on the order of 50 mrad. However, in order to obtain a benchmark in comparing these values, the trigger studies were performed on higher p_T processes, with electrons from $Z \to ee$ and $\Upsilon \to ee$ decays (see Fig. 9.4). The RMS for these latter samples have a ϕ resolution in the range of 10–20 mrad, improving with p_T and indicating at least a factor of two difference from that obtained for the J/ψ. This behavior is a result of the p_T difference between the three samples and helps motivate the need in developing methods to improve the L3 ϕ-match for low-p_T electrons.

As summarized in Table 9.2, the η and ϕ calculated in the trigger simulator for calorimeter clusters use a primary vertex determined from track reconstructed by L3. Unfortunately, the actual vertex used was not saved in the ntuple[1]. The η-resolutions appear in Fig. 9.2b for $R_{cone} = 0.2$ and Fig. 9.3b for $R_{cone} = 0.4$. The distributions indicate that the resolution in either an η or ϕ match between tracking and the calorimeter tends to be roughly 2–3 $\times$ larger than the match between the MC electrons and the calorimeter on one hand and/or tracker on the other — see Figs. 9.1c and 9.1d. Additional studies

[1]This oversight is presently being studied. Here, modifications to the software were made such that the calorimeter η is computed for each event with respect to the origin, thereby defining the pseudorapidity of the detector, η_{det}. Subsequently, the track's z coordinate at the distance of closest approach (DCA) to the z=0 axis defines the event's primary vertex, $z_\circ$, allowing the tracker η to be taken with respect to this coordinate. For each event, a match in η between the calorimeter and tracker can be done by translating and recalculating the calorimeter's η wrt $z_\circ$.

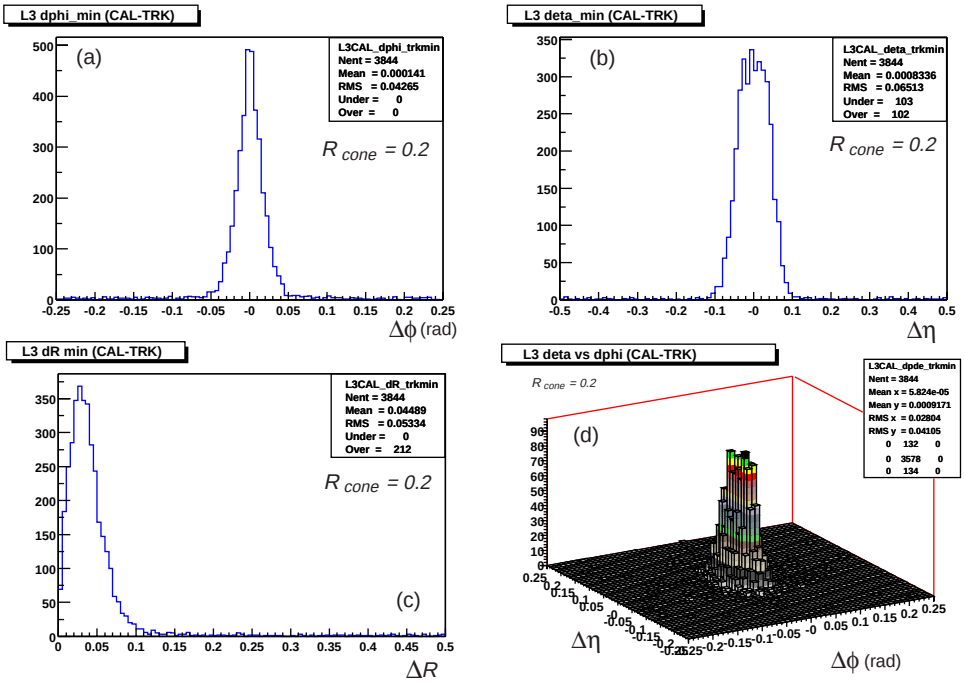

Figure 9.2: Distributions for (a) $\Delta\phi$, (b) $\Delta\eta$, and (c)ΔR for tagged electrons in global tracks and calorimeter clusters in the J/ψ sample. A value of R_{cone} = 0.2 has been used to define L3 calorimeter clusters. The correlation in $\Delta\eta$ with $\Delta\phi$ is also shown in (d).

are presently being performed to improve the calorimeter resolution.

Matching Resolution II: Central Preshower and Calorimeter

Distributions for the matching performance between the CPS and calorimeter systems using R_{cone} = 0.2 and 0.4 are shown in Figs. 9.5 and 9.6, respectively. Once again the match in η appears broad. However, the match in ϕ yields a mean centered about zero with an RMS of 17.6 mrad (20.3 mrad) for a R_{cone} setting at 0.2 (0.4). Lowering the cone size improves the resolution by 10-15%.

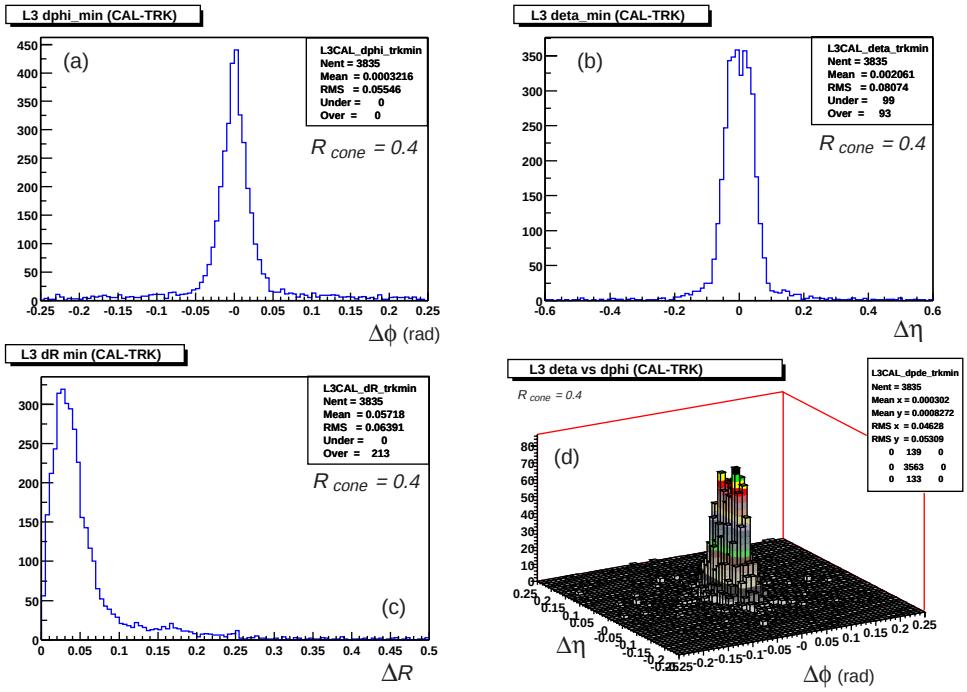

Figure 9.3: Distributions for (a) $\Delta\phi$, (b) $\Delta\eta$, and (c)ΔR for tagged electrons in global tracks and calorimeter clusters in the J/ψ sample for $R_{cone} = 0.4$. The correlation in $\Delta\eta$ with $\Delta\phi$ is also shown in (d).

Matching Resolution III: Tracker and Central Preshower

The remaining comparison for matching tagged electrons involves the central tracker and CPS. The performance is summarized in Fig. 9.7. A bimodal distribution is immediately observed when comparing the ϕ between a track and CPS. This effect, illustrated in Fig. 9.8, is simply due to a change in the magnetic field near the radius of the CPS. The present track extrapolation assumes a uniform 2 Tesla field up to the CPS radius and does not properly treat the presence of a field outside the solenoid's fiducial volume. Any match in ϕ between the preshower and tracker requires a first-order correction at the CPS radius. Although the field is small (*i.e.*, $\mathcal{O}(\mathcal{B}) \sim 0.2$ Tesla), the value is sufficient to distinguish oppositely charged particles in the preshower volume.

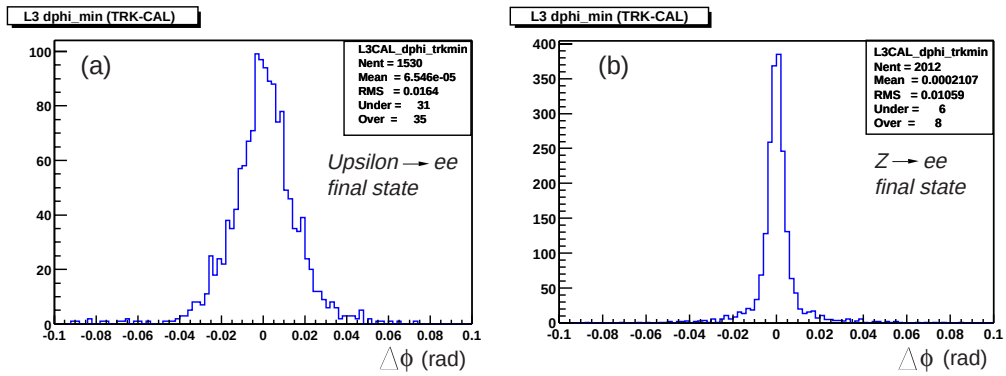

Figure 9.4: $\Delta\phi$ distribution for electrons matched in the global tracker and calorimeter for (a) $\Upsilon \rightarrow ee$ and (b) $Z \rightarrow ee$ final states.

Subsequently, a clear bimodal $\Delta\phi$ distribution results from the track propagation (see Fig. 9.7) with each peak corresponding to either positively ($\Delta\phi > 0$) or negatively ($\Delta\phi < 0$) charged tracks of similar p_T, equally separated at $< \Delta\phi > \simeq 0$. One method for correction requires applying charge dependent corrections that flip the $\Delta\phi$ residuals for negatively charged tracks from $\Delta\phi \rightarrow -\Delta\phi$ [123]. For the J/ψ sample, the so-called "Q-flip" not only improves the $\Delta\phi$ resolution (as shown in Fig. 9.7d) from approximately 4.3 to 3.3 mrad but also introduces an offset, $\Delta\phi_{offset} = -2.6$ mrad. The precise value for $\Delta\phi_{offset}$ is obtained through a Gaussian fit of the tracker-CPS $\Delta\phi$ distribution after the Q-flip. Nevertheless, the offset can easily be corrected for and re-shifted in the final match. As shown in Fig. 9.9, such corrections yield a CPS-TRK ϕ-resolution of 3.28 mrad ($\simeq 0.19°$), translating to roughly 2.4 mm at the CPS radius. This indicates a resolution much finer (*i.e.,* $\times \sim 3$ smaller) than the width of a triangular preshower scintillator strip.

The match in z using the two subsystems is shown in Fig. 9.7c. The distribution shows a core centered about zero with RMS ~ 8.20 mm. Theoretically, the resolution in z should improve gradually with higher p_T tracks. This, however, does not appear to be the case for electrons in Z or Υ final

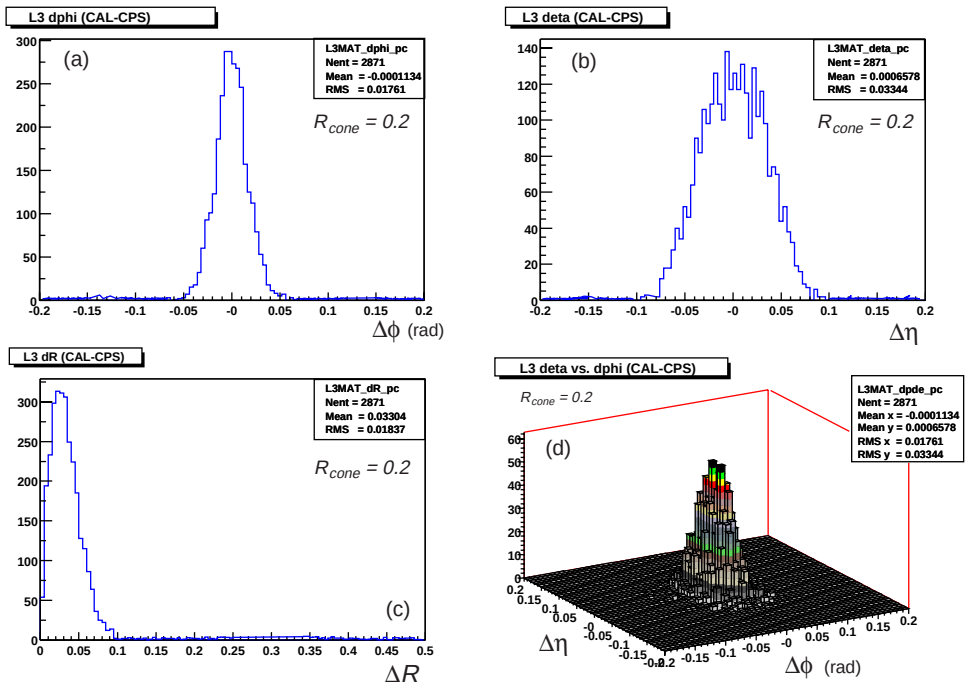

Figure 9.5: Distributions for (a) $\Delta\phi$, (b) $\Delta\eta$, and (c)ΔR for calorimeter and CPS clusters using tagged electrons in the J/ψ sample. Results are for calorimeter clusters with $R_{cone} = 0.2$. The correlation in $\Delta\eta$ with $\Delta\phi$ is also shown in (d).

states (see Fig. 9.10), presently indicating that the match is dominated by the extrapolated track's z-resolution. Improvements to Δz are under study.

Invariant Mass Resolution: Monte Carlo, Tracker and Calorimeter

One powerful technique in identifying potential J/ψ candidates and rejecting backgrounds is to require the presence of two leptons with their invariant mass peaked near the accepted value of the J/ψ mass at 3.096 GeV [7]. The invariant mass can be determined using the relationship:

$$M(l_{12}) = \sqrt{2E_{T1}E_{T2}(\cosh(\Delta\eta_{12}) - \cos(\Delta\phi_{12}))} \tag{9.2}$$

where E_{T1}, E_{T2} are the transverse energies of the leptons with η, ϕ separations

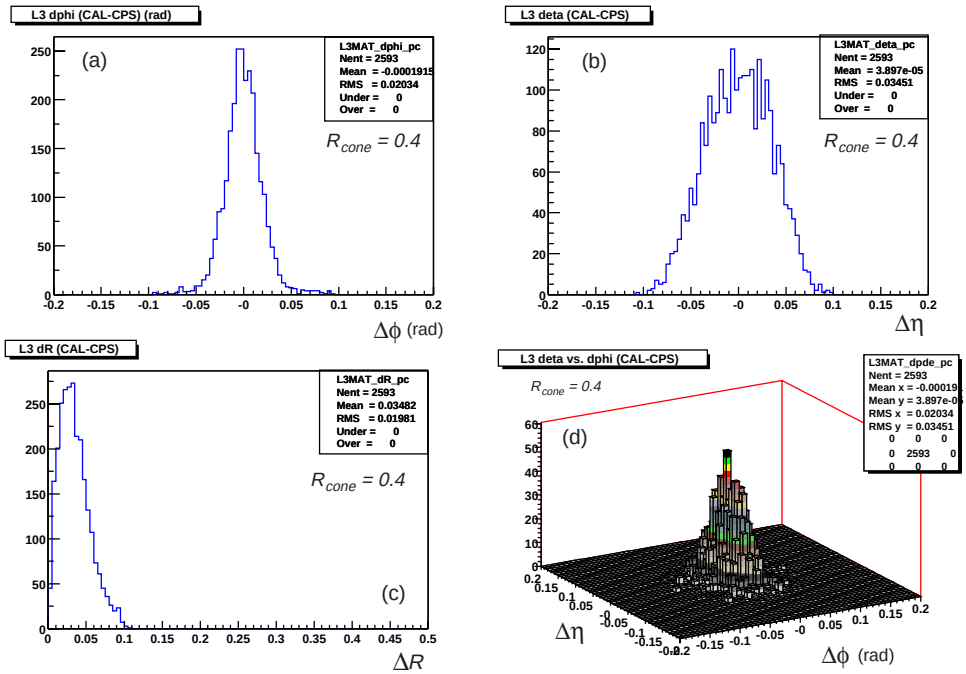

Figure 9.6: Distributions for (a) $\Delta\phi$, (b) $\Delta\eta$, and (c)ΔR for calorimeter and CPS clusters using tagged electrons in the J/ψ sample. Results are for calorimeter clusters with $R_{cone} = 0.4$. The correlation in $\Delta\eta$ with $\Delta\phi$ is also shown in (d).

$\Delta\eta_{12}$ and $\Delta\phi_{12}$, respectively. Since the mass of the electron is completely negligible compared to the measurable momenta, one replaces the transverse energies in Eq. 9.2 with the transverse momenta $p_{T1,2}$. As a reference, the separation in η and in ϕ for each electron pair from the J/ψ, and as a function of the reconstructed mass, is summarized in Figs. 9.11 and 9.12, respectively. Similar distributions for a QCD background sample is shown in Fig. 9.13. Note that for events lying outside the J/ψ mass value, pairs tend to be either close (low mass) or nearly back-to-back (high mass).

Applying Eq. 9.2 to electrons from the J/ψ using physical variables from a) MC, b) calorimeter, and d) tracking produces a mass resolution shown in Figs. 9.14a, b, and d, respectively. Combining the $E_{T1,2}$ determined from the

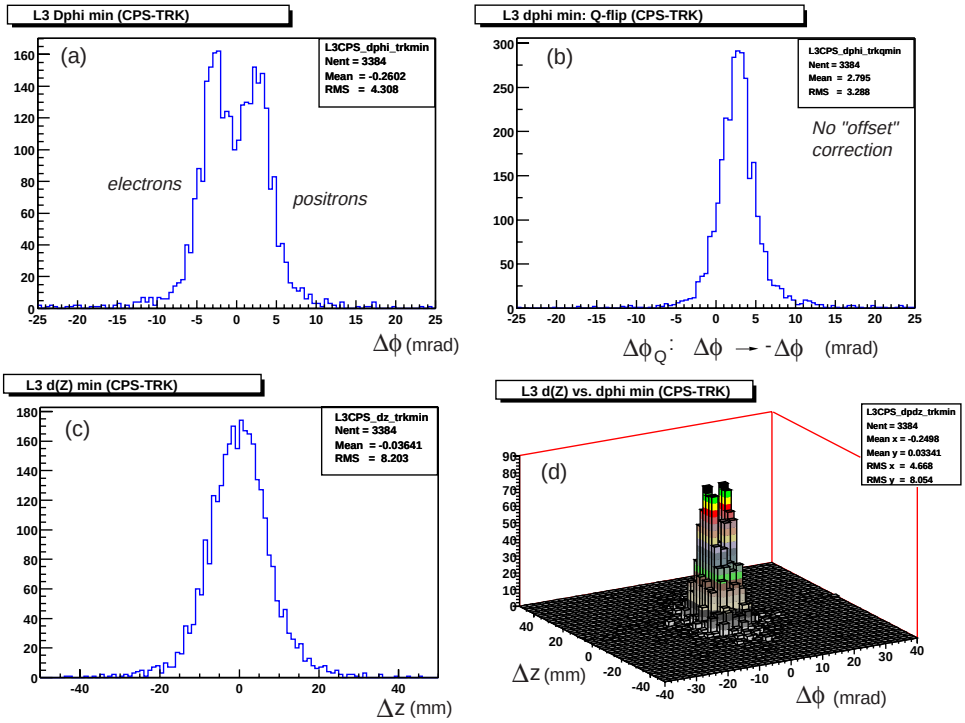

Figure 9.7: Distributions for (a) $\Delta\phi$ and (c) Δz for tracks and CPS clusters using tagged electrons in the J/ψ sample. The correlation between these two variables is given in (d). Also shown in (b) is the $\Delta\phi_{Q-flip}$ distribution without offset corrections, described in the text.

calorimeter with the $\Delta\phi_{12}$ and $\Delta\eta_{12}$ obtained using track information results in a mass peak shown in Fig. 9.14c. A direct comparison of the last three distributions clearly indicates that tracking information alone yields a mass closest to the expected J/ψ mass. A radiative tail arising from bremsstrahlung in the detector material [121] is also distinctly observable at low masses. Further, the calculation based on calorimeter variables yields a mass of $\simeq$ 2.5 GeV, approximately 20%, too low. A low value suggests an uncertainty in the calorimeter's energy scale for low-p_T electrons. Nonetheless, since the tracker yields an improved resolution than that of the calorimeter (*i.e.*, $\sim \times$ 2.5 smaller) [31], the mass calculated by tracking information alone is sufficient

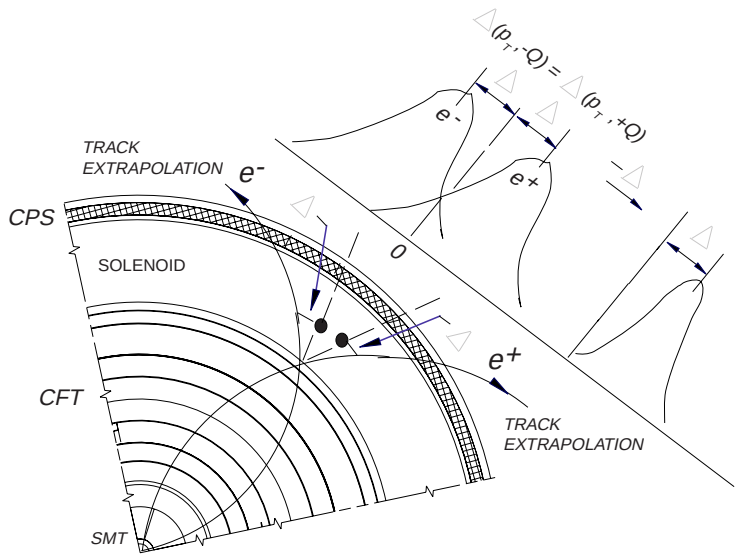

Figure 9.8: Schematic of the bimodal distribution in $\Delta\phi$ observed in the match between the tracker and CPS. See text for further discussion.

to identify J/ψ's over QCD backgrounds.

9.3.2 Event Preselection: L1 and L2 Simulation

Prior to developing a Level 3 trigger for the J/ψ, all events, including background samples, must satisfy L1 and L2 trigger conditions. Events accepted by L1 are fed into a L2 simulator such that a L2 accepted sample can subsequently be used for L3 studies. As alluded to earlier, since the DØ software is still in its development, any L1, L2, and L3 trigger simulation requires the use of two different releases of DØTrigSim. The first release processes events through L1 and L2, while the second applies the L3 filtering algorithm. A record is kept of the event numbers that pass the various triggers.

The conditions for the L1 and L2 trigger are given in Table 9.4. The specifications at these two trigger levels reflect the current DØ Trigger List and trigger simulator. It should be noted that the current study did not aim to optimize the L1 and L2 triggers on the $J/\psi \to ee$ sample and/or to

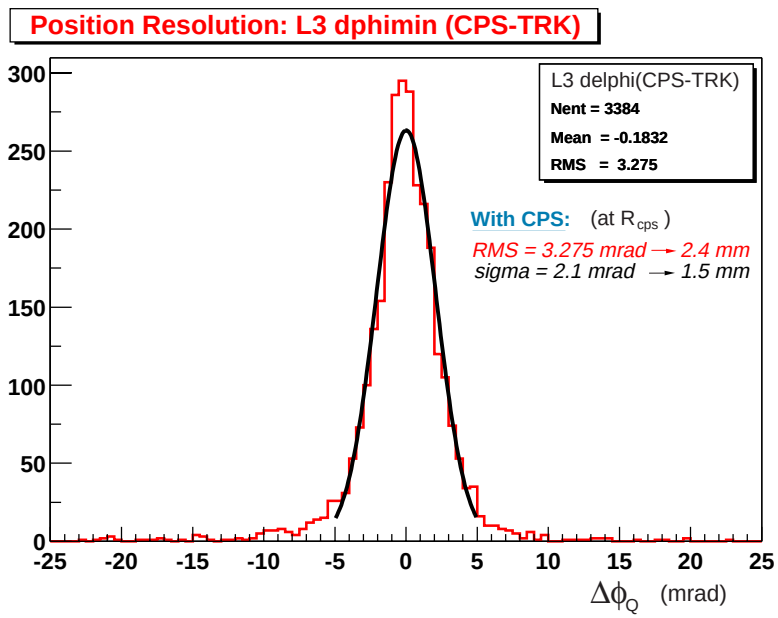

Figure 9.9: $\Delta\phi$ distribution for CPS clusters and tracks after correcting for the offset resulting from the "Q-flip". The distribution has been fitted to a Gaussian to determine an order of magnitude of the resolution in ϕ.

maximize background rejection. One main reason for this is that a number of resources (such as the L1 and L2 filtering tools) are presently being developed or simply do not yet exist. Instead, the results presented in this thesis take a L1 and L2 accept and focus on measuring the performance at Level 3. In fact, as evidence by Table 9.5, the rate of background events passing a L1 or L2 accept is clearly in excess of the total bandwidth allowed at these trigger levels. It is assumed that as trigger conditions gradually become more sophisticated during the run, sufficient rejection power will become available. The L1 and L2 conditions given in Table 9.4 have been carefully chosen so as to give an initial approximation to J/ψ triggers for DØ during Run II.

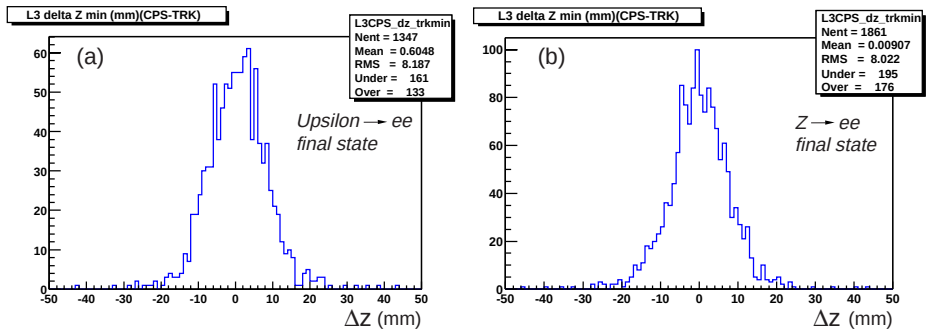

Figure 9.10: Match in z for CPS clusters and tracks for (a) $\Upsilon \to ee$ and (b) $Z \to ee$ final states.

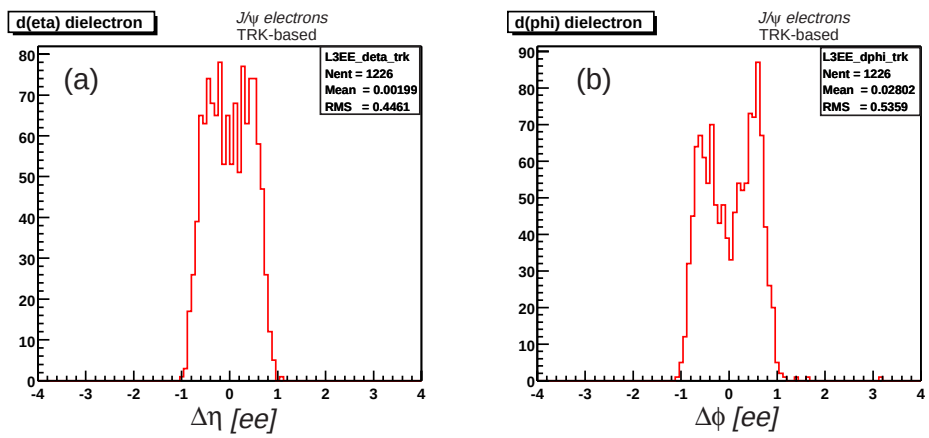

Figure 9.11: Separation of electron pairs from the J/ψ in (a) η and (b) ϕ.

9.3.3 Classification of Electrons at Level 3

The matching resolutions between the subsystems outlined in Sec. 9.3.1 provide a useful guide to develop the L3 selection algorithm on J/ψ (and low-p_T) electrons. The technique, summarized by the schematic in Fig. 9.16, begins by requiring a calorimeter cluster that satisfies certain basic selection criteria given in Table 9.6. The selection is kept quite loose to prevent any initial loss in signal efficiency. However, it reduces the QCD background significantly. Since the present resources only provide CPS information at L3, those clusters confined within the central calorimeter fiducial region, -1.2 $\leq \eta \leq$ 1.2, are

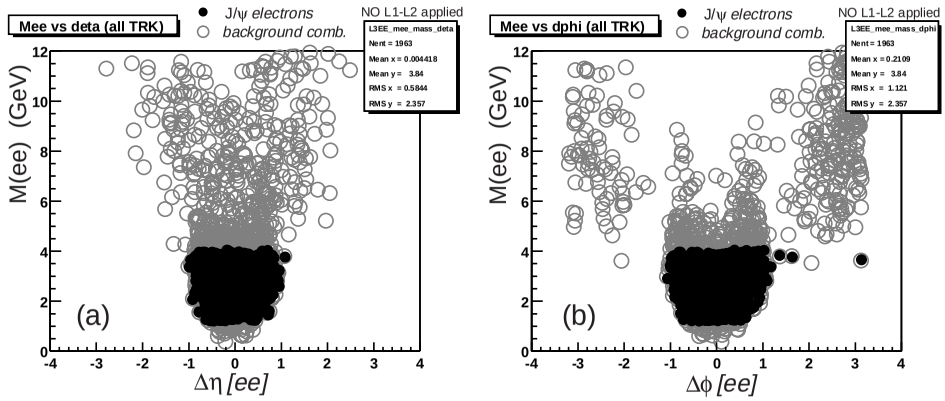

Figure 9.12: Distribution for the separation of lepton pairs (a) in η and (b) in ϕ, as a function of the reconstructed invariant mass in the J/ψ sample, respectively. Shown is the distribution for electron pairs from J/ψ (closed-circle) and from background combinations (open-circle).

accepted. The fraction of electromagnetic energy in the calorimeter, EM_{frac}, is also used. The value is defined by [124]:

$$EM_{frac} = \frac{\sum_{i=1}^{4} E_i}{E_{TOT}} \tag{9.3}$$

where E_i is the energy of a cluster deposited in the EM layers 1 through 4, and E_{TOT} is its total energy in a calorimeter tower (*i.e.,* sum of energies in EM layers 1-4, FH, and CH). As shown in Fig. 9.15, a cut at $EM_{frac} > 0.8$ is chosen. The calorimeter E_T threshold was set at 1.0 GeV in view of the observation that the calorimeter-based J/ψ mass (see Sec.9.3.1) indicates an energy scale uncertainty. An electron is "cal-tagged" provided that the reconstructed calorimeter cluster matches a MC electron within a radius of $\Delta R < 0.12$. This value is chosen based on the $\Delta\eta_{det}$ and $\Delta\phi$ matching distributions for the calorimeter and MC electrons, as given in Fig. 9.1. Similar to the methods used in Sec. 9.3.1, electrons can also be "trk-tagged" by allowing global tracks to match a MC electron within a radius of $\Delta R < 0.1$ (see Fig. 9.1).

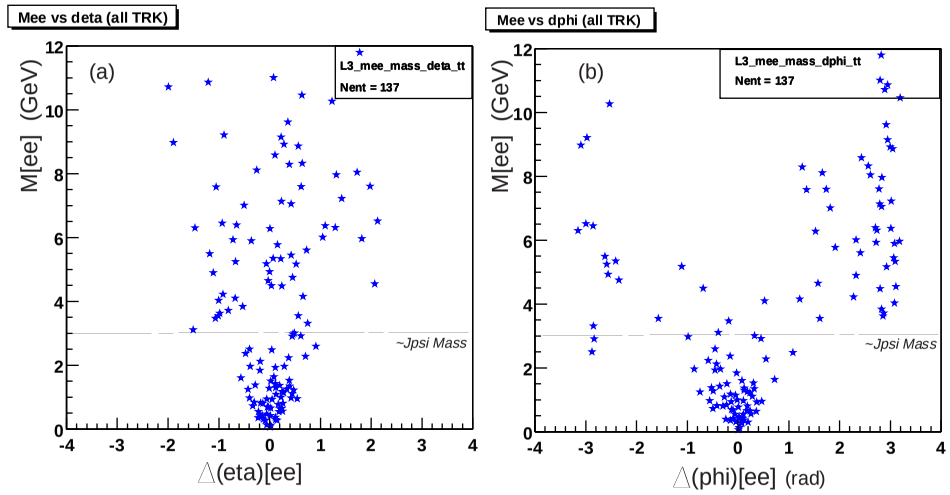

Figure 9.13: Distribution for the separation of lepton pairs in (a) η and (b) ϕ as a function of the reconstructed invariant mass for the QCD $p_T > 20$ GeV sample.

Each central calorimeter EM cluster that passes these basic requirements is subsequently matched to a track (CPS cluster) provided it is contained within a window: $|\Delta\eta| < 0.1$ (0.12) and $|\Delta\phi| < 0.1$ (0.12) rad. These values are based on the matching distributions given in Figs. 9.17 and 9.18 with the tracker and preshower, respectively. Any passing electron is respectively identified as either a "CAL-TRK" match or "CAL-CPS" match. As summarized in Fig. 9.16, electrons can thus be classified into four mutually independent categories:

- Type 1: CPS cluster and Track match requirement with calorimeter clusters; since all detector systems are included, such electrons are labeled: *golden*.
- Type 2: Calorimeter and CPS cluster requirement; No track match.
- Type 3: Calorimeter cluster and track match requirement; No CPS cluster match.
- Type 4: Calorimeter cluster only; No CPS cluster or track match.

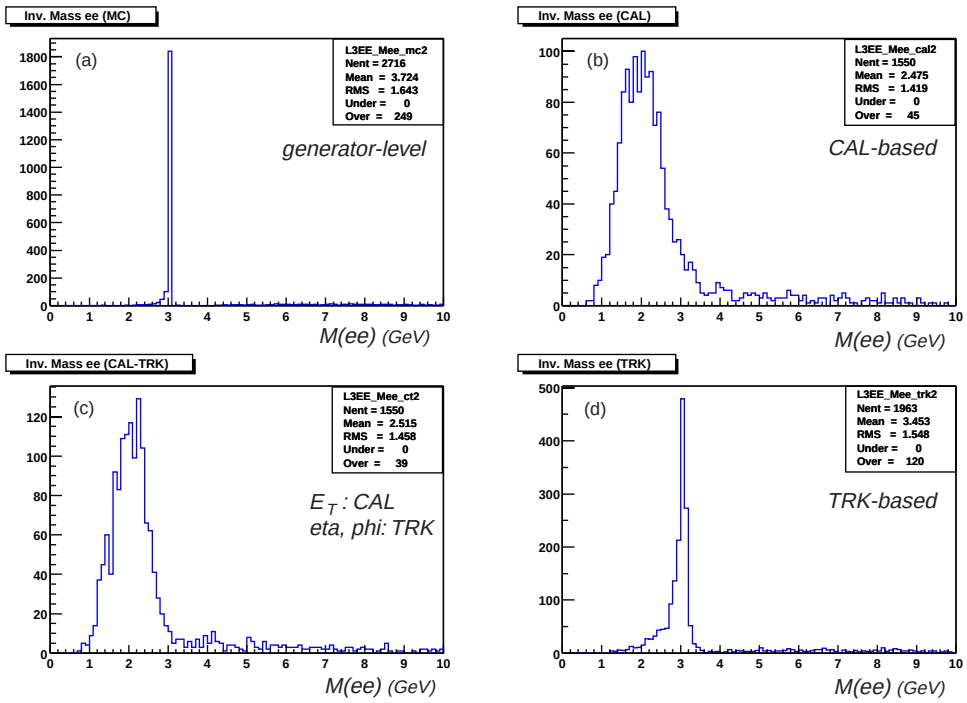

Figure 9.14: Invariant mass resolutions for $e^{\pm}$ pairs from J/ψ decays. Shown are reconstructed mass (using Eq.—9.2)from (a) MC generator-level, (b) calorimeter-based variables, (c) combined calorimeter E_T with track's $\Delta\phi$ and $\Delta\eta$ measurement, and (d) track-based variables.

Trigger	Definition	Description
Level 1	TDL(1.5, os); CEM(2,1.5)	2 opposite-sign (os) CFT track + CPS matches with p_T >1.5 GeV; and 2 EM objects (CAL) with E_T >1.5 GeV
Level 2	L2EM(2, 1.5, 0.8, q)	2 CAL-based EM clusters with: $E_T > 1.5$ GeV, $EM_{frac} > 0.8$, q = CPS-CAL match in 3×3 calorimeter tower array

Table 9.4: Summary of the L1 and L2 triggers for L3 event pre-selection.

Sample	Total Events (Rate in kHz) into L1	Level 1 "Accept" (Rate in kHz)	Level 2 "Accept" (Rate in kHz)
$J/\psi \to ee$	2076	1572	1422
QCD 2 GeV	15250 (1260)	156 (12.9)	108 (8.9)
QCD 5 GeV	13000 (266)	467 (9.6)	331 (6.8)
QCD 10 GeV	12750 (19.7)	2240 (3.5)	1721 (2.66)
QCD 20 GeV	16000 (1.1)	8547 (0.592)	6979 (0.480)

Table 9.5: Number of events in signal and QCD background samples passing the L1 and L2 triggers specified in Table 9.4. Values in parentheses indicate the corresponding rates in kHz at the input of L1 and at the output of each trigger level (see also Sec. 9.3.6).

	Selection Requirement
a) Calorimeter η taken wrt primary vertex at (0,0,0): η_{det}	< 1.2
b) Calorimeter E_T	> 1.0 GeV
c) EM fraction, EM_{frac}	> 0.8

Table 9.6: Basic selections applied to calorimeter clusters at Level 3.

By default, electrons contained in each of the four categories are mutually exclusive such that the hit efficiency for all individual subsystems within each type adds up to the total calorimeter efficiency. In order to limit the rates to within the trigger bandwidth, a track requirement is deemed necessary. Thus, the J/ψ study considers only electrons of Type 1 and 3. For higher p_T processes such as Z decays, candidates from all four categories can be considered. This simply follows by the construction of a Type 2 and 4 electron, which sets a minimum calorimeter E_T-threshold at 10.0 GeV, thereby preventing any J/ψ (or low-p_T) signal from passing. Such conditions represent tighter selections imposed within each type and are discussed below.

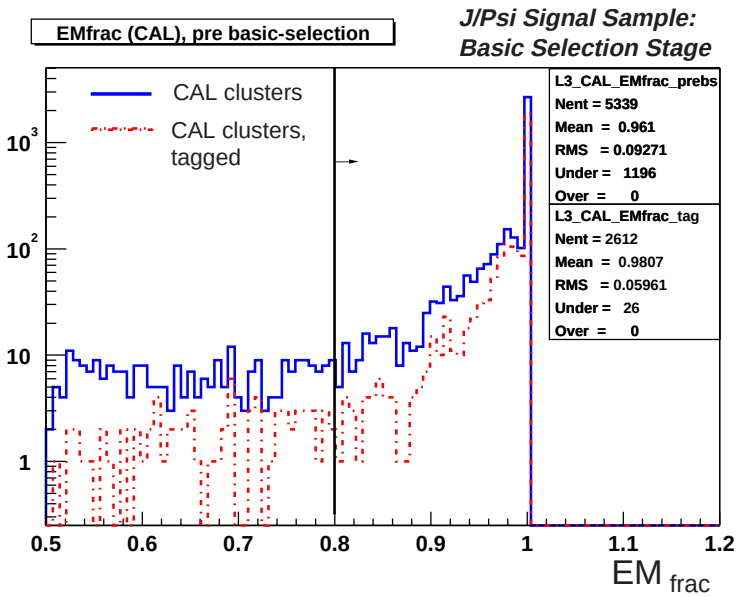

Figure 9.15: EM_{frac} measured within the central calorimeter fiducial. Shown is the distribution for reconstructed clusters (solid-line) and tagged-electron tracks (dashed-line). An initial cut at 0.8 is applied for basic selection of electrons.

Relationships and Combinations of Type 1 and Type 3

It is evident that the inclusion of a match using the preshower in Type 1 poses a "tighter" electron-ID when compared to that of Type 3 (see Fig. 9.16). This follows directly by the requirement that all three subsystems: track, CPS, and calorimeter be implemented for Type 1 but only two (the tracker and calorimeter) be used in Type 3. For the J/ψ, the means of determining the signal efficiency is to identify those events yielding a proper invariant mass, within a defined asymmetric mass window — a condition that requires the presence of at least two electron candidates. By construction, a pair can have at most three different combinations for electron types. The most stringent condition is to require each electron to be of Type 1. A less stringent requirement is one in which one electron is of Type 1 (*i.e.,* a so-called "tight" electron) while

	Electron Matching Requirements
a) Identify Track Match (CAL-TRK match)	$\lvert\Delta\phi\rvert < 0.1$ rad, $\lvert\Delta\eta\rvert < 0.1$
b) Identify Cluster Match (CAL-CPS match)	$\lvert\Delta\phi\rvert < 0.12$ rad, $\lvert\Delta\eta\rvert < 0.12$

Table 9.7: Definitions of an electron match for identifying (a) tracks and (b) CPS clusters with the calorimeter, as needed by the algorithm described in the text.

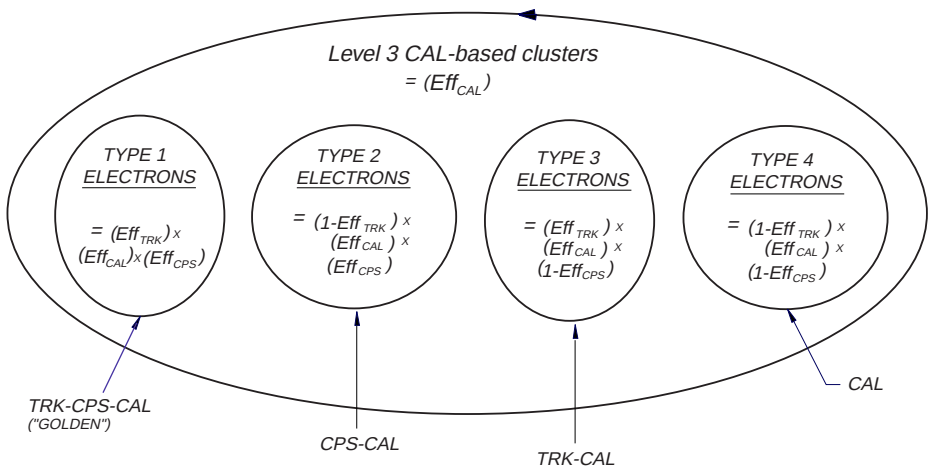

Figure 9.16: Schematic of the Level 3 algorithm for electron identification and selection. The sum of the efficiencies for the electron categories Type 1 through 4 yield the total calorimeter efficiency, Eff_{CAL}.

the other is of Type 3. This combination allows loosening the requirements on the pair while aiming to maintain sufficient background rejection. The least stringent condition on a pair requires both electrons be of Type 3. This combination may be subject to large background rates. For the remainder of this thesis, the i or j^{th} electron in a pair will be denoted as Type 1, T1, and/or Type 3, T3.

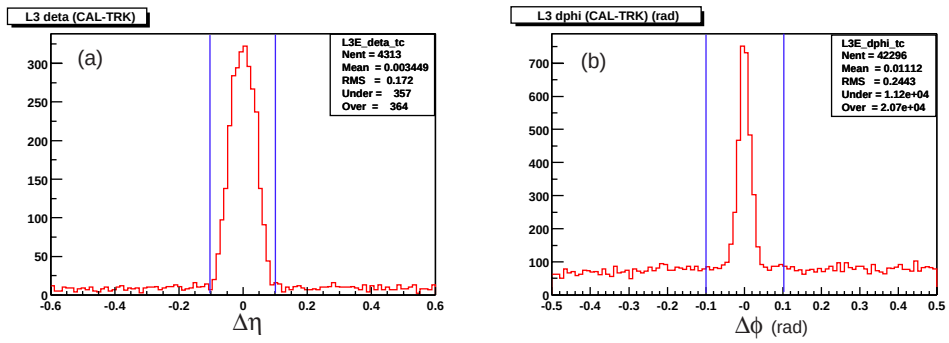

Figure 9.17: Distributions of matching between calorimeter clusters and global tracks for electron selection in (a) η and (b) ϕ for the J/ψ sample.

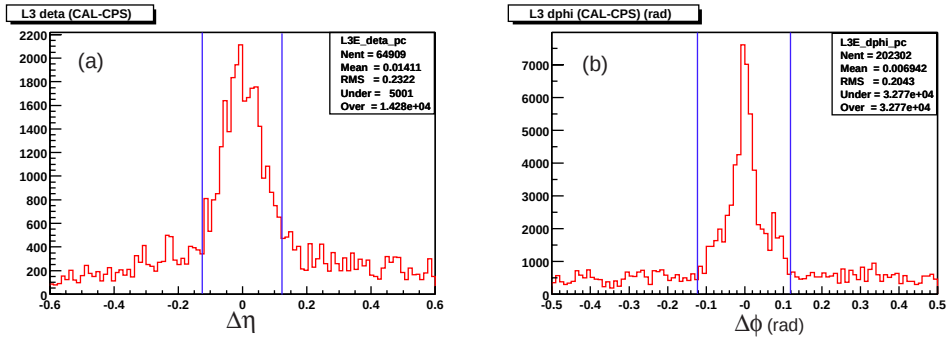

Figure 9.18: Distributions of matching between calorimeter and preshower clusters for electron selection in (a) η and (b) ϕ for the J/ψ sample.

Type 1 Electrons	*Number of Electron Clusters (Events)*				
	J/ψ	QCD Background Processes			
		2 GeV	5 GeV	10 GeV	20 GeV
Number of Events	(1422)	(108)	(331)	(1721)	(6979)
a) Post-Basic Selection	2513	182	564	2977	12687
b) Type 1 requirement: CAL-TRK match and CAL-CPS match	2157	13	66	491	3256
c) $\|\Delta z\| < 25.0$ mm	1924	6	19	173	1025
d) $\|\Delta\phi_{corr}\| < 12.0$ mrad	1931	5	13	112	722
e) $\|\Delta z\| < 25.0$ mm and $\|\Delta\phi_{corr}\| < 12.0$ mrad	1827	4	6	55	367
Rejection, $\mathcal{R} \equiv$ a)/e)	0.73±0.02	46^{+44}_{-15}	94^{+64}_{-27}	54^{+7}_{-6}	35±2
f) Calorimeter EM fraction, $EM_{frac} > 0.9$	2118	11	53	382	2379
g) $\Delta R=\sqrt{(\Delta s^2 + \Delta z^2)}$, $\Delta R < 25.0$ mm	1863	5	19	89	532
h) $EM_{frac} > 0.9$ and $\Delta R < 25.0$ mm	1832	5	10	67	425

Table 9.8: Number of electron cluster candidates for both J/ψ and QCD background events passing various trigger conditions in Type 1 after L1 and L2 triggers have been applied. The values for (a) correspond to the basic selection cuts given in Table 9.6, performed prior to the Type 1 requirement in (b). Variables in (c,d) correspond to the two tighter cuts studied in a Type 1 category; these together yield the final "regular" cut (e) imposed on a Type 1 candidate. Those cuts in (f)-(h) are shown only to compare their rejection capability with (e) on QCD samples and are not used in the final analysis. The corresponding values for the J/ψ electron efficiency and QCD rejection, $\mathcal{R}$, (per candidate) with statistical errors are given.

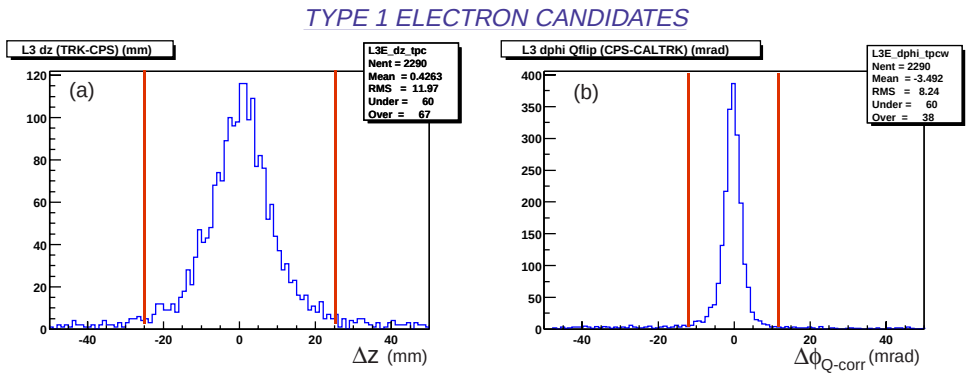

Figure 9.19: Type 1 selection variables and cuts implemented for electron identification on J/ψ sample: track-preshower match in (a) z and in (b) ϕ after correcting for magnetic field effects at the CPS radius. Also, shown are the intervals in which selections have been made.

Type 1 Electrons

Once the four type categories are established, additional selection requirements can be imposed to further purify Type 1 (or 3) electrons. Any variables, however, must be chosen with the rejection of QCD background processes while maintaining a good signal efficiency. For Type 1, the primary means of accomplishing this is to use selections incorporating joint SMT and CFT tracks (*i.e.,* global tracks) and the CPS (see Figs. 9.19 and 9.20 for J/ψ signal and QCD processes, respectively). As a reference, Table 9.8 contains the number of electron candidates for both L1-L2 pre-processed J/ψ signal and QCD background samples passing various trigger conditions set for Type 1. The table illustrates the level of rejection achieved by the various cuts used.

For global tracks and CPS, it is more natural to consider matching in the z coordinate than in η. For Type 1, electrons within $|\Delta z| = |z_{cps} - z_{trk}| < 25.0$ mm have been chosen. In order to obtain a 3-dimensional match, matching in ϕ between the tracker and CPS is also considered. Here, once the $\Delta\phi$ has been corrected for the non-zero magnetic field at the CPS radius, candidates

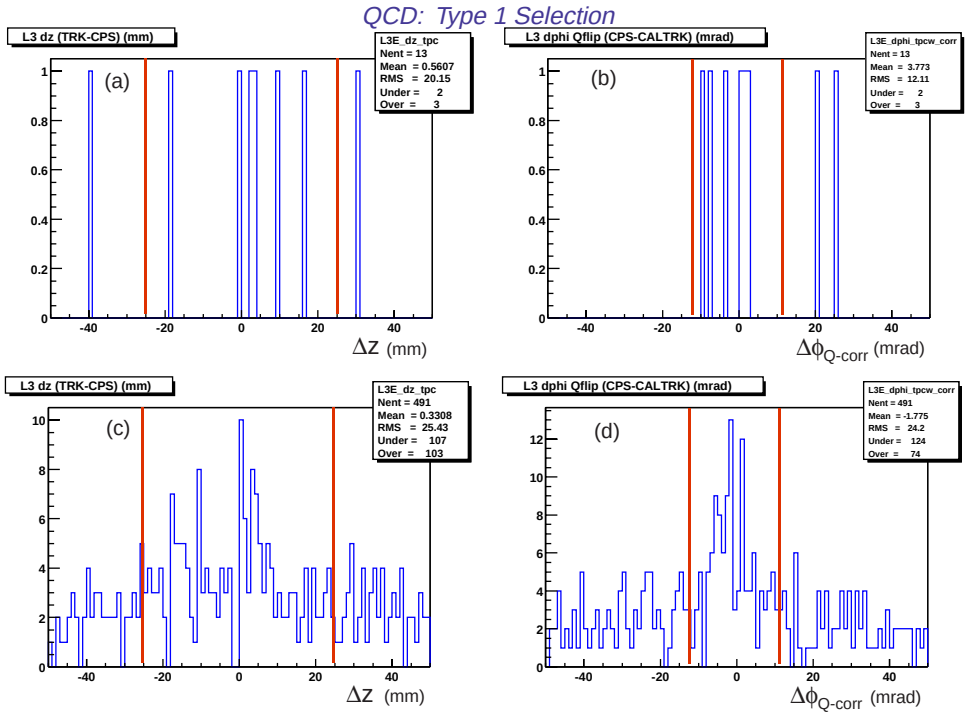

Figure 9.20: Similar distributions as in Fig. 9.19 for Type 1 selections implemented on (a-b) QCD $p_T > 2$ GeV and (c-d) QCD $p_T > 10$ GeV samples.

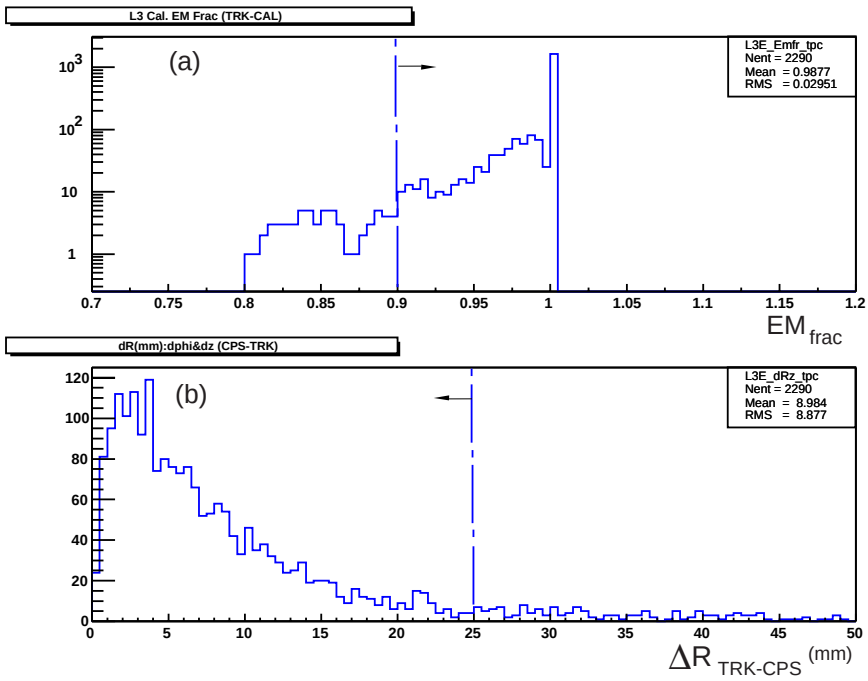

Figure 9.21: Miscellaneous selection variables studied for Type 1 electrons from the J/ψ: (a) calorimeter EM_{frac} and (b) ΔR match between a track and preshower cluster. See text for complete discussion.

must pass $|\Delta\phi_{corr}| = |\Delta\phi - \Delta\phi_{offset}| < 12.0$ mrad.

The number of clusters that pass the Δz and $\Delta\phi$ matches are independently measured. The resulting numbers are given in Table 9.8 (see entries (c,d)) . However, only those electrons that match in both ϕ and z define the final Type 1 candidate (see Table 9.8, entry (e)) and are used in the remainder of the analysis.

The rejection and discriminating power from the ϕ and z match should provide enough capability to limit the L3 rates without introducing a significant loss in signal efficiency. Nonetheless, additional variables have also been analyzed in order to determine their level of rejection on QCD samples. One such variable is the EM fraction, EM_{frac}, measured in the calorimeter (and also used for Type 3 electrons — see Sec. 9.3.3). A cut at a reasonable value

of 0.9 is chosen from the corresponding distribution (see Fig. 9.21a), but as listed in Table 9.8, it only has a minor effect on the background when compared to either Δz and/or $\Delta\phi$ conditions. One can also combine EM_{frac} with a track-CPS matching variable, ΔR, defined through the following:

$$\Delta s = R_{cps}\Delta\phi_{corr} \tag{9.4}$$

$$\Delta R = \sqrt{\Delta s^2 + \Delta z^2} \tag{9.5}$$

where R_{cps} is the CPS radius (in mm). The relation in Eq. 9.5 is valid under the approximation $R_{cps} \gg \Delta s$. Fig. 9.21b shows the distribution of ΔR on the J/ψ signal electrons. Although a combined $EM_{frac} > 0.9$ and $\Delta R < 25.0$ mm cut does provide rejection on the background (see Table 9.8), it is less powerful than a Δz and $\Delta\phi_{corr}$ matching requirement. Moreover, various other permutations can be used that combine any other variable. Also, variables such as the E/p ratio measured with the calorimeter and inner tracker can be considered (see Fig. 9.22). However, since Δz and $\Delta\phi_{corr}$ provide a sufficient handle on QCD rejection, a cut on E/p is not used for the present J/ψ L3 trigger.

Type 3 Electrons

Type 3 provides the second category for electrons and requires only a tracker-calorimeter match (see Fig 9.16). This type is considered to test whether the selection requirements can be relaxed, thereby helping to recover efficiency. One then relies on the presence of two candidates satisfying the J/ψ invariant mass to control QCD rates. Such relaxations will be shown in Sec. 9.3.6 to have a large impact on trigger efficiencies (and rates) when compared to those incorporating Type 1 candidates exclusively. As a reference,

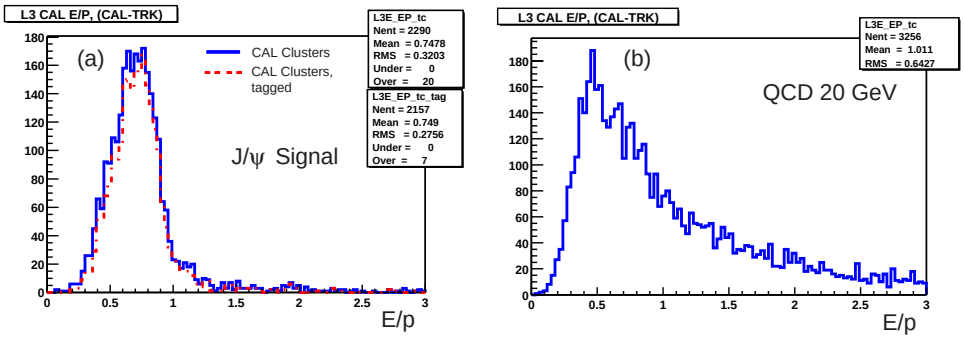

Figure 9.22: Distribution of E/p measured at L3 for a) signal and b) QCD. In (a), the reconstructed clusters (solid-line) are overlapped with tagged-electron tracks (dashed-line).

Table 9.9 lists the number of clusters that pass triggers defined in Type 3.

Tighter selection on Type 3 electrons can simply come from a combination of a track and calorimeter and/or any measured variable in the calorimeter itself (see Fig. 9.23). Two requirements are chosen. The first is simply the ϕ match, shown in Fig. 9.23a, between the calorimeter cluster and a track (*i.e.*, $\Delta\phi = \phi_{cal} - \phi_{trk}$). Other variables such as an η match between the calorimeter and tracker as well as the calorimeter cluster E_T have also been studied. Since, at present, both the calorimeter's η resolution and energy scale require work (see Sec. 9.3.1 for discussion), a match using $|\Delta\phi| < 0.05$ rad is defined for Type 3. Second, in an effort to improve QCD rejection, the EM fraction, EM_{frac}, measured in the calorimeter is also incorporated. As shown for J/ψ events in Fig. 9.23b, candidates that pass $EM_{frac} > 0.9$ are accepted. Taken together, these two conditions plus the original T3 definition define a Type 3 electron. Distributions for QCD 2 GeV and higher p_T (10 GeV) processes are illustrated in Fig. 9.24. Comparing Fig. 9.20 with Fig. 9.24, it is evident that the rejection power on QCD with Type 1 requirements is much stronger than that with Type 3.

Type 3 Electrons	*Number of Electron Clusters (Events)*				
	J/ψ	QCD Background Processes			
		2 GeV	5 GeV	10 GeV	20 GeV
Number of Events	(1422)	(108)	(331)	(1721)	(6979)
a) Post-Basic Selection	2513	182	564	2977	12687
b) Type 3 req'mnt: CAL-TRK match	2378	42	165	1079	5721
c) $\lvert\Delta\phi\rvert < 0.05$ rad	2352	34	135	832	4303
d) Calorimeter EM frac., $EM_{frac} > 0.9$	2334	34	135	872	4247
e) $EM_{frac} > 0.9$ and $\lvert\Delta\phi\rvert < 0.05$ rad	2311	26	110	663	3172
Rejection, $\mathcal{R} \equiv$ a)/e)	0.92±0.02	$7.0^{+0.97}_{-0.77}$	5.1±0.4	4.5±0.2	4.0±0.1

Table 9.9: Number of electron cluster candidates for both J/ψ and QCD background events passing various trigger conditions in Type 3 after applying L1 and L2 triggers. The values for (a) correspond to the basic selection cuts given in Table 9.6, performed prior to the Type 3 requirement in (b). The variables in (c,d) provide the tighter conditions studied in the Type 3 category; these together yield the final variables (e) used on a Type 3 candidate. The corresponding values for the J/ψ electron efficiency and QCD rejection, $\mathcal{R}$, (per candidate) with statistical errors are given.

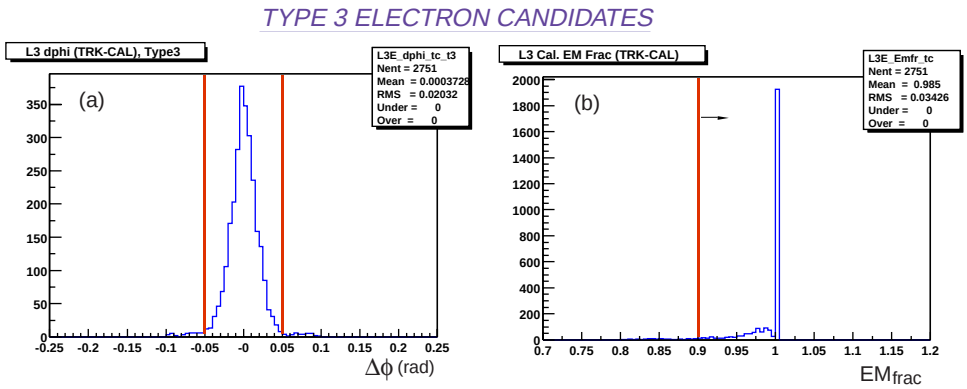

Figure 9.23: Type 3 selection variables and cuts implemented for electron identification in the J/ψ sample: (a) ϕ-match between the tracker and calorimeter and (b) EM fraction measured in the calorimeter. Also, shown are the intervals in which selections have been made.

Comments on Electron Selection and QCD Rejection

Although an extended discussion on trigger efficiency and QCD rejection is given in Sec. 9.3.6, it is important to note here that the tighter conditions set on a candidate within a type category have been meant to suppress QCD processes. For example, if the Δz and $\Delta\phi$ match between the CPS and track was not applied to a Type 1 electron but instead only the basic selections used, the efficiency for J/ψ electrons would be higher. However, as indicated in Tables 9.8 and 9.9, the background rejection per electron candidate with the basic selection would not be adequate. For the Type 1 selection, a sample dependent rejection factor of at least 35 ± 2 has been achieved for a corresponding electron efficiency of 0.73 ± 0.02. For the Type 3 selection, a rejection of at least 4.0 ± 0.1 is observed for an electron efficiency of 0.92 ± 0.02. The ratio of these numbers, 8.75 ± 0.45, demonstrates the power of the CPS to reject fake electron candidates.

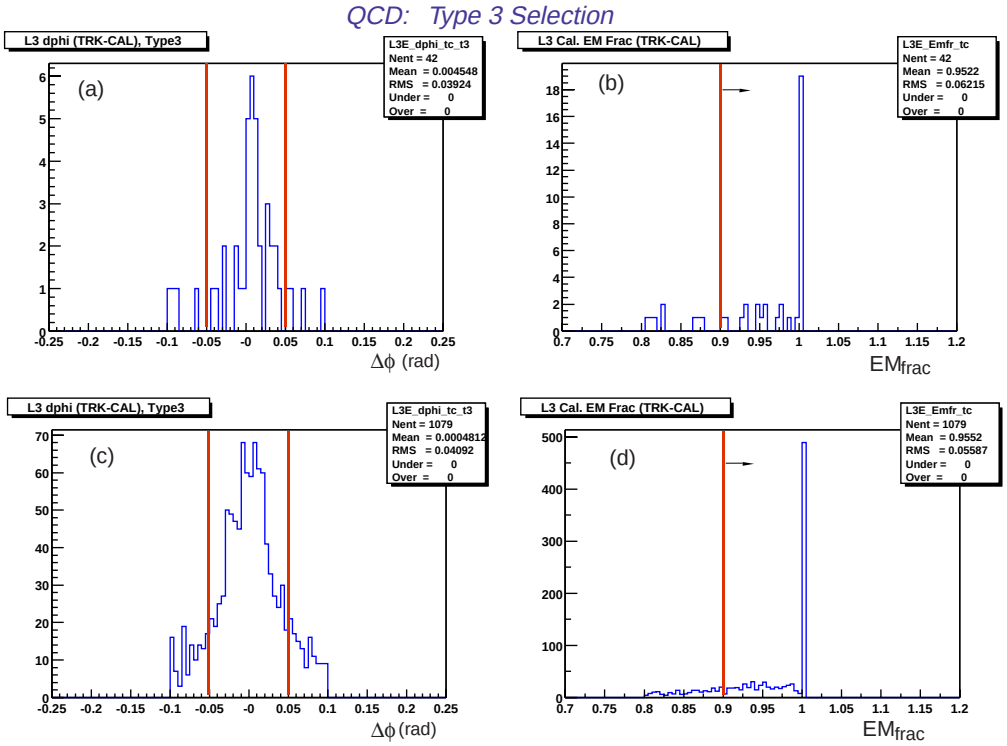

Figure 9.24: Similar distributions as in Fig. 9.23 for Type 3 selections implemented on (a-b) QCD $p_T > 2$ GeV and (c-d) QCD $p_T > 10$ GeV samples.

Type 2 and Type 4 Electrons

Two other electron types are available within the L3 selection algorithm presented here. The selections imposed in each of these types are listed in Table 9.10. The primary rejection variable is the measured calorimeter E_T threshold at 10.0 GeV. Lowering this limit would allow some level of acceptance for lower p_T electron samples such as from J/ψ. However, the 10 GeV threshold has been set *a priori* within the DØ trigger framework and has been meant mainly to trigger on electrons from higher p_T physics processes. Since no J/ψ passes a Type 2 or Type 4 requirement, no further discussion is given in this thesis.

Type 2 Electrons	Type 4 Electrons
a) Type 2 requirement: CAL-CPS match	a) Type 4 requirement: CAL clusters only
b) $\lvert\Delta\phi\rvert = \lvert\phi_{cal} - \phi_{cps}\rvert < 0.05$	b) Calorimeter, $E_T > 10$ GeV
c) Calorimeter, $E_T > 10$ GeV	c) Calorimeter, $EM_{frac} > 0.9$
d) Calorimeter, $EM_{frac} > 0.9$	—

Table 9.10: Summary of Type 2 and 4 electron selection requirements.

9.3.4 CPS Detector Efficiency

Each event for the J/ψ sample was processed through the selection criteria, and the information from that event stored. The total number of electron clusters passing each candidate type (*i.e.,* Type 1 or 3), $N_{clus}^{Type1,3}$, has been given in Table 9.11 for the two different calorimeter cluster cone sizes studied. By construction, the CPS efficiency, ϵ_{CPS} is determined through the relationship:

$$\epsilon_{CPS} = \frac{N_{clus}^{Type1}}{N_{clus}^{Type3}} \times 100\% \tag{9.6}$$

The value of ϵ_{CPS} indicates the efficiency for identifying a CPS-cluster match in the L3 trigger algorithm. Using Eq. 9.6, a CPS detection efficiency on the order of 80% is possible with a rejection of 8.75 (as quoted in Sec. 9.3.3). Additionally, the efficiency varies little ($\sim$1%) for the two calorimeter R_{cone} values. Efficiencies higher than 80% are not observed; this can be due to the strip and cluster energy thresholds set at L3 as well as some contribution from the rate at which electrons fail to shower in the lead ($\simeq$13% at η=0) [125]. Nonetheless, the value does indicate that the preshower responds effectively in measuring EM-clusters.

R_{cone}	*L3: Number of clusters — J/ψ*		
	L3 Total	Type 1	Type 3
0.2	2513	1827	2311
0.4	2196	1570	1951

Table 9.11: Total number of clusters passing electron Type 1 and 3 for R_{cone} = 0.2 and 0.4.

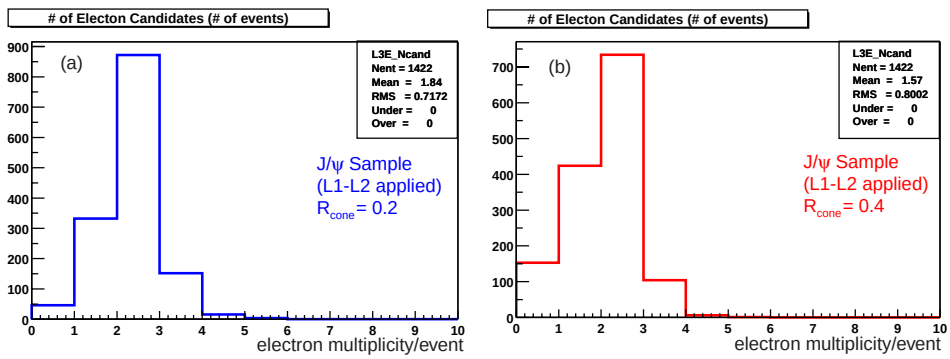

Figure 9.25: Number of candidates per events for J/ψ sample using calorimeter cluster cone sizes of (a) 0.2 and (b) 0.4. In either case, only those events with two or more electrons are used for the invariant mass calculation. Note the improvement in the number of events with two electrons for ΔR=0.2.

9.3.5 J/ψ Invariant Mass

Once a set of candidates pass the basic selections and Type 1 and 3 definitions, the identified electron pairs can be used to determine the dilepton mass (see Eq.9.2). A histogram indicating the candidate multiplicity per event for the J/ψ is given in Figs. 9.25(a,b) for two cone sizes R_{cone} = 0.2 and 0.4, respectively.

Since, as described in Sec. 9.3.1, the resolution from the tracker in measured energy/momentum is finer than that in the calorimeter, the invariant mass computation is based solely on track information of the electron pair. The mass is reconstructed and analyzed according to:

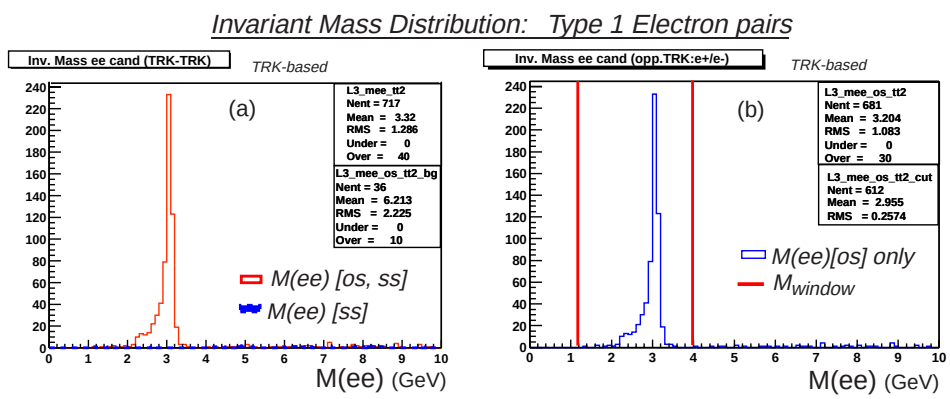

Figure 9.26: Invariant mass distribution for Type 1 pairs using R_{cone}=0.2. Given is the track-based results for (a) opposite- (os) and same- (ss) sign pairs (open-histogram), and same-sign pairs (shaded-histogram). The distribution in (b) shows results for only os pairs with the mass window shown by the vertical lines. See text for further discussion.

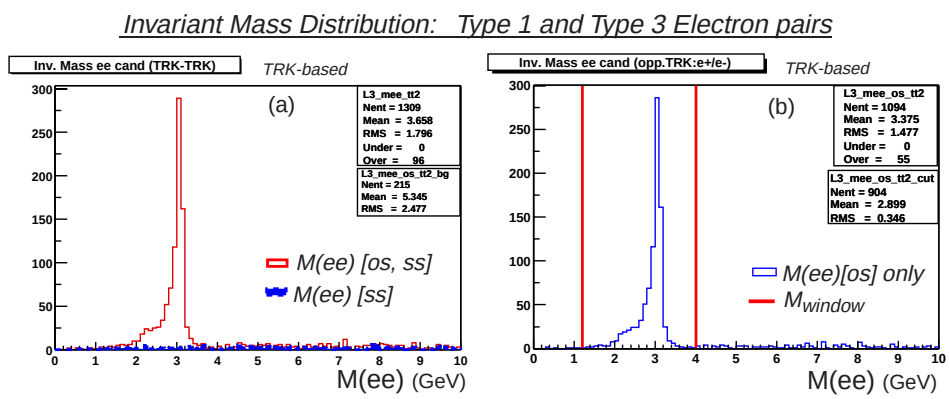

Figure 9.27: Similar invariant mass distribution as Fig. 9.26 for pairs where at least one electron is of Type 1 while the other is either Type 1 or 3. See text for further discussion.

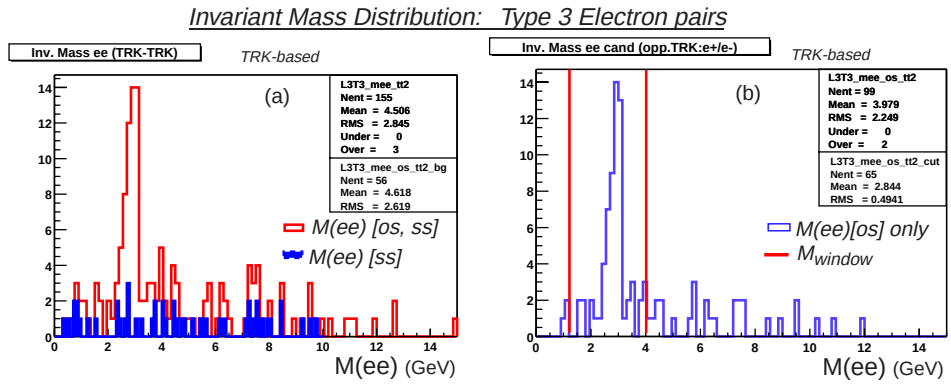

Figure 9.28: Similar invariant mass distribution as Figs. 9.26 and 9.27 for Type 3 pairs. See text for further discussion.

1. Invariant Mass using opposite-sign (os) + same-sign (ss) candidates; these yield a distribution corresponding to all candidates available from the algorithm. For a J/ψ decay, those pairs with a same sign cannot be identified as a J/ψ.

2. Invariant Mass using os + ss candidates within an asymmetric mass window, M_{window}: $M_{LL} < M(e_1e_2) < M_{UL}$, where the lower- (LL) and upper-limits (UL) are chosen at $M_{LL} = 1.2$ GeV and $M_{UL} = 4.0$ GeV, respectively, in order to maintain an interval sufficiently wide for signal.

3. Invariant Mass using only os candidates with no mass window.

4. Invariant Mass from (3) with M_{window}: $1.2 < M(e_1e_2) < 4.0$ GeV. The resulting events determine the L3 trigger efficiency for the J/ψ.

Fig. 9.26 yields the mass distributions for Type 1 electron pairs processed using $R_{cone} = 0.2$, taking into consideration a) the sign of the candidate and b) the mass window for opposite-sign only pairs. Also, Fig. 9.27 shows the same distributions where at least one electron is of Type 1 while the other is either Type 1 or Type 3. Clearly, the latter yields a larger event sample and

hence, an increased trigger efficiency (see Sec. 9.3.6). Finally, as reference, Fig. 9.28 illustrates the distribution for a Type 3 pair. From such plots, the signal efficiency and background rate are calculated and discussed next.

9.3.6 L3 J/ψ Trigger: Signal Efficiency and Rates

The Level 3 J/ψ trigger is given in terms of those events that contain oppositely charged pairs each of a particular electron type (*i.e.,* Type 1 and/or Type 3) contained within the mass window defined in Sec. 9.3.5. The signal efficiency is measured from only these events and is computed by:

$$\epsilon_{signal} = \frac{N_{events}(os, M_{window})}{N_{events}(\text{Total})} \tag{9.7}$$

For the L3 analysis, $N_{events}(\text{Total}) = 1422$, and refers to the total events at the output of L1-L2 triggers. For the combined L1-L2-L3 efficiency, $N_{events}(\text{Total})$ $= 2076$, the number of events at the input of L1.

The efficiency by itself is meaningless and is only interesting in conjunction with the level of QCD rejection achieved. A measure of the rejection is given in terms of the trigger rate at a beam luminosity, $\mathcal{L}$, or equivalently, the average number of minimum-bias interactions, $< N_{mb} >$, expected at $\mathcal{L}$. For the QCD samples studied here, $< N_{mb} > = 0.7$. This corresponds to a Run II luminosity of $\mathcal{L} = 3.2 \times 10^{31}$ cm^{-2}s^{-1} with a 396 ns bunch spacing. These values represent the nominal running conditions for the experiment in Run IIa. The rate, R, is then evaluated by:

$$R = (\mathcal{L} \times \sigma_{QCD})(F_{pass}) \tag{9.8}$$

where σ_{QCD} is the QCD cross-section (p_T-dependent), listed in Table 9.3, and F_{pass} is the fractional number of events passing a trigger. Conveniently, the

	Number of Events: J/ψ					
	$R_{cone} = 0.2$			$R_{cone} = 0.4$		
	e_i=T1 e_j=T1	e_i=T1 e_j=T1 *or* T3	e_i=T3 e_j=T3	e_i=T1 e_j=T1	e_i=T1 e_j=T1 *or* T3	e_i=T3 e_j=T3
a) N_{events}(Total)	1422	1422	1422	1422	1422	1422
b) os + ss, No M_{window}	717	1309	155	561	997	95
c) os + ss, M_{window}	614	956	79	489	763	58
d) os, No M_{window}	681	1094	99	536	859	66
e) os, M_{window}	612	904	65	488	730	49
L3 Signal Efficiency (%)	43	64	4.5	34	51	3.4

Table 9.12: Number of events in the J/ψ sample passing various mass conditions listed in the text. The events have been grouped according to electron pairs of Type 1 (T1) and/or Type 3 (T3). Results for both $R_{cone} = 0.2$ and 0.4 are given as is the final estimate of the L3 signal efficiency.

rate out of L3 can be taken as the product of the rate into L1, listed in Table 9.5, and F_{pass} using the L3 algorithm.

Table 9.12 provides the values for the number of events passing the four reconstructed mass distributions listed in Sec. 9.3.5, for two different calorimeter clustering cone sizes studied with the J/ψ. It is immediately evident that reducing R_{cone} does improve the signal efficiency by 7-12% when requiring electrons to be of Type 1. The same setting is run on QCD samples to verify the level of background rejection. The estimate for QCD events passing the required L3 trigger appears in Table 9.13 with the corresponding rates given in parentheses. For lower-p_T QCD processes (*i.e.*, $p_T > 2$, 5 GeV) with at least one electron taken as Type 1, zero events ($R \simeq \mathcal{O}(0\text{ Hz})$) pass the opposite-sign

and M_{window} trigger.

The statistical sensitivity of the 2 GeV QCD sample can only provide an upper-limit for the L3 J/ψ trigger rate. The two events passing the basic selection criteria (Table 9.13) correspond to a rate of 166 Hz. Application of tighter electron selection criteria reduce this to zero events. One can improve the sensitivity by assuming that the probability of a given track to fake an electron is uncorrelated with other tracks in the event. The rejection of the Type 1 selection for the 2 GeV QCD sample is, from Table 9.8, 46^{+44}_{-15}. The estimate of the overall Type 1 rejection, R'_{T1}, can be refined by including the information from higher p_T bins using the following formula:

$$R'_{\mathrm{T1,T3}} = \frac{\sum\limits_{p_T\ bin} w_i R_i}{\sum\limits_{p_T\ bin} w_i}, \tag{9.9}$$

where R_i is the rejection determined from the ith p_T-bin and w_i is the corresponding weight defined using the corresponding QCD cross sections (see Table 9.3) as $\sigma_i/\sigma_{\mathrm{tot}}$, where σ_{tot} is the total QCD cross section. Using the results of Table 9.8, the estimated value of the R'_{T1} is 54^{+38}_{-13}. Analogously, using the results of Table 9.9, the rejection of the Type 3 selection is $R'_{\mathrm{T3}} = 6.7 \pm 1.1$. In each case, the error is dominated by the statistics of the 2 GeV sample.

The rejection of the Level 3 J/ψ trigger can be estimated as:

$$\begin{aligned} R(\mathrm{Type1-Type1}) &= R'_{\mathrm{T1}} \times R'_{\mathrm{T1}} \times R_{mass,os}, \\ R(\mathrm{Type1-Type3}) &= R'_{\mathrm{T1}} \times R'_{\mathrm{T3}} \times R_{mass,os}, \end{aligned} \tag{9.10}$$

where $R_{mass,os}$ is the rejection from requiring the electron candidates have opposite sign and satisfy the mass window requirement. The value of $R_{mass,os}$ is determined from the QCD 2 GeV sample using events that have at least

one Type 1 or Type 3 candidate, which have also satisfied the Level 1 and Level 2 requirements. In these events, each candidate is in turn paired with all other tracks found in the event to form pseudo-J/ψ candidates. The value of $R_{mass,os}$ is measured to be $146/49 = 3.0 \pm 0.4$.

Using Eq. 9.10, the estimated rejections are: $R(\text{Type1} - \text{Type1}) = 8750^{+8750}_{-3200}$ and $R(\text{Type1} - \text{Type3}) = 1085^{+800}_{-350}$. The errors are dominated by the statistics of the 2 GeV QCD sample. The corresponding event rates for the assumed Level 1 and Level 2 trigger on QCD 2 GeV events, using Table 9.5, is 1.0 ± 0.4 Hz for Type 1 pairs and 8.2 ± 2.7 Hz for Type 1-Type 3 pairs, yielding a total rate of 9.2 ± 2.7 Hz.[2] It should be noted that applying the above method and comparing the expected rate for the Type 3-Type 3 pairs with entry (c) of Table 9.13 gives 66 ± 18 Hz vs. an observed 83 Hz (QCD 2 GeV) and 50 ± 14 Hz vs. an observed 22 Hz (QCD 5 GeV); both values are consistent given the observed rates are each based on one event passing. The agreement suggests that rates determined using Eq. 9.10 are robust.

The predicted rate is at the upper-end of the available bandwidth; however, given the inherent uncertainties in the simulation, one can conclude that the trigger meets the requisite criteria. It should be stressed that this rate is based on a L1-L2 trigger that results in an unrealistic value of 8.9 kHz into L3. Clearly, improvements to Level 1 and Level 2 are required. If one assumes a prescale factor of 20, necessary to reduce the rate into Level 3 to $\mathcal{O}(500)$ Hz, then the proposed Level 3 triggers results in a rate out of Level 3 of 0.46 ± 0.14 Hz, well within the bandwidth constraints.

If one imposes each electron in a pair to be of Type 1, more than adequate QCD rejection is achieved, suggesting that this requirement is too stringent. Instead, the looser condition, where at least one electron is of Type 1 while

[2]For the event rates, the errors have been symmetrized by taking the uncertainty in the rejection that establishes an upper-bound to the central value.

Level 3 Trigger	*QCD Rate in Hz (Number of Events)*				
	Estimate	L3 Observed			
		2 GeV	5 GeV	10 GeV	20 GeV
Basic Selection + (os, M_{window})	—	166 (2)	—	—	—
(a) e_i=T1, e_j=T1: os, M_{window}	1.0±0.4	0 (0)	0 (0)	0 (0)	0 (0)
(b) e_i=T1, e_j=T1 or T3: os, M_{window}	8.2±2.7	0 (0)	0 (0)	1.5 (1)	1.2 (18)
(c) e_i=T3, e_j=T3: os, M_{window}	66±18	83 (1)	22 (1)	15 (10)	5.2 (75)

Table 9.13: Summary of the L3 QCD background rate for (a) Type 1, (b) Type 1 and Type 1 or 3, and (c) Type 3 pairs passing the trigger requirement of two opposite-sign (os) electrons, i, j, contained within a mass window, M_{window}, of $1.2<M(ee)<4.0$ GeV. For comparison, the basic selection rate with the QCD 2 GeV sample is also given. The L3 Observed columns are based on the output of the L3 algorithm, whereas the Estimate represents the QCD 2 GeV rate determined from Eq. 9.10. The values in parentheses denote the number of events passing the trigger.

the other can be either Type 1 or 3, not only significantly improves the efficiency (*i.e.,* from 43% to 64%) but still maintains an acceptable level of QCD rejection. The purity of the J/ψ sample selected can be determined from the fraction of events with a same-sign pair contained in the mass window before applying the opposite-sign requirement. The estimated purity is 94±1%. Note that the mass window utilized has been chosen such that the side-bands to the J/ψ signal could be used offline to monitor the backgrounds. Finally, as can be seen from Tables 9.12 and 9.13, an even looser trigger accepting combination of e_1= T3 and e_2 = T3 would make only a small improvement (4.5%) in signal efficiency, while having the QCD background rate rise dramatically. Therefore, a J/ψ trigger with a Type 3 pair is not viable.

Given the above discussion, the triggers in entries (a,b) of Table 9.13 are

Sample	post-MC (L1 rate)	Level 1	Level 2	Level 3	Overall ($\times 10^{-2}$)
$J/\psi \to ee$	1.04%	0.76	0.90	0.64	0.45
QCD 2 GeV	1.26 MHz	0.010	0.69	0.001	0.00073
QCD 5 GeV	266 kHz	0.036	0.71	0.0007	0.0018
QCD 10 GeV	19.7 kHz	0.018	0.77	0.0006	0.0076
QCD 20 GeV	1.1 kHz	0.053	0.82	0.0025	0.11

Table 9.14: Summary of signal efficiencies and QCD background rejection at each trigger level using triggers described in Tables 9.4 and 9.5 for L1-L2 and in Table 9.13 (triggers (a,b)) for L3. For the J/ψ, the overall efficiency considers MC generator-level effects. For QCD, the rejection capability at each stage is listed. Here, the L3 acceptances for QCD 2, 5 GeV are estimated from Eq. 9.10, whereas for QCD 10, 20 GeV, the values represent the rates observed with the L3 algorithm. All results correspond to $\mathcal{L}$=3.2$\times 10^{31}$ cm^{-2}s^{-1}.

chosen as the desired Level 3 J/ψ triggers. Including these with the L1 and L2 triggers outlined in Sec.9.3.2, Table 9.14 summarizes the performance of the DØ trigger system studied on the J/ψ and QCD background samples. Here, included with the QCD rejection capability is the signal efficiencies at the generator and trigger levels. One notes that the overall J/ψ efficiency is substantially lower ($< 1\%$) than at any individual trigger level since this value includes detector fiducial and kinematic acceptance effects.

9.3.7 Signal Improvements

Consulting the electron candidate multiplicity per J/ψ event given in Fig. 9.25, it is observed that a substantial number of events are identified as having zero or only a single electron candidate and, by definition, will fail the L3 J/ψ trigger. Moreover, since the L1 and L2 trigger both require two EM objects, it can be argued that a subset of these events may be misidentified at L1 and L2 as well as at L3. Because parameters and tools in the trigger

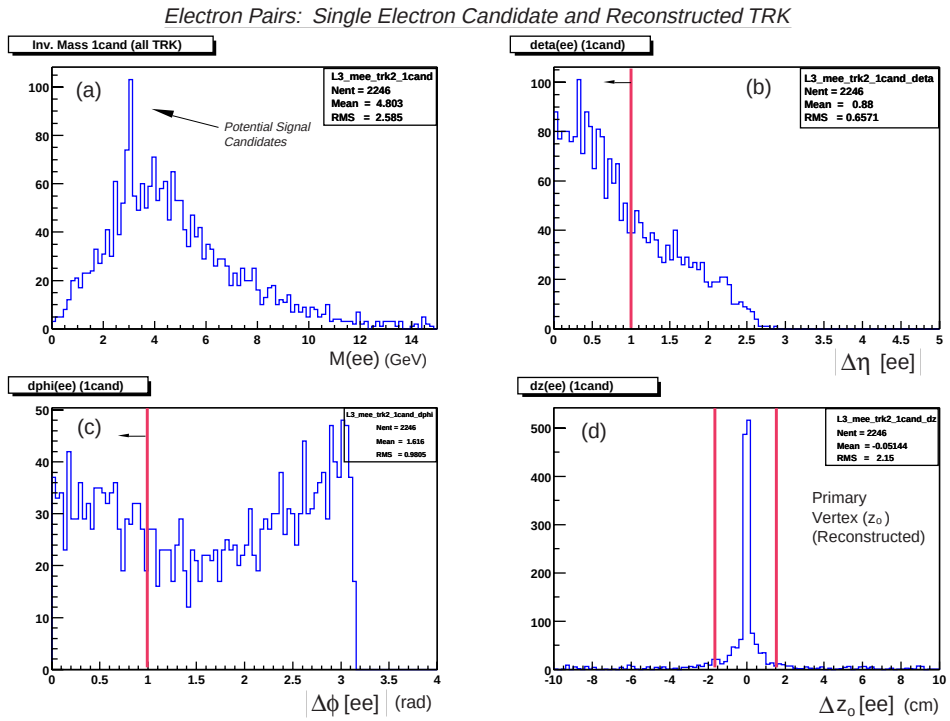

Figure 9.29: (a) Invariant mass distribution as for single electron candidates in the J/ψ signal sample paired with L3 reconstructed tracks. Also shown are corresponding (b) $\Delta\eta$, (c) $\Delta\phi$, and (d) $\Delta z_\circ$ distribution for all pairs. Results for $R_{cone} = 0.2$ are shown.

framework are interdependent, the effect is difficult to isolate to any individual trigger level. The interdependent parameters for L3 include a) the calorimeter clustering $E_T > 1.0$ GeV threshold set within the L3 filtering tool, b) the single-layer cluster energy threshold (set at 3.6 MeV) for identifying a 3D cluster in the CPS, c) selection cuts defined in the L3 algorithm developed here, d) matching resolutions from the different subsystems that are eventually incorporated for electron-ID, and/or e) the cone size for calorimeter clustering. In fact, processing the J/ψ and varying many of the values in (a)-(d) only has a minor effect on the single-electron candidate events (*i.e.,* at the 1-3% level). Instead, a significant change occurs when R_{cone} is reduced from 0.4 to 0.2.

Here, events with zero (single) electron decrease from 153 (424) at $R_{cone} = 0.4$ to 46 (332) at $R_{cone} = 0.2$. This change is on the order of 18-20% for the single electron case and motivates an effort to improve the signal efficiency with the remaining 332 event subset.

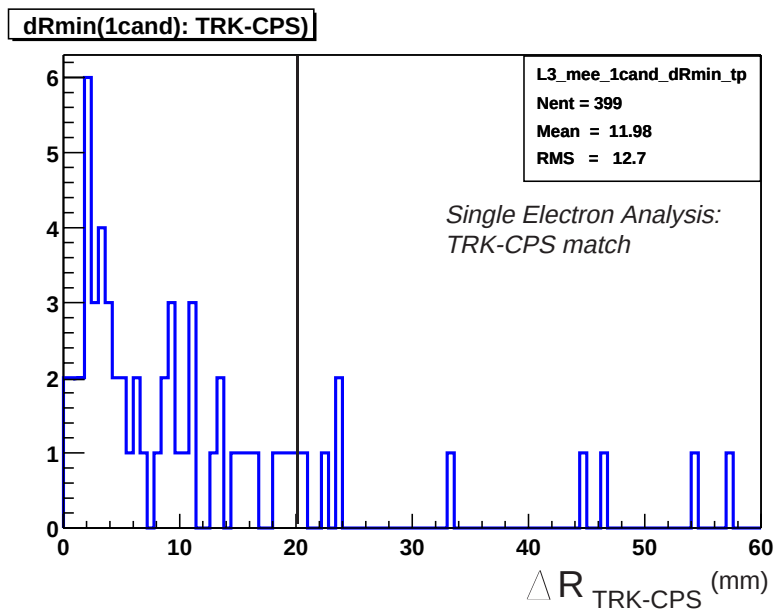

Figure 9.30: ΔR matching distribution for L3 tracks and preshower clusters needed for single electron candidate and L3 track pairing. Value for the cut has been chosen to help suppress QCD backgrounds during invariant mass reconstruction.

One method for gaining trigger efficiency while maintaining rejection is to identify events that contain a single Type 1 electron candidate, e_1, and pair each with all L3 tracks, e_2^{TRK}, thereby reconstructing an invariant mass, $M(e_1,e_2^{TRK})$. Such a mass distribution for the 332 events is given in Fig. 9.29a. Clearly, superimposed on the large background, is a mass peak near 3.0 GeV, indicating J/ψ candidates. In order to isolate the background, the trigger must introduce some level of bias by requiring the pair be separated in $\Delta\phi$ and $\Delta\eta$. The optimal values for each can be obtained by observing the reconstructed

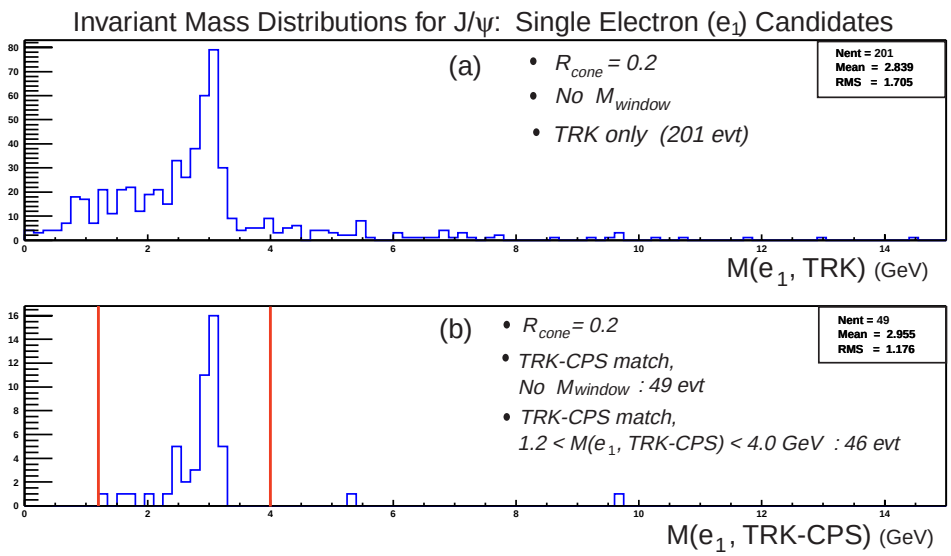

Figure 9.31: Invariant mass distribution for single electron candidates in the J/ψ signal sample paired with L3 reconstructed tracks requiring (a) η, ϕ, and common vertex conditions. Also given is the corresponding distribution requiring (b) a track-preshower match. The mass window in (b) is shown by the vertical bars.

mass as a function of each variable on events with at least two or more lepton candidates (see Secs. 9.3.1 and 9.3.5). These distributions are summarized in Figs. 9.11 and 9.12. One observes that pairs for the J/ψ can be quite collimated (see also Ref. [109]), and thus, a value of $|\Delta\phi(\mathrm{ee})| < 1.0$ rad and $|\Delta\eta(\mathrm{ee})| < 1.0$ is taken. Moreover, a pair must originate from a common vertex, $z_\circ$, with $|\Delta z_\circ(\mathrm{ee})| < 1.6$ cm (see Fig. 9.29). The resulting mass is shown in Fig. 9.31a. Although a significant amount of background is removed, the same criteria when applied on the QCD 2 GeV sample allow two events ($R \simeq 160$ Hz) to pass. Therefore, the e^{TRK} must match a CPS cluster as well, defined by Eqs. 9.4 and 9.5, in a radius $\Delta R < 20.0$ mm (see Fig. 9.30). Finally, a mass window of $1.2 < M(e_1, e_2^{TRK-CPS}) < 4.0$ GeV is imposed. Such a trigger yields a mass distribution shown in Fig. 9.31b. It provides an additional 46 events (out of 332) for potential J/ψ candidates, which add to the 904 events (see Table 9.12) from the previous trigger to improve the L3 efficiency from 63.6% to 66.8%. It further illustrates the use of the preshower as an effective tool in removing backgrounds.

The same trigger is applied to the QCD event samples. Requiring a track-CPS match for the second electron, zero events pass the 2, 5, and 10 GeV samples, and in the 20 GeV sample, a single event passes. This translates to a rate of about 0.07 Hz and is negligible when compared to previous values. Therefore, this algorithm can be incorporated with that discussed in Sec. 9.3.6 to provide a means for gaining signal efficiency.

9.3.8 Study of L3 b-tagging

The J/ψ sample can also be used to study the semi-leptonic decay of the b-quark. One will recall that two of the electrons: e_{ij}, where $i, j = 1{,}2$ and $i \neq j$ decay from the J/ψ and establish the J/ψ mass or $M(e_{ij}) < 3.2$ GeV

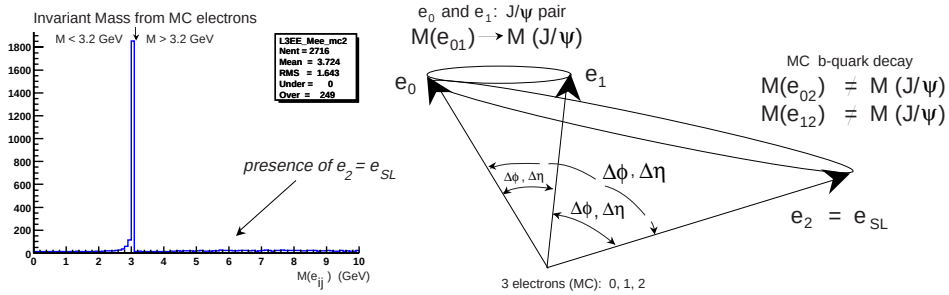

Figure 9.32: Figurative example of three MC-level electrons in the J/ψ sample. Two of these arise from J/ψ decays while the third must be from the semi-leptonic decay of the b-quark.

Variable	*L3: ($b \to e$)*	
	R_{cone}=0.2	R_{cone}=0.4
N_{SL}^{Total}	174 jets	174 jets
N_{FID}^{TRK}	124 cand	124 cand
N_{e}^{Type1}	61 cand	48 cand
ϵ_{tag}	49.2%	38.7%
F_e	71.3%	71.3%
$\epsilon_{tag} \times$ BR($b \to e$)	4.1%	3.2%

Table 9.15: Summary of yields for tagging the electron in the semi-leptonic decay of the b using the J/ψ signal sample with $R_{cone} = 0.2$ and 0.4. Included with the tagging efficiency is the overall performance from the potential method. See text for definition of variables.

(see Fig. 9.32). At the MC-level, the presence of a third electron is attributed to the semi-electronic decay of a b-quark in the event. A mass value greater than 3.2 GeV arises by incorrectly pairing a J/ψ electron with that from the b. The presence of these so-called "semi-leptonic" electrons, e_{SL}, is known at the generator-level from the invariant mass distribution and is "tagged". Subsequently, any reconstructed Type 1 electron candidate that matches this "tagged" e_{SL} is identified, establishing a method for b-tagging studies.

An introductory study using such an algorithm is presented here. In terms

of the MC e_{SL} candidates with TRK match, N_{FID}^{TRK}, and those that are Type 1, N_e^{Type1}, the tagging efficiency, ϵ_{tag}, can be computed using:

$$\epsilon_{tag} = \frac{N_e^{Type1}}{N_{FID}^{TRK}} \tag{9.11}$$

Similarly, taking into consideration the total number of events with a possible semi-leptonic decay, N_{SL}^{Total}, the fraction of electrons with a track in the fiducial volume, F_e, is defined as:

$$F_e = \frac{N_{FID}^{TRK}}{N_{SL}^{Total}} \tag{9.12}$$

Using these definitions, the results for the two different cluster cone sizes are summarized in Table 9.15. Of course, the overall tagging performance is obtained by incorporating the $\sim$10% branching ratio for $b \rightarrow e$ decays. Although the values seem low at the present time, the study presents a possible direction in developing an online algorithm for b-tagging.

Chapter 10

Summary and Conclusions

The Forward Preshower provides a direct opportunity in extending the physics program for DØ. The detector is designed to work together with the central tracking system and the electromagnetic calorimeters to aid in triggering, particle identification, and energy resolution. It will substantially assist in low-p_T electron identification. Each of these measurement capabilities has helped determine the choice in technology as well as defined the methods and requirements necessary for the construction, installation, and alignment of the system at DØ. A detailed outline of each aspect has been presented. Commissioning of the completed detector has begun, and algorithms needed in reconstructing physics signatures are being developed.

Additionally, a means for online identification of low-p_T electron pairs, in particular, from J/ψ decays has been studied. Such a L3 trigger, summarized in Table 10.1, has indicated that at least 60% of signal can be reconstructed with sufficient rejection of fakes originating from QCD dijet processes. Likewise, the requirement that at least one electron be matched in all three subsystems: central tracker, preshower, and calorimeter (*i.e.,* Type 1) has shown that preshower information is crucial in reducing the QCD background content. The use of the granular resolution for low-p_T electrons with the preshower

Trigger Description	Parameter Settings
a) L3 Calorimeter clustering	$R_{cone} = 0.2$, $EM_{frac} > 0.8$ $E_T^{CAL} > 1.0$ GeV (uncertainties about E-scale)
b) L3 Preshower clustering	Cluster Energy: $E_{thrsh} > 3.6$ MeV
c) L3 algorithm	Electron-pair: $e_{i,j}$ i≠j, satisfying: i) $e_{i,j}$ = Type 1 (opposite-sign track, $1.2 < M(e_i, e_j) < 4.0$ GeV) ii) e_i = Type 1 and e_j = Type 1 or Type 3 (opposite-sign track, $1.2 < M(e_i, e_j) < 4.0$ GeV) iii) e_1 = Type 1 and e_2 = TRK-CPS match using $\|\Delta R\| < 20.0$ mm; and $\|\Delta\eta(e_1, e_2)\| < 1.0$, $\|\Delta\phi(e_1, e_2)\| < 1.0$ rad, $\|\Delta z_\circ(e_1, e_2)\| < 1.6$ cm

Table 10.1: Summary of the Level 3 J/ψ trigger for DØ using preshower information described in the thesis. Details on the exact definitions and requirements for each variable as well as for Type 1 and 3 are presented in Chap. 9.

was a primary motivation in designing and constructing the CPS and FPS detectors for DØ in Run II.

The study has also optimized a number of the techniques and variables associated within the DØ software framework. Of course, many of these do require further investigation — *e.g.,* the uncertainty in the calorimeter energy scale and its matching performance [114]. Improved methods are also needed to reduce trigger rates at L1 and L2. At the same time, J/ψ decays with the Forward Preshower, whose L3 filtering tools require development, need to be incorporated. The limited statistics available in both the signal and QCD samples only estimates the performance of the L3 algorithm, and by no means are the studies reported in this thesis final. It is assumed that as the software gradually develops and the resources become available for steady-state detector operation, the approach will become more sophisticated; nonetheless,

the analysis does provide a first method for low-p_T electron-ID using signals from an integrated DØ detector.

The trigger described here, in addition to several other low- (and high-) p_T filters, is presently being adapted into DØ. Meanwhile, as the run progresses, all of these triggers are expected to significantly enhance the capabilities of the detector on a number of physics processes such as B-physics, W and top final states, and Higgs and SUSY searches. Preshower information will continue to play an important role in such measurements. Additionally, the design and methods used for the preshower assembly and readout will promote newer technologies and thereby help develop improved tools for particle detection.

Bibliography

[1] M. K. Gaillard *et al.,* "The Standard Model of Particle Physics", *Rev. Mod. Phys.* (1998).

[2] F. Halzen and A. Martin. *Quarks & Leptons: An Introductory Course in Modern Particle Physics.*, John Wiley & Sons, Inc., (1984).

[3] B. Abbot *et al.,* (DØ). "Measurement of the W Boson Mass Using Large Rapidity Electrons", *Phys. Rev. D* **62:**092006, (2000).

[4] W. E. Burcham and M. Jobes. *Nuclear and Particle Physics.*, Longman Scientific & Technical, (1995).

[5] G. L. Kane. *Modern Elementary Particle Physics.*, Addison-Wesley, 1993. (Updated edition).

[6] D. J. Griffiths. *Introduction to Elementary Particles.*, John Wiley & Sons, Inc., (1987).

[7] Particle Data Group. *Review of Particle Physics.*, *Eur. Phys. J.* C 3, 1-794; Springer-Verlag, (1998).
(URL: http://pdg.lbl.gov/)

[8] LEP Working Group for Higgs Boson Searches, "Search for the Standard Model Higgs Boson at LEP", Int. Conf. on High Energy Physics of the European Phys. Soc., Budapest, Hungary; hep-ex/0107029, (2001).

[9] T. Han *et al.,* "Exploiting $h \to W^*W^*$ decays at the upgraded Fermilab Tevatron", *Phys. Rev. D* **59:**093001, (1999) and references therein.

[10] UA1 Collaboration (CERN). *Phys. Rev. Lett.,* **122B:**103, (1983).

[11] UA2 Collaboration (CERN). *Phys. Rev. Lett.,* **122B:**476, (1983).

[12] UA1 Collaboration (CERN). *Phys. Rev. Lett.,* **126B:**398, (1983).

[13] UA2 Collaboration (CERN). *Phys. Rev. Lett.,* **129B:**130, (1983).

[14] S. Abachi *et al.,* (DØ). "Observation of the Top Quark", *Phys. Rev. Lett.,* **74:**2632, April 1995.

[15] F. Abe *et al.,* (CDF). "Observation of Top Quark Production in $p\bar{p}$ Collisions with the Collider Detector at Fermilab", *Phys. Rev. Lett.,* **74:**2626, April 1995.

[16] T. Kafka (*for the E872-DONUT Collaboration*). "E872-The Direct Observation of the ν_τ", *Nucl. Phys. B Proc. Suppl.,* **70:**204-206, 1999.

[17] LEP Electroweak Working Group, "A Combination of Preliminary Electroweak Measurements and Constraints on the Standard Model", hep-ex/0112021, (2001).
(URL: http://lepewwg.web.cern.ch/LEPEWWG/)

[18] S. Snyder. *Measurement of the Top Quark Mass at DØ.* PhD thesis, State University of New York at Stony Brook, Stony Brook, New York, USA, May 1995.

[19] A. S. Turcot (for the DØ and CDF Collaborations). "Higgs Hunting á la Tevatron", XXXVth Rencontres de Moriond, Les Arcs, France, (2000).

[20] D. E. Johnson. "Instrumentation Requirements for the Fermilab Main Injector", Internal Main Injector Note 76, (unpublished, 1992).

[21] R. A. Carrigan, Jr. and W. P. Trower. *Particles and Forces: At the Heart of Matter – Readings from Scientific American Magazine,* W. H. Freeman & Co., New York. (1986). See R. R. Wilson's January 1980 article on "Next Generation of Particle Accelerators", Pp. 59-79.

[22] L. M. Lederman. *Scientific American,* **264**(3):48-55, March 1991.

[23] Fermi National Accelerator Laboratory, Batavia, Illinois (USA). Tevatron Run II Handbook. Internal FNAL Note.
(URL: http://www-bd.fnal.gov/runII/index.html)

[24] W. J. Thompson. *Search for the Top Quark in the Muon + Jets Channel at DØ.* PhD thesis, State University of New York at Stony Brook, Stony Brook, New York, USA, February 1994.

[25] S. Abachi *et al.,* (DØ). "The DØ Detector", *Nucl. Instrum. Methods,* **A338**, 185 (1994).

[26] For additional information, see URL: http://www-d0.fnal.gov/hardware/upgrade/upgrade.html and links therein.

[27] The DØ Collaboration. "DØ Silicon Tracker Technical Design Report", Internal DØ Note 2169, (1994).

[28] A. Bean (for the DØ Collaboration). "Design of an Upgraded DØ Silicon Microstrip Tracker for Fermilab Run IIb", *Conf. Proc. of the 7th International Conference on Advanced Technology and Particle Physics,* Como, Italy, submitted to World Scientific, (2001).

[29] The DØ Collaboration. "DØ Run IIb Silicon Detector Upgrade: Technical Design Report", Internal DØ document (unpublished), (2001).

[30] J. Womersley (for the DØ Collaboration). "Run II has begun", preliminary results presented at the California Institute of Technology HEP Seminar, available from the author, (2001).
(see also URL: http://www-d0.fnal.gov/ womersle/womersle.html)

[31] The DØ Collaboration. "The DØ Upgrade Central Fiber Tracker: Technical Design Report", (1997).
(URL: http://d0server1.fnal.gov/projects/SciFi/cft_home.html)

[32] Kuraray International, 200 Park Ave., New York, NY 10166, USA. Tel. +01 (212) 986-2230.

[33] G. Gutierrez. "Central Fiber Tracker Mechanics: Ribbon Data", Internal DØ Document, (2001).
(URL: http://d0server1.fnal.gov/projects/sciFi/mechanical/documentation.html)

[34] D. Lincoln, private communication.

[35] D. Lincoln (for the DØ Collaboration), *Nucl. Instr. Meth.,* **A453**, 177–181 (2000).

[36] K. Del Signore *et al.,* "The Central Preshower Detector: A Core Dump of Useful Information", Internal DØ Note 3647, (1999).

[37] DØ Calorimeter Electronics Group. "TDR: Calorimeter Electronics Upgrade for Run 2", Ver. 1.7, (unpublished, 1998).
(URL: http://www-d0.fnal.gov/ d0upgrad/calelec/intro/tdr/tdrformat.htm)

[38] S. J. Wimpenny *et al., Nucl. Instrum. Methods,* **A279**, 107–113 (1989).

[39] P. Franzini *et al., Nucl. Instrum. Methods,* **A289**, 438–445 (1990).

[40] A. L. Spadafora *et al., Nucl. Instrum. Methods,* **A315**, 279–284 (1992).

[41] H. Aihara *et al., IEEE Trans. Nucl. Sci.,* **38**(2), 398–402 (1991).

[42] R. Kehoe. "Hadronic Calibration of DØ Calorimetry", *Frascati Calorimeter Conference, Conf. Proc.,* June 1996. Fermilab Conf-96/284-E.

[43] L. Sawyer *et al.,* (ICD Group). "Technical Design Report for the Upgrade of the ICD for DØ Run 2", Internal DØ Note 2686, (1997).

[44] B. Baldin *et al.,* (Muon Group). "Technical Design of the Central Muon System", Internal DØ Note 3365, (updated version, 1998).

[45] V. Abramov *et al.,* (Muon Group). "Technical Design Report for the DØ Forward Trigger Scintillation Counters", Internal DØ Note 3237, (1997).

[46] G. Alexeev *et al.,* (Muon Group). "Technical Design Report for the DØ Forward Muon Tracking Detector Based on Mini-drift Tubes", Internal DØ Note 3366, (1997).

[47] J. Butler *et al.,* (Muon Group). "The DØ Muon System Upgrade", Internal DØ Note 2780, (1996).

[48] For an extended description of trigger parameters, see URL: http://www-d0.fnal.gov/computing/trigsim/trigsim.html and links therein.

[49] G. C. Blazey (for the DØ Collaboration). "The DØ Run II Trigger", 10th IEEE Real-Time Comp. App. in Nuclear, Particle and Plasma Physics, Beaue, France, Conf. Proc., (1997).

[50] A. Lo, *et al.,* (Luminosity Monitor Group). "Luminosity Monitor Technical Design Report", Internal DØ Note 3320, (1997).

[51] V. Zutshi, private communication.

[52] P. Renton. *Electroweak Interactions.*, Cambridge University Press, (1990).

[53] The DØ Collaboration. "The DØ Upgrade: The Detector and Its Physics", Fermilab Pub-96/357-E, (1996).
(URL: http://higgs.physics.lsa.umich.edu/dzero/d0doc96/d0doc.html)

[54] N. Amos *et al.,* (CPS Group). "Design Report of the Central Preshower Detector for the DØ Upgrade", Internal DØ Note 3014, (1996).

[55] A. Gordeev *et al.,* (FPS Group). "Technical Design Report of the Forward Preshower Detector for the DØ Upgrade", Internal DØ Note 3445, (1998).

[56] B. Abbott *et al.,* (DØ). "A Measurement of the W Boson Mass at the Fermilab $p\bar{p}$ Collider", *Phys. Rev. D.,* **58:**092003. (1998).

[57] B. Abbott *et al.,* (DØ). "A Measurement of the W Boson Mass Using Large Rapidity Electrons", *Phys. Rev. D.,* **62:**092006. (2000).

[58] D. Amidei *et al.* "Future Electroweak Physics at the Fermilab Tevatron: Report of the *tev_2000* Study Group", Internal DØ Note 2589 & CDF Note 3177, (1996).

[59] B. Abbott *et al.,* (DØ). "Determination of the Absolute Jet Energy Scale in the DØ Calorimeters", *Nucl. Instrum. Methods,* **A424**, 352 (1999).

[60] B. Abbott *et al.,* (DØ). "The Isolated Photon Cross Section in $p\bar{p}$ Collisions at $\sqrt{s}$=1.8 TeV", *Phys. Rev. Lett.,* **84:**2786, (2000).

[61] The DØ Collaboration. "Report to 1996 PAC: DØ Upgrade: Forward Preshower, Muon System, Level 2 Trigger", Internal DØ Note 2834; Fermilab-FN-639, (1996).

[62] F. Sauli. *Instrumentation in High Energy Physics,* Vol. 9, World Scientific, (1993). See discussion on "Fast Scintillators for High Radiation Levels", by S. Majewski and C. Zorn, Pp. 157-280.

[63] H. Hecht. *Optics,* 2nd Ed., McGraw-Hill & Co. Publishers, (1993).

[64] H. Leutz. "Scintillating Fibers", *Nucl. Instrum. Methods,* **A364** 422 (1995).

[65] M. Adams *et al.,* (for the DØ Collaboration). "A Detailed Study of Plastic Scintillating Strips with Axial Wavelength Shifting Fiber and VLPC Readout", *Nucl. Instrum. Methods,* **A366** 263 (1995).

[66] D. Lincoln, private communication.

[67] D. Lincoln. Report on "CPS Technology", DØ Central Preshower Technical Internal Review, Batavia, Illinois, copies available from the author, (1996).

[68] M. Chung, private communication.

[69] Bicron Corporation, 12345 Kinsman Road, Newbury, OH 44065-9677, USA. Tel. +01 (216) 564-2251.

[70] For CPS: RDN Corporation, 160 Covington Drive, Bloomingdale, IL 60108, USA. Tel. +01 (630) 595-4876.
For FPS: Itasca Plastics, 3750 Ohio Ave., Itasca, IL 60143, Tel. +01 (630) 250-9101.

[71] M. Adams *et al.,* (for the DØ Collaboration). "A New Detector Technique Using Triangular Scintillating Strips to Measure the Position of Minimum Ionizing Particles", *Nucl. Instrum. Methods,* **A378** 131 (1996).

[72] Borcherding *et al.,* (CTT group). "Technical Design Report for the L1/L2 Tracking Trigger", Ver. 5, Internal DØ Note 3551, (1998).

[73] D. Lincoln (for the DØ Collaboration). "A Large Statistics Study of the Performance and Yields of Generation-6 VLPCs (HISTE-VI)", *Nucl. Phys. B.,* **78** 281 (1999).

[74] A. Bross *et al.* "Characterization and Performance of VLPCs for the DØ Upgrade at the Fermilab Tevatron", *Conf. Proc. of the* 5th *Int. Conf. on Position-Sensitive Detectors,* (1999).

[75] Rockwell International, 444 High St., Suite 400, Palo Alto, CA 94301, USA. Tel. +01 (650) 325-7145.

[76] The Boeing Company, 3370 Miraloma Ave., Anaheim, CA 92803, USA. Tel. +01 (714) 762-4195.

[77] N. W. Ashcroft and N. D. Mermin. *Solid State Physics.*, Saunders College Publishing and references therein, (1976).

[78] P. Baringer *et al.* "Cosmic-Ray Tests of the DØ Preshower Detector ", *Nucl. Instrum. Methods,* **A469** 295 (2001).

[79] P. Grannis (for the FPS Group), "SIFT Operating Paramaters for Preshowers", Collection of Internal DØ Documents, (2000-2001).
(URL: http://d0server1.fnal.gov/users/grannis/afe/afe.html)

[80] P. Grannis, private communication.

[81] K. Del Signore (for the DØ Collaboration). "Forward and Central Preshower Detectors for the DØ Upgrade", *AIP Conf. Proc., SciFi97: Workshop on Scintillating Fiber Detectors,* Notre Dame, Indiana, (1997).

[82] A. Patwa (for the DØ Collaboration). "The Preshower Detector for DØ in Run II", document available from the author, New Perspective Conference, Batavia, Illinois (1999).

[83] Arcadia Supply, Inc., 67 Erie Boulevard, Albany, NY 12204, USA. Tel. +01 (518) 434-6213.

[84] J. Kotcher, private communication.

[85] K. Krempetz, private communication.

[86] A. Gordeev, private communication.

[87] J. Kotcher, private communication.

[88] S. Margulies and M. Chung. "Development of a Multichannel Fiber-to-Fiber Connector for the DØ Upgrade Tracker", Photoelectronic Detectors, Cameras, and Systems, eds. C.B. Johnson and E.J. Fenyves, Proc. SPIE 2551, Pp. 10-16, (1995).

[89] M. Chung and S. Margulies. "Development of a Multichannel Fiber-to-Fiber Connector for the DØ Upgrade Tracker", 1995 IEEE Nuclear Science Symposium, Vol. 43, No. 3, (1996).

[90] A. Lucotte. "Forward Preshower Technical Design Review: Trigger Studies", Internal DØ Review Presentation, available from the author, (1998).

[91] A. Lucotte. "Tests of FPS Configuration from the L1 Trigger Point of View", Series of internal DØ documents, (1999).
(see URL: http://www-d0.fnal.gov/~lucotte/FPS/geometry.html)

[92] A. Patwa (for the DØ Collaboration). "Scintillator-Fiber-Based Inner Tracking Detectors for the DØ Experiment at Fermilab", *Conf. Proc. of the 7th International Conference on Advanced Technology and Particle Physics,* Como, Italy, submitted to World Scientific, (2001).

[93] DuPont Corp. Canada, Tel. +11 (905) 821-5193.
(URL: http://www.dupont.com/)

[94] Light transmission in connector channels was measured by the DØ University of Illinois (Chicago) group using a green light-emitting diode and photodiode. Complete description of the set-up appears in Refs. [88, 89].

[95] A. Bross, private communication.

[96] The diamond fly-cut tool for polishing fibers and/or connectors was designed and made in the Physics Department, Fermilab, Batavia, IL 60510, USA.

[97] M. X. Liu, private communication.

[98] A. Patwa *et al.,* (FPS Group). "Mapping Scheme for FPS Large, Small, Special Modules", Collection of Internal DØ Documents, (2000).
(see documents in: //d0server4.fnal.gov/projects/FPS/waveguides/FPS_module_mapping_docs/)

[99] Nichia Corp., 491 Oka, Kaminaka-Cho, Anan-Shi, Tokushima 774-8601, Japan. Tel. +81 (884) 22-2311.

[100] A. Talalaevskii, private communication.

[101] R. Smith and O. Oshinowo, private communications.

[102] The DØ Collaboration. "Technical Specification for a 2 T Solenoid for DØ at Fermilab", Spec. No. E823-94-01, Rev 1, (1994).

[103] E. Gallas (for the DØ Collaboration), "Installation and Alignment of the DØ ICD for Run II", Internal DØ Note 3433, (1999).

[104] K. Krempetz, private communication.

[105] R. Partridge, private communication.

[106] A. Patwa, (FPS Group). "FPS Clear Waveguide Routing Scheme", Internal DØ Document, available from the author, (2000).
(see: //d0server4.fnal.gov/projects/FPS/waveguides/fps_waveguide_cassette_map_final.ppt)

[107] Y. Gershtein. "Simulation of Level 1 Trigger Rates for B meson Decays", Internal DØ Note 3432, (1998).

[108] P. Grannis. "J/ψ Triggers in the Central Region", Internal DØ Note 3506, (1998).

[109] A. Lucotte. "Study of a $J/\psi \to ee$ Trigger in the Forward Rapidity Region for the DØ Upgrade", Internal DØ Note 3566, (1998).

[110] A. Boehnlein. "DØ Level 3 Online Lessons", DØ Internal Document, (2000).
(see URL: http://www-d0.fnal.gov/~cope/l3/L3mainpage.html)

[111] For complete details, see URL: http://www-d0.fnal.gov/computing/tools/software_tools.html and links therein.

[112] T. Sjostrand *et al.* "PYTHIA 6.2: Physics and Manual", *Computer Physics Comm.,* **135:**238; hep-ph/0108264, (2001).

[113] For an extended discussion, see also URL: http://www-d0.fnal.gov/computing /MonteCarlo/MonteCarlo.html and links therein.

[114] A. Patwa *et al.* "Study of the Level 3 Electron Trigger for $B \to J/\psi\ K_s$, where $J/\psi \to ee$ Final States", DØ Internal Note 3952, (2002).

[115] R. Brun *et al.* "ROOT: An Object-Oriented Data Analysis Framework", User's Guide v0.7, Edited by: Fermilab, Batavia, Illinois, (2001).

[116] For more details, see URL: http://www-d0.fnal.gov/computing/trigsim /general/triglists.html and links therein.

[117] K. Yip, private communication.

[118] L. Babukhadia (for the DØ Collaboration). "First Look at Trigger Rates", Internal DØ Document, available from the author, (2001).

[119] T. Bose (for the DØ Collaboration). See URL: http://www .nevis.columbia.edu/∼tulika/trigterms.html for definitions of variables.

[120] A. Patwa (for the DØ Collaboration). Report on "Electron Triggering and B-Physics with J/ψ", Internal DØ Document, available from the author, (2001).

[121] V. Jain, private communication.

[122] V. Büscher. "Calorimeter Clustering Tool for the DØ Level 3 Trigger at Run II", Internal DØ Note, available from the author, (1999).

[123] A. Turcot. Report on "Electron Identification using the CPS", Internal DØ Document, available from the author, (2000).

[124] V. Büscher, private communication.

[125] A. Turcot, private communication.